Institut für Angewandte Photophysik
Fachrichtung Physik
Fakultät Mathematik und Naturwissenschaften
Technische Universität Dresden

Intraband Dynamics in the Optically Excited Wannier-Stark Ladder Spectrum of Semiconductor Superlattices

Dissertation
zur Erlangung des
akademischen Grades
Doctor rerum naturalium
(Dr. rer. nat.)

vorgelegt von

Ben Rosam

geboren am 23. Oktober 1973 in Schlema

Dresden 2004

verteidigt am 22.04.2005

Contents

Publications

Parts of this work have been published or presented:

Articles

[1] B. Rosam, D. Meinhold, F. Löser, V. G. Lyssenko, S. Glutsch, F. Bechstedt, F. Rossi K. Köhler, and K. Leo: *Field-Induced Delocalization and Zener Breakdown in Semiconductor Superlattices*, Phys. Rev. Lett. **86**, 1307 (2001)

[2] F. Löser, B. Rosam, D. Meinhold, V. G. Lyssenko, M. Sudzius, M. M. Dignam, S. Glutsch, F. Bechstedt, F. Rossi, K. Köhler, and K. Leo: *Nonlinear transport in superlattices: Bloch oscillations and Zener breakdown*, Physica E **11**, 268 (2001).

[3] S. Glutsch, F. Bechstedt, B. Rosam, and K. Leo: *Zener tunneling effect of excitons in shallow superlattices*, Phys. Rev. B **63**, 085307 (2001).

[4] D. Meinhold, B. Rosam, F. Löser, V. G. Lyssenko, F. Rossi, Jian-Zhong Zhang, K. Köhler, and K. Leo: *Polarization revival of a Bloch-oscillating wave packet in conjunction with resonant Zener tunneling*, Phys. Rev. B **65**, 113302 (2002).

[5] B. Rosam, K. Leo, M. Glück, F. Keck, H. J. Korsch, F. Zimmer, and K. Köhler: *Lifetime of Wannier-Stark states in semiconductor superlattices under strong Zener tunneling to above-barrier bands*, Phys. Rev. B **68**, 125301 (2003).

[6] Lijun Yang, Ben Rosam, Jean-Marc Lachaine, Karl Leo, and M. M. Dignam: *Intraband Polarization and Terahertz Emission in Biased Semiconductor Superlattices with Full Excitonic Basis*, Phys. Rev. B **69**, 165310 (2004).

[7] B. Rosam, L. Yang, K. Leo, and M. M. Dignam: *Terahertz Generation by Difference-Frequency Mixing of Exciton Wannier-Stark Ladder States in Biased Semiconductor Superlattices*, Appl. Phys. Lett. **85**, 4612 (2004).

[8] Lijun Yang, Ben Rosam, Karl Leo, and M. M. Dignam: *Density-dependent THz emission in biased semiconductor superlattices: From Bloch oscillations to plasma oscillations*, Phys. Rev. B, submitted.

Conference Contributions

[1] **B. Rosam**, D. Meinhold, F. Löser, V. G. Lyssenko, K. Leo, S. Glutsch, F. Bechstedt, and K. Köhler: *Field-Induced Delocalization and Zener Breakdown in Semiconductor Superlattices*, Sixth International Workshop on Nonlinear Optics and Excitation Kinetics in Semiconductors, Marburg, Germany, 2000.

[2] B. Rosam, **D. Meinhold**, F. Löser, V. G. Lyssenko, K. Leo, M. Glück, A. R. Kolovsky, H. J. Korsch, and K. Köhler: *Lifetime Broadening of Wannier-Stark States under Strong Zener Tunneling*, Quantum Electronics and Laser Science Conference, Baltimore, United States, 2001.

[3] **D. Meinhold**, B. Rosam, F. Löser, V. G. Lyssenko, and K. Leo: *Observation of wave packet revivals in semiconductor superlattices*, Quantum Electronics and Laser Science Conference, Baltimore, United States, 2001.

[4] **B. Rosam**, D. Meinhold, F. Löser, V. G. Lyssenko, S. Glutsch, F. Bechstedt, F. Rossi, M. Glück, A. R. Kolovsky, H. J. Korsch, K. Köhler, and K. Leo: *Dynamics of Zener Tunneling in Semiconductor Superlattices*, The 12th International Conference on Nonequilibrium Carrier Dynamics in Semiconductors, Santa Fe, United States, 2001.

[5] **F. Löser**, B. Rosam, D. Meinhold, V. G. Lyssenko, M. Sudzius, M. M. Dignam, S. Glutsch, F. Bechstedt, F. Rossi, K. Köhler, and K. Leo: *Nonlinear transport in superlattices: Bloch oscillations and Zener breakdown*, Rutherford Memorial Workshop on Semiconductor Nanostructures, Queenstown, New Zealand, 2001

[6] D. Meinhold, V. G. Lyssenko, K. Leo, and **B. Rosam**: *Polarization revival of a Bloch-oscillating wave packet at resonant Zener tunneling in GaAs shallow superlattices*, 10th International Symposium on Nanostructures, St. Petersburg, 2002. Proceedings of SPIE **5023**, June 2002, 498–500.

[7] C. P. Holfeld, B. Rosam, **D. Meinhold**, S. Glutsch, W. Schäfer, J. Zhang, M. Glück, H. J. Korsch, F. Rossi, K. Köhler, and K. Leo: *New results on high-field transport in semiconductor superlattices*, invited talk, 26th International Conference on the Physics of Semiconductors , Edinburgh, 2002. Institute of Physics Conference Series Number 171, 177–184, 2002.

[8] **B. Rosam**, D. Meinhold, K. Leo, F. Keck, M. Glück, H. J. Korsch, and K. Köhler: *Strong reduction of the lifetime of Wannier-Stark states in semiconductor superlattices by tunneling to higher bands*, 13th International Conference on Nonequilibrium Carrier Dynamics in Semiconductors, Modena, 2003.

1 Introduction

It is an issue of fundamental importance in solid-state physics to explore the carrier spectrum and carrier dynamics in a periodic potential in the presence of a uniform static electric field. Closely related is the understanding of the field-dependent optical and transport properties of semiconductors. The knowledge is important for applications, for example to the construction of semiconductor heterostructures with engineered properties which have far-reaching applications, with opto-electronic devices being a key example.

In their early works, F. Bloch [1] (1928) and C. Zener [2] (1934) predicted two fundamental quantum mechanical phenomena of competing nature which have been a topic of great interest and controversy over the last decades. For high electric fields, Bloch predicted the oscillatory spatial motion of carriers in the periodic dispersion relation of an energy band. Zener showed that interband tunneling of carriers can occur for high fields leading to an electrical breakdown. These pioneering findings triggered a long-standing theoretical debate, whether the coherent carrier *Bloch oscillations* can exist or instead the intraband coherence is destroyed by *Zener tunneling* to higher bands. A related question is whether or not the Wannier-Stark ladder discretization of the carrier spectrum is observable.

A milestone of research on this issue was the proposal to realize semiconductor crystals with an artificial periodicity, *semiconductor superlattices*, by L. Esaki and R. Tsu [3] in 1970. Advances in semiconductor epitaxial growth technology allowed them to be grown. In superlattices, the carrier band structure can be tailored by the proper choice of their geometry. Therefore, they became a playground for the study of coherent high-field transport phenomena in a periodic potential with applied static electric field. Key experimental results[1] could be obtained: for example, the demonstration of negative-differential-conductivity in transport measurements [7], the observation of Wannier-Stark ladder resonances in the optical spectrum [8, 9] and its dynamic analog, Bloch oscillations in four-wave-mixing experiments [10, 11].

In this work, semiconductor superlattices were employed to investigate the intraband dynamics in the optically excited Wannier-Stark ladder spectrum. The work is dedicated to the investigation of both high-field transport phenomena which were introduced above. It is organized as follows: In the first Chapter, the employed semiconductor heterostructure system is introduced. It is followed by an introductory

---

[1] Reviews on the experimental results on the optical response of superlattices and transport phenomena are given in [4–6].

discussion of the eigenspectrum and the carrier dynamics in a biased superlattice. The third Chapter presents the experimental results of the investigation of Zener tunneling in the tailored miniband structure of superlattices. The fourth Chapter addresses the manipulation of the dynamics of Bloch oscillations detected in Terahertz experiments. Exciton effects are shown to decisively influence the intraband dynamics of Bloch oscillating wave packets. Furthermore, findings are discussed which demonstrate a highly nonlinear Terahertz response of the superlattice mediated by exciton-exciton interaction. Finally, the results are summarized and an Outlook is given.

Zener Tunneling in Semiconductor Superlattices

In 1960, G. H. Wannier [12] found that the energy spectrum of carriers in a periodic potential under a static electric field consists of equally spaced eigenstates, the Wannier-Stark ladder. However, he already pointed out that the associated states are metastable. This was emphasized by Avron et al. [13], who proved that the energy spectrum in general is continuous[2].

In contrast, many of the key experiments in superlattices could be described by one-band models which explicitly neglect tunneling between the bands. However, both experiments and theory showed that tunneling can play a decisive role in superlattices in the high-field regime. Based on the interaction of a finite number of bands (which was first discussed in theory [16]), the signature of resonant tunneling between discrete electron Wannier-Stark ladder states has been observed in the interband spectrum of biased superlattices [17–19]. It was shown that the resonant coupling of states leads to an abrupt delocalization of their wave function. Sibille et al. [20] demonstrated resonances in the current-voltage curve which could be attributed to sequential tunneling transport. Resonant tunneling to above-barrier states in superlattices was observed by Helm et al. [21] in transport experiments and in the infrared absorption of the superlattice.

Recently, it was shown by theory [22] that for high fields, the electrical breakdown can only be described by the coupling of an (in principle) infinite number of bands which causes the concept of localized Wannier-Stark states to fail completely.

In this work, semiconductor superlattices with narrow band gaps were employed to address the investigation of the electrical breakdown due to Zener tunneling. For comparison, the findings for a superlattice with wide gaps are presented where strong resonant tunneling was found to cover the Zener behavior.

In the experiments, the field-dependent evolution of the Wannier-Stark ladder states in the presence of strong intersubband coupling was investigated by detecting the optical interband spectrum[3]. The experiments explored the impact of tunneling

---

[2] For a comprehensive overview on the theoretical approaches to the topic, see [14, 15].

[3] First results on this topic were gained in the author's Diploma work [23]. Selected findings are

on the localization length of the Wannier-Stark ladder states and their polarization lifetime. Superlattices with different geometries were employed, to clarify the influence of the particular miniband structure on the Zener tunneling behavior. The experiments investigated the validity of the Wannier-Stark ladder picture over an extremely large field interval. It is shown that the Wannier-Stark ladder quantization gradually "dissolves" if tunneling comes into play.

Time-resolved experiments were performed to probe the interband polarization decay in the Zener tunneling regime and directly measure the intersubband tunneling rate.

Intraband Dynamics of Exciton Wannier-Stark Ladder Wave Packets

The intraband dynamics of Wannier-Stark ladder wave packets can be directly measured by Terahertz emission experiments [24, 25] which detect the intraband polarization associated with the dipole moment of the excited states.

The investigation of carrier wave packets in semiconductor heterostructures started with Leo et al. [26], who observed wave packet quantum beats in double-quantum well samples by interband pump-probe experiments. Shortly after, Roskos et al. [27] were first to report experimental evidence that the observed wave packet oscillations are associated with carrier oscillations in real space. This was accomplished by the time-resolved measurement of the emitted Terahertz signal. The dynamics of carrier wave packets in the periodic potential of semiconductor superlattices is of special interest because Bloch oscillations can be investigated, allowing for the first observation in interband spectroscopy [10, 11]. Shortly after, Waschke et al. [28] succeeded in demonstrating the Terahertz emission by Bloch oscillations in superlattices.

Interestingly, theory [29–31] predicted that the dynamics of the Bloch oscillating wave packets can be manipulated by controlled optical excitation. A few years later, Sudzius et al. [32] were first to give experimental evidence of this effect. The authors showed the tunability of the Bloch oscillation amplitude in spectrally-resolved four-wave-mixing experiments. However, in interband spectroscopy, the intraband dipole is not directly measured [33, 34]. Therefore, in this work, Terahertz emission experiments were employed to monitor the intraband dynamics of Bloch oscillations under selective optical excitation.

Throughout this work, the results on the Terahertz response of superlattices to the optical interband excitation are discussed in an exciton picture because the findings clearly reveal the significance of Coulomb correlations. First, Bolivar et al. [35] gave experimental evidence of exciton effects in the Terahertz emission of biased superlattices. These findings required the inclusion of Coulomb correlations into a theoretical model [36] of the intraband dynamics of carriers. Surprisingly only a few

---

presented here in order to discuss the topic in a complete and conclusive picture.

experimental studies investigated further the impact of exciton-exciton interactions on the intraband dynamics in superlattices. Instead, important consequences on the Terahertz response were recently predicted in theory. For example, Lachaine et al. [37] found a possible mechanism for stimulated emission due to the exciton asymmetry of the Wannier-Stark ladder. Recently, Liu et al. [38] showed the Coulomb enhancement of intraband transition matrix elements.

In this work, a Terahertz time-domain spectroscopy experiment was set up to investigate the Terahertz emission of a wide band gap superlattice structure. In the experiment, the excitation conditions could be accurately controlled to address the Terahertz emission under selective excitation of the Wannier-Stark ladder spectrum. By means of this experimental technique, the following issues were addressed:

(i) The manipulation of the Bloch oscillation amplitude by selective optical excitation was studied.

(ii) The effect of Coulomb coupling on the Terahertz emission was explored. It is demonstrated that the results can only be explained in an full exciton picture.

(iii) The direct measurement of the intraband dipole of single Wannier-Stark ladder excitons was addressed by the selective excitation with a narrow pump spectrum.

(iv) Effects of the highly nonlinear intraband response of the superlattice were studied which are mediated by Coulomb interactions. This included the investigation of a previously unknown mechanism, the non-adiabatic generation of Bloch oscillations.

(v) The Terahertz generation by difference-frequency mixing was observed under selective optical excitation with two narrow laser lines. The experiments findings demonstrate the resonant enhancement of the Terahertz emission due to exciton interaction.

1.1 The Semiconductor Superlattice: A Model System

In the narrow minibands of semiconductor superlattices, a multitude of novel transport effects have been investigated which cannot be observed in the wide bands of bulk materials. Since the carrier band structure of semiconductor superlattices can be arbitrary designed, they are used as a model system of research of fundamental effects in solid-state physics.

In the search for negative-differential-conductivity devices, Esaki and Tsu [3] published in 1970 the brilliant idea of constructing an artificial periodic semiconductor crystal by growing a periodic structure of alternating layers of semiconductors with different band gaps (see Figure 1.1). It results in a one-dimensional superlattice with a large effective lattice constant (typically on the order of 100 Å). The synthetic periodicity is imposed on the atomic lattice, consequently, the Brillouin zone of the bulk material folds into mini-Brillouin zones with narrow minibands.

To manufacture semiconductor heterosystems, sophisticated epitaxial growth techniques have been developed which reached a high accuracy. These technologies (a valuable overview is given by Fujiwara [39]) allow control of semiconductor growth on a monolayer scale with interface roughnesses also in the monolayer range.

This Section gives a brief survey of the well established heterostructure material system GaAs/(Ga, Al)As which was employed in this work. The band gap of the ternary alloy $\mathrm{Ga_{1-x}Al_xAs}$ (the barrier material) is larger than the band gap of GaAs

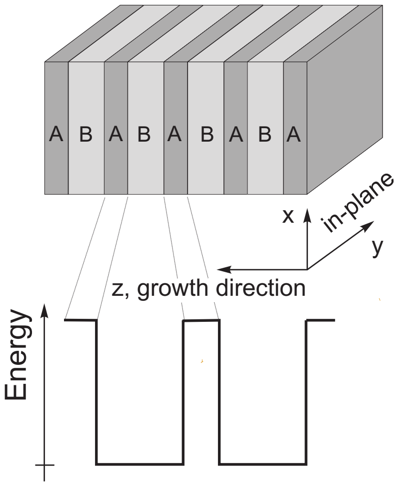

Figure 1.1: Scheme of a superlattice sample: *Top*: Periodically grown layers of semiconductors with different band gaps. The carriers experience quantum confinement in the growth direction, whereas in-plane they move freely. *Bottom*: The lower conduction band edge which is periodically modulated along the growth direction.

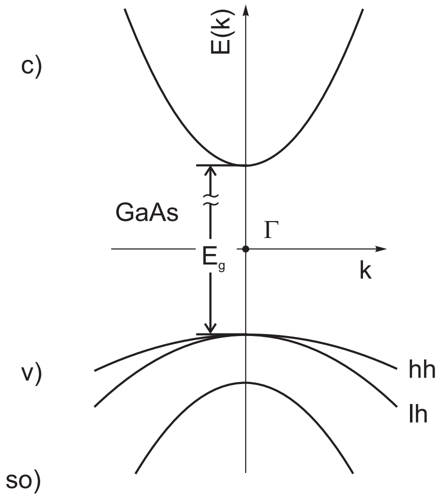

Figure 1.2: Scheme of the conduction, valence and split-off bands for bulk GaAs near the Γ point. The lower valence band is split into a light-hole and a heavy-hole band for $k \neq 0$. The band gap of GaAs is 1.519 eV (0K) [42]. The split-off energy for GaAs is 0.341 eV (at 4.2 K) [42].

(the well material) and can be adjusted by the Aluminum mole fraction x [41],

$$\mathrm{Ga_{1-x}Al_xAs} : \mathrm{E_g}^{\mathrm{Barrier}}(\Gamma, \mathrm{T}=0) = 1.519 + 1.25\mathrm{x}\,[\mathrm{eV}]\,. \tag{1.1}$$

$\mathrm{Ga_{1-x}Al_xAs}$ is a direct semiconductor for $\mathrm{x} \leq 0.4$ which is assumed for all following discussions. Under this assumption, a type I superlattice is established, where holes and electrons are localized in the same layers (the GaAs layers). The small lattice mismatch (less than 1%) of the two materials is a prerequisite for achievement of high-quality hetero-interfaces.

The quantum wells are composed of GaAs. Therefore, the bulk GaAs band structure will be briefly discussed. Figure 1.2 sketches the valence and conduction band of bulk GaAs in vicinity of the Γ-point. Close to the band edge, the dispersion can be approximated by a parabola. From its curvature, the effective mass, $m^{*-1} = (1/\hbar^2)\,\partial^2\mathrm{E}/\partial\mathrm{k}^2$ can be deduced. The conduction band is due to the coupling between the parent atomic s-orbitals. It is twofold degenerate with $\mathrm{j} = 1/2, \mathrm{m_j} = \pm 1/2$. The valence band is made up by the atomic p-orbitals. Due to spin-orbit coupling, it splits into a fourfold degenerate (at $k = 0$) lower valence band with $\mathrm{j} = 3/2$ and a split-off band with $\mathrm{j} = 1/2$. For $k \neq 0$, the lower valence band separates into a heavy-hole (hh) band with $\mathrm{m_j} = \pm 3/2$ and a light-hole (lh) band with $\mathrm{m_j} = \pm 1/2$.

The unit cell of a superlattice is a quantum well. Therefore, we first discuss the potential energy diagram and the energy spectrum for an isolated quantum well (see upper part of Figure 1.3). The rectangular potential is constructed by sandwiching a thin layer of the semiconductor with a small gap between semiconductor

	m^*_e/m_0	m^*_hh/m_0	m^*_lh/m_0
GaAs	0.067	0.51	0.082

Table 1.1: Effective mass of lowest conduction band electrons and lowest valence band holes (heavy and light holes) close to the Γ point (from [40]).

material with a wider band gap. The structure is described by the well thickness a and the band edge offsets. The band gap difference between well and barrier material ($\mathrm{E_g^B - E_g^W}$) is divided into the conduction and the valence band offset. For GaAs/$\mathrm{Ga_{1-x}Al_xAs}$ the conduction band offset ratio ($\Delta\mathrm{E_{cb}}/(\mathrm{E_g^B - E_g^W})$) is 0.58 [41]. Hence, for a typical structure with x = 0.3, the barrier height is around 220 meV for electrons and 160 meV for holes. The modulation of the band edge leads to one-dimensional quantum confinement of the carriers. Thus, the bulk energy bands split into discrete states in the growth direction. To each discrete quantum level $\mathrm{E_n}$, a continuum of states is assigned due to the free motion in the plane of the quantum well. The density of states displays the two-dimensionality of the system. For each subband of the in-plane motion, the density of states is constant and the sum over all states results in a "staircase" dependence.

For the quantum well states, the confinement energy depends on the carrier effective mass. For a quantum well with infinitely high barriers, the quantization energy levels are given by $\mathrm{E_n} = (\hbar^2/2m^*_{\mathrm{e,h}})\,(\pi/a)\,\mathsf{n}^2$ [43], where n is an integer. The eigenenergies are inversely proportional to the effective mass of the carrier. Hence, the degeneracy of the heavy-hole and light-hole band is removed. On the other hand, in-plane the hole masses reverse [43]. Therefore, heavy-hole and light-hole subbands mix for higher in-plane wave vectors.

A superlattice sample (see Figure 1.3) is a periodic assembly of a large number of quantum wells separated by thin barriers. The carriers can couple through the thin barriers. Hence, the degenerate quantum well states interact and broaden into minibands with a width defined by the coupling strength of the states. Due to the high effective mass of holes, the coupling of hole states is small which leads to narrow minibands. The superlattice miniband formation induces a profound change in the density of states.

In principle, the band structure of the superlattice can be derived directly from the atomic states of the material. However, if barrier and well thicknesses are substantially larger than the atomic lattice constant, a representative *effective superlattice potential* can be found. Additionally, the wave functions can be separated into an atomic component and an *envelope function* component. The latter solely describes the confinement effects due to the effective potential. Since only states close to the bulk band edge are under consideration, usually a constant effective mass is assumed (*effective mass approximation*).

From the above considerations, it follows that the band structure of superlattices can be tailored and therefore customized with respect to the physical effects addressed. In this work, the phenomena of Bloch oscillations and Zener tunneling were investigated in superlattices. To study single miniband transport, interminiband tunneling has to be small. Hence, for the investigation of Bloch oscillations, a superlattice with large miniband gaps was employed, whereas the Zener tunneling effect was investigated in superlattices with narrow minigaps.

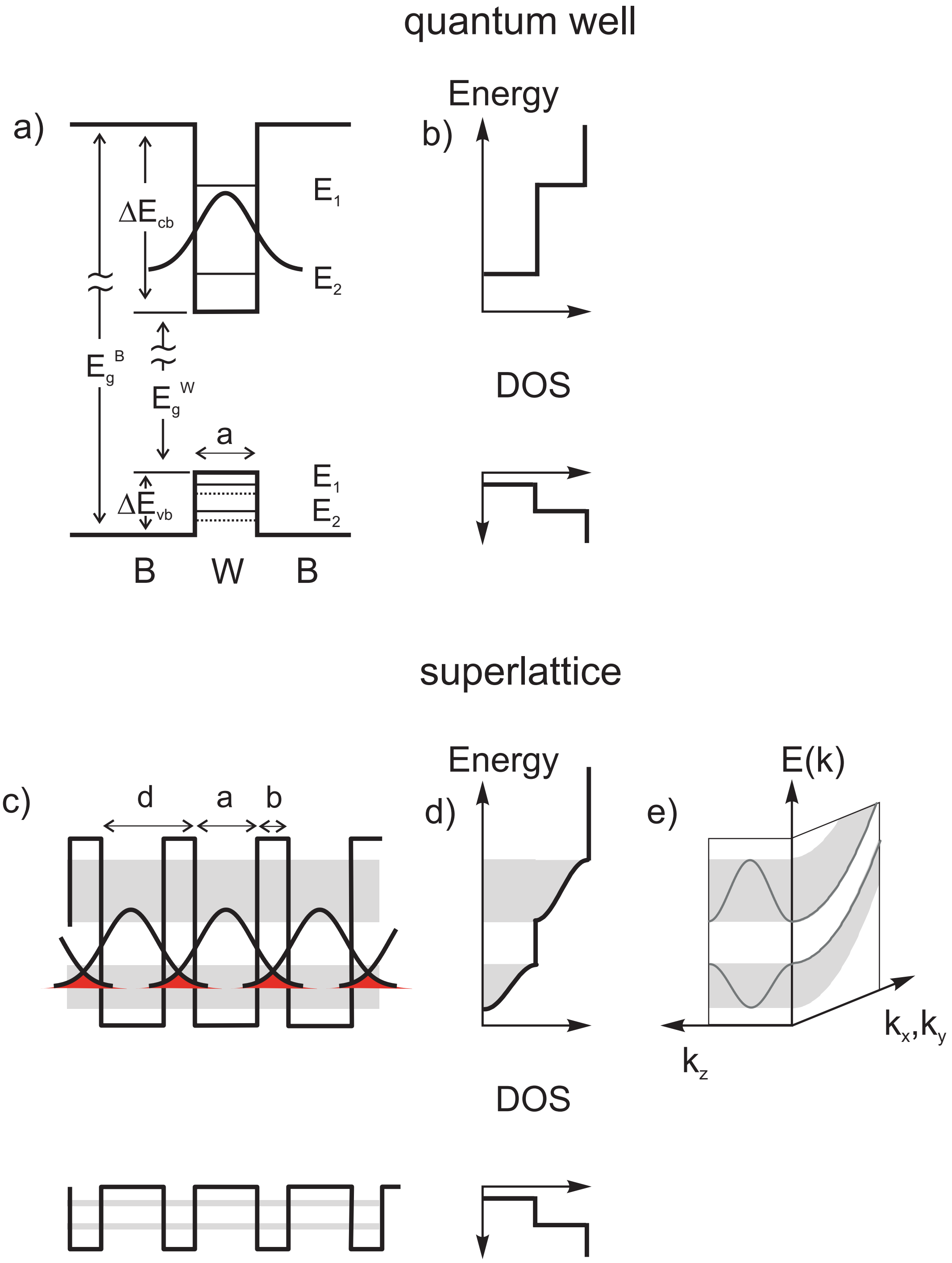

Figure 1.3: $\mathrm{GaAs/(Ga,Al)As}$ - Semiconductor Heterostrutures. *a)* Valence and conduction band edge profile for a quantum well at the Γ-point. **W**ell: GaAs, **B**arrier: $\mathrm{Ga_{1-x}Al_xAs}$. Spatial confinement leads to discrete states which are labeled by $\mathrm{E_n}$. For the lowest electron state, the wave function is sketched. For the valence band, (*solid line*) heavy-holes experience a smaller quantization energy than (*dashed line*) light-holes. *b)* Density of states for the two-dimensional subbands. *c)* Periodic band edge profile of a superlattice with the lattice constant $d = a + b$. The coupling through thin barriers leads to miniband formation. *d)* Density of states for the quasi three-dimensional structure. *e)* Electron miniband with sinusoidal dispersion in the growth direction and a parabolic dispersion of the in-plane motion.

2 The Eigenspectrum of Biased Semiconductor Superlattices

The designable miniband structure of a semiconductor superlattice provides a playground for the investigation of the spectrum and the dynamics of carriers in a periodic potential accelerated by an applied electric field. In this Chapter, the fundamental aspects of finding the energy spectrum of carriers in a biased superlattice are explained[1]. Here, the basis of the treatment is the tight-binding model. In a first step, the miniband spectrum is found for zero field. Secondly, under applied field, in a one-band description, the formation of Wannier-Stark ladder states is shown. The exciton nature of the interband optical excitations is reviewed in the third Section. The full exciton picture provides a three-dimensional description of the superlattice energy spectrum. Next, Bloch oscillations are discussed in the semi-classical and in the Wannier-Stark ladder picture. Furthermore, it is discussed how the dynamics of Bloch oscillating carrier wave packets can be manipulated by selective excitation. In the final Section, the effect of Zener tunneling is introduced. If the coupling between bands cannot be neglected, the carrier states have to be described in a multi-band picture.

2.1 Flat-Field Energy Spectrum of a Superlattice

In the following, the spectrum of a semiconductor superlattice in the absence of an external electric field is discussed. Due to the periodic potential of the bulk semiconductor crystal, the carrier eigenfunctions can be represented as so-called Bloch waves [1],

$$\psi_{\lambda,\boldsymbol{k}}(\boldsymbol{r}) = \frac{1}{\sqrt{V}}\,\mathrm{e}^{i\boldsymbol{k}\boldsymbol{r}}\,u_{\lambda,\boldsymbol{k}}(\boldsymbol{r}); \quad u_{\lambda,\boldsymbol{k}}(\boldsymbol{r}+\boldsymbol{R}) = u_{\lambda,\boldsymbol{k}}(\boldsymbol{r})\,, \tag{2.1}$$

where V is the normalization volume, $\boldsymbol{k}$ the wave vector, $u_{\lambda,\boldsymbol{k}}(\boldsymbol{r})$ the lattice periodic Bloch function of the band with index λ, and $\boldsymbol{R}$ an arbitrary lattice vector.

---

[1] The following textbooks [4, 14, 43, 44] are recommended for further reading.

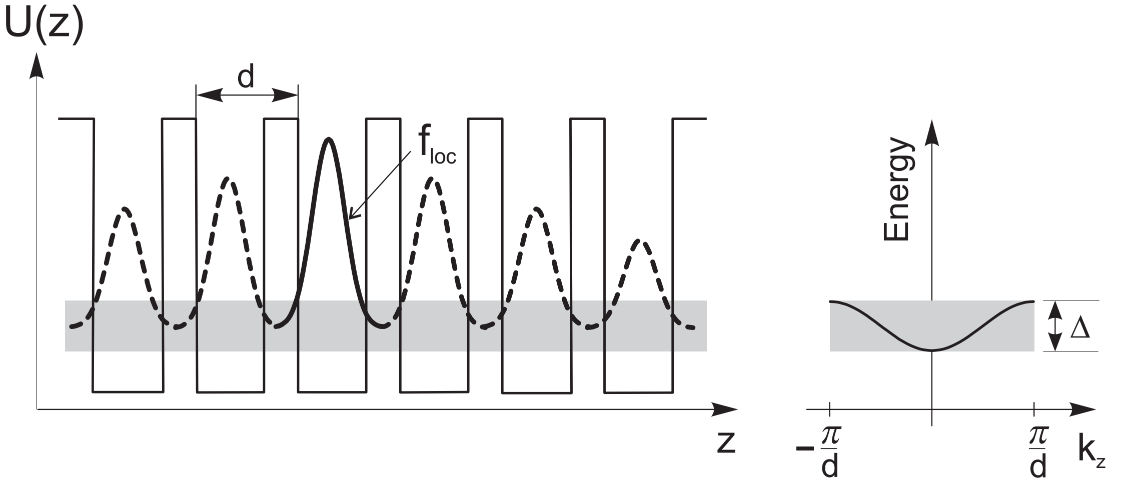

Figure 2.1: *Left*: Schematic representation of a Bloch wave tight-binding eigenfunction for zero field. Only the lowest miniband is shown. *Right*: The sinusoidal dispersion relation is plotted in the Brillouin zone.

The Hamiltonian for carriers in a superlattice potential reads

$$\mathcal{H} = -\frac{\hbar^2}{2m^*_{\|\mathrm{W,B}}}\frac{\partial^2}{\partial \boldsymbol{r}_\|^2} - \frac{\hbar^2}{2m^*(z)}\frac{\partial^2}{\partial z^2} + \mathcal{U}(z)\,. \tag{2.2}$$

The interaction with the atomic lattice is represented by the effective masses, where $m^*_{\|\mathrm{W,B}}$ is the effective mass in the well and in the barrier, respectively. The effective mass in the growth direction is $m^*(z)$. The potential $\mathcal{U}$ describes the periodic superlattice potential, with $\mathcal{U}(z) = \mathcal{U}(z+d)$.

The carriers experience one-dimensional quantum confinement, whereas the direction of confinement (the growth direction, z) and of free motion in the quantum well planes ($(x,y) = \mathbf{r}_\|$) can be treated separately. Additionally, since the superlattice has abrupt hetero-interfaces and the layer thicknesses are much larger than the atomic lattice constant, the carrier eigenfunction can be described in the envelope function approach,

$$\psi_{\mathrm{k_z},\boldsymbol{k}_\|} = \frac{1}{\sqrt{V}}\,\mathrm{e}^{i\boldsymbol{k}_\|\boldsymbol{r}_\|}u_{\boldsymbol{k}}(\boldsymbol{r})\chi_{\mathrm{k_z}}(z)\,, \tag{2.3}$$

where the envelope function $\chi_{\mathrm{k_z}}(z)$ describes the quantum confinement. The envelope function can be found by solving the time-independent Schrödinger equation for the z-dependent terms of the flat-field Hamiltonian (Equation 2.2),

$$\left\{-\frac{\hbar^2}{2m^*(z)}\frac{\partial^2}{\partial z^2} + \mathcal{U}(z)\right\}\Psi(z) = \mathrm{E}\;\Psi(z)\,, \tag{2.4}$$

which is invariant to the action of the translation operator $\mathcal{T}_\mathsf{n}$ which translates z by $\mathsf{n}d$ (n being an integer). Therefore, the envelope function can also be represented as Bloch waves with $\mathrm{k_z}$ as quantum number. For narrow band superlattices, the states can be found with a tight-binding ansatz which has its conceptual counterpart in atomic physics by the LCAO method [43]. The ansatz yields to Bloch wave eigenfunctions follow,

$$\chi_{\mathrm{k_z}}(z) = \frac{1}{\sqrt{V}} \sum_{\mathsf{n}} \mathrm{e}^{i\mathrm{k_z}\mathsf{n}d} f_{\mathrm{loc}}(z - \mathsf{n}d)\,, \tag{2.5}$$

where $f_{\mathrm{loc}}(z)$ are the carrier eigenfunctions of an isolated quantum well. The coupling of the degenerate quantum well levels leads to miniband formation. In the nearest-neighbor approximation, a sinusoidal dispersion relation follows,

$$\mathrm{E}_\lambda(\mathrm{k_z}) = \mathrm{E}^0_\lambda + \mathrm{S}_\lambda + \frac{\Delta_\lambda}{2}\cos(\mathrm{k_z}d)\,, \tag{2.6}$$

where E^0_λ is the single-well quantization energy level and S_λ represents the self-energy. Each eigenstate of the single-well problem gives rise to a miniband which are labeled with the index λ. If no band index is given, the discussion is restricted to the first miniband. The miniband width Δ_λ depends on the spatial overlap of the neighboring states and is given by four times the nearest-neighbor transfer integral:

$$\Delta_\lambda = 4 \int f_{\mathrm{loc},\lambda}(z - d)\mathcal{U}(z) f_{\mathrm{loc},\lambda}(z) dz\,. \tag{2.7}$$

Figure 2.1 summarizes the results in the flat-field case.

2.2 Wannier-Stark Ladder States

In this work, the main interest addresses the case, when carriers in the periodic superlattice potential when subjected to a static electric field. The electric field is applied in the z direction. The one-dimensional Hamiltonian (see Equation 2.4) in this case is

$$\mathcal{H}_{\mathrm{z}} = -\frac{\hbar^2}{2m^*(z)}\frac{\partial^2}{\partial z^2} + \mathcal{U}(z) + eFz\,, \tag{2.8}$$

where eFz is the linear electric field potential. Again, the problem can be described with a tight-binding ansatz: the carrier (envelope) eigenfunctions are expanded into localized single-well functions. In the nearest-neighbor approximation the expansion coefficients are given by Bessel functions of the first kind of order n. The well-known *Wannier-Stark ladder states* are the resulting eigenstates [12,45]. The Wannier-Stark eigenfunctions are

$$\chi_\eta(z) = \frac{1}{\sqrt{V}} \sum_{\mathsf{n}} J_{\mathsf{n}-\eta}\left(\frac{\mathcal{L}}{d}\right) f_{\mathrm{loc}}(z - \mathsf{n}d)\,, \tag{2.9}$$

where

$$\mathcal{L} = \Delta/(eF) \tag{2.10}$$

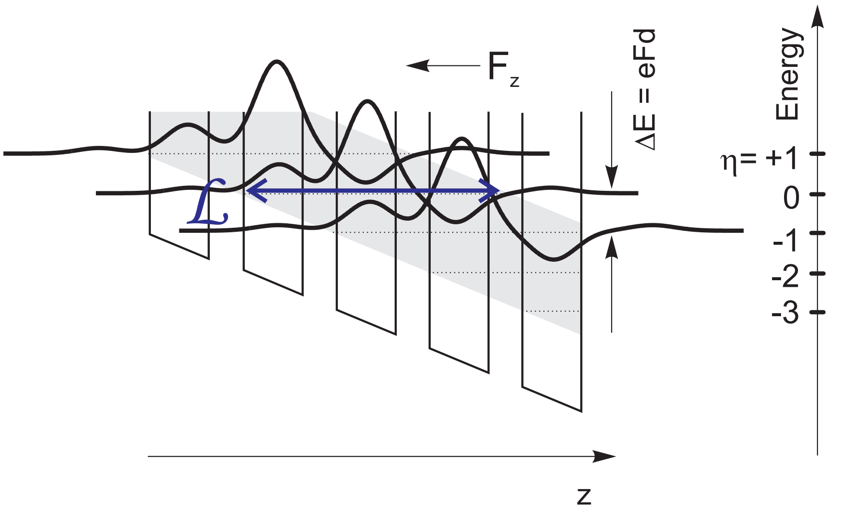

Figure 2.2: Scheme of Wannier-Stark ladder states for electrons. The states expand over several superlattice periods. The characteristic localization length $\mathcal{L}$ can be visualized as the cross-section of the tilted miniband. The states are labeled by the Wannier-Stark ladder index η.

represents a characteristic localization length of the states. The wave functions obey a discrete translation symmetry, $\psi_{\eta+\mathsf{n}}(z) = \psi_\eta(z + \mathsf{n}d)$, with η being an integer.

The resulting eigenspectrum of the carriers is discrete and equidistant, scaling linearly with the electric field strength,

$$\mathrm{E}_\eta(F) = \mathrm{E}_0 + \eta e F d\,. \tag{2.11}$$

It is commonly called *Wannier-Stark ladder*. The energy E_0 is equal to the single-well confinement energy of an arbitrarily chosen well, for which η is zero.

Figure 2.2 illustrates the electron Wannier-Stark ladder states. The applied field removes the degeneracy of the miniband states, leading to a discrete Wannier-Stark ladder spectrum. The energy difference between neighboring states is equal to the change of the electric field potential over a superlattice period. The spatial extent of the states is given by the localization length $\mathcal{L}$. With increasing field, the nearest-neighbor coupling is gradually suppressed and the states experience a localization. This effect is known as *Wannier-Stark localization*[2]. In the high field limit, the wave function turns into the single-well function because only the term $J_0(\mathcal{L}/d \ll 1) \to 1$ contributes to the sum in Equation 2.9[3], ($J_{\mathsf{n}\neq 0}(\mathcal{L}/d \ll 1) \to 0$). The system then resembles a multiple quantum well sample.

---

[2] A milestone of research on the spectrum of biased superlattices was the first experimental evidence for the Wannier-Stark ladder states and their field-induced localization by Mendez et al. [8] and Voisin et al. [9].

[3] The tight-binding ansatz uses field-independent single-well functions. Hence, the quantum-confined Stark effect is not described in this model, which would cause an energetic red-shift and further spatial localization.

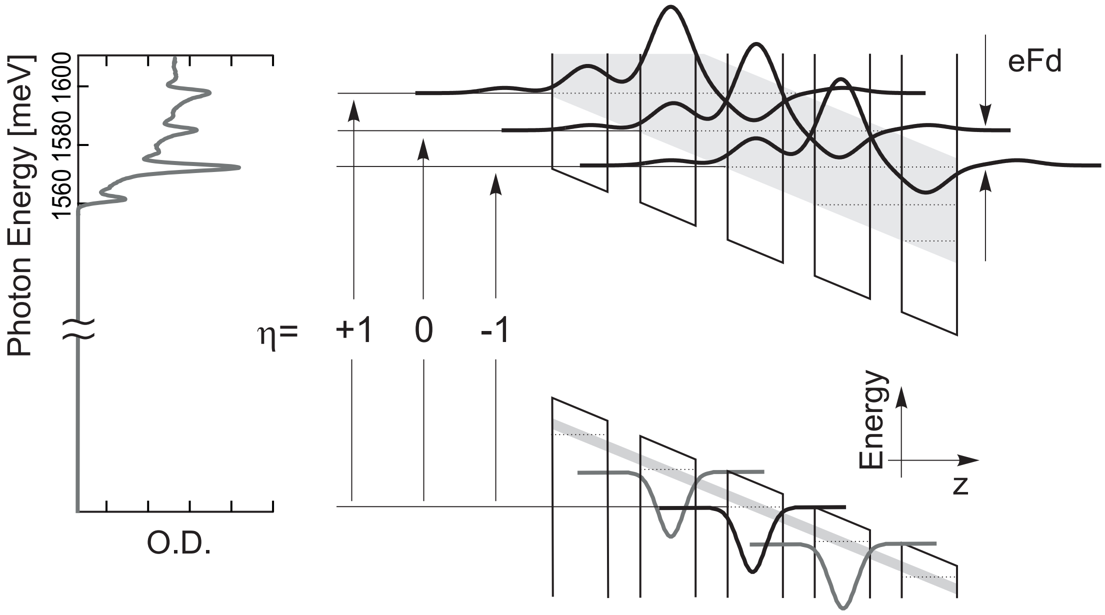

Figure 2.3: *Right*: Optical interband transitions from the localized hole states probe the electron Wannier-Stark ladder. *Left*: Exemplary experimental low-temperature interband absorption spectrum. The absorption peaks can be attributed to particular Wannier-Stark ladder transitions, $\eta = 0, \pm 1$, (which are actually of exciton nature, as it will described in the following Section 2.2.2).

2.2.1 Wannier-Stark Ladder States Detected in the Optical Spectrum

Experimentally, the spectrum of the biased superlattice can be tested by monitoring the optical interband transitions. In Figure 2.3, possible interband transitions between the Wannier-Stark ladder states of electrons and holes are shown. It is seen that the localization length is different for the two kinds of carriers. Differently, the hole state is localized due to its high effective mass, whereas the electron state spans over several superlattice periods. Hence, the electron Wannier-Stark ladder is probed by interband transitions from the localized hole state. Relative to the hole site, the index η labels the transitions to the different electron Wannier-Stark ladder states. With $\eta = 0$, the vertical Wannier-Stark ladder transition is labeled, for which the hole and electron states are centered on the same well. The transition energy for $\eta = 0$ is field-independent. Non-vertical transitions ($\eta \neq 0$) occur with electron states which are centered on adjacent wells. Clearly, for each hole states a Wannier-Stark ladder is observed.

Additionally, from each electron and hole miniband a Wannier-Stark ladder emerges. The visibility of particular ladders in the optical spectrum is determined by selection rules which will be discussed below.

Figure 2.4 depicts the linear field-dependence of the Wannier-Stark ladder transition energies mirroring the linear field-dependence of the eigenenergy of Wannier-

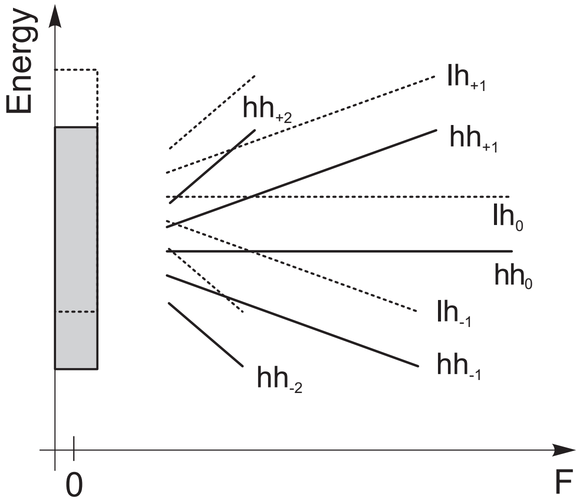

Figure 2.4: Fan chart of Wannier-Stark ladder transitions, representing the linear field-dependence of the states. For zero field, a combined electron-hole miniband is sketched. Transitions are possible between the heavy-hole and electron band (hh$_{\pm\eta}$) (*solid lines*). A second fan is observed for the transitions from the light-hole to the electron band (lh$_{\pm\eta}$) (*dashed lines*).

Stark ladder states (Equation 2.11). The graph is called a "fan chart" because the transitions spread out linearly with the field strength F. Apart from heavy holes, light holes are present which experience a larger confinement energy. Hence, light-hole transitions are observed as a second fan, blue-shifted relative to the heavy-hole fan. However, light-hole transitions (without excitonic effects) have a three times smaller oscillator strength [44] in comparison to the respective heavy-hole transition.

In the following, the selection rules of the optical interband transitions will be briefly discussed. The probability of the optical transition is calculated using Fermi's golden rule. This term multiplied by the photon energy gives the amount of energy absorbed per unit time,

$$\frac{d\mathrm{E}}{dt} = \frac{2\pi}{\hbar} \sum_{\mathrm{f,i}} |\langle \mathrm{c,f}|\boldsymbol{\mu} \cdot \boldsymbol{E}_{\mathrm{L}}|\mathrm{v,i}\rangle|^2 \delta(\mathrm{E}_{\mathrm{c,f}} - \mathrm{E}_{\mathrm{v,i}} - \hbar\omega)\hbar\omega\,, \tag{2.12}$$

where $\boldsymbol{\mu}$ is the vector of the transition operator and $\boldsymbol{E}_{\mathrm{L}}$ the electric field vector of the laser field. In the dipole approximation, the transition operator is given by $\boldsymbol{\mu} = (-e)\mathbf{r}$. It is summed over all possible resonantly coupled initial states in the valence band $|\mathrm{v,i}\rangle$ and final states in the conduction band $|\mathrm{c,f}\rangle$. The absorption coefficient is the total absorbed power, divided by a normalization volume V and the intensity of the incident light (time-average of the Poynting vector, equal to $2|\boldsymbol{E}_{\mathrm{L}}|^2/(\mu_0 c_0)$. It is given by [14]

$$\alpha(\omega) = \frac{\omega}{c_0 n} D(\omega)\,, \text{with} \tag{2.13}$$

$$D(\omega) = \frac{1}{V}\frac{1}{\epsilon_0} \sum_{\mathrm{f,i}} |\langle \mathrm{c,f}|\boldsymbol{\mu} \cdot \boldsymbol{\xi}|\mathrm{v,i}\rangle|^2 \pi\delta(\mathrm{E}_{\mathrm{c,f}} - \mathrm{E}_{\mathrm{v,i}} - \hbar\omega)\,, \tag{2.14}$$

where c_0 the speed of light in vacuum and $\boldsymbol{\xi}$ the polarization vector of the laser field. The term $D(\omega)$ is the optical density of states.

The transition matrix elements $\mu_{\mathrm{cf,vi}}$ can be analyzed in the envelope function representation (Equation 2.3) by separating the spatially fast (the Bloch functions) and slow-varying part (the envelope function) of the eigenfunction. It can then be transformed to a sum over the product of the Bloch function dipole matrix elements and the electron and hole envelope functions at the lattice sites ($\mathbf{R}_i$) [44]:

$$\mu_{\mathrm{cf,vi}} \approx \sum_{\boldsymbol{R}_\mathrm{i}} \chi_\mathrm{e}(\boldsymbol{R}_\mathrm{i})\chi_\mathrm{h}(\boldsymbol{R}_\mathrm{i})\mathrm{e}^{i(\boldsymbol{k}_{\|\mathrm{h}}-\boldsymbol{k}_{\|\mathrm{e}})\boldsymbol{R}_\mathrm{i}} \int\limits_{\mathrm{cell}} u_{\mathrm{c},\boldsymbol{k}}\ \boldsymbol{\mu}\cdot\boldsymbol{\xi}\ u_{\mathrm{v},\boldsymbol{k}} d\boldsymbol{r}\,. \tag{2.15}$$

Importantly, the transition matrix element governs the selection rules. The integral describes the selection rules due to the Bloch functions of the atomic lattice. For GaAs, optical transitions between the p-like valence band states and the s-like conduction band states are allowed because of the parity change which is necessary for the dipole interaction. The exponential factor in the first term calls for vertical in-plane transitions ($\boldsymbol{k}_{\|\mathrm{h}} - \boldsymbol{k}_{\|\mathrm{e}} = 0$). Apart from that, the sum over the envelope function product in the z direction allows only transitions between confined states with the same envelope function symmetry under space reflection. This condition allows for possible transitions between minibands with $(\lambda_\mathrm{e} - \lambda_\mathrm{h}) = 2\mathsf{n}$ (with $\mathsf{n} = 0, 1, 2, \ldots$). The selection rules are strictly valid only for zero field. With applied field, the symmetry is broken and weakly allowed transitions emerge.

Above, the carrier states are found in a one-dimensional picture considering the envelope function component in the growth direction only. As seen, this approach suggests peaks in the absorption spectrum, one for each Wannier-Stark ladder transition. However, for each Wannier-Stark ladder state, an in-plane subband exists. Therefore, the two-dimensionality of the spectrum should rather be mirrored by a stair case-like optical density. Nevertheless, the focus on the one-dimensional picture is justified since in practice the absorption is dominated by a peak structure which resembles the prediction of the one-dimensional model. These absorption peaks are excitonic in nature which will be discussed in the following.

2.2.2 Exciton Wannier-Stark Ladder Transitions

In the previous Sections, carriers are treated as free-particles in a one-dimensional picture. In experiments, however, the superlattice spectrum is usually detected by the photo-injection of electron-hole pairs via optical interband transitions. Consequently, due to the Coulomb interaction, it is rather exciton Wannier-Stark ladders than free-particle Stark ladders which are monitored.

Soon after the first experimental results on Wannier-Stark ladder transitions in superlattices, the properties of the exciton transitions were studied theoretically [46–48] describing experimental spectra in great detail [49, 50]. In the beginning, the models included bound exciton states only. Simulations in a full exciton picture (including the exciton continuum) were first established by Whittaker et al. [51].

In this work, in order to explain the experimental findings, theoretical results based on the exciton theory developed by Dignam and Sipe [47, 48] are presented. Therefore, some fundamental facts about the theory are stated here. First, the authors write down the two-particle Hamiltonian for the exciton envelope function

$$\mathcal{H}(z_{\mathrm{e}}, z_{\mathrm{h}}, r) = \mathcal{H}_0(z_{\mathrm{e}}, z_{\mathrm{h}}, r) + \mathcal{U}^{\mathrm{e}}(z_{\mathrm{e}}) + \mathcal{U}^{\mathrm{h}}(z_{\mathrm{h}}) + eFz \tag{2.16}$$

where the terms $\mathcal{U}^{\mathrm{e,h}}(z_{\mathrm{e,h}})$ are the superlattice potential for electron and hole respectively. The first term comprises the kinetic energies and the Coulomb coupling,

$$\begin{aligned}\mathcal{H}_0(z_{\mathrm{e}}, z_{\mathrm{h}}, r) = & -\frac{\hbar^2}{2\mu(z_{\mathrm{e}}, z_{\mathrm{h}})}\frac{1}{r}\frac{\partial}{\partial r}\left[r\frac{\partial}{\partial r}\right] - \frac{\hbar^2}{2}\frac{\partial}{\partial z_{\mathrm{e}}}\frac{1}{m^*_{\mathrm{ez}}(z_{\mathrm{e}})}\frac{\partial}{\partial z_{\mathrm{e}}} \\ & -\frac{\hbar^2}{2}\frac{\partial}{\partial z_{\mathrm{h}}}\frac{1}{m^*_{\mathrm{hz}}(z_{\mathrm{h}})}\frac{\partial}{\partial z_{\mathrm{h}}} - \frac{e^2}{\sqrt{\epsilon(r^2 + (z_{\mathrm{e}} - z_{\mathrm{h}})^2)}}\,,\end{aligned} \tag{2.17}$$

where r is the in-plane electron-hole separation. The layer-dependent in-plane electron-hole reduced effective mass is given by $\mu^{-1} = m^{*-1}_{\|\mathrm{e}} + m^{*-1}_{\|\mathrm{h}}$. Most importantly, the last term describes the Coulomb coupling of electron and hole motion. That is why, in case of excitons, the confined (z) and the unconfined (x,y) coordinates are coupled [52].

For the in-plane motion, only excitons with vanishing center-of-mass momentum (vertical transitions) ($\boldsymbol{K}_{\|} = 0$) are optically active. Therefore, the center-of-mass in-plane motion is not considered any further.

The exciton is an electrically neutral particle. Hence, it is also invariant under translation of its center-of-mass coordinate in the z direction (by nd) in the presence of an electric field. Therefore, excitons (as two-particle unit) are delocalized[4]. For the z-component, this can be represented by a Bloch wave like ansatz of the exciton envelope function, whereas the Bloch function is given in its spatial representation as a Wannier function [47]

$$\psi_{\mathsf{n}}^{\mathrm{K_z}}(z_{\mathrm{e}}, z_{\mathrm{h}}, r) = \frac{1}{\sqrt{V}}\sum_{\mathsf{m}} \mathrm{e}^{i\mathrm{K_z}\mathsf{m}d}\sum_{\mathsf{l}} b_{\mathsf{l}}^{\mathsf{n}}\phi_{\mathsf{l}}(r, z_{\mathrm{e}} - \mathsf{m}d, z_{\mathrm{h}} - \mathsf{m}d)\,, \tag{2.18}$$

where $\mathrm{K_z}$ is the exciton center-of-mass wave vector in the growth direction. Again, only the ψ_{n}^{0} exciton states are optically allowed. To find the Wannier functions ($W_{\mathsf{l}}^{\mathsf{n}} = \sum b_{\mathsf{l}}^{\mathsf{n}}\phi_{\mathsf{l}}$), the state is expanded into a two-well exciton basis with different electron-hole separation ($\mathsf{l}d$) (illustrated in Figure 2.5). The index n in Equation 2.18 is the discrete quantum number of the motion in the z direction. In the high-field regime (when the states get gradually localized), it becomes the exciton analog of the Wannier-Stark ladder transition index η (see Equation 2.11).

From above arguments on selection rules (see Section 2.2.1), it follows that only exciton envelope functions with s-like symmetry are optically allowed [44]. Therefore,

---

[4] However, optical interband excitation monitors the energy spectrum of the relative motion.

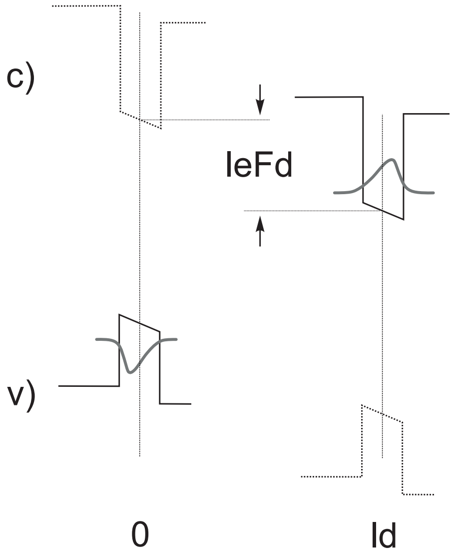

Figure 2.5: Schematic drawing of the two-well exciton ground state in the biased superlattice potential. The single-well electron state in the conduction band and the single-well hole state in the valence band are separated by l superlattice periods. Since the inner-well electric potential drop is treated, the model also accounts for the quantum-confined Stark effect.

s-like variational functions are taken as single-well functions to construct the two-well state basis [47]

$$\phi_{\mathsf{l}}(z_\mathrm{e}, z_\mathrm{h}, r) = \left(\frac{2}{\pi}\right)^{1/2} \lambda \mathrm{e}^{-\lambda r} f_{\mathsf{l}}^{\mathrm{e}}(z_\mathrm{e} - \mathsf{l}d) f_{\mathsf{l}}^{\mathrm{h}}(z_\mathrm{h})\,, \tag{2.19}$$

where the first term describes the in-plane s-like distribution with λ as a variational parameter. The functions $f^{\mathrm{e,h}}$ are the single-well functions for electron and hole which also contain variational parameters. The Hamiltonian is solved in a tight-binding framework. The ground-state wave function is found numerically in a variational approach.

The ground state of the exciton spectrum are bound 1s excitons. However, apart from this, higher excited states exist. In this work, it was found that especially the states of the exciton ionization continuum (of the unconfined relative electron-hole in-plane motion) play a considerable role in intraband dynamics. Recently, Yang et al. [53] incorporated higher excited exciton states in the model by Dignam and Sipe [47]. To describe the continuum states, the two-well basis function $\phi_{\mathsf{l}}(z_\mathrm{e}, z_\mathrm{h}, r)$ (Equation 2.19) is expanded into a set of s-symmetry in-plane states (1s,2s,3s, ... continuum) with increasing exciton Bohr radius.

In conclusion, the effect of the Coulomb interaction on the optically observed spectrum can be summarized as follows:

[I] In a first step, the spectrum of 1s exciton states only is discussed. Due to the Coulomb interaction, the in-plane relative motion is confined. Consequently, the system becomes quasi-one-dimensional along the growth direction. Therefore, the *absorption spectrum of bound excitons well resembles the one-dimensional free-carrier density of states* [22].

In general, the attractive Coulomb interaction alters the electron-hole overlap. This is illustrated in Figure 2.6 which sketches the effective Coulomb miniband

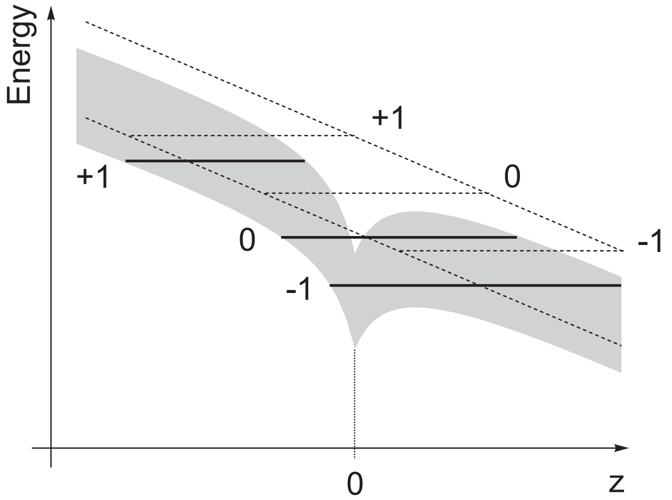

Figure 2.6: Scheme of the effective miniband structure (*shaded area*) for the relative electron-hole motion. The Coulomb potential of the hole localized at $z = 0$ is superimposed on the linear electric field potential. The exciton Wannier-Stark states are marked as *solid lines*. For comparison, the equidistant free-particle states are plotted as *dotted lines*.

potential for an electron. Obviously, that the Wannier-Stark ladder states with negative η will have a larger probability density at the hole site (at $z = 0$) compared to states with positive η. The Coulomb attraction enhances the effective electric field strength for electrons in the $\eta > 0$ state and weakens it for $\eta < 0$. Hence, an *asymmetry is induced on the Wannier-Stark ladder* in term of oscillator strength and exciton binding energy. Both quantities are larger for $\eta < 0$ than for $\eta > 0$ (if states with equal $|\eta|$ are compared) since they scale with the overlap integral. The Coulomb interaction leads to a *non-equidistant Wannier-Stark ladder* splitting. Thus, Equation 2.11 has to be modified to

$$\mathrm{E}_\eta(F) = \mathrm{E}_0^{free} + \eta eFd - \mathcal{E}_\eta(F)\,, \tag{2.20}$$

where the term $\mathcal{E}_\eta(F)$ represents the field-dependent exciton binding energy. As stated above, the binding energy varies for the different exciton states. Therefore,

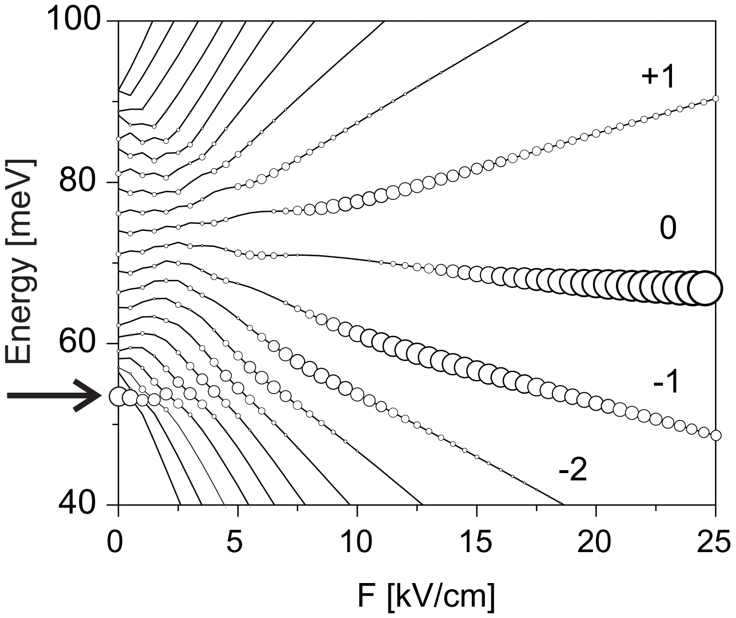

Figure 2.7: Calculated exciton fan chart of 1s heavy-hole excitons. The energy axis is given relative to the band GaAs edge. The diameter of the circles correspond to the oscillator strength of the transitions. The arrow marks the energetic position of the flat-field exciton.

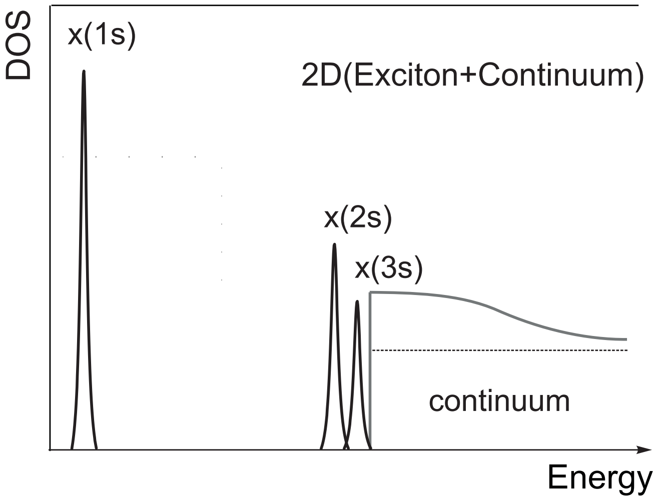

Figure 2.8: Two-dimensional exciton spectrum of a quantum well. Apart from the ground state (1s), higher bound exciton states (2s,3s) and the continuum states are shown. Due to Coulomb interaction, the optical density of states for the continuum is larger at the band-edge than for high-energy transitions (*dashed line*, non-interacting case). This effect is described by the Sommerfeld factor.

for low field strengths, exciton states with different η may cross in energy in cases where the difference in binding energy exceeds the electric field splitting [50]. The effect is particularly prominent in narrow band superlattices. Additionally, it is observed that exciton transitions with negative η strongly couple to the zero field miniband exciton state when both become degenerate (discussed in [54]).

The effects are illustrated in Figure 2.7 which displays the calculated 1s exciton fan chart of an $a = 67\,\text{Å}$, $b = 17\,\text{Å}$, GaAs/Ga$_{0.7}$Al$_{0.3}$As superlattice. The calculation was carried out by M. M. Dignam according to the Dignam and Sipe model [47]. In the low-field range, the transitions with negative η have a larger oscillator strength compared to their counterparts with positive index. The Coulomb-induced non-equidistance of the Wannier-Stark transitions and the coupling to the flat-field exciton state are also observed. Since the Coulomb effects scale with the electron-hole overlap, they are only significant for transitions with small index and for low field strength.

[II] In a second step, the complete exciton spectrum is considered. Figure 2.8 shows a

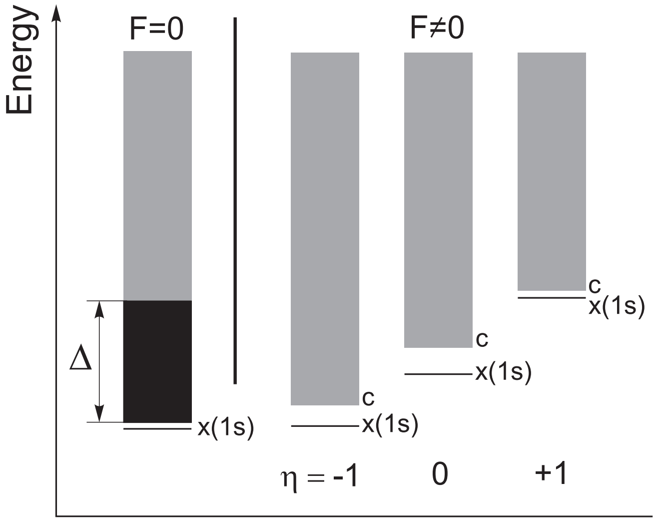

Figure 2.9: Illustration of the three-dimensional exciton Wannier-Stark ladder spectrum. *Left*: For $F = 0$, a flat-field exciton state is observed energetically below the miniband. *Right*: In the Wannier-Stark regime, due to the electric-field driven localization, the exciton states become more and more two-dimensional. Transitions to bound excitons (*bars*) and to exciton continuum subbands (*shaded rectangles*) are observed.

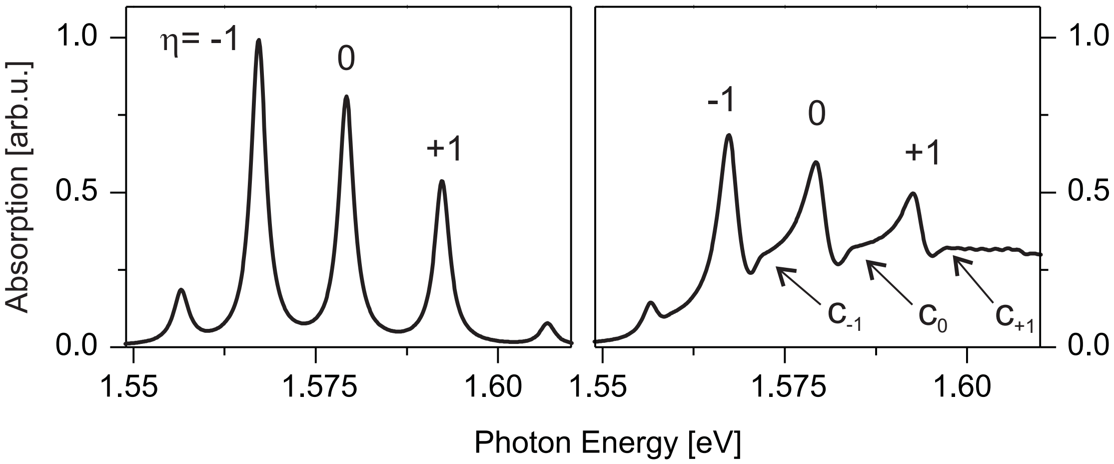

Figure 2.10: Theoretical heavy-hole exciton absorption spectra for $F = 15$ kV/cm. *Left*: Without exciton continuum states: The asymmetry of the transitions oscillator strength is clearly seen. *Right*: With exciton continuum included: The continuum subband edges are marked by c_η.

schematic drawing of the exciton spectrum in a quantum well. Excited bound exciton states as well as continuum states are plotted. The Coulomb interaction redistributes oscillator strength to lower energy. It modifies the step-like two-dimensional optical density of states. Figure 2.9 schematically illustrates the exciton Wannier-Stark ladder spectrum. In the flat-field case, an exciton forms energetically below the miniband. For an applied field, the degenerate exciton states decouple in exciton resonances of the Wannier-Stark ladder transitions.

Interestingly, the Coulomb coupling also mediates the quantum mechanical interference between the optical transitions to (i) bound exciton states and to (ii) the degenerate continuum states of energetically lower Wannier-Stark ladder excitons. The effect is known as *Fano resonances* [55]. The Fano effect in superlattices was predicted in theory [51, 56] and recently investigated in the optical spectrum of superlattices by Holfeld et al. [57].

In Figure 2.10, two calculated absorption spectra (by Yang [53]) of an $a = 67\,\text{Å}$, $b = 17\,\text{Å}$, GaAs/Ga$_{0.7}$Al$_{0.3}$As superlattice are shown which nicely illustrate the statements made above. The left absorption graph gives the 1s exciton ground state absorption only. In the graph on the right hand side, continuum states are included. Small steps mark the band edges of the continuum subbands. Fano broadening mainly becomes visible by the asymmetry of the absorption peaks. Experimental absorption spectra are discussed in detail in the following Chapter 3.

2.3 Wave Packets of Wannier-Stark Ladder States: Bloch Oscillations

In this Section, the effect of carriers performing Bloch oscillations in a periodic potential in the presence of a static electric field is surveyed. The phenomenon will first be introduced in the k-space framework, the semiclassical picture. In the second part, the description based on Wannier-Stark ladder states is discussed. In this framework, it will be discussed how the composition of the Bloch oscillating wave packet can be directly tailored by selective optical excitation, allowing the optical control of the Bloch oscillation dynamics. The textbooks [4, 5] and review articles [25, 58] are especially recommended for further detailed reading.

In k-space, the situation was first theoretically addressed by F. Bloch [1] as early as in 1928. Using semiclassical arguments, he formulated his well-known acceleration theorem

$$\hbar \frac{\partial \boldsymbol{k}}{\partial t} = e\boldsymbol{F}\,, \tag{2.21}$$

from which follows that the wave vector $\boldsymbol{k}$ of the carrier Bloch state changes linear with time if a dc field is present,

$$\boldsymbol{k} = \boldsymbol{k}_0 + e\boldsymbol{F}t/\hbar\,. \tag{2.22}$$

Therefore, a carrier wave packet (formed by a symmetric distribution of superposed k-states, centered around some $\boldsymbol{k}_c$) will move with a real-space group-velocity given by the gradient of the dispersion relation

$$\hbar \boldsymbol{v}(\boldsymbol{k}_c) = \left. \frac{\partial \boldsymbol{E}(\boldsymbol{k})}{\partial \boldsymbol{k}} \right|_{\boldsymbol{k}_c} . \tag{2.23}$$

In this picture, the wave functions are still given by Bloch waves, whereas the effect of the dc field on the states is considered by a time-dependent $\boldsymbol{k}$. These wave functions are known as Houston functions [59].

For a gedanken experiment, a wave packet is assumed to be centered around the Γ-point when the field, parallel to the growth direction, is switched on. For a superlattice, a sinusoidal dispersion relation was found (Equation 2.6). Thus, the real-space group-velocity of the wave packet is given by

$$v(t) = \frac{\Delta d}{2\hbar} \sin\left(\frac{eFd}{\hbar} t\right) . \tag{2.24}$$

This corresponds to a spatial oscillation of the wave packet:

$$z(t) = z_0 - \frac{\Delta}{2eF} \cos\left(\frac{eFd}{\hbar} t\right) . \tag{2.25}$$

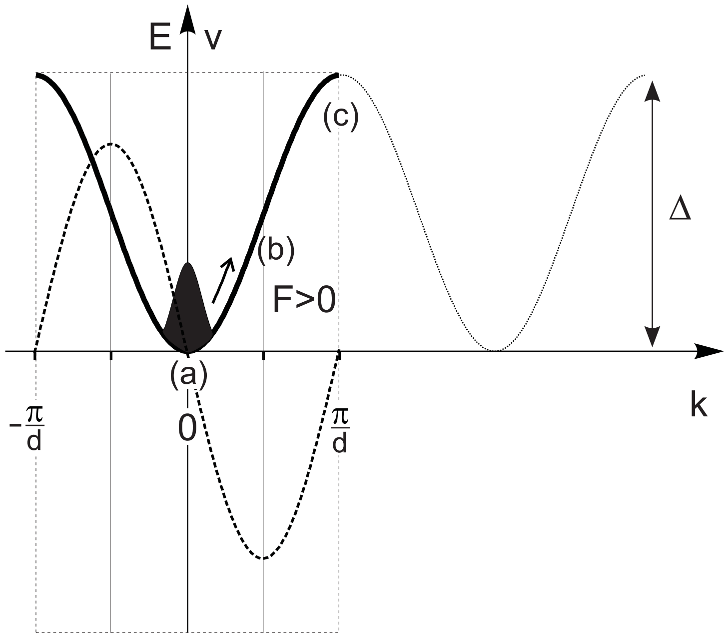

Figure 2.11: Schematic illustration of the coherent, field-driven motion of a carrier wave packet (described in the text). (*thick solid line*) The dispersion relation in the reduced Brillouin zone. (*dashed line*) The real-space velocity v is the first derivative of the dispersion with respect to k.

In Figure 2.11, the wave packet motion is illustrated in the reciprocal space. The wave packet accelerated by the static field gains kinetic energy by traveling along the dispersion. It reaches the maximal real-space velocity at the miniband center (b), where the curvature of the dispersion changes sign, so does the carrier effective mass. When the Brillouin zone boundary is reached (c), the wave packet is Bragg reflected by the superlattice potential and reverses its propagation direction in space. By the subsequent deflection at the lower miniband edge, the wave packet completes a full Bloch oscillation cycle. The phenomenon is independent of the particular shape of the dispersion relation and is known as *Bloch oscillations*[5].

From Equation 2.25, expressions can be derived for the Bloch oscillation frequency ω_B (Bloch oscillation period $T_\mathrm{B} = \frac{2\pi}{\omega_\mathrm{B}}$) as well as the Bloch oscillation amplitude L_B,

$$\omega_\mathrm{B} = \frac{eFd}{\hbar} \longrightarrow T_\mathrm{B} = \frac{h}{eFd}\,, \tag{2.26}$$

$$L_\mathrm{B} = \frac{\Delta}{eF}\,. \tag{2.27}$$

It is evident that the semiclassical Bloch oscillation amplitude (Equation 2.27) is equal to the localization length of Wannier-Stark ladder states (Equation 2.10) which indicates the analogy between the Houston function picture and the Wannier-Stark state picture. Indeed, F. Rossi [58] pointed out that these two pictures are equivalent quantum-mechanical representations which follow from different gauges of the electro-magnetic potential. In the Wannier-Stark picture (which will be discussed in the following Section 2.3.1), Bloch oscillations originate from the quantum interference between different Wannier-Stark states.

---

[5] Actually, Bloch oscillations were first predicted by C. Zener [2].

So far, Bloch oscillations could not be observed in bulk crystals, because the coherent carrier motion is destroyed by scattering and tunneling processes before the carrier can fulfill a complete Bloch cycle[6]. The condition for the observation of Bloch oscillations can be written as $\tau\omega_B \gg 1$ (where here τ is an effective scattering time). In this context, bulk crystals are not favorable, because the Bloch oscillation period is long and scattering as well as tunneling rates are high. For instance, in bulk GaAs a very efficient momentum scattering has been shown [61][7]. Recently, an extremely fast intervalley transfer ($\Gamma \rightarrow L$) in $\{100\}$ GaAs (on the order of 20 fs [63]) was demonstrated which is an additional mechanism inhibiting Bloch oscillations.

However, in semiconductor superlattices, the concept of the Wannier-Stark ladder (the spectral analog of Bloch oscillations) could be experimentally verified. Wannier-Stark ladder states in the superlattice spectrum were first reported in photoluminescence and electroluminescence measurements [8, 9]. Due to the artificial periodicity of superlattices, the bulk bands fold into a mini-Brillouin zone. Thus, the Bloch oscillation period shrinks by a/d (where a is the atom lattice constant and d the superlattice period). Indeed, Bloch oscillations could be observed in biased superlattices by time-resolved optical experiments. The first proof was accomplished by the detection of quantum beat oscillations in four-wave-mixing experiments [10, 11]. These first experiments triggered an intense research on this phenomenon. Key experimental findings are comprehensively reviewed in [4]. Apart from investigations in biased superlattices, Bloch oscillations were also observed in alternative systems, e.g., for cold atoms in accelerating optical lattices [64], and for light propagation in periodic dielectric systems [65, 66].

2.3.1 Manipulation of the Dynamics of Bloch Oscillations

In this work, the manipulation of the dynamics of Bloch oscillations was investigated for spectrally selective excitation. In the following, the underlying physics will be surveyed in the Wannier-Stark ladder picture. In theory [30, 67], this matter was illustratively addressed by analyzing the Bloch wave packet evolution under different excitation conditions.

In the Wannier-Stark picture, Bloch oscillations are quantum beats between Wannier-Stark ladder transitions excited via a common ground states (the localized hole state). The electron wave packet can then be represented by the superposition

---

[6] For fast scattering, the carriers stay close to the bottom of the miniband and move at a constant drift velocity. This leads to Drude transport [60]. Instead, in the absence of scattering, Bloch oscillations inhibit transport causing a dynamic localization of the carriers [6].

[7] A comprehensive overview on experimental results on scattering processes in semiconductors is given in [62]

of Wannier-Stark ladder states (Equation 2.9) with amplitudes C_η

$$\Phi(z,t) = \sum_\eta C_\eta \mathrm{e}^{-i\eta\omega_\mathrm{B} t} \sum_\mathsf{n} J_{\mathsf{n}-\eta}\left(\frac{\mathcal{L}}{d}\right) f_\mathrm{loc}(z - \mathsf{n}d)\,. \tag{2.28}$$

The quantum beat frequency is given by the eigenenergy differences of the states which corresponds to the Wannier-Stark ladder splitting[8]. The wave packet oscillates with $\omega_\mathrm{B} = eFd/\hbar$ which equals the Bloch frequency found in the semiclassical picture (Section 2.3).

The position of the wave packet centroid is given by the expectation value of z [30]

$$\langle \Phi \mid z \mid \Phi \rangle = d \sum_\eta C_\eta^2 \eta + \cos(\omega_\mathrm{B} t)\ \mathcal{L} \sum_\eta C_{\eta-1} C_\eta\,, \tag{2.29}$$

which corresponds to an effective electron-hole displacement associated with an *electric dipole in the z direction*. The first term in the above Equation 2.29 describes a static displacement of the wave packet relative to the hole site. The second term tells that the quantum interference of the Wannier-Stark ladder states leads to a spatial oscillation of the wave packet centroid with an amplitude given by $A_\mathrm{z} \equiv \mathcal{L} \mid \sum C_{\eta-1} C_\eta \mid$ with $\sum C_\eta^2 = 1$. The upper limit of the Bloch oscillation amplitude is the semiclassical amplitude with $\mathcal{L} = L_\mathrm{B}$. However, it is possible to choose the initial conditions such that $A_\mathrm{z} \ll \mathcal{L}$. In particular, the amplitudes C_η can be chosen such that the resulting wave packet has a zero amplitude ($A_\mathrm{z} = 0$) [29–31]. In this case, it would evolve in a so-called *breathing mode*, expanding and contracting symmetrically.

In optical experiments, the Bloch wave packet is coherently excited by a short laser pulse whose spectrum has to encompass at least two Wannier-Stark ladder transitions. By controlling the spectral position and width of the laser pulse, one can control the initial wave packet conditions and consequently its evolution. This will be discussed in the following. If a transform-limited laser pulse with a Gaussian spectrum is incident, it would compose a wave packet of Wannier-Stark ladder states according to Equation 2.28 with amplitudes [30],

$$C_\eta \propto \frac{O_\eta}{\Omega_\mathrm{L}}\, \mathrm{e}^{-(\mathrm{E}_\eta - \hbar\omega_\mathrm{L})^2/2(\hbar\Omega_\mathrm{L})^2}\,. \tag{2.30}$$

The exponent describes the spectral weight of the Gaussian laser pulse at the Wannier-Stark ladder transition energy. The central laser pulse energy is given by $\hbar\omega_\mathrm{L}$, and the spectral width by Ω_L. The term O_η is proportional to the overlap integral between the electron Wannier-Stark ladder state (centered at ηd) and the hole wave function localized at $z = 0$. The O_η are the one-dimensional interband

---

[8] The system is described by only one Bloch frequency. This is a representation of the sinusoidal dispersion relation which follows from the approximation of nearest-neighbor coupling. If terms beyond the nearest neighbor coupling are taken into account, higher harmonics would appear.

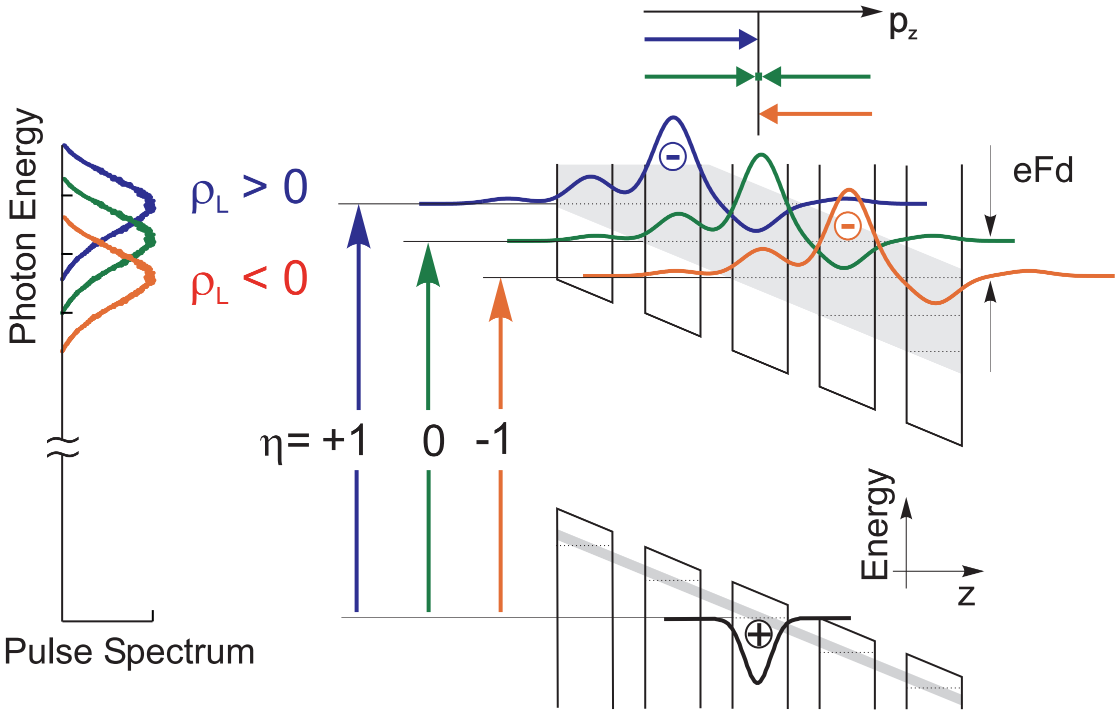

Figure 2.12: Schematics of the excitation of the Wannier-Stark ladder by laser pulses with different central energies. For $\varrho_\mathrm{L} < 0$ ($\varrho_\mathrm{L} > 0$) the laser spectrum mainly excites Wannier-Stark ladder transitions with $\eta < 0$ ($\eta > 0$). The electric dipole between the positive hole charge and the negative charge of the electron wave packet is denoted by p_z. It changes sign for excitation below and above the Wannier-Stark ladder center.

transition matrix elements (see Equation 2.15) which can be calculated according to [30]

$$O_\eta = J_{-\eta}\left(\frac{\mathcal{L}}{d}\right)\left[\frac{2}{\pi a_0^2}\right]^{1/2}\int dx f^\mathrm{e}(z_\mathrm{e}=x)f^\mathrm{h}(z_\mathrm{h}=x)\,, \tag{2.31}$$

where a_0 is the in-plane exciton Bohr radius. It is good to note that the term $J_{-\eta}$ is the tight-binding-single-well function amplitude of the electron at the hole site. The eigenstates are 1s Wannier-Stark ladder exciton states. However, for simplicity, here, exciton effects in the z direction are ignored.

Firstly, the influence of the spectral width of the exciting laser pulse on the Bloch oscillation dynamics is discussed in two limiting cases. In case the width is smaller than the Wannier-Stark ladder splitting, only a single Wannier-Stark ladder state is excited and no Bloch oscillation occurs. If, on the other hand, the spectral width of the pulse is comparable to the miniband width, all Wannier-Stark ladder states are combined in the wave packet. This symmetric excitation around the Wannier-Stark ladder center leads to a breathing motion with zero amplitude. For both modes of excitation, the representation in k-space would be a fully occupied dispersion relation with no net velocity of the carriers; which in the first case is due to the "long-lasting" excitation process ($1/\Omega_\mathrm{L} > T_\mathrm{B}$) and in the second case due to the

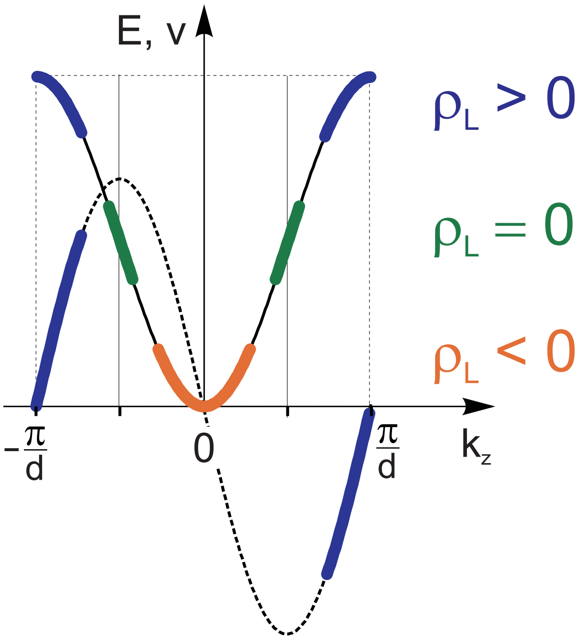

Figure 2.13: Corresponding to Figure 2.12, the excitation by laser pulses at different central energies is illustrated in the k-space picture. The corresponding cases $\varrho_\mathrm{L} < 0$ (excitation at the bottom), $\varrho_\mathrm{L} = 0$ (at the center) and $\varrho_\mathrm{L} > 0$ (at the upper edge of the miniband) are shown. For $\varrho_\mathrm{L} = 0$, each Bloch state with $v(\mathrm{k})$ has a counterpart Bloch state with $-v(-\mathrm{k})$ resulting in a breathing motion. For illustration, the velocity distribution of the wave packet constituents is depicted for excitation with a high-energy pulse. In general, a spectrally broad distribution will cause a small spatial amplitude, because a large portion of the distribution moves with opposite velocity.

broad laser spectrum.

Secondly, for a fixed spectral width of the laser pulse, let us consider the influence of the laser pulse energy. In the following, the laser energy is given relative to the vertical Wannier-Stark ladder transition energy (the energetic center of the Wannier-Stark ladder), $\mathrm{E}_{\eta=0}$. For this, the detuning parameter $\varrho_\mathrm{L} = (\hbar\omega_\mathrm{L} - \mathrm{E}_{\eta=0})/\hbar\omega_\mathrm{B}$ is introduced. In general, it can be seen from simulations [47] that the wave packet amplitude increases with increasing $|\varrho_\mathrm{L}|$. The semiclassical limit can be reached if the laser is detuned far from the Wannier-Stark ladder center. For a central excitation of the Wannier-Stark ladder (i.e., $\varrho_\mathrm{L} = 0$) the wave packet oscillates in a breathing mode. The different excitation schemes are summarized in Figure 2.12.

The corresponding excitation schemes in k-space are depicted in Figure 2.13. For $\varrho_\mathrm{L} = 0$, the miniband is excited at its center which results in the breathing motion. For an excitation with $\varrho_\mathrm{L} < 0$, a k-distribution close to the miniband bottom is excited, and for $\varrho_\mathrm{L} > 0$ miniband a distribution close to the upper band edge, respectively. In this picture, it becomes clear that a k-distribution favorable to reach the semiclassical amplitude limit can only be created for an excitation far off the miniband center.

In the following, the influence of both parameters, the laser pulse energy and the spectral width of the pulse, on the permanent dipole and the oscillation amplitude of the wave packet is surveyed in more detail by simulating the wave packet evolution for $\varrho_\mathrm{L} < 0$, $\varrho_\mathrm{L} = 0$, and $\varrho_\mathrm{L} > 0$. The results are shown in Figure 2.14. The wave packets were calculated according to Equation 2.28 of an $a = 67\,\text{Å}$, $b = 17\,\text{Å}$, $\mathrm{GaAs/Ga_{0.7}Al_{0.3}As}$ superlattice. An electric field of 14 kV/cm corresponds to a localization length $\mathcal{L} = 2.3d$. The excitation parameters are described in detail in the figure caption.

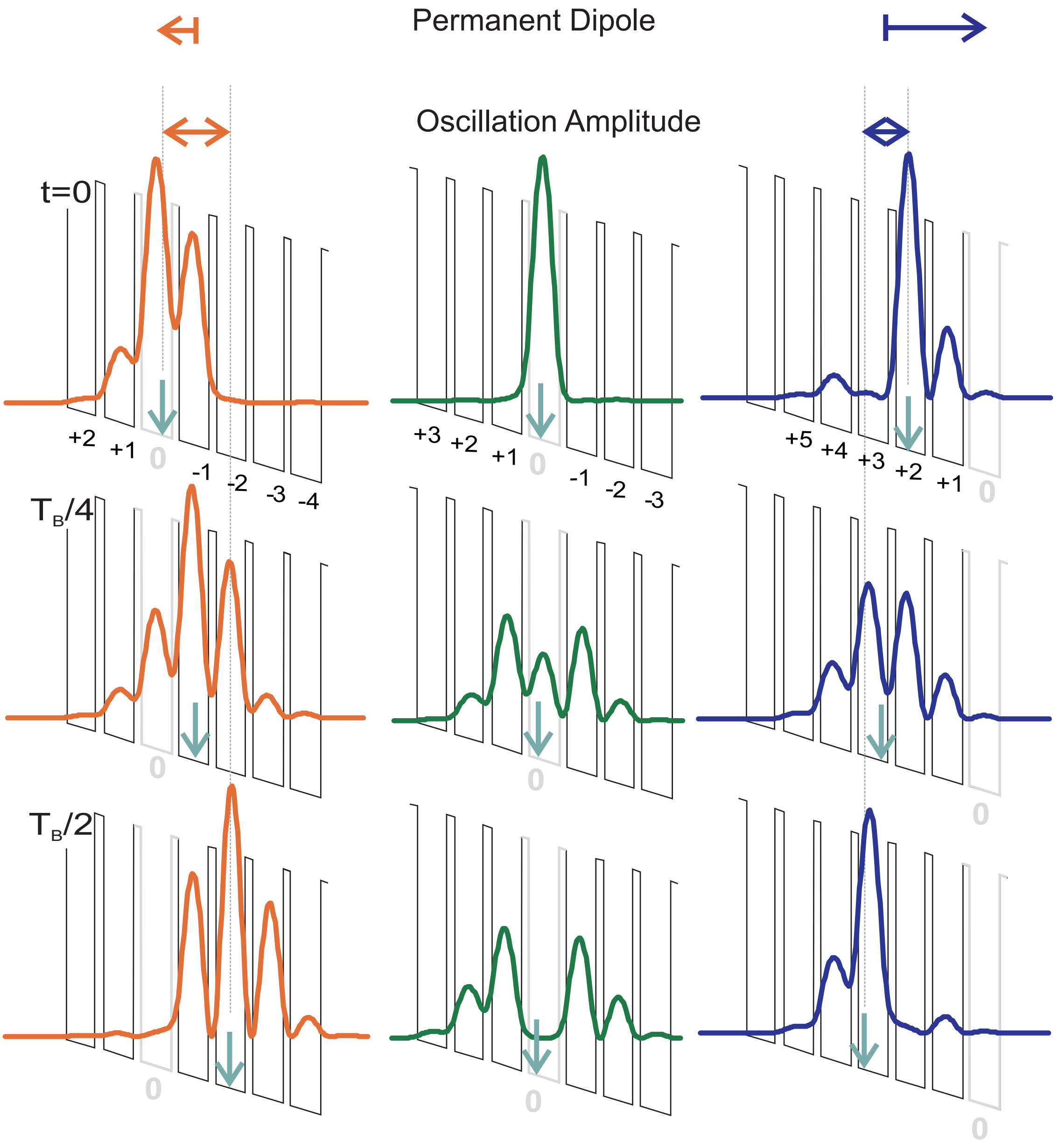

Figure 2.14: Wave packet dynamics for different excitation conditions. The wave packet dynamics is snap-shot in the first half Bloch cycle. The vertical arrows mark the wave packet centroid. The top horizontal arrows give the permanent electric dipole and the dipole of the electron Bloch oscillation relative to the localized hole. *Left* : The Gaussian laser pulse has a spectral width of $\Omega_\mathrm{L}/\omega_\mathrm{B} = 1.4$. The pulse energy is at $\varrho_\mathrm{L} = -2.5$. Thus, the transitions with $\eta = [-5, -4, -3, -2, -1, 0]$ are excited. The amplitudes of the wave packet constituents (Equation 2.30) are calculated to be $C_\eta \propto [0, 0, 0.1, 0.24, 0.42, 0.2]$. The wave function is already localized to a certain extent, therefore $\eta = -5, -4$ are not excited. *Center* : Symmetric excitation of the Wannier-Stark ladder around its center with $\Omega_\mathrm{L}/\omega_\mathrm{B} = 1.4$ and $C_\eta \propto [0.09, 0.7, 1, -0.7, 0.09]$. It leads to a breathing motion. *Right* : A spectrally narrow laser pulse spectrum with $\Omega_\mathrm{L}/\omega_\mathrm{B} = 0.5$ excites the transitions $\eta = +2, +3$ with equal amplitudes, $C_\eta \propto [0.08, -0.08]$,($\varrho_\mathrm{L} = +2.7$). The Bloch oscillation starts with opposite phase compared to the excitation at $\varrho_\mathrm{L} < 0$. A sign change in the permanent dipole of the wave packet in comparison with $\varrho_\mathrm{L} < 0$ is also observed.

In the left column, the wave packet evolution is shown for excitation with a broad laser spectrum centered between the $\eta = -3$ and the $\eta = -2$ transition. In the center column, the Wannier-Stark ladder is centrally excited, inducing a symmetric, the breathing mode motion. In the right column, the results are presented if the Wannier-Stark ladder is excited at high energy by a narrow laser spectrum.

It is seen that for $\varrho_\mathrm{L} \neq 0$, the wave packets oscillate around a permanent dipole which changes sign when the laser is tuned through the Wannier-Stark ladder spectrum. For the excitation at $\varrho_\mathrm{L} = -2.5$ (left hand side) with a broad laser spectrum (the wave packet consists of four Wannier-Stark ladder states), the Bloch oscillation amplitude almost reaches the semiclassical limit with $A_\mathrm{z} \approx 2d$. For $\varrho_\mathrm{L} = +2.7$ (right hand side), a smaller oscillation amplitude is observed with $A_\mathrm{z} \approx 1.2d$ which is due to the narrower laser spectrum which effectively excites only two states.
Additionally, it becomes clear that the electron wave packet always starts its evolution in vicinity to the hole. In the first half cycle of the oscillation, it then moves away from the hole charge. Thus, the *phase of the Bloch oscillation* also changes sign when the laser spectrum is tuned through the Wannier-Stark ladder spectrum. In analogy, in k-space, the phase inversion of the Bloch oscillation can be attributed to the sign change of the effective mass. A k-distribution at the miniband bottom has a positive effective mass, but at the upper miniband edge the distribution carries a negative effective mass.

Clearly, in a real system, exciton effects have to be considered, since the wave packet is composed of exciton Wannier-Stark ladder states. As discussed in Section 2.2.2, the Coulomb interaction induces an asymmetry on the Wannier-Stark ladder. Therefore, the creation of a pure breathing mode is not possible. However, when exciting the Wannier-Stark ladder close to its center, a minimum of the Bloch amplitude was predicted [47]. On the other hand, for small ϱ_L, exciton effects are especially large [50] which leads to strong beating because of a large non-equidistance of the Wannier-Stark ladder splitting. Thus, the wave packet starts with a small amplitude but gains amplitude with time. Nevertheless, when intraband damping is included in the model, an amplitude minimum can be clearly predicted.

In experiment, the manipulation of the dynamics of Bloch wave packets by controlled optical excitation was first demonstrated by Sudzius et al. [32] in a $\mathrm{GaAs/(Ga, Al)As}$ superlattice.

In this work, time-resolved Terahertz spectroscopy was employed to directly monitor the dynamics of the intraband dipole of Bloch oscillations. It was investigated how the amplitude and the phase of the Bloch oscillation can be manipulated by selective optical excitation. Furthermore, exciton effects are resolved in the intraband dynamics of Bloch oscillations. The results are presented in Chapter 4.

2.4 Wannier-Stark Ladder States in the Regime of Zener Tunneling

A second focus of this thesis lies on the study of Zener tunneling between Wannier-Stark ladders in biased superlattices. In the presence of tunneling between the bands, important consequences on the carrier spectrum and the dynamics of carriers are expected.

In the previous Sections, the carrier spectrum of a biased superlattice was discussed for an isolated miniband. The one-band approximation implicitly assumes that the electric field-induced tunneling to higher bands is negligible. This leads to stationary states whose wave functions completely localize in the high-field limit. Many of the key experimental findings in superlattices can be sufficiently described by one-band models. However, for very high fields the confinement by the superlattice potential is effectively weakened and one expects that the carriers start to tunnel out of the wells, which is related to the coupling to higher band states.

The experimental findings of this work conclude on the long-standing discussion over the fundamental question, whether Wannier-Stark ladder resonances exist in the spectrum of carriers in a periodic potential under an applied electric field (see Introduction). In the experiment, different field regimes can be clearly identified with increasing field strength: the Wannier-Stark ladder regime, the regime of Wannier-Stark localization and the regime of strong Zener tunneling. For the first two field intervals, the concept of Wannier-Stark ladders lives on as resonances, i.e., quasi-bound states with long lifetime, whereas in the high-field regime, the Wannier-Stark ladder picture breaks down.

Zener Tunneling in the Optical Spectrum

The experimental results are compared to calculations carried out by S. Glutsch [14, 22]. He calculates the optical density of electron and holes states of the biased superlattice (Equation 2.14) by employing an efficient energy-space algorithm. The calculation considers an (in principle) infinite number of bands.

In their work, Glutsch et al. [22] compare the numerical results with results found by applying a one-band model, the Kane model [68]. In Figure 2.15, example wave functions are plotted. It is convincingly illustrated that the Kane model fails to describe tunneling in the high-field regime. In the high-field limit, the Kane model gives nearly symmetric, localized wave functions. This does not account for the real situation where coupling to higher bands comes into play. The numerical results show that the wave function starts to asymmetrically delocalize. It is interesting to discuss the limit for extreme fields, at which the superlattice potential can be neglected. In this case, the wave functions become Airy functions which are associated with a continuous energy spectrum. Consequently, with increasing field, the carrier

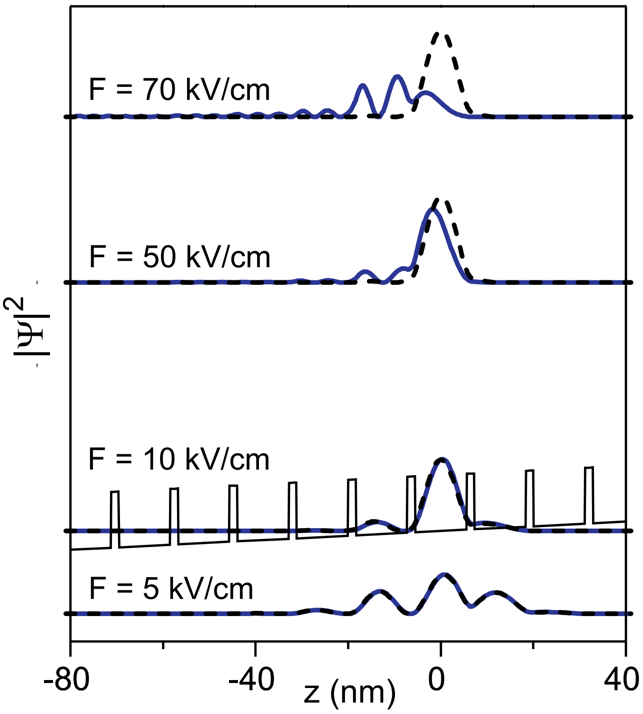

Figure 2.15: Eigenfunctions (modulus square) found for different field strengths. The numerically exact solution (*solid line*) is compared with the Kane approximation (*dashed line*). The effective potential $\mathcal{U}(z) + eFz$ is depicted as a *thick solid line*. The calculation was carried out by S. Glutsch [22] for a GaAs/Ga$_{0.7}$Al$_{0.3}$As superlattice with $a = 11.1\,\mathrm{nm}$ and $b = 1.7\,\mathrm{nm}$. For $F = 5\,\mathrm{kV/cm}$, the nearly symmetric Wannier-Stark ladder function is extended over several superlattice periods. For increased fields ($F = 10\,\mathrm{kV/cm}$), the localization of the state is noted. For higher fields, the exact solution deviates from the Kane model. A field-induced delocalization of the wave function is clearly observed which is not correctly described by the one-band picture.

spectrum of the superlattice gradually evolves from Wannier-Stark ladder resonances to a continuum of states.

The Original Zener Theory

In a pioneering work, Zener [2] studied in 1934 the tunneling of carriers between energy bands due to an electric field. The model successfully described the electrical breakdown in semiconductors by means of semiclassical tunneling theory (for a thorough discussion, see the review paper by M. Holthaus [69]). In our work, we tested if the original Zener relation can describe intersubband tunneling in superlattices. Applied to the superlattice case, the tunneling rate between two bands is modeled by

$$\gamma(F) = \frac{ed|F|}{2\pi\hbar} \exp\left(\frac{-m^* d(\Delta \mathrm{E})^2}{4\hbar^2 e|F|}\right), \tag{2.32}$$

where d is the superlattice period, m^* the effective electron mass and ΔE the band gap.

This equation, referred to as the Zener equation, predicts a smooth increase of the tunneling rate as function of field, because Zener models the situation as tunneling into a continuum of (weakly-bound) states. In the following, this behavior will be termed as *non-resonant* Zener tunneling, in contrast to *resonant* tunneling between discrete Wannier-Stark ladder states.

Lifetime of Wannier-Stark States

By experiments in an alternative periodic potential, cold sodium atoms in an accelerating optical lattice, Barucha et al. [70] observed that the tunneling probability of the atoms out of the confinement of the cosine shape potential shows both resonant and non-resonant features.

These experiments triggered a number of theoretical works which modeled the lifetime of Wannier-Stark states of such an optical lattice, e.g., References [69, 71]. Based on the model established by M. Glück et al. [71], a theory was developed which directly calculates the *intrinsic tunneling lifetimes of Wannier-Stark ladder states* in superlattices [15, 72], whereas the lifetime is is determined by the probability of tunneling between the bands. In this work, theoretical results are presented which were calculated by F. Keck [73]. The numerical calculation was based on a complex-energy scattering theory[9]. The model results in the calculation of metastable Wannier-Stark states which correspond to complex-energy poles ($\mathrm{E}-i\Gamma/2$) of an appropriate defined scattering matrix [71]. The real part gives the quasi-energy of the state. The imaginary part is inversely proportional to the intrinsic tunneling lifetime. For a single resonance, the lifetime is equal to $1/\gamma = \hbar/\Gamma$, where γ is the tunneling probability and Γ corresponds to a (here HWHM) line broadening in the absorption. Since the optical spectrum is measured in the experiment, the optical density of states was calculated. An analytic expression was found to describe the absorption spectrum ($D(\omega)$) between hole and electron states in terms of resonance Wannier-Stark ladder states. In the theoretical spectrum, a Gaussian was fitted to the absorption peaks to extract the linewidth of the transitions. In this way, the experimentally observed pronounced line broadening due to Zener tunneling was successfully modeled.

It is necessary to note that the method employs an analytic representation of the superlattice potential [15]. The potential is composed of single wells of the following form

$$\mathcal{U}(z)(x) = \frac{\mathcal{U}(z)_0}{2}\left[\tanh\left(\sigma(z+b/2)\right) - \tanh\left(\sigma(z-b/2)\right)\right] , \tag{2.33}$$

which is a smoothed square-box potential of the width b. The variable σ defines the smoothness of the potential. The shape of the potential is assumed to be the same for electrons and holes. By direct comparison to the experimental results, the parameter σ and $\mathcal{U}(z)_0$ are slightly varied to obtain good agreement.

---

[9] In the framework of the complex-energy method, the resonant coupling between discrete states was intensively studied in [15, 74]. It was shown that depending on how strongly the states are bound, anticrossings or real crossings in energy appear if the states are brought into resonance. Corresponding to the strength of interaction, the lifetime of the crossing states alters, e.g., for strong interaction, the states exchange their stability index.

3 Zener Tunneling Effect in Semiconductor Superlattices

In this Chapter, the impact of Zener tunneling on the optical spectrum of biased semiconductor superlattices is investigated. Based on these findings, conclusions about the change of the carrier wave function and the tunneling probability of the states can be drawn. Additionally, time-resolved experiments directly address the dynamics of carriers in the regime of Zener coupling to higher bands. The Chapter begins with a survey of the fundamentals of coherent optical interband spectroscopy which are discussed in the framework of a two-level system. This is followed by an introduction into the employed experimental techniques. In the second part of the Chapter, the experimental results are presented. The carrier spectrum in the presence of strong Zener tunneling was monitored in linear absorption experiments. The results of two superlattice samples with different band structures are compared. In the final part, the results of four-wave mixing experiments are presented which measure the Zener tunneling time.

In 1934, Zener [2] described the fundamental effect of interband tunneling which can lead to an electrical breakdown. An open question is: can this effect be observed for intersubband tunneling in superlattices? Resonant tunneling between two Wannier-Stark ladders was first treated in theory [16]. As discussed in the Introduction above, several works were dedicated to the investigation of resonant tunneling in the optical and transport properties of superlattices. As far as the author is aware, resonant tunneling in conjunction with the non-resonant Zener effect has never been reported to play a role in the interband absorption of superlattices.

In this Section, we study the Zener effect in the optical absorption spectrum of superlattices. We demonstrate that the nature of the Wannier-Stark ladders which being of fundamental interest, is also highly relevant for optical experiments on superlattices. The motivation of this work was to understand the influence of Zener tunneling on the carrier spectrum and the states lifetime. Here, Zener tunneling in the electron Wannier-Stark ladder spectrum of superlattices is investigated.

3.1 Techniques of Optical Interband Spectroscopy

In the following, some fundamental aspects of the coherent optical response of semiconductors in the framework of the optical Bloch equations are discussed.

The optical excitation of an ensemble of transitions introduces coherence into a system. Here, coherence means a definite phase relation between the individual photo-excited dipole moments. This *macroscopic polarization* acts as a source term in Maxwell's equations determining the linear and nonlinear response of the system. By the investigation of the response, information on the coherent regime which follows excitation by an ultrashort laser pulse can be gained. In the context of this work, the focus lies with the investigation of the dynamics of Zener tunneling of carriers which destroys the coherence of the system.

The easiest way to discuss the coherent dynamics is to describe the transitions by assuming an ensemble of two-level systems with ground state $|0\rangle$ and excited state $|1\rangle$ (see Figure 3.1). The statistical properties of the system can be evaluated in the framework of the density matrix formalism, where the density matrix operator is given by

$$\rho = \sum_{\mathsf{n}} p_{\mathsf{n}} |\Psi_{\mathsf{n}}\rangle\langle\Psi_{\mathsf{n}}|, \tag{3.1}$$

and p_{n} describes the probability to find the system in state $|\Psi_{\mathsf{n}}\rangle$. The expectation value of an operator $\mathcal{O}$ is given by $\langle\mathcal{O}\rangle = \mathrm{Tr}\{\mathcal{O}\rho\}$. The time-dependence of the density matrix is defined by the Liouville equation,

$$i\hbar\frac{\partial\rho}{\partial t} = [\mathcal{H},\rho] = [(\mathcal{H}_0 + \mathcal{H}_{\mathrm{inter}} + \mathcal{H}_{\mathrm{relax}}),\rho]\ , \tag{3.2}$$

where $\mathcal{H}_0$, is the Hamiltonian of the unperturbed system, $\mathcal{H}_{\mathrm{inter}}$ gives the interaction with the optical field and $\mathcal{H}_{\mathrm{relax}}$ describes the relaxation of the system to the thermal equilibrium.

Each two-level system is characterized by its state vector,

$$|\Psi_{\mathsf{n}}(t)\rangle = c_{0,\mathsf{n}}(t)|0\rangle + c_{1,\mathsf{n}}(t)|1\rangle\ . \tag{3.3}$$

For optical interband transitions, the two-level system consists of the ground hole state and the excited electron state.

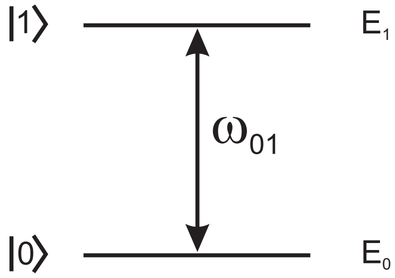

Figure 3.1: Transition scheme of a two-level system with eigenenergies E_0 and E_1.

The density matrix can then be written as

$$\rho = \sum_{\mathsf{n}} p_{\mathsf{n}} \begin{bmatrix} |c_{1,\mathsf{n}}|^2 & c_{1,\mathsf{n}} c^*_{0,\mathsf{n}} \\ c_{0,\mathsf{n}} c^*_{1,\mathsf{n}} & |c_{0,\mathsf{n}}|^2 \end{bmatrix} \tag{3.4}$$

where the diagonal elements give the *population* of the levels. The off-diagonal elements mirror the *coherence* between the two-level systems. If, for example, the amplitudes $c_{0,\mathrm{n}}, c_{1,\mathrm{n}}$ would be equal for all systems, but their phase was randomly distributed, the off-diagonal elements would vanish. For an existing phase relationship, the elements are non-zero. They give the coherence state of a *macroscopic polarization.*

The interaction with the optical field vector $\boldsymbol{E}$ is described in the dipole approximation via the dipole matrix element $\mathcal{H}_{\mathrm{inter}} = -\boldsymbol{\mu} \cdot \boldsymbol{E}$, where $\mu_{ij} = -\langle i | e\boldsymbol{r} | j \rangle$ is the transition matrix element between the states $|i\rangle$ and $|j\rangle$.

The term $\mathcal{H}_{\mathrm{relax}}$ accounts for the recombination and scattering processes of the system. In the simplest approach, a Markovian behavior is assumed with constant relaxation times[1]

$$[\mathcal{H}_{\mathrm{relax}}, \rho]_{\mathrm{ii}} = -\rho_{\mathrm{ii}}/T_1 \tag{3.5}$$

and

$$[\mathcal{H}_{\mathrm{relax}}, \rho]_{\mathrm{ij},(\mathrm{i} \neq \mathrm{j})} = -\rho_{\mathrm{ij}}/T_2 \,, \tag{3.6}$$

where T_1 is the *carrier recombination time* (also commonly referred to as the *longitudinal relaxation rate*) and $1/T_2$ is the rate at which the coherent superposition state loses its phase relation. Therefore, it is usually called *dephasing time* (*transversal relaxation rate*). Under the assumption of independent scattering channels, the scattering rates due to the various mechanisms sum up to

$$\frac{1}{T_2} = \frac{1}{T_2^*} + \frac{1}{2T_1} + \frac{1}{T_{\mathrm{E}}} + \frac{1}{T_{\mathrm{k}}} \,, \tag{3.7}$$

where T_2^* is the pure phase scattering and T_{E} and T_{k} summarize all energy and momentum relaxation rates of the system.

In practical cases, the temporal form of the exciting laser pulse can be described by an envelope function (in scalar notation)

$$E(t) = E_{\mathrm{L}}(t) \mathrm{e}^{-i\omega_{\mathrm{c}} t} + E^*_{\mathrm{L}}(t) \mathrm{e}^{i\omega_{\mathrm{c}} t} \,. \tag{3.8}$$

In the rotating wave approximation, only near-resonance contributions are considered and the optical phase term $\mathrm{e}^{-i\omega_{\mathrm{c}} t}$ can be separated.

---

[1] This approximation is valid in the limits of a very fast or very slow response of the bath (into which the studied system is embedded) compared to the system-bath interaction.

For an ensemble of independent two-level systems[2], the equations of motion describing population and polarization are known as optical Bloch equations which follow from the Liouville relation 3.2 [76]

$$\begin{aligned}
\frac{\partial \rho_{10}}{\partial t} &= -\left[i\Delta_{10} + \frac{1}{T_2}\right]\rho_{10}(t) + \frac{i}{\hbar}\{\mu_{10}[\rho_{00}(t) - \rho_{11}(t)]E_{\mathrm{L}}(t)\}\,, && (3.9)\\
\frac{\partial \rho_{00}}{\partial t} &= -\left[\frac{\rho_{00}(t) - 1}{T_1}\right] + \frac{i}{\hbar}[\mu_{01}\rho_{10}(t)E^*_{\mathrm{L}}(t) - \rho_{01}(t)\mu_{10}E_{\mathrm{L}}(t)]\,, && (3.10)\\
\frac{\partial \rho_{11}}{\partial t} &= -\left[\frac{\rho_{11}(t)}{T_1}\right] + \frac{i}{\hbar}[\mu_{10}\rho_{01}(t)E_{\mathrm{L}}(t) - \rho_{10}(t)\mu_{01}E^*_{\mathrm{L}}(t)]\,, && (3.11)
\end{aligned}$$

where $\Delta_{10} = \omega_{10} - \omega_{\mathrm{c}}$. The set of coupled equations is then usually solved in a perturbation expansion. The resulting hierarchy of relations describes the orders of interaction with the optical field

$$\rho = \rho^{(0)} + \rho^{(1)} + \rho^{(2)} + \ldots\,, \tag{3.12}$$

where the corresponding macroscopic polarization of the n(th) order is given by

$$\langle P^{(\mathrm{n})}\rangle = N\,\mathrm{Tr}\{P\rho^{(\mathrm{n})}\}\,, \tag{3.13}$$

with N as the number density in the system.

The equations are solved iteratively. Before excitation, the system is considered to rest in thermal equilibrium, i.e., $\rho_{00}(0) = 1, \rho_{11}(0) = 0$. Consequently, the equations for odd powers (of ρ) for the interaction with the optical field describe the coherent dynamics of the linear and the nonlinear interband polarizations. For even powers, the population matrix elements are calculated. The above concept is the microscopic basis of the description of nonlinear optical effects where the material response is usually expressed by the susceptibility $\chi^{(\mathrm{n})}$.

In the simplest case, the optical pulse is assumed to be a δ-pulse impinging at time $t = 0$. The first-order polarization (in scalar notation) is then given by [62]

$$P^{(1)}(t) = N(\mu_{01}/i\hbar)E_{\mathrm{L}}\exp(-t/T_2)\Theta(t)\,, \tag{3.14}$$

where Θ is the Heaviside function. It decays exponentially with T_2. In the second-order, the population of the upper level is found to be

$$n_{11}(t) = N|\mu_{01}|^2/\hbar^2|E_{\mathrm{L}}|^2\exp(-t/T_1)\Theta(t)\,, \tag{3.15}$$

which decays exponentially with T_1.

---

[2] Coulomb interaction between the states can lead to a profound change of the optical response (exciton formation, many-body effects [75]) which is treated in the concept of semiconductor Bloch equations (see e.g. [43], for an introduction).

3.2 Experimental Techniques

Following the arguments of Section 2.4, the Zener tunneling effect will induce a pronounced impact on the carrier spectrum. The measurement of the spatial extent of the carrier wave function and the Zener tunneling probability as function of field was addressed in linear absorption spectroscopy. Additional information on the dynamics of Zener tunneling and the nature of line broadening were gained by time-resolved measurements. In particular, four-wave mixing experiments were carried out. In this Section, the experimental techniques are reviewed.

3.2.1 Linear Absorption Spectroscopy

Based on Fermi's golden rule, an expression for the absorption coefficient (see Equation 2.13) was given in Section 2.2.1. From this, the dielectric function can be derived which equals the relation found for an ensemble of classical, charged, harmonic oscillators driven at ω_j [43]. If an additionally damping constant is introduced, the dielectric function, here in the CGS-sytem, reads [44]

$$\epsilon(\omega) = 1 + \frac{4\pi e^2}{m} \sum_\mathrm{j} \frac{\mathrm{f}_\mathrm{cv,j}}{(\omega_\mathrm{j}^2 - \omega^2) - i\gamma_\mathrm{j}\omega}\,, \tag{3.16}$$

where m is the free electron mass and γ the damping constant. It is summed over the ensemble of interband transitions. The quantity $f_\mathrm{cv,j}$ is the *oscillator strength* of the transition and given by the dipole transition matrix element (see also Section 2.2.1):

$$\mathrm{f}_\mathrm{cv,j} = \frac{2m\omega}{\hbar}|\langle \mathrm{c}|\boldsymbol{\mu}\cdot\boldsymbol{\xi}|\mathrm{v}\rangle_\mathrm{j}|^2\,. \tag{3.17}$$

The oscillator strength is equal to the number of oscillators per unit volume [43]. For an isolated transition, the integral over the absorption line is related to the oscillator strength as

$$\int \alpha(\mathrm{E})d\mathrm{E} = \frac{\pi e^2 h}{mnc}\mathrm{f}_\mathrm{cv}\,. \tag{3.18}$$

Equation 3.16 describes the dielectric function as superposition of *homogeneously broadened* transitions, where each is associated with a *Lorentzian absorption line*. The linewidth Γ_h of a single homogeneously broadened transition corresponds to the dephasing rate (Equation 3.7), i.e., the sum over all scattering channels, as given in [77],

$$\Gamma_\mathrm{h} = \frac{2\hbar}{T_2}\,. \tag{3.19}$$

In summary, it is seen that for a single homogeneously broadened transition, the integral over the absorption peak is a measure of the matrix element of the transition. Thus, the oscillator strength is a measure of the *wave function overlap* of electron and hole (Equation 2.15) the field-dependence of which can be investigated in this way.

Additionally, by the analysis of the linewidth in linear absorption, the field-dependence of dephasing mechanisms can be investigated (Equation 3.19), in particular Zener tunneling. The latter is expected to lead to a field-induced line broadening. Conclusions can only be drawn directly for a purely *homogeneously broadened* transition. However, in a realistic system, often inhomogeneous broadening occurs. An *inhomogeneously broadened* transition is a distribution of homogeneously broadened transitions with slightly varying resonant frequencies. The effect can be caused by random fluctuations of the sample properties (e.g. alloy fluctuations or interface roughness) and can often be described by a Gaussian distribution of a width Γ_{inh}. In most cases, it is difficult to safely determine the dominating broadening mechanism from the linear absorption spectrum. In principle, the particular line-shape provides information on the broadening. For dominating homogeneous broadening, a Lorentzian line would result, and for inhomogeneous broadening a Gaussian line, respectively. In intermediate cases a so-called Voigt function would describe the lineshape. However, the analysis is usually complicated due to background noise because the outer wings of the peaks have to be analyzed. Nevertheless, by looking at four-wave mixing experiments in combination with linear absorption measurements the nature of the broadening can be clarified. Once the broadening is known, the four-wave mixing technique provides access to directly measure the homogeneous linewidth.

3.2.2 Time-Resolved Spectroscopy, Transient Four-Wave-Mixing

In four-wave-mixing experiments, the coherently emitted transient third-order polarization is mapped out in time-domain. For further reading on four-wave mixing spectroscopy, the textbooks [76, 78] are recommended.

As will be shown below, the decay time of the transient four-wave mixing signal is on the order of the dephasing time of the transition. In semiconductors, this typically means that a time-resolution in the femtosecond (10^{-15} s) to picosecond (10^{-12} s) regime is required. State of the art laser systems can provide ultrashort pulses to accomplish this time-resolution in optical experiments. For GaAs heterostructures, modelocked Titanium-Sapphire (Ti:Sapphire) lasers are usually employed because the emission wavelength matches the band gap and pulses as short as a few femtoseconds can be produced. The availability of various laser systems producing ultrashort pulses at different energies and with large peak intensities triggered the development of many experimental techniques to investigate time-resolved linear and nonlinear optical properties of matter.

Time-resolved optical experiments are *correlation techniques* which sample the transient optical response of the material after excitation by an ultrashort pulse. A

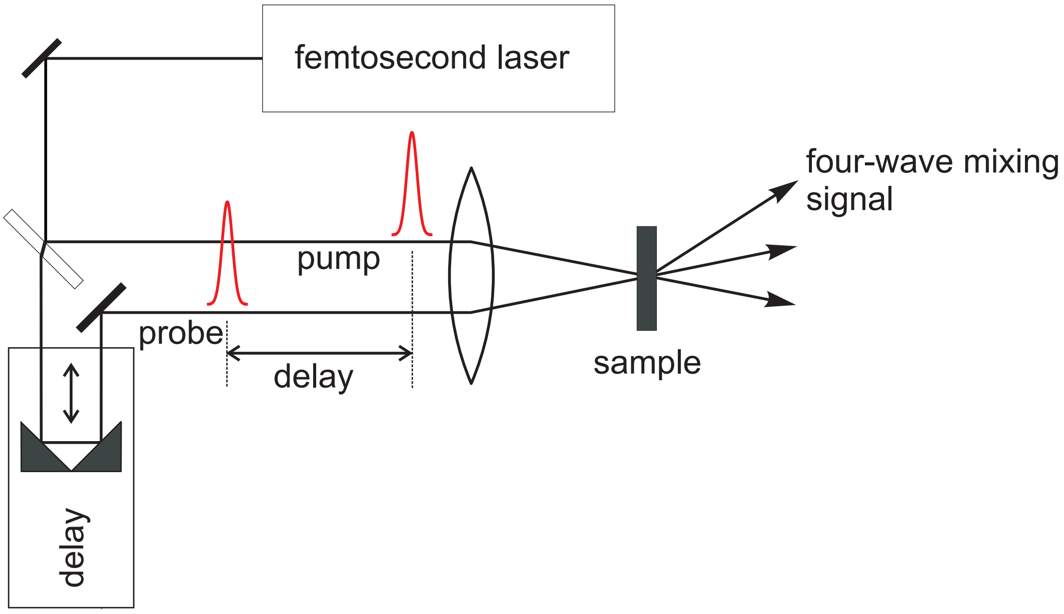

Figure 3.2: Schematics of a two-beam correlation experiment. The nonlinear response of the material is mapped out as function of delay between pump and probe pulse. The emission of the four-wave mixing signal is sketched.

typical two-beam set-up is depicted in Figure 3.2. A train of pulses is generated by a femtosecond laser which is split into pump and probe pulse trains. The experiment then measures the nonlinear change of the material's optical properties induced by the pump pulse as function of the time delay between pump and probe pulse. The temporal evolution of the nonlinear effect can be mapped out. Typically, the correlation-time is scanned by driving a variable delay stage.

In four-wave-mixing experiments, the third-order nonlinear polarization is measured. In general, the material response is expressed by the third-order susceptibility tensor,

$$P^{(3)}_{\mathrm{m}} = \chi^{(3)}_{\mathrm{ijkm}} E_{1,\mathrm{i}}(\boldsymbol{k}_1) E_{2,\mathrm{j}}(\boldsymbol{k}_2) E_{3,\mathrm{k}}(\boldsymbol{k}_3). \tag{3.20}$$

The interaction of the electric fields of three incoming beams (mediated by the material) leads to the emission of a fourth output beam at a linear combination of the input frequencies. In this work, *degenerate* four-wave-mixing spectroscopy was employed which means that all input laser fields have the same frequency (ω_{L}). Additionally, the experiments were carried out in the *self-diffraction geometry* where one laser field interacted twice with the material. In the case where the pump pulse is the $\boldsymbol{k}_1$-beam and the probe pulse the $\boldsymbol{k}_2$-beam, a third-order polarization will be emitted in the background-free direction,

$$\boldsymbol{k}_{P^{(3)}} = 2\boldsymbol{k}_2 - \boldsymbol{k}_1 \,, \tag{3.21}$$

following the phase-matching condition. In this direction, the output polarization will oscillate at ω_{L}. The experimental arrangement is schematically drawn in Figure 3.3. The basic physical principle of the method is described as follows: The

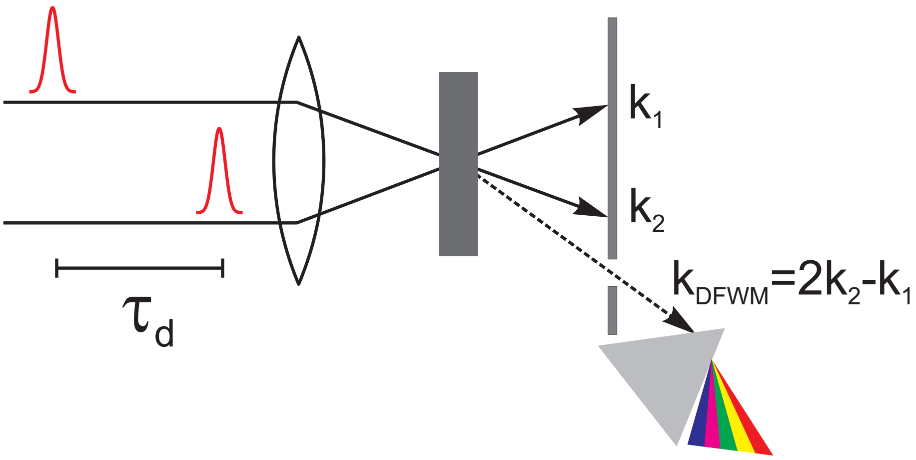

Figure 3.3: Schematics of a degenerate four-wave-mixing experiment in self-diffraction geometry. The emitted four-wave-mixing signal is spectrally resolved.

pump pulse excites a macroscopic polarization which instantaneously starts to dephase. The electric field of the probe pulse (arriving after the delay time τ_d) interacts twice with the sample. First, it again excites a polarization. The probe pulse polarization interferes with the fraction of the pump pulse polarization which remained coherent. This induces a spatial population grating (with the grating vector $\boldsymbol{k}_2 - \boldsymbol{k}_1$) leading to a periodic modulation of the optical constants of the system. Second, the probe beam is diffracted off this grating into the direction $2\boldsymbol{k}_2 - \boldsymbol{k}_1$. The modulation depth of the grating and in turn the diffraction efficiency depends on the coherence decay of the pump beam polarization. Hence, by scanning the time delay, information on dephasing is gained.

Let us discuss the experiment in two limiting cases: (i) for dominating homogeneous broadening and (ii) for dominating inhomogeneous broadening of the transition. The well-known analysis by Yajima and Taira [79] accounts for the four-wave-mixing response of independent two-level systems in these two limits. The nonlinear response was calculated by solving the optical Bloch equations up to the third-order. For δ-pulses, the following analytic solution is found:

[I] The linear polarization excited by the pump pulse decays exponentially with the dephasing time T_2 (Equation 3.14). After the arrival of the probe pulse at $t = \tau_\mathrm{d}$, an exponentially decaying third-order polarization is predicted,

$$P^{(3)}_{\mathrm{h},221}(t) = -iN(\mu_{01}/\hbar)^3 E_{\mathrm{L},1}E_{\mathrm{L},2}E_{\mathrm{L},2}\exp(-t/T_2)\Theta(\tau_\mathrm{d})\Theta(t-\tau_\mathrm{d})\,. \tag{3.22}$$

This free-induction decay is characterized by the decay rate $1/T_2$. In the experiment, the time-integrated four-wave-mixing intensity is measured as function of τ_d,

$$I^{(3)}_{\mathrm{h},221}(t) \propto I_{\mathrm{L},1}I^2_{\mathrm{L},2}\exp(-2\tau_\mathrm{d}/T_2)\,. \tag{3.23}$$

[II] For an inhomogeneously broadened ensemble, the situation is more difficult. The phases of the different frequency components evolve at different rates. Thus, the macroscopic polarization induced by the pump pulse rapidly decays due to destructive interference. However, the probe pulse induces a rephasing of the polarizations. This leads to the emission of a photon echo [76] at τ_d after the arrival of the probe pulse. This doubles the time interval after which the coherence state of the polarization, induced by the pump pulse, is tested. Thus, the time-integrated four-wave mixing intensity is predicted to decay twice as fast,

$$I^{(3)}_{\mathrm{inh},221}(t) \propto I_{\mathrm{L},1} I^2_{\mathrm{L},2} \exp(-4\tau_\mathrm{d}/T_2)\,. \tag{3.24}$$

In summary, the difference between homogeneous and inhomogeneous broadening is a factor of 2 in the decay constant (τ_fwm) of the four-wave-mixing signal,

$$\mathrm{hom} : T_2 = 2\tau_\mathrm{fwm} \;\; / \;\; \mathrm{inhom} : T_2 = 4\tau_\mathrm{fwm}\,. \tag{3.25}$$

To extract the dephasing time T_2 from the detected four-wave-mixing decay, the nature of broadening has to be known which is a priori not the case.

However, the two cases of broadening can be distinguished by comparing the linewidth Γ found in linear absorption and the dephasing time found in four-wave-mixing experiments. Only in the case of a dominant homogeneous broadening: The dephasing time calculated from Γ via Equation 3.19 equals $T_2 = 2\tau_\mathrm{fwm}$. In this case, the dephasing time directly follows from the linewidth

$$T_2[\mathrm{ps}] = \frac{1.32}{\Gamma\,(\mathrm{FWHM})[\mathrm{meV}]}\,, \tag{3.26}$$

which is Equation 3.19 in practical units. Otherwise, the sample is predominantly inhomogeneously broadened or some intermediate state is present.

3.3 Zener Tunneling in Designed Bandstructures

In this work, the investigation of Zener tunneling in the electron miniband structure of biased superlattices was addressed. For this, specially designed superlattices with low barriers as well as a superlattice structure with high barriers were employed.

In the *shallow superlattices*, the resulting band gaps are particularly narrow. Therefore, pronounced Zener tunneling could be observed over a large field interval. Additionally, in these samples, the tunneling decay of Bloch oscillations due to the coupling to higher bands could be directly observed for the first time [80].

The superlattice geometries were designed by modeling the single-particle carrier spectrum with the help of a transfer-matrix model. For this, software by M. Fox et al. [81] was used. Two shallow GaAs/$Al_xGa_{1-x}As$ superlattice structures were investigated which will be referred to as SampleA and SampleB. The geometrical and electronic parameters are summarized in Table 3.1.

The free-particle miniband structure of the samples was calculated by Stephan Glutsch by the numerical solution of the Hamiltonian in the effective mass ap-

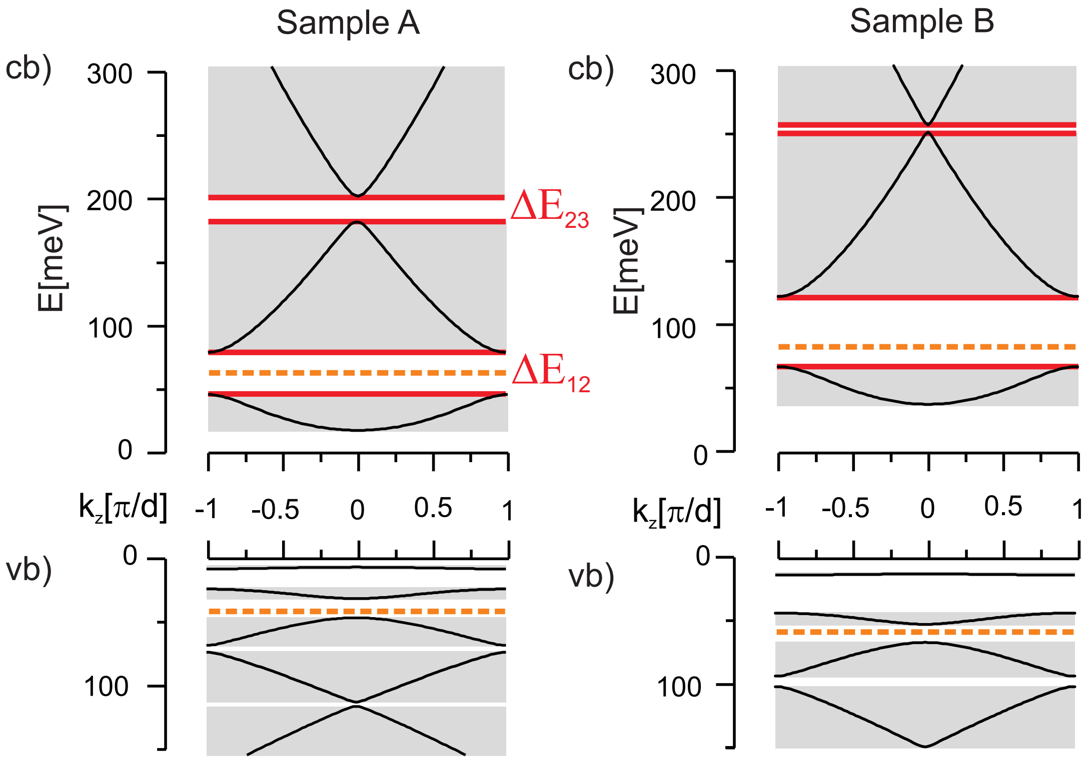

Figure 3.4: *Left*: SampleA: *Top*: Electron miniband structure of the conduction band. The band gaps between the electron minibands are labeled by $\Delta E_{\lambda,\lambda'}$. *Bottom*: Hole minibands of the valence band. The lower hole minibands appear almost dispersion-less. *Right*: Miniband structure of SampleB. The dashed lines denote the barrier heights, ΔE_{cb} and ΔE_{vb}.

Parameter	SampleA	SampleB	SampleC
a	7.6 nm	5.0 nm	11 nm
b	3.9 nm	5.4 nm	1.7 nm
d=a+b	11.5 nm	10.4 nm	12.7 nm
x_{Al}	0.08	0.11	0.3
ΔE_{cb}	60 meV	83 meV	220 meV
ΔE_{vb}	40 meV	55 meV	160 meV

Table 3.1: Parameters of the shallow superlattice samples, SampleA and SampleB, as well as SampleC with deep wells, where a is the well width, b the barrier width and x_{Al} the Aluminum mole fraction. The conduction band barrier height is given by ΔE_{cb}. The valence band barrier height is represented by ΔE_{vb} (see Figure 1.3).

proximation [14]. Figure 3.4 shows the results. Both superlattice structures allow for only one electron miniband below the barrier. Therefore, Zener tunneling between the bound electron states to states of above-barrier bands is addressed. The calculation yields the following relevant band parameters: SampleA(SampleB) have an almost equal width of the first electron miniband $\Delta_1 = 28(30)$ meV. Both samples have the same energetic distance between the center of the first electron miniband to the barrier edge of about 30 meV. The widths of the second miniband were $\Delta_2 = 102(130)$ meV. The band gap size between first and second miniband is $\Delta E_{12} = 34(55)$ meV and between second and third miniband are $\Delta E_{23} = 20(5)$ meV.

Additionally, interminiband tunneling was investigated in a *high-barrier superlattice* with wide band gaps. This structure will be termed SampleC. The geometrical

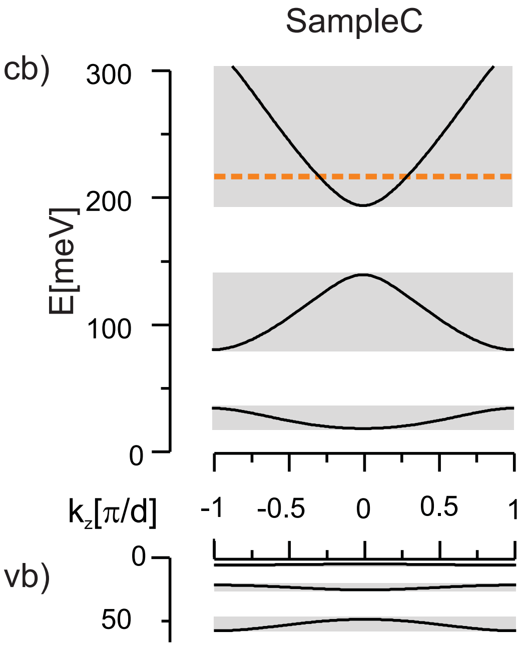

Figure 3.5: SampleC: *Top*: Electron miniband structure. *Bottom*: Hole minibands. The dashed line denotes the conduction band barrier height.

and electronic parameters are also given in Table 3.1. The miniband structure is given in Figure 3.5. The superlattice potential allows two bound electron minibands below the barrier. The relevant band parameters are: $\Delta_1 = 15\,\mathrm{meV}$, $\Delta_2 = 60\,\mathrm{meV}$, $\Delta\mathrm{E}_{12} = 45\,\mathrm{meV}$, and $\Delta\mathrm{E}_{23} = 55\,\mathrm{meV}$.

Sample Preparation for Transmission Experiments

The GaAs/$\mathrm{Ga_{1-x}Al_xAs}$ superlattice samples were grown by Klaus Köhler from the Fraunhofer-Institut für Angewandte Festkörperphysik in Freiburg using molecular-beam epitaxy. The intrinsic superlattice with 35 periods was embedded in buffer layers all grown on a $\{100\}$, n^+ GaAs wafer substrate. The buffer layers do not affect the optical characteristics of the superlattice sample. They ensure a linear drop of the electric potential across the superlattice and prevent diffusion of dopants into the superlattice zone.

To apply the dc field, a semitransparent Cr(1 nm)/Au(5 nm) Schottky contact was evaporated on top of the active layer structure. On the n^+ doped substrate side, an ohmic contact was formed by evaporating and annealing a 250 nm thick Sn/Au (20%/80%) alloy film. By applying a reverse biased voltage, an internal field was induced with strongly hampered current injection. The Schottky contact operates up to a certain threshold voltage. To prevent the destruction of the sample a current compliance limit was always set (maximal current of 3 mA). The external voltage was applied by a source-measure-unit (SMU 236 manufactured by Keithley).

To allow for transmission experiments, firstly, the contacted sample was glued with the Schottky side upside down onto a c-axis oriented sapphire substrate. Secondly, the GaAs substrate of each sample was partially removed by wet etching [82].

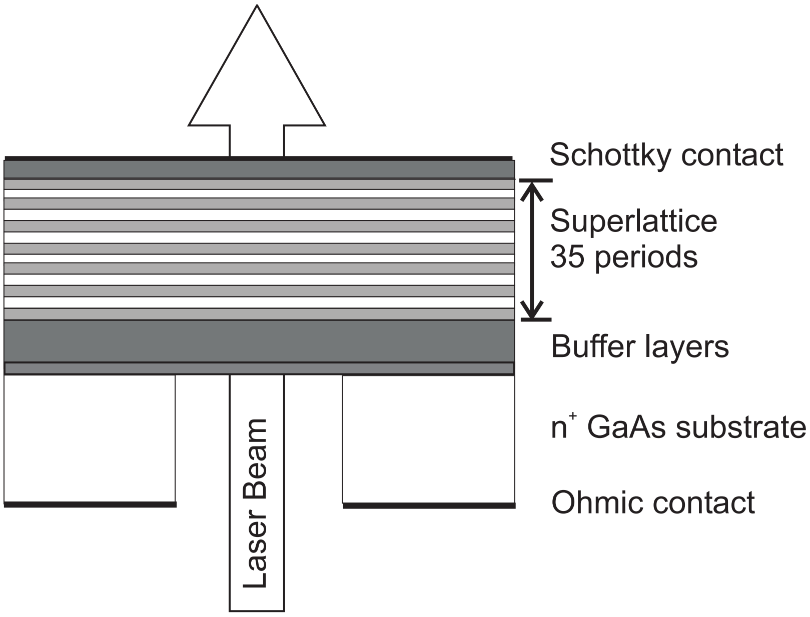

Figure 3.6: Schematic drawing of a sample prepared for transmission experiments. The layer structure of the semiconductor heterostructure comprising the superlattice and the metal contacts is depicted. The sample can be optically accessed in the area were the GaAs substrate was removed by wet-etching.

A scheme of a readily prepared sample is depicted in Figure 3.6.

Internal Field Calibration

To calibrate the internal field, low-density linear absorption spectra are measured as function of applied voltage. In most cases, an overall linear dependence of the internal field on the voltage was observed. Thus, the peak positions of the hh_{-1} and hh_{+1} excitons (usually very prominent in the spectra) could be linearly fitted over a large voltage range. To some extent this averages over exciton asymmetry. Then, according to Equation 2.11, the internal field was calibrated. It was found that the external voltage drops over a length of $1\,\mu$m which corresponds to the thickness of the intrinsic region of the heterostructure.

Due to internal space charges already present for zero external voltage, a Wannier-Stark ladder splitting is observed. This built-in field has to be compensated by the external voltage. Additionally, in optical experiments, photo-generated carriers accumulate at the high edge barriers of the buffer layers. The induced dipole field screens the external voltage as it is illustrated in Figure 3.7. This *field screening* is strongly dependent on the photo current (depending on the particular excitation parameter) and had to be compensated by the external voltage. Therefore, for optically selective excitation, the internal field was monitored to have accurate control over the excited transitions.

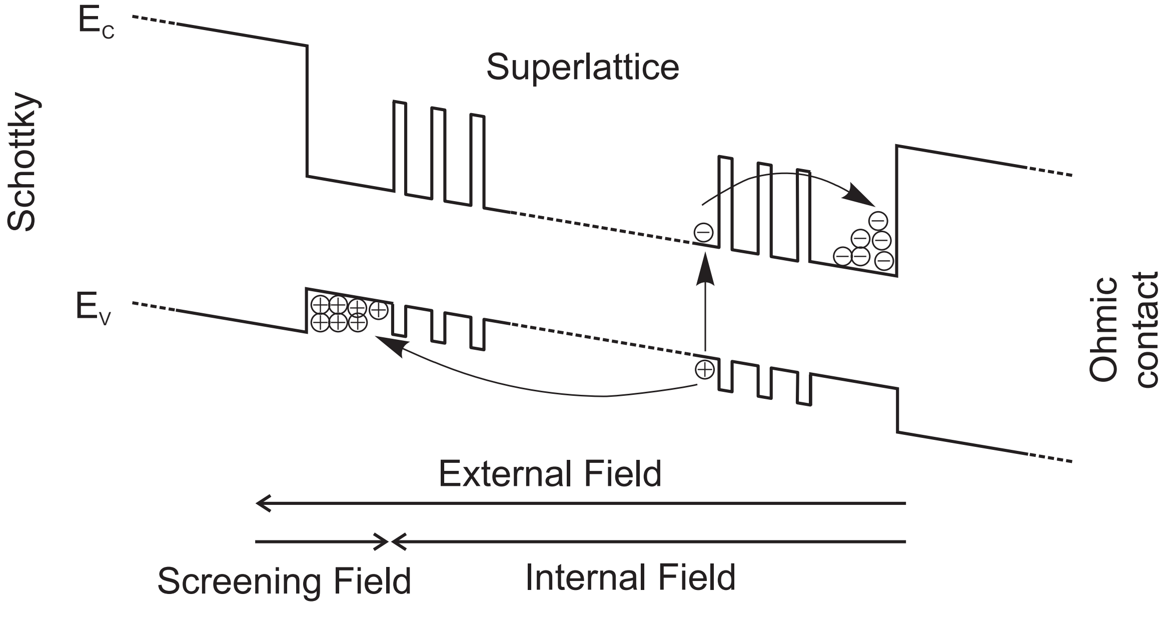

Figure 3.7: Schematic band edge diagram for the intrinsic region of the heterostructure. Photo-generated carriers accumulate at the high barriers of the buffer layers. The induced dipole field screens the external field.

From the measured photo current, the density of photo-excited carriers can be evaluated, if carrier recombination during transport across the heterostructure is neglected. The time-averaged carrier sheet density per well can then be found by

$$\mathrm{n_{cd}} = \frac{N_c}{AN_{\mathrm{wells}}} = \frac{I_{\mathrm{photo}}}{AN_{\mathrm{wells}}R_{\mathrm{rep}}e}\,, \tag{3.27}$$

where N_c is the total number of photo-generated carriers. The repetition rate of the laser was $R_{\mathrm{rep}} = 82\,\mathrm{MHz}$, the number of wells was $N_{\mathrm{wells}} = 35$ and A is the area of the laser spot. The spot diameter was approximated by the FWHM of the radial intensity profile of the pump beam.

3.4 Experimental Set-Up

All optical experiments were carried out in transmission geometry. The sample was held at 10 K in a helium vapor driven cold-finger cryostat (Microstat, manufactured by Oxford Instruments).

In the linear absorption measurements, a halogen lamp was used as light source. In transmission, the sample was imaged onto a square slit. This restricted the sample area from which the transmitted light was collected to a small spot of about $100 \times 100\,\mu$m. Thus, possible averaging due to lateral electric field fluctuations was reduced. The transmitted beam was focused by a second lens onto the entrance slit of a 0.5 m monochromator (Model 500M from Jobin-Yvon) equipped with a 1200 lines/mm grating. The spectrum was dispersed onto an optical multichannel detector, a thermo-electrically cooled charge-coupled device with a 256 × 1024 pixel array (TE/CCD-1024EM/UV detector from Princeton Instruments). The camera was read out by a ST133 (16Bit) controller from Roper Scientific which forwarded the spectral data to a computer.

For time-resolved measurements, near-infrared laser pulses were generated by a standard Kerr-lens modelocked Ti:Sapphire laser system (Tsunami manufactured by Spectra-Physics) which emits pulses with a typical duration of around 75 fs at a repetition rate of 82 MHz. It was continuously pumped by 5 Watts of a diode pumped Nd:YVO$_4$ laser which is equipped with an intra-cavity second-harmonic-generation (Millenia from Spectra Physics).

For the four-wave mixing experiments, pump and probe beam were focused onto the sample by a 75 mm lens to a spot of $35\,\mu$m diameter. The sample surface was imaged onto a CCD camera. Thus, the spatial overlap of the beams could be easily adjusted. The signal emitted in the phase-matched direction $2\boldsymbol{k}_2 - \boldsymbol{k}_1$ was selected by a small aperture to reduce the collection of stray light. The time-integrated four-wave mixing signal was spectrally resolved by coupling the signal into the same spectrometer system described above.

3.5 Experimental Results and Discussion

In this Section, experiments are discussed which observe intersubband Zener tunneling in superlattices. In the first part, results on linear optical absorption measurements are presented, where two kinds of samples are discussed: (i) a superlattice with several electron minibands within the superlattice potential (a high-barrier superlattice), and (ii) superlattices with low barriers which support only one miniband within the superlattice potential (shallow-barrier superlattices). In the shallow-barrier superlattices, the Zener effect is observed in a much more pronounced manner. The experimental findings clearly demonstrate the Zener breakdown in the optical spectrum. By detailed analysis of the absorption spectra, conclusions on localization length and the lifetime of the electron Wannier-Stark ladder states in the Zener regime can be drawn. A complex interplay between resonant and non-resonant tunneling is observed. In the discussion, the specific behavior can be attributed to the particular miniband structure of the samples. The findings are well modeled by theory.

In the second part of the Section, the results of the investigation of the dynamics of Zener tunneling is discussed. The impact of Zener coupling on the decay of the interband polarization was measured by four-wave-mixing experiments.

3.5.1 Zener Breakdown in a High-Barrier Superlattice

Firstly, the results of field-dependent absorption measurements for SampleC, a strongly-coupled superlattice structure with high barriers, are reviewed. The miniband structure was given in Section 3.3. It was shown that two below-barrier electron minibands exist.

Figure 3.8 displays a gray scale map of the linear absorption as function of dc field over the field interval of $F = [0 \ldots 97.5]\,\mathrm{kV/cm}$. The spectra were differentiated along the wavelength axis. Afterwards, the wavelength axis was converted to an energy axis[3]. This strongly enhances the visibility of weak transitions. For direct comparison, Figure 3.9 presents the gray scale map of the absorption according to calculations which were carried out by S. Glutsch [22] (see discussion in Section 2.4). The theoretically evaluated optical density of states (Equation 2.14) was then differentiated with respect to the energy axis. From the theory graph, transitions are clearly identified which cannot be resolved in the experiment. It is important to note that (i) the model does not include Coulomb correlations and (ii) it does not consider light-hole states. Despite these simplifications, experiment and theory agree in great detail.

The peaks, which are observed in the linear absorption spectra, are due to the op-

---

[3] In all gray scale maps presented in this Section, the absorption spectra were differentiated according to this procedure.

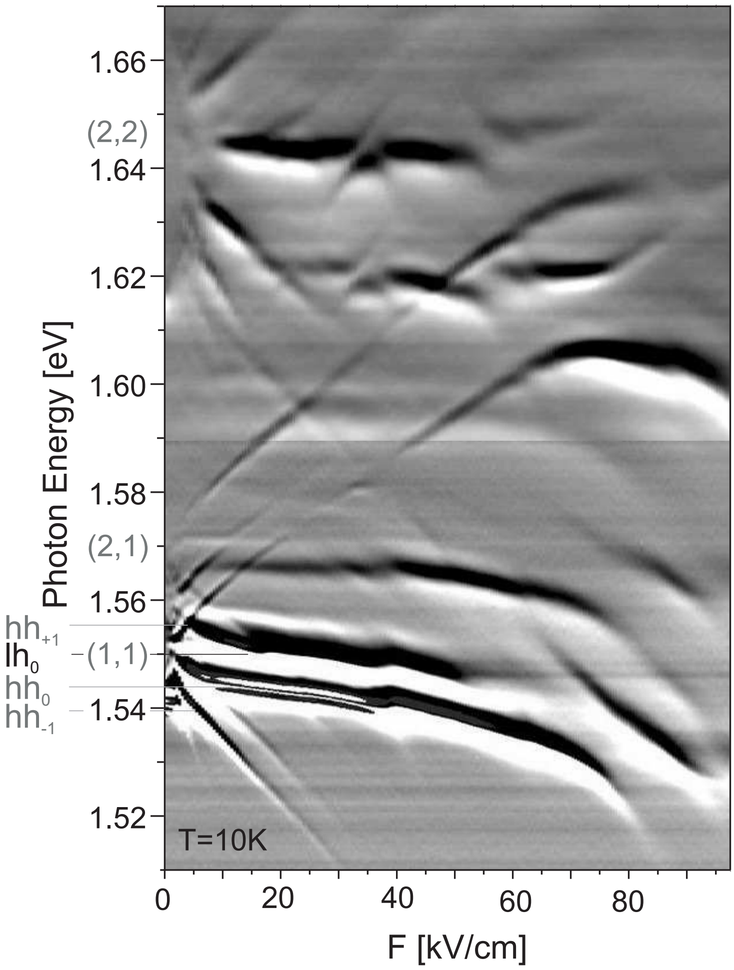

Figure 3.8: SampleC: Experiment: Gray scale map of linear absorption spectra. The most prominent Wannier-Stark ladder fans are marked by the miniband indices (λ, λ'), where λ is the hole and λ' the electron miniband index. For the (1,1) Wannier-Stark ladder, various heavy-hole transitions are labeled as well as the vertical (1,1) light-hole transition. For $F > 60$kV/cm, the transitions suddenly change slope, broaden and decrease in oscillator strength which is a clear signature of the Zener breakdown. Taken from [23].

tical excitation of 1s exciton states, as it was discussed in Section 2.2.2. It was argued above, that the 1s exciton spectrum (due to the bound in-plane motion) resembles the one-dimensional free-particle spectrum of the biased superlattice. Here, this conclusion is convincingly verified since the experimental absorption graph (dominated by the 1s exciton transitions) and the theory graph (a purely 1D calculation neglecting Coulomb interaction) compare very well[4]. Therefore in the following, Zener tunneling will be discussed in a one-dimensional framework.

Let us discuss the experimental results. For fields up to 20 kV/cm, different Wannier-Stark ladder fans are seen to evolve out of the 1D miniband of the superlattice. At first glance, two prominent Wannier-Stark ladder fans are observed in experiment which can be attributed to optically allowed transitions (Section 2.2.1) with equal miniband index $(\lambda = \lambda')$. The (λ, λ')=(1,1) transitions, between the first hole and the first electron miniband, are centered around 1.55 meV, and the (2,2)

---

[4] Nevertheless, features of the exciton Wannier-Stark ladder spectrum are visible in experiment. As discussed in Section 2.2.2, Coulomb interaction leads to an asymmetry in oscillator strength which is larger for transitions with negative Wannier-Stark ladder index $(\eta < 0)$ compared to transitions with $\eta > 0$. The exciton binding energy scales correspondingly which leads to non-equidistant Wannier-Stark ladder splittings.

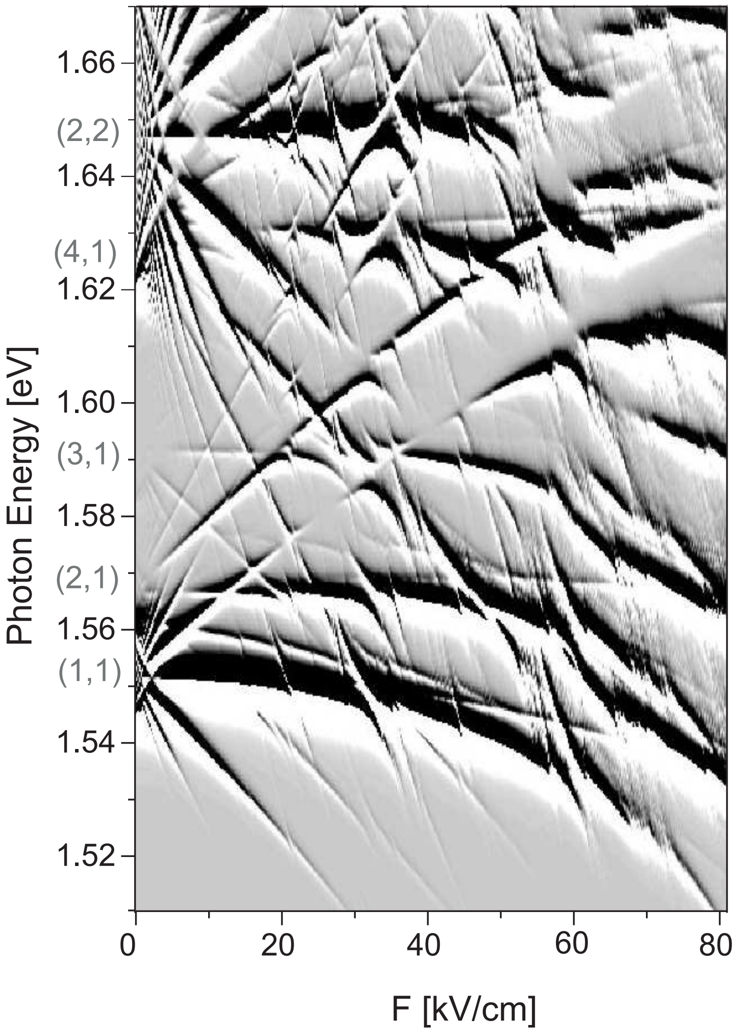

Figure 3.9: SampleC: Theoretical results: Gray scale of the field-dependent spectra of the optical density of states. Wannier-Stark ladder transitions between various (hole, electron) minibands are labeled. The calculation well reproduces the experiment resolving the complex tunneling behavior between different Wannier-Stark ladder states in great detail. Resonant tunneling is observed of the (1,1) Wannier-Stark ladder with (2,2) transitions. For $F > 60\,\mathrm{kV/cm}$, the non-resonant Zener coupling to bundles of above-barrier states is noted as an irregular pattern. Taken from [83].

transitions between the second hole and the second electron miniband, centered around 1.645 meV. In contrast to theory, in the experiment a second (slightly blue-shifted) (1,1) fan of transitions is observed which arises from transitions between the first light-hole miniband and the first electron miniband.

The Wannier-Stark ladder regime extends up to about $F = 25\,\mathrm{kV/cm}$. For higher field strengths, non-vertical Wannier-Stark transitions ($\eta \neq 0$) cease to exist. This is caused by the progressive Wannier-Stark localization (Section 2.2). On the other hand, the vertical transitions gain oscillator strength. The (1,1) vertical heavy-hole transition (hh_0) becomes a strong, sharp absorption peak. Since at high fields, the optical selection rules are less restrictive, transitions between minibands of different index ($\lambda \neq \lambda'$) additionally emerge.

For $F > 40\,\mathrm{kV/cm}$, the (1,1) and the (2,1) hh_{+1} transitions again gain oscillator strength, whereas the $\eta < 0$ transitions have already vanished. This effect can be assessed as a signature of the field-induced delocalization of the electron wave function as it was introduced in Section 2.4. The electron wave function delocalizes asym-

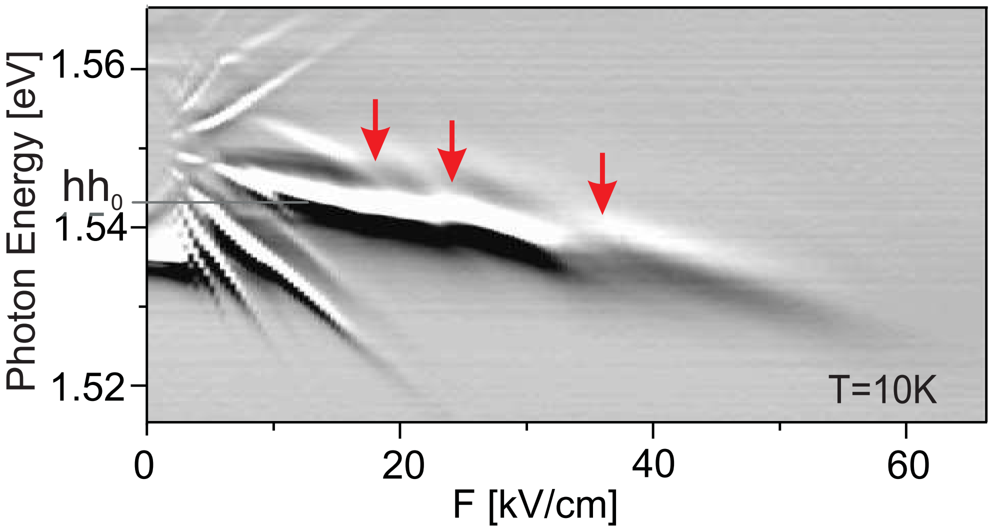

Figure 3.10: SampleA : Experiment : Gray scale map of linear absorption spectra measured as function of field. The photon energy interval of the (1,1) Wannier-Stark ladder is shown. Zener tunneling is observed as an interplay between resonant tunneling (indicated by arrows) and non-resonant tunneling to higher above-barrier states. The latter leads to a gradual vanishing of the (1,1) hh$_0$ transition for $F > 35\,\mathrm{kV/cm}$.

metrically to the downward potential side and the oscillator strength of transitions with $\eta > 0$ increases.

For $F > 60\,\mathrm{kV/cm}$, a distinct change in field-dependence and oscillator strength of the transitions is noted. Various points of anticrossing due to resonant tunneling between different below-barrier Wannier-Stark states are observed. Additionally, above-barrier states cross which are observed in the theoretical graph as bundles of thin lines. In this high-field regime, due to a gradually increasing tunneling probability to higher states, the transitions of the first electron miniband are seen to change their slope, broaden and ultimately, to vanish. The effect can be seen as the spectral analog of the electrical *Zener breakdown*.

3.5.2 Field-Induced Delocalization of Wannier-Stark Ladder States

In the following Section, the Zener tunneling effect is addressed in strongly-coupled superlattices with shallow barriers, SampleA and SampleB. As introduced in Section 3.3, these structures allow only one bound electron miniband below the barrier. Hence, the Zener tunneling to states of the above-barrier spectrum is directly addressed and not obscured by the resonant coupling between below-barrier bands as observed above in the deep-well structure.

Firstly, the linear absorption of SampleA is discussed. Figure 3.10 presents the

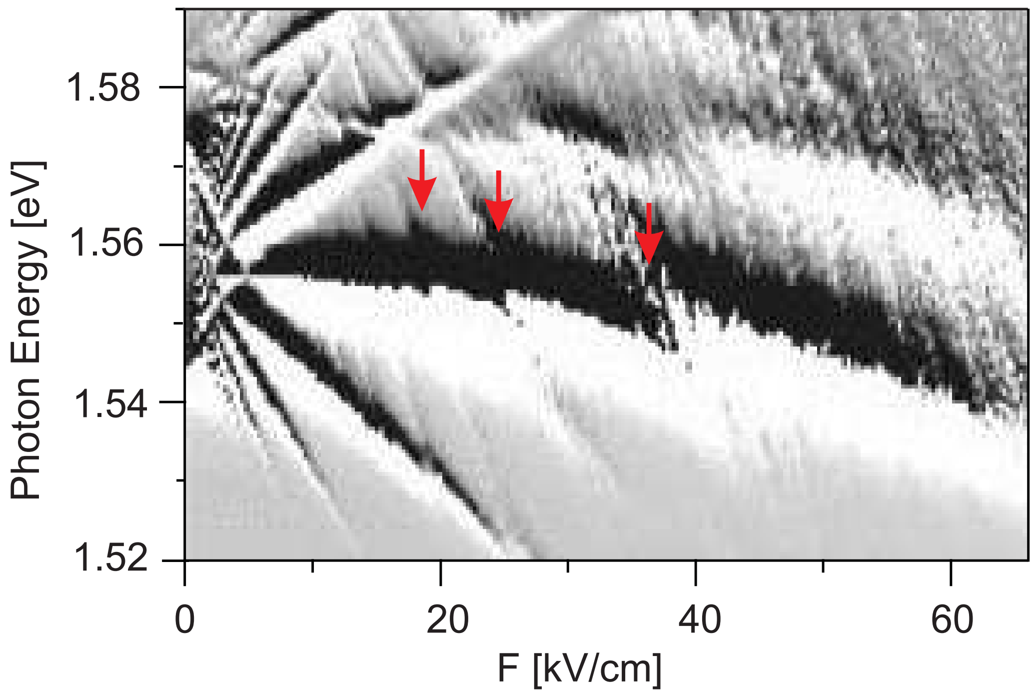

Figure 3.11: SampleA : Theory : Gray scale map of field-dependent optical density of states. Corresponding to the experimental graph (Figure 3.10), the energy interval of the (1,1) Wannier-Stark ladder fan is shown. The Zener breakdown observed in experiment is well reproduced. The arrows mark anticrossings due to resonant tunneling. They correspond to those in Figure 3.10. Taken from [80].

gray scale map of linear absorption spectra measured as function of dc field. In the presented spectral interval, the Wannier-Stark ladder transitions between the first heavy-hole and the first electron miniband are visible. Additionally, the (1,1) (light-hole) Wannier-Stark ladder is detected as a weak, blue-shifted doublet.

Three field regimes can be clearly classified: (i) Up to $F = 20\,\mathrm{kV/cm}$, the Wannier-Stark ladder fan of transitions with different η is clearly observed. (ii) For $F > 20\,\mathrm{kV/cm}$, the localization of the electron Wannier-Stark ladder states causes non-vertical Wannier-Stark ladder transitions to vanish and the vertical transition to gain oscillator strength. In a one-band model, the Wannier-Stark eigenfunction localized down to a single-well function would remain like this for increasing field. (iii) Here, instead, for $F > 35\,\mathrm{kV/cm}$, the vertical transition is observed to be modified strongly. The (1,1) hh_0 transition broadens and ultimately vanishes for $F > 50\,\mathrm{kV/cm}$. This is a clear indication for the field-induced delocalization of the electron wave function due to Zener tunneling.

In comparison to theory (displayed in Figure 3.11), for the high-field regime, the tunneling can be identified as taking place between a multitude of continuum-like above-barrier states which are seen as an irregular pattern for $F > 35\,\mathrm{kV/cm}$. Additionally, resonant coupling (marked by arrows) is observed to states which are

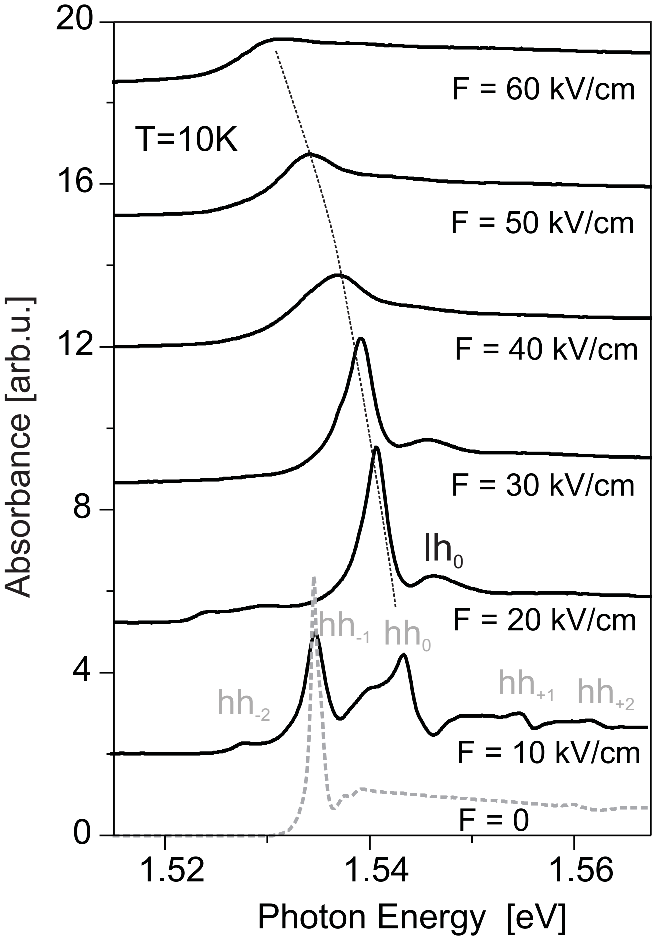

Figure 3.12: SampleA: Experimental absorption spectra for increasing field strength. In the flat-field case (*dashed line*) the strong absorption peak of the heavy-hole exciton is seen, as well as the absorption of the 1D miniband states. The miniband absorption is slightly modulated at the upper and the lower edge due to saddle point excitons [51]. For $F = 10\,\mathrm{kV/cm}$, different heavy-hole Wannier-Stark transitions are labeled. The localization regime ($F = 20, 30\,\mathrm{kV/cm}$) is followed by the tunneling induced delocalization. The guide for the eye (*thin dashed line*) traces the (1,1) hh_0 transition which gradually broadens and almost vanishes for high fields. These particular spectra were reproduced in detail by Glutsch et al. [84] employing a multi-band calculation including exciton correlations.

visibly evolve from above-barrier bands. Hence, the interplay of resonant and non-resonant tunneling (which is further analyzed in Section 3.5.3) dissolves the electron wave function leading to a pronounced Zener breakdown.

In Figure 3.12, single absorption spectra of SampleA for different fields are shown[5]. The spectrum for $F = 10\,\mathrm{kV/cm}$ represents the Wannier-Stark ladder regime. In this field regime, the electron Wannier-Stark ladder wave function extends over several superlattice periods. Therefore, heavy-hole Wannier-Stark ladder transitions with different η are observed. The asymmetry of the absorption lines and an additional broadening in this field regime is caused by Fano coupling [57] which is mediated by the Coulomb interaction of the 1s exciton states with the degenerate exciton continuum of states with smaller η (see also discussion in Section 2.2.2)[6]. For $F \geq 20\,\mathrm{kV/cm}$, the electron Wannier-Stark state is almost localized in one well. Non-vertical Wannier-Stark ladder transitions vanish and the vertical hh_0 transi-

---

[5] The absorption spectra were corrected for spectral modulations due to Fabry-Perot interferences in the sample and the spectral response of the detection.

[6] To selectively address the Zener effect, Fano coupling can be suppressed by applying a magnetic field parallel to the electric field [85,86]. This leads to a quantization of the in-plane motion by forcing the carriers onto Landau levels.

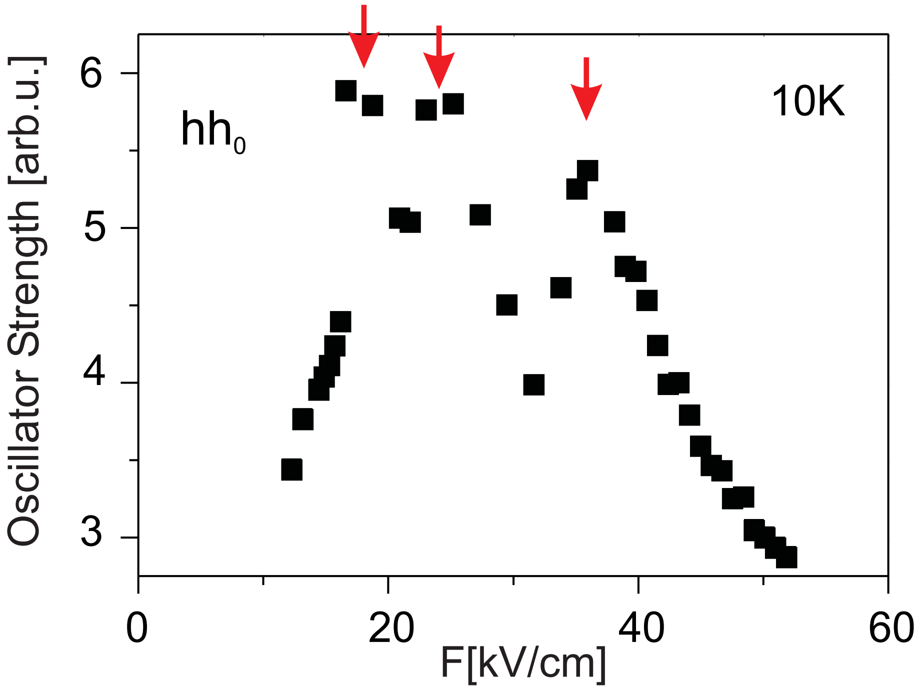

Figure 3.13: SampleA: Oscillator strength of the (1,1) hh_0 Wannier-Stark ladder transition as function of field. Tunneling resonances to above-barrier states are marked by arrows (which correspond to those in Figure 3.10). For $F > 40\,\mathrm{kV/cm}$, a gradual decrease of oscillator strength gives evidence of the tunneling-induced delocalization of the electron wave function. Taken from [23].

tion appears as a strong absorption peak. The localization regime is followed by a field-induced delocalization. Starting from $F = 35\,\mathrm{kV/cm}$, a gradually increased broadening of the hh_0 transition and its distinct decrease in oscillator strength is noted. The hh_0 transition evolves energetically parallel to the vertical light-hole transition (lh_0). It disappears as a clear spectral feature already for $F = 40\,\mathrm{kV/cm}$. This indicates that the light-hole state also Zener-delocalizes at high fields.

In order to quantitatively verify the different field regimes, the absorption spectra were analyzed. The area under the absorption peak is a measure of the oscillator strength of the transition (Equation 3.18). The latter was evaluated for the (1,1) hh_0 transition as function of field by fitting a Gaussian to the absorption peak. The results are plotted in Figure 3.13. From theory it is known that the heavy-hole states are localized over the whole field region. Thus, with the evaluation of the oscillator strength, the localization of the electron wave function is directly traced as function of field (see discussion in Section 3.2.1). Figure 3.13 depict that the oscillator strength of the (1,1) hh_0 transition first grows with increasing field strength and reaches its highest value at about $F = 25$ kV/cm. The maximum has a pronounced structure due to the anticrossings with above-barrier states. At these anticrossings, the degenerate states strongly couple which leads to an exchange of oscillator strength and an energetic splitting between the transitions. The absorption peaks of the individual anticrossing transitions could not be resolved in the spectra.

Therefore, the oscillator strength represents the integral over the whole absorption peak leading to the observed resonances. Most importantly, a gradual decrease of the oscillator strength is observed for $F > 35\,\mathrm{kV/cm}$. This can be attributed to the non-resonant tunneling of the electron wave function to a continuum-like above-barrier spectrum[7]. The results demonstrate, that *the interplay of resonant and non-resonant Zener tunneling leads to the field-induced spatial delocalization of the below-barrier electron wave function* [80].

3.5.3 Tunneling-Reduced Lifetime of Wannier-Stark Ladder States

The field-induced delocalization of the Wannier-Stark ladder state due to an increased tunneling probability is shown to be associated with a reduction polarization coherence lifetime of the states. The lifetime of the electron Wannier-Stark states is monitored by measuring the rate of the coherence decay of the interband polarization of Wannier-Stark ladder transitions. In the spectral domain, it can be accessed by the linewidth of the optical transitions. Therefore, in a first step, the Zener tunneling is investigated in interband absorption spectroscopy. In a second step, with four-wave-mixing experiments, the polarization decay time is directly determined.

In the first part of this Section, it is focused on the comparison of Zener tunneling behavior in SampleA and SampleB.

Results on SampleA

Figure 3.14 displays the line width (HWHM) of the (1,1) hh_0 Wannier-Stark transition as function of field for SampleA. The absorption peak of the transition was fitted to a Gaussian. For medium fields ($F = [10 \ldots 20]\,\mathrm{kV/cm}$), in the Wannier-Stark ladder regime, the linewidth stays almost constant[8]. In this field region, Fano coupling broadens the absorption line and induces a spectral asymmetry [57]. Therefore, in this field range, the line can only be approximately fitted. However, we are more interested in the behavior at higher fields at which the Wannier-Stark localization of the electron wave function suppresses Fano coupling and broadening due to Zener tunneling starts to dominate. For fields $F > 30\,\mathrm{kV/cm}$, a drastic increase

---

[7] The quantum-confined Stark effect, which leads to the spatial separation of electron and hole wave function, will also partially contribute to a decreasing oscillator strength of the interband transition. However, it cannot explain the spectral characteristics which are observed. Hence, Zener tunneling is clearly the dominating field-dependent phenomenon responsible for the drop in oscillator strength.

[8] For flat-field, a linewidth of 1.3 meV (FWHM) was determined. For SampleB (discussed below), it was found in four-wave-mixing experiments that the $F = 0$ exciton linewidth is predominantly inhomogeneous broadened (e.g., due to fluctuations of the well width). The results can be generalized to SampleA which is very similar in parameters.

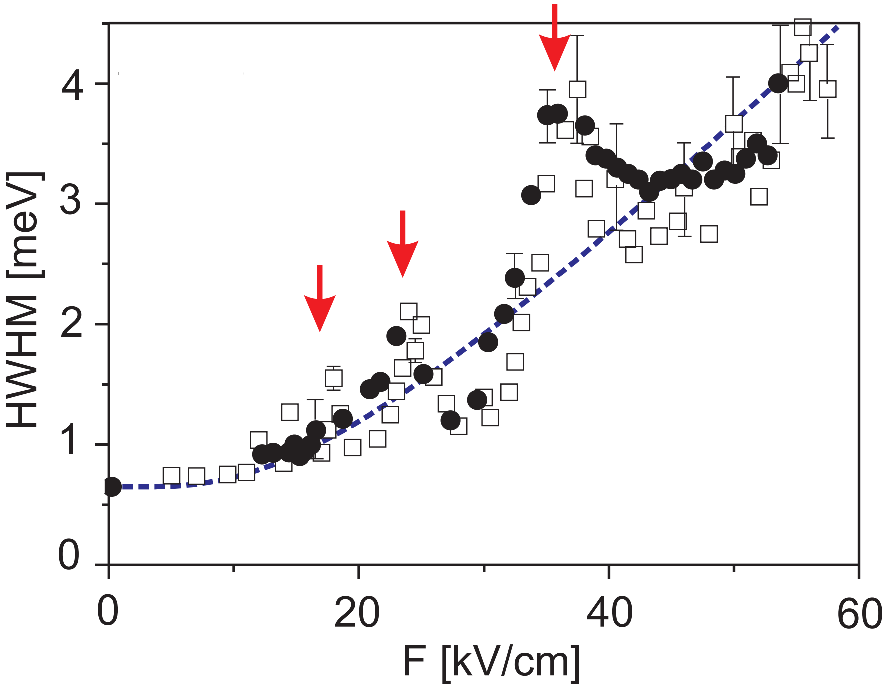

Figure 3.14: SampleA: Linewidth Γ of the (1,1) hh_0 Wannier-Stark ladder transition as a function of field. (*filled circles*) Experiment [23], (*hollow squares*) theory. (*dashed line*) The result of the Zener equation (Equation 2.4) well describes the overall increase in linewidth. A peak structure due to resonant tunneling is superimposed. The resonances are marked by arrows which correspond to those in Figure 3.13.

in linewidth is observed. Hence, the coupling to states of higher bands is no longer negligible.

From the original Zener theory [2], one would expect a continuous increase of the linewidth. For comparison, a fit to the Zener equation (Equation 2.4) is given in Figure 3.14. Zener tunneling is assumed to be the dominant field-dependent dephasing channel. The broadening observed at flat-field is assumed to originate from field-independent broadening mechanisms and was added as a constant. It is visible that the fit can only describe the overall behavior. The graph shows superimposed oscillations which are due to resonant coupling of Wannier-Stark ladder states of the first miniband states with states of the second miniband which were also visible in Figure 3.10 and 3.13.

In Graph 3.14, the theoretical results of the complex-energy model developed by Glück et al. [71] (which was introduced in Section 2.4) are also displayed. The calculation was carried out by F. Keck [73]. In the theory, the lifetime of the metastable Wannier-Stark ladder states is directly calculated. It is determined by the tunneling probability of the states. Hence, the evaluated lifetime corresponds to an inverse tunneling probability. Theory calculates energy levels and states in the valence and conduction band and subsequently the optical density of states $D(\omega)$[9]. A Gaussian is then fitted to the dominant peak of the absorption spectrum. A field-independent broadening was taken into account by convoluting $D(\omega)$ with a Gaussian, to ensure an equal linewidth for $F = 0\,\mathrm{kV/cm}$ between experiment and theory. Theory well reproduces the interplay of the continuous increase of the linewidth and the peaks structure due to resonant Zener tunneling.

Example error bars, both for experiment and theory, are plotted to account for uncertainties in the peak fitting. For theory, the fitting is approximate for strong fields and in the vicinity of tunneling resonances because the line shape becomes asymmetric. For experiment, for strong fields only the low-energy side of the absorption can be fitted since on the high-energy side in-plane absorption and the light-hole transition are superimposed. Additionally, the decreasing oscillator strength of the transition causes larger uncertainties.

Details on the used parameters for the theoretical modeling are given in [73]. In the theoretical model, the agreement with experiment is improved by a slight variation of the scaled variables (which consider barrier height, effective carrier masses as well as a smoothing of the potential). For SampleA, the optimization procedure led to a smoothing parameter of $\sigma = 2.5$ (Equation 2.33). This corresponds to a deviation from rectangular potential by 3 monolayers, being the distance from the point where the potential reaches 50 % of the barrier height to the points where the potential reaches 10 % or 90 % of the barrier height. There is no doubt that a rectangular potential can not be realized in nature since the Al atoms are distributed randomly in the barrier. The effects of alloy fluctuation and interface roughness have been subject of several publications, e.g. see Ref. [87–89]. For future investigations, it would be desirable to measure directly the abruptness of the potential barriers to support the results.

Results on SampleB

For comparison, Figure 3.15 displays the field-dependence of the linewidth of the (1,1) hh_0 transition for SampleB (as well as its oscillator strength). In contrast to SampleA, the linewidth curve of SampleB seems to follow the Zener equation. Only marginal oscillations due to resonant tunneling are superimposed. Additionally, in comparison to SampleA, a smaller increase of linewidth with field is noted.

For high fields, theory reproduces this behavior quantitatively. Thus, Zener tunneling is shown to be the dominating broadening mechanism, for $F > 50\,\mathrm{kV/cm}$. However, to obtain good agreement with experiment a larger smoothing of the potential ($\sigma = 1.3$) than for sample A had to be introduced. It corresponds to a

---

[9] In Figure 1 in Reference [73], an excellent agreement between experimental absorption spectra and the calculation is shown for the Zener regime. Theory well reproduces the tunneling-induced line broadening.

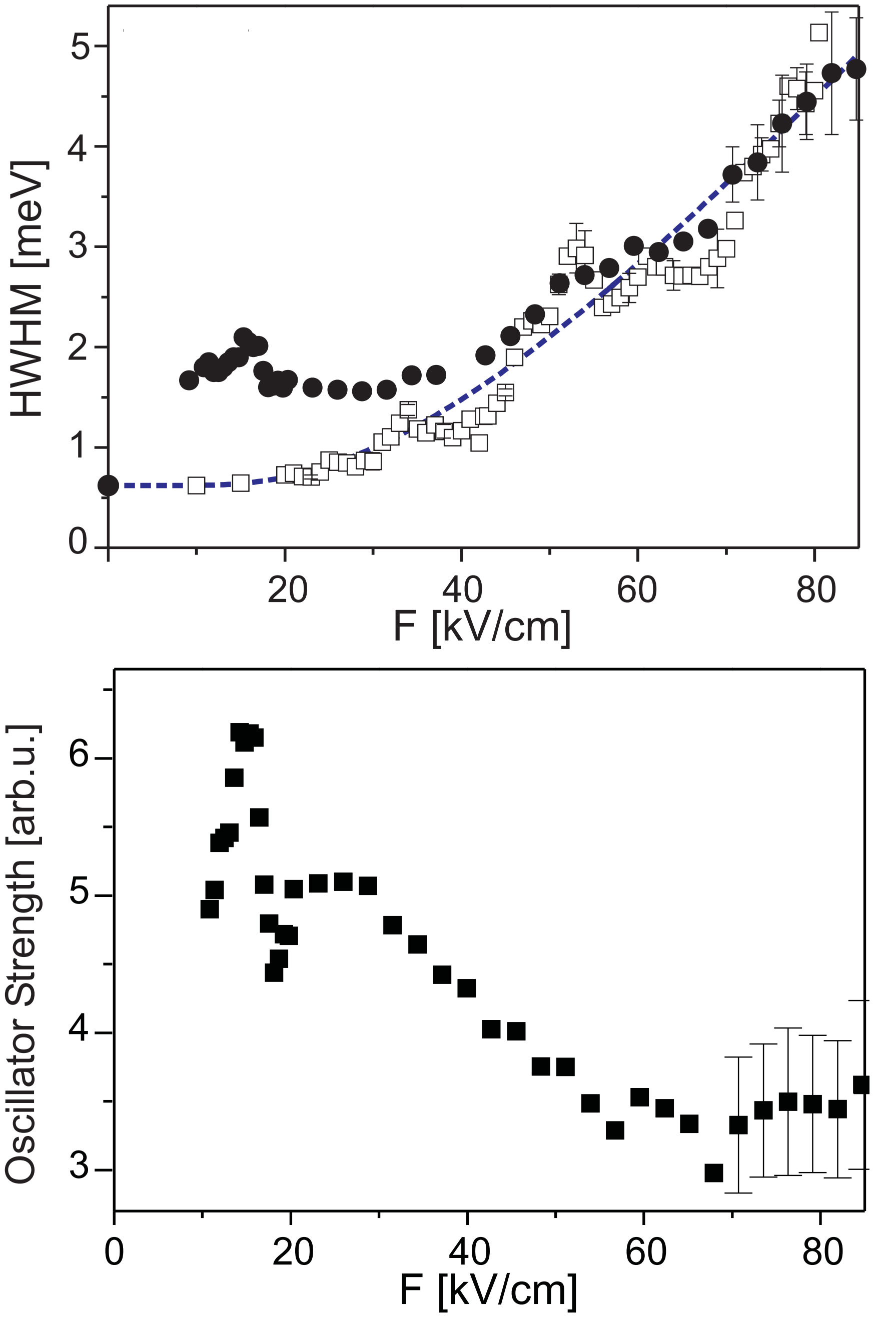

Figure 3.15: SampleB: *Top*: Linewidth Γ of the (1,1) hh_0 Wannier-Stark ladder transition as a function of field. (*filled circles*) Experiment, (*hollow squares*) theory. (*dashed line*) The fit to the Zener equation (Equation 2.4) well describes the line broadening. An almost continuous increase of the linewidth is seen. *Bottom*: The oscillator strength of the (1,1) hh_0 Wannier-Stark ladder transition as a function of field. For $F > 30\,\mathrm{kV/cm}$, a pronounced drop of oscillator strength is observed which is evidence for the field-induced delocalization of the electron wave function in the Zener regime. In comparison to SampleA (Figure 3.13), peaks due to resonant tunneling are almost absent. Only very small oscillations are visible.

deviation from a rectangular potential by 5 monolayers (see the above discussion).

The experimental data of SampleB could be nicely fitted to the Zener equation (Equation 2.4). To account for the linewidth at $F = 0$, again a constant was added. From the fit, the band gap ΔE_{12} between the first electron miniband with states of the second electron miniband can be extracted. The value $\Delta E_{12} = 51\,\mathrm{meV}$ has been found which is in reasonable agreement with the band gap obtained from the calculated miniband structure which will be presented in the following Section.

Direct Comparison of SampleA and SampleB

The substantially different Zener tunneling behavior between SampleA and SampleB can be explained by the characteristics of the different band structure. This will be shown in this Section.

The most important difference between the two miniband structures is the size of the band gaps. SampleB has an approximately symmetric potential (well width $\approx$ barrier width) leading to a dominant first coefficient in the Fourier expansion of the potential and, therefore, to a particular large first band gap[10]. The dispersion relations of SampleA and SampleB are shown in Figure [4] in Reference [73]. The band structure was calculated by the smoothed potential which was employed for modeling the linewidth. Theory gave the following results: Only the first two band gaps ΔE_{12} and ΔE_{23} need to be considered in the discussion which most decisively influence the Zener effect. Higher gaps rapidly shrink in size with increasing index. The values for SampleA(SampleB) are $\Delta E_{12} = 31(44)\,\mathrm{meV}$ and $E_{23} = 17(7)\,\mathrm{meV}$[11]. In comparison to SampleA, SampleB has a larger ΔE_{12} and a smaller ΔE_{23}.

The different Zener tunneling behavior of the two superlattice structures can be further explored by analyzing the field-dependent absorption measurements which encompass also the spectral range of above-barrier transitions. In Figure 3.16, the experimental and theoretical results for SampleA are presented. Two prominent fan structures can be identified to be due to (1,1) and (2,2) Wannier-Stark ladder transitions. Here, it becomes evident that the anticrossings (marked by arrows) of the (1,1) hh_0 transition can be explained by the resonant tunneling to states of the second electron miniband. The states of the second electron miniband are energetically above the barrier. Nevertheless, a (2,2) Wannier-Stark ladder fan is seen to emerge around $E = 1.66$ eV. This verifies that the gap ΔE_{23} is large enough to effectively suppress tunneling to higher above-barrier bands at least up to moderate fields. Therefore, the *states of the first above-barrier band experience a Wannier-Stark localization.*

---

[10] In first-order perturbation theory, the size of the gaps are defined by the corresponding Fourier coefficients of the periodic potential [90].

[11] These values deviate slightly from what was given in the miniband structures above (Section 3.3). Nevertheless, both models show the same relative sizes of the band gaps for the two superlattice geometries.

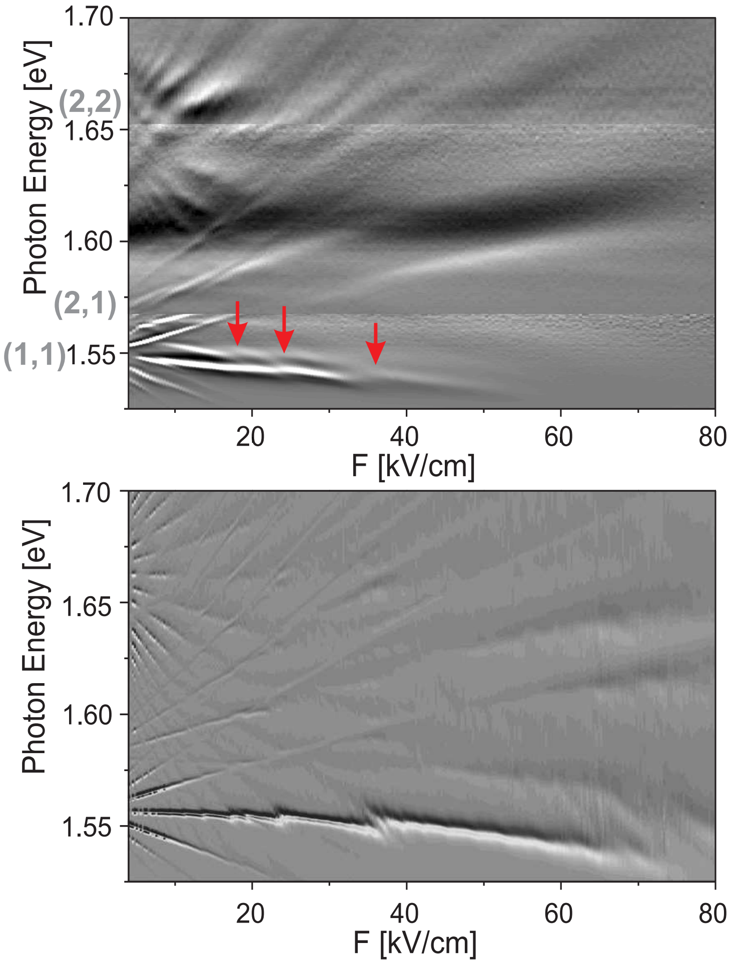

Figure 3.16: SampleA: Gray scale map of absorption spectra. The spectral interval of the (1,1) Wannier-Stark ladder fan was already displayed in Figure 3.10. *Top*: Experiment: Wannier-Stark ladder fans between different hole and electron minibands are denoted. Interestingly, the second electron miniband (energetically above the barrier) also evolves into a Wannier-Stark ladder which leads to resonant tunneling with the states of the first electron miniband. Taken from [23]. *Bottom*: Theory: The spectrum of $(\partial D/\partial \omega)$ is shown. The results well reproduce the experiment. Taken from [73].

For SampleB, the results are given in Figure 3.17. Only one prominent Wannier-Stark ladder fan is seen which can be attributed to (1,1) transitions. In comparison to SampleA, the first above-barrier miniband does not emerge into a Wannier-Stark ladder. Only weak spectral features are observed. In theory, also only very small remnants of a (2,2) fan are seen. These characteristics can be explained by the small second band gap (ΔE_{23}) of SampleB. Via the narrow gap, tunneling between the above-barrier bands is promoted which inhibits the spatial localization of the above-barrier states. Thus, resonant tunneling of states of the first and the second miniband was not observed. The situation in SampleB resembles the situation treated by Zener [2]. Thus, the tunneling probability is well described by the original Zener equation (compare with Figure 3.14). In SampleB, tunneling is addressed between states of an electron band and an almost continuous spectrum emerging from the strongly coupled above-barrier states. Additionally, the weaker rise of the tunneling probability for SampleB can be attributed to the larger first band gap.

In summary: (i) According to the Zener equation (Equation 2.4), the size of the first band gap defines the overall increase of the Zener tunneling probability with increasing field. (ii) In case of a large second band gap, tunneling is inhibited and above-barrier states experience Wannier-Stark localization. For a small second band

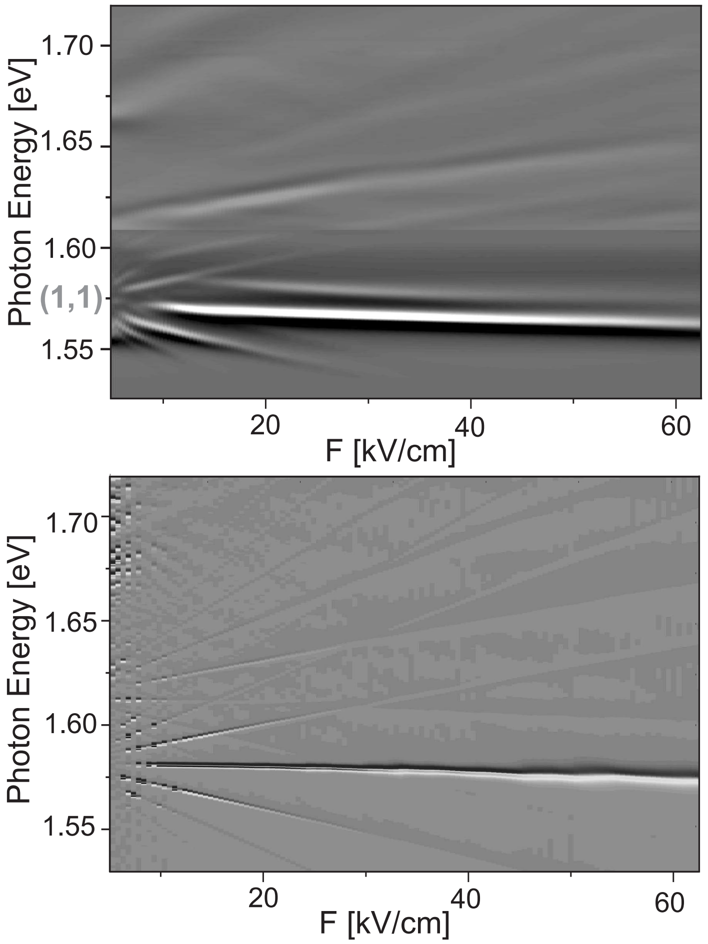

Figure 3.17: SampleB: Gray scale map of absorption spectra. *Top*: Experiment: The formation of a Wannier-Stark ladder is only observed for the lowest electron miniband. Taken from [23]. *Bottom*: Corresponding theoretical results Taken from [73].

gap, above-barrier bands mix strongly which suppresses spatial localization.

Let us briefly discuss the Zener tunneling in some general terms. In the original Zener [2] paper, the tunneling rate is proportional to the product of the probability density of a Bloch state at the Brillouin-zone boundary "leaking" through the band gap multiplied by the rate at which the carrier reaches the zone boundary (the Bloch oscillation frequency). In this theory, the carriers tunnel virtually into a continuum of states. Additionally, correlations between successive Bloch oscillation cycles are neglected. These assumptions are justified in cases where the states of the upper band have a small lifetime due to strong tunneling to higher bands. In other words, this holds if the second band into which the carriers tunnel is empty and the states are weakly bound.

In the time-domain, one can argue that in the case of a large second band gap, the intraband coherence time of the carriers in the second band increases. If the coherence time reaches the range of a few Bloch oscillation cycles, the assumptions of Zener are no longer valid, and in its place the effect of resonant tunneling is observed. If resonant tunneling occurs in the Wannier-Stark regime, the dynamics of a Bloch oscillating wave packet are strongly influenced. In these shallow superlattices, an intraband interference decay of Bloch oscillations was demonstrated when resonant tunneling to states of the first above-barrier band occurs [80]. Along with this, a polarization revival was observed which could be attributed to a partial back reflection of the wave packet at the second band gap which in turn partially tunnels back into the first miniband [85].

Dynamics of Zener Tunneling of Wannier-Stark States

In linear absorption, a tunneling-induced broadening of the absorption line was observed, whereas the technique does not allow homogeneous and inhomogeneous broadening to be distinguished. Although the results suggest that homogeneous broadening dominates for high fields, it is important to quantitatively determine the contributions.

Following the arguments from Section 3.2.2, four-wave-mixing experiments are a suitable tool for measuring the interband dephasing time T_2, if either kind of broadening dominates. Additionally, it is possible to determine an effective electron transfer time into above-barrier states, if Zener tunneling becomes the dominant dephasing mechanism.

In this work, four-wave-mixing experiments were carried out in a self-diffraction geometry. The experimental techniques and the experimental set-up are reviewed in the Sections 3.2.2 and 3.4. The interband coherence of the (1,1) hh_0 transition in SampleB was measured as function of field, whereby only this single transition was resonantly excited for all fields. This was accomplished by adjusting the spectral width of the laser pulse and its central energy. The pulse duration was varied from 300 to 100 fs. The carrier density was on the order of $10^9\,\mathrm{cm}^{-2}$ per well. It was kept constant by adjusting the pump pulse intensity to ensure a constant contribution of carrier-carrier scattering.

In the experiments, an exponential decay of the four-wave-mixing signal was resolved. Assuming a homogeneously broadened transition, the dephasing time T_2 was calculated from the decay time by $T_2 = 2\tau_{\mathrm{fwm}}$ (Equation 3.25). The results are displayed in the top panel of Figure 3.18. For medium fields, an increase of the dephasing time is observed which can be attributed to the decrease of Fano coupling [57]. For higher field strengths ($F > 50\,\mathrm{kV/cm}$), the impact of Zener tunneling as a strong dephasing mechanism seems to dominate the polarization decay. In this field interval, Zener tunneling was also demonstrated in linear absorption to cause a pronounced line broadening. For comparison, the inverse linewidth taken from Graph 3.15 (Left) was plotted in Figure 3.18 according to the Relation 3.26. In the Zener regime, for $F > 50\,\mathrm{kV/cm}$, an overall quantitative agreement between the inverse linewidth and the dephasing time is noted. Hence, it can be concluded that the Zener tunneling leads to a purely homogeneously broadened transition. In this field regime, the time of the electron tunneling transfer into above-barrier states can

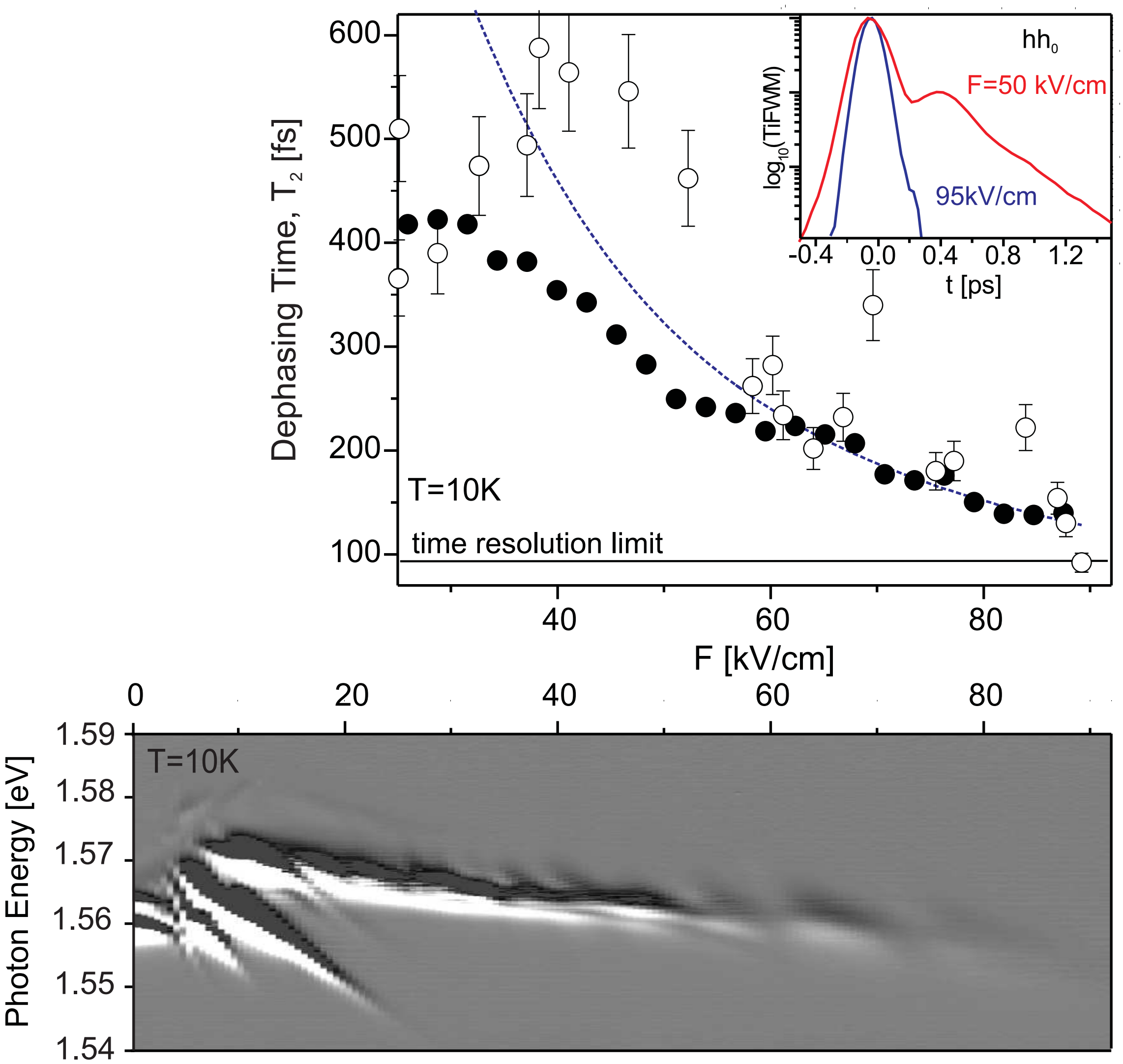

Figure 3.18: SampleB: *Top*: (*open circles*) Dephasing time of the (1,1) hh$_0$ transitions as function of field. (*filled circles*) Inverse linewidth of the (1,1) hh$_0$ absorption peak. As guide for the eye, the Zener tunneling rate (Equation 2.4) is plotted as a *dashed line*. For high fields, Zener tunneling becomes the dominant dephasing mechanism. It is observed to lead to homogenous broadening. *Inset*: Example four-wave-mixing transients. For $F = 95\,\mathrm{kV/cm}$ the signal decays within the cross-correlation of the pulses. *Bottom*: Gray scale map of four-wave mixing spectra as function of field. Modulations of the linewidth of the (1,1) hh$_0$ transition are observed which are due to resonant tunneling to above-barrier states. These weak features cannot be resolved in linear absorption. For fields at which a smaller linewidth is observed, an accordingly longer dephasing time was determined.

be directly deduced from the four-wave-mixing decay, e.g., for $F = 75\,\mathrm{kV/cm}$, it is equal to 160 fs.

Apart from the overall decrease in dephasing time, resonances are observed. The physics behind them will be clarified in the following. The four-wave-mixing intensity is highly sensitive to resonances of the optical density of states (it depends to the eighth order on the transition dipole matrix element [91]). Thus, even the smallest modulations of the transitions linewidth can be observed. Figure 3.18 (Bottom) displays a gray scale map of four-wave-mixing spectra. The spectra were detected for the time-overlap of pump and probe pulse. The laser pulse spectrum was centered around 1.56 eV. It had a spectral width of $\Delta\varepsilon_{\mathrm{L}} = 25\,\mathrm{meV}$. The central feature of the graph is the (1,1) hh_0 transition. For high fields, the tunneling induced line broadening of the transition is clearly observed which causes the transition to eventually vanish for $F > 85\,\mathrm{kV/cm}$. However, a broken feather structure is additionally superimposed which cannot be resolved as such a clear feature in linear absorption (in comparison with Figure 3.17). The modulations are due weak tunneling resonances to above-barrier states. These resonances are certainly lead to the small modulations on the linewidth curve of SampleB (Figure 3.15) which are observed in experiment and more clearly in theory. Obviously, the very small second band gap of SampleB induces a minute localization effect on the above-barrier states. For field strengths in between the points of resonant tunneling, the transition has a smaller linewidth, e.g., a sharpening of the line is clearly observed for $F \approx 65\,\mathrm{kV/cm}$. At these fields (for $F > 50\,\mathrm{kV/cm}$), the dephasing time also shows peaks in Figure 3.18[12].

---

[12] In the four-wave-mixing experiment, the internal field was determined for higher fields by analyzing the spectral position of the (1,1) hh_0 transition, whose field-dependence is weak. Therefore, an uncertainty of the internal field has to be taken into account. The error interval was estimated to be $\pm 2\,\mathrm{kV/cm}$.

4 Terahertz Emission of Exciton Wannier-Stark Ladder Wave Packets in Semiconductor Superlattices

Time-resolved Terahertz experiments were employed to investigate the intraband dynamics of Wannier-Stark ladder wave packets. The Chapter begins with the discussion of the mechanisms underlying coherent Terahertz emission in biased superlattices. Next, the experimental technique and the measurement set-up are covered. The main Section is dedicated to the presentation of the experimental results and their discussion. First, the manipulation of the Bloch oscillation amplitude is addressed. The results can only be understood in the framework of a full exciton picture. Second, by selective optical excitation, the Terahertz emission of single Wannier-Stark ladder states was investigated. Third, the generation of tunable, narrowband Terahertz radiation by difference-frequency mixing is reported. For this, the exciton Wannier-Stark ladder spectrum was selectively excited by two spectrally narrow laser lines.

The Terahertz (THz) region of the electromagnetic spectrum can only be loosely defined as the region between infrared light and microwave radiation. This spectral range is of critical importance for the investigation of carrier or quasi-particle excitations in molecular and condensed matter physics (e.g., rotational and vibrational resonances of molecules, binding energies of bound states like excitons, and the confinement energies in semiconductor heterostructures lie in the THz region). The time-scale of the THz regime also coincides with tunneling and quasi-particle scattering rates.

$$1\,\mathrm{THz} \longleftrightarrow T = 1\,\mathrm{ps} \longleftrightarrow h\nu = \mathrm{E} = 4.14\,\mathrm{meV} = 33.4\mathrm{cm}^{-1} \longleftrightarrow \lambda = 300\mu\mathrm{m}$$

The development of suitable THz sources and sensitive detectors has initiated very intense research in this field which also paved the way for potential applications [92].

Dynamics of Bloch Oscillating Wave Packets

In this work, the dynamics of carrier wave packets, in particular Bloch oscillations, in semiconductor superlattices was investigated. After the first observation of Bloch oscillations in interband spectroscopy [10,11], Waschke et al. [28] first reported experimental evidence from THz experiments that this wave packet oscillation is associated with a real-space oscillating dipole. Subsequent results on THz emission of Bloch oscillations were yielded by Roskos et al. [93] who were able to show Bloch oscillations evolving in the second miniband of a superlattice. Martini et al. [94] demonstrated the superradiant THz emission of the macroscopic polarization of Bloch oscillating dipoles.

In wide-band superlattices, very recently, interesting results on transient transport phenomena were reported. Overshoot velocities for the transient ballistic band transport [95] were detected by THz experiments. The authors showed the clear cross-over from Drude miniband transport to the Bloch oscillations regime at room temperature [96, 97]. From experimental results of the latter publication, Shimada et al. [98] claimed to have found the signature of THz gain in superlattices.

A major part of the experiments performed in this work was initiated by the results of four-wave-mixing experiments which reported the manipulation of Bloch oscillating wave packets [32]. The effect was introduced in Section 2.3.1. The authors were able to show an amplitude minimum of the Bloch oscillation, the breathing mode motion, for the excitation close to the Wannier-Stark ladder center[1], whereby the intraband dipole was detected by spectrally-resolved degenerate-four-wave-mixing experiments. This method was developed by Lyssenko et al. [100]. The authors temporally resolved spectral oscillations (peak shifts) of the Wannier-Stark ladder transition energies which synchronously evolved with the quantum beat signal originating from Bloch oscillations. In a simplified capacitor-like model, the intraband dipole of the Bloch oscillating wave packet was taken to adiabatically screen the externally applied field. Thus, the Wannier-Stark ladder was used as a linear field sensor to resolve the intraband dipole of the Bloch oscillation which periodically modulates the Wannier-Stark splitting.

Theoretical modeling of the situation was stimulated by these experimental results. For a combined static and Terahertz (THz) field along the growth axis, the time-resolved four-wave-mixing spectra (including Coulomb interaction) were calculated. The simulations verify that spectral oscillations of the transition energies are

---

[1] The minimum of the Bloch oscillation amplitude was observed for small detuning to the low energy side. This finding contradicts to what is expected in the exciton picture. The latter would predict an amplitude minimum for small positive detuning. Because, due to Coulomb interactions, the overlap integral for transitions with negative η is larger than for their positive counterparts. This asymmetry could in principle be balanced by shifting the intensity maximum of the laser spectrum slightly to the high energy side of the Wannier-Stark ladder. The discrepancy was resolved by Löser et al. [99] who showed that intraband scattering shifts the symmetry point of the Wannier-Stark ladder to the low energy side.

linked to amplitude and phase of the ac field [34] (for time-resolved linear absorption spectra [33]). In very recent work [101], the self-generated intraband ac field (due to Bloch oscillations) is included self-consistently in the calculation of the $\chi^{(3)}$ response of the system. The model explains the peak shifts as a frequency mixing effect of the optical and the Terahertz fields. It can be stated that with the time-resolved detection of the four-wave-mixing spectra, one does not have direct and linear access to measure the intraband dipole of the wave packet. Nevertheless, the technique is undisputably a suitable method to mirror the temporal evolution of the wave packet.

However, the direct measurement of the intraband polarization was addressed by other techniques, such as the transmittive electro-optic sampling technique established by Dekorsy et al. [102]. In these experiments, the anisotropy of the dielectric constant which is induced by the dipole field of the Bloch oscillating wave packet is time-resolved. However, this method does not linearly measure the intraband dipole since the electro-optic coefficient is probed at the resonant frequencies of the interband transitions. Hence, it is not spectrally flat. In a subsequent work, the performance of the technique was verified also for off-resonant probing [103], where the sensitivity was low because of the small electro-optic effect.

Here, we employ THz emission experiments to investigate the intraband dynamics after selective excitation of the Wannier-Stark ladder spectrum. By means of these experiments, the manipulation of the intraband dynamics of Bloch oscillations under controlled optical excitation was directly addressed. Furthermore, this allows direct measurement of the intraband dipole of single Wannier-Stark ladder transitions. The experiments give clear evidence that exciton-exciton interaction plays a central role in the intraband dynamics of semiconductor superlattices. The exciton coupling is shown to induce a highly nonlinear response in the THz emission.

Difference-Frequency Mixing of Exciton Wannier-Stark Ladder Transitions

This work investigates the difference-frequency response of the biased superlattice on the selective excitation by two spectrally narrow laser lines.

For many applications, tunable quasi-monochromatic THz sources are desirable [92]. To realize such sources, the scheme of difference-frequency mixing under two-color excitation in nonlinear media is a promising way. In this context, much work was done to investigate the second-order nonlinear response of a variety of materials, e.g., semiconductor compound materials (e.g., GaAs), poled $LiNbO_3$ and organic crystals like DAST [92]. The down-conversion of ultra-short laser pulses in thin GaSe crystals was shown to be a powerful technique to generate ultrashort THz pulses which can be used for time-resolved spectroscopy (see, e.g., reference [104]). However, with these methods, large THz amplitudes can only be extracted in operation with ultrashort pulses resulting in broadband radiation.

For the generation of strong, quasi-monochromatic THz radiation, optical difference-frequency mixing in semiconductor heterostructures came into focus due to the large nonlinear response of intraband transitions. A giant second-order response can be expected in non-symmetric systems due to a large dipole-matrix element of transitions between the confined carrier states [44]. In addition, the systems have the potential to achieve the double-resonance condition by the appropriate design of the carrier spectrum.

In experiment, large quadratic susceptibilities were first observed via second-harmonic generation of CO_2 laser lines exciting intersubband transitions in doped quantum-wells. The effect was also shown in electrically biased quantum-wells [105] and double quantum-well structures [106, 107]. In comparison to bulk GaAs, susceptibilities higher by up to three orders of magnitude were reported [106]. The powerful opportunities of band-structure engineering were nicely illustrated when in a designed energy scheme of a double quantum well, Sirtori et al. [108] showed a resonant frequency-tripling via the mixing of intersubband transitions.

In the following, Sirtori et al. [109] demonstrated for the first time *THz generation* by optical difference-frequency mixing of electronic intersubband transitions in a doped double quantum well. Terahertz generation by the mixing of interband excitations in a double quantum-well was investigated in theory by Belyanin et al. [110]. In a follow-up publication the authors [111] explained the potential idea of a three-terminal semiconductor laser device which emits coherent THz radiation. They proposed difference-frequency mixing of the two interband laser fields (via an intersubband transition of hole states) as mechanism for THz generation without relying on laser action on the THz field.

Recently, quantum cascade lasers reached the THz spectral range [112–114]. Once these devices will achieve continuous-wave and high-temperature operation, they are certainly favorable radiation sources due to their high-power output, but they *lack of tunability* of the emitted THz radiation.

Biased superlattices, where the inversion symmetry is broken by an applied dc field, are promising systems because of an in-situ tunability arising from the ability to adjust to the double-resonance condition for maximum conversion efficiency just by changing the applied dc field. Recently, difference frequency-mixing in superlattices was theoretically studied, for the resonant excitation of interband transitions [38, 115, 116][2] and for the excitation of intersubband transitions [117].

However, THz emission experiments with spectrally shaped pulses driving interband transitions have not been performed yet. In this work, an experimental study of THz generation in biased semiconductor superlattices by difference-frequency mixing is reported. By the control of the bichromatic excitation and the spectrum of the superlattice, the second-order response of the superlattice was mapped out. The experiments clearly reveal the exciton enhancement of the intraband transitions.

---

[2] For the interband excitation, Korovin et al. [115] predicted a large difference-harmonic susceptibility for biased SSL (up to an order of magnitude larger than in bulk GaAs).

4.1 Intraband Dynamics Monitored in Terahertz Spectroscopy

In the experiment, a laser beam illuminates the sample and photo-generates carriers in well-defined states. The carriers get accelerated by the applied field, inducing a time-varying polarization which in turn is accompanied by the emission of THz radiation. The observable, macroscopic polarization emerges from the superposition of single microscopic dipoles $p = e\,x$ which are created by the displacement of the elementary charge e by a distance x. The acceleration of the charge ($\ddot{x}$) leads to the emission of electromagnetic dipole radiation. In the far-field (distance $|\boldsymbol{r}| \gg \lambda$), the electric field of a Hertzian Dipole is given in polar coordinates by

$$\boldsymbol{E}(\boldsymbol{r},t) = \frac{\sin\theta}{4\pi\epsilon_0\epsilon_r c^2}\frac{\ddot{p}(t)}{|\boldsymbol{r}|}\,\mathbf{e}_\theta\,, \tag{4.1}$$

where $\mathbf{e}_\theta$ is the unit vector for the azimuthal direction. The Poynting vector points in the propagation direction $\mathbf{e}_r$

$$\boldsymbol{S}(\boldsymbol{r},t) = \frac{\sin^2\theta}{16\pi\epsilon_0\epsilon_r c^3}\frac{\ddot{p}(t)^2}{|\boldsymbol{r}|^2}\,\mathbf{e}_r = |\boldsymbol{E}(\boldsymbol{r},t)|^2\pi\epsilon_0\epsilon_r c\,\mathbf{e}_r\,. \tag{4.2}$$

A typical excitation geometry is shown in Figure 4.1. The sample is tilted by an angle α. The optical beam excites the dipoles over an area which ideally should be large compared to the emitted wavelength. In this case, a directed THz emission can be expected, colinear with the transmitted and the reflected optical beams. The optimal emission of the single dipole (oriented in the growth direction) is perpendicular to the dipole axis (parallel to the surface). Nevertheless, the direction of emission is defined by the interference of the radiation of the coherent single dipoles which has a component in the forward and the reflection direction of the laser beam. The spatial emission characteristics result from a phase-array like action of the illuminated elements of the sample [118]. Here, a linear lateral phase occurs as a result of the tilted sample. The spatial emission characteristics of a Bloch oscillating sample was explicitly investigated by Martini [119] in experiment and by Victor et al. [120] in theory. The theory is based on the calculation of the Fraunhofer diffraction pattern of the emitting aperture. The directed emission of THz radiation was shown for experimental situations that are comparable to the ones used in this work. A description of the experimental details is given in the Section 4.4 below.

4.1.1 Mechanisms of Terahertz Emission in Biased Superlattices

In this Section, we will discuss how the macroscopic polarization is related to the transient evolution of the microscopic dipoles after excitation by an ultrashort pulse.

Following the arguments of Section 2.3, Bloch oscillations can be described as quantum interference between different Wannier-Stark ladder states. A broadband

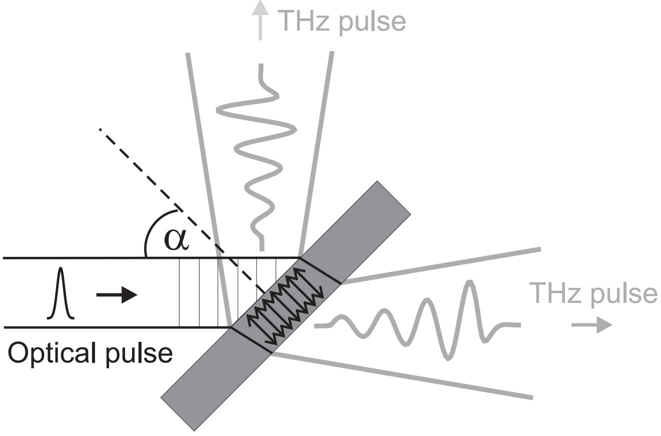

Figure 4.1: Illustration of the excitation geometry in the THz emission experiment. THz transients are emitted from the coherent dipole ensemble into cones colinear with the transmitted and the reflected optical beams.

laser pulse impinging on a biased superlattice excited various Wannier-Stark ladder transitions which are coherently coupled via a common ground state (the localized hole state). The quantum beats of the interband polarizations are accompanied with an oscillating intraband polarization of the electron Bloch oscillation (for now, we will discuss the situation in a single-particle picture, omitting exciton effects).

A direct way to trace amplitude and phase as well as the dynamics of the intraband polarization is the detection of the emitted THz radiation. The mechanisms of THz generation after the optical pumping of the Wannier-Stark ladder transitions will be discussed in the following. The simplest picture, in which quantum beat interferences can be described, is a three-level system (illustrated in Figure 4.2). The optical Bloch equations are found by extending the relations of the two-level system (as it was discussed in Section 3.1) with a second interband transition ($|0\rangle \longleftrightarrow |2\rangle$). Here, we focus on the description of the *intraband coherence* between the two upper levels ($|1\rangle \longleftrightarrow |2\rangle$). The equation of motion of the intraband polarization is given by [121]

$$\frac{\partial \rho_{12}}{\partial t} = -\left[i\omega_{12} + \frac{1}{T_{12}}\right]\rho_{12}(t) + \frac{i}{\hbar}[\mu_{10}\rho_{02}(t)E_{\mathrm{L}}(t) - \rho_{10}(t)\mu_{02}E^{*}_{\mathrm{L}}(t)]\,, \tag{4.3}$$

where T_{12} is the intraband dephasing time. The intraband polarization oscillates with the difference frequency $\omega_{12} = \omega_{01} - \omega_{02}$ which, in case of Bloch oscillations, is the Bloch frequency.

Terahertz radiation results from the induced far-infrared polarization in the growth direction which is given by the z-component of the expectation value of the macroscopic dielectric polarization density [121]

$$\langle P_z\rangle(t) \propto |e|\{\underbrace{\rho_{11}(t)(z_{00} - z_{11}) + \rho_{22}(t)(z_{00} - z_{22})}_{\text{permanent dipole}} - \underbrace{2z_{12}Re[\rho_{12}(t)]}_{\text{charge oscillations}}\}\ , \tag{4.4}$$

where the $\mu_{ij}\mathbf{e}_z = ez_{ij}$ are the intraband dipoles of the contributing Wannier-Stark states. The relation is a general expression and requires the calculation of the density

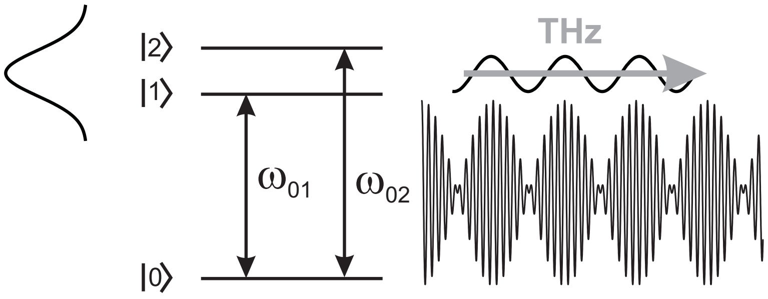

Figure 4.2: Transition scheme of a three-level system which is excited by a broadband laser pulse. The intraband polarization oscillates at the beat frequency of the interband polarization.

matrix elements. The intraband polarization and population matrix elements result from second-order interaction with the electric field (see Section 3.1)[3].

Maxwell's equations predict that a time-varying macroscopic polarization will lead to the emission of an electromagnetic transient proportional to $\ddot{P}_z(t)$. Hence, Equation 4.4 explains two mechanisms leading to THz emission which show different temporal characteristics:

[I] The first two terms in Equation 4.4 account for the difference of *permanent intraband dipoles* (ez_{ii}) between ground and excited states. This intraband polarization depends on the population of the upper state and is time-dependent only during the excitation process. Therefore, it will be referred to as the *initial dipole* signal. For a given temporal laser pulse envelope, the amplitude of the emitted signal scales with the amplitude of the permanent intraband dipole.

[II] The third term in Equation 4.4 indicates that *charge oscillations* (carrier wave packets) can be a source of THz emission. In the approximation of excitation by a δ-pulse, the second-order density-matrix element can be calculated to be

$$\rho_{12}^{(2)}(t) = \frac{\mu_{10}\mu_{20}}{\hbar^2}|E_0|^2 \mathrm{e}^{-i(\omega_{12}-i/T_{12})t}\Theta(t) \ , \tag{4.5}$$

where $\Theta(t)$ is the Heaviside function. The term describes Bloch oscillations. Here, a damping constant of the intraband coherence is introduced, the intraband dephasing time T_{12}.

For the excitation of the Wannier-Stark ladder by a broadband laser pulse, the contributions of all excited states have to be summed,

$$\langle P_z\rangle(t) \propto |e|\{\Sigma_i \rho_{ii}(t)(z_{00} - z_{ii}) - 2\sum_{i>j>0} z_{ij} Re[\rho_{ij}(t)]\} \ , \tag{4.6}$$

where the first term is the net permanent dipole. In the second term, the sum over z_{ij} describes the total amplitude of the Bloch wave packet. Also in the second term,

---

[3] Therefore, from the point of view of nonlinear optics, THz generation can be seen as difference-frequency mixing (a $\chi^{(2)}$ process) in a nonlinear non-centrosymmetric medium.

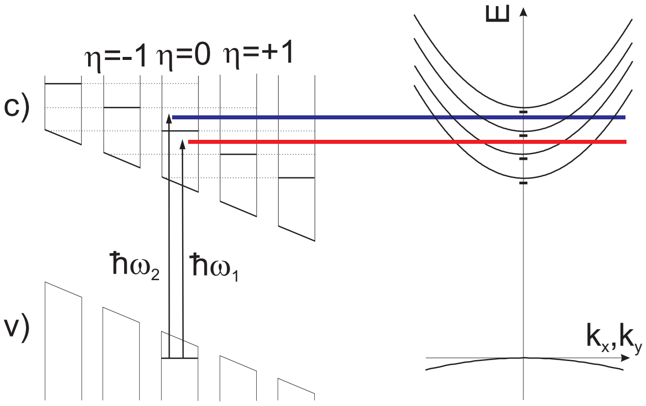

Figure 4.3: Schematic drawing of the bichromatic interband excitation of the Wannier-Stark ladder states in a biased superlattice (see Section 2.2.1). The transitions are of exciton nature (see Section 2.2.2). *Right*: The excitation of in-plane continuum states is illustrated.

$Re[\rho_{ij}(t)]$ gives the dynamics of the wave packet (Equation 4.5) and it gives the dependence on the oscillator strength of the interband transitions and the incident light intensity (the amplitude of the intraband polarization is proportional to the carrier density).

In summary, Relation 4.6 explains that with the time-resolved detection of the emitted THz signal, it is possible to directly access information on the amplitude and the phase of Bloch oscillations as well as the amplitude of the permanent intraband dipoles of Wannier-Stark states.

4.2 Mechanisms of Difference-Frequency Mixing in Biased Superlattices

To probe the difference-frequency response of the biased superlattice, the sample was excited by two narrow, coherently coupled laser lines. The excitation scheme is illustrated in Figure 4.3. Following the above arguments, two mechanisms can be responsible for subsequent THz emission:

[I] The optical excitation builds up a population in Wannier-Stark ladder states. If the states have a permanent intraband dipole, the interband excitation creates *polarized electron-hole pairs*. This is associated with a step-like temporal evolution in the intraband polarization which leads to a transient THz signal [122]. It can be termed *population-driven THz emission*.

[II] The pulse may excite a superposition of dipole-coupled states, creating a *wave packet* which undergoes Bloch oscillations. The associated oscillating intraband dipole then induces THz radiation.

To describe the emission amplitude of the second-order polarization, the difference-frequency susceptibility is the key quantity[4]. For excitation by two monochromatic laser lines (at ω_1 and ω_2) the susceptibility (if only the resonant contributions are considered) is given by [115]

$$\chi^{(2)}_{i_1,i_2,i_3}(\Delta\omega, \omega_1, -\omega_2) \approx \sum_{\nu_v,\nu_c,\nu_c'} \frac{(\mu_{i_1})_{\nu_c',\nu_c}(\mu_{i_2})_{\nu_c,\nu_v}(\mu_{i_3})_{\nu_v,\nu_c'}}{(\varepsilon_{\nu_c} - \varepsilon_{\nu_c'} - \hbar\Delta\omega - i\hbar\Gamma_{\text{intra}})} \tag{4.7}$$
$$\times \left[\frac{1}{(\varepsilon_{\nu_c} - \varepsilon_{\nu_v} - \hbar\omega_1 - i\hbar\Gamma_{\text{inter}})} - \frac{1}{(\varepsilon_{\nu_c'} - \varepsilon_{\nu_v} - \hbar\omega_2 + i\hbar\Gamma_{\text{inter}})} \right].$$

The sum comprises the hole states in the valence band with quantum numbers ν_v and the electron states in the conduction band with ν_c, respectively. The μ_i are the dipole matrix elements in the direction of the electric field component E_i. Phenomenological damping constants ($\Gamma_{\text{intra}}, \Gamma_{\text{inter}}$) are introduced. If both laser lines are resonant with interband transitions which are in addition strongly intraband dipole-coupled, the difference-frequency signal has a maximum. This case is known as the *double-resonance condition*. The total amplitude of the generated difference-harmonic is defined by the dipole matrix elements.

---

[4] For applications, the spatial dimensions of the emitting samples may exceed the THz wavelength. In this case, also the obeyance of the phase-matching condition decides over efficient THz output.

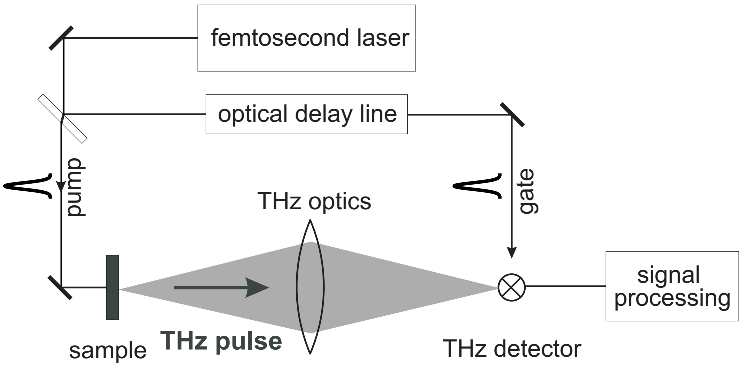

Figure 4.4: Schematic drawing of the basic set-up of a THz time-domain emission experiment. The coherently emitted THz pulse is sampled by gate pulse with variable delay.

4.3 Experimental Techniques

In this Section, first the experimental method is introduced in general terms. After that, the free-space electro-optic detection of THz radiation is reviewed. In particular, results on the modeling of the spectral response of electro-optic crystals are presented. In the final part, the experimental THz detection set-up is explained. Additionally, details are given on the employed pulse shaping apparatus and pulse monitoring set-up.

4.3.1 Terahertz Time-Domain Spectroscopy

Terahertz time-domain spectroscopy is a correlation technique (see Section 3.2.2) which allows the *time-resolved measurement of amplitude and phase* of the electric field of THz transients. In the THz spectral range, the duration of the available laser pulses is shorter than a typical cycle of the THz electro-magnetic field. In addition, detectors recently became available which are sensitive to the electric field at THz frequencies.

For a review of time-domain THz spectroscopy, the reader is referred to the article by Nuss and Orenstein [123] and references therein. The general set-up is described on the basis of Figure 4.4 which shows a schematic drawing of a THz time-domain experiment for emission spectroscopy.

The laser pulses are generated by a femtosecond laser system. A beam-splitter divides the beam into a pump and a gate beam. The pump pulse excites the sample which emits a coherent THz transient into free space. The radiation is collected and focused onto a detector.

This measurement technique allows the time-domain to be mapped out by variably delaying the gate pulse with the help of an optical delay line. This technique is only sensitive to coherently emitted signals, because pump and gate pulse originate

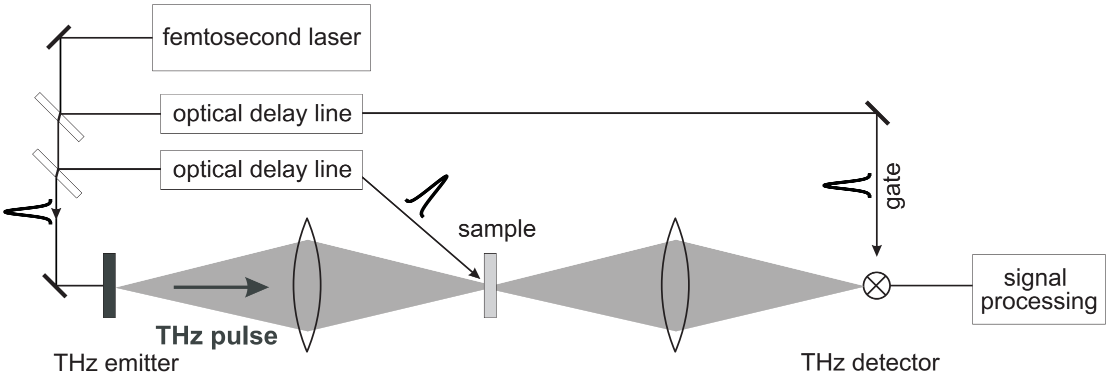

Figure 4.5: Schematic drawing of the basic set-up of a THz time-domain spectrometer measuring the dielectric function of the sample in the THz spectral domain. With the help of a second delay line an optical pump - THz probe experiment can be performed.

from a common source. For each particular delay between the pulses, the detection accumulates the synchronized coherent signal and suppresses the unsynchronized incoherent thermal background.

The emission experiment can be easily extended to realize a THz time-domain spectrometer, as shown in Figure 4.5. The transmission of a known THz signal through the sample, placed in the THz beam path, is measured. Since the amplitude and phase of the transmitted electric field are monitored, the real and the imaginary parts of the dielectric function can be extracted simultaneously. Similarly, this arrangement may be used to investigate the THz response of the sample after optical excitation. This is known as optical pump - THz probe experiment.

Time-Gated THz Electric Field Detectors

There are two well established THz electric field detectors, *photo-conductive dipole antennas* and *electro-optic crystals*.

Historically, the first detectors available were photo-conductive dipole antennas as, e.g., employed by Exter et al. [124] in the first reported free-space THz time-domain experiment. In general, the geometry of the antennas is as follows: A metal stripe, about $5-10\,\mu$m wide on a substrate acts as a Hertzian dipole. In the center, it is has a very narrow gap, on the order of a few microns. Underneath the gap, a photo-conductive material is placed which acts as a so-called Auston switch [125]. A laser pulse which is focused onto the gap excites free carriers. The carriers get separated by the incident THz electric field which is also focused onto the gap. This leads to a transient current signal. For monitoring the induced current which is a measure of the electric field, the dipole is connected by impedance matched feed lines.

The upper bandwidth limit of the antenna is set by the carrier lifetime of the photo-conductive material. Two materials with sub-picosecond lifetime are commonly employed, ion implanted silicon on a sapphire substrate or GaAs grown at low temperatures. The latter seems to be the preferred material with carrier lifetimes below 500 fs [126]. Originally, photo-conductive antennas used to have a very limited bandwidth, with the maximum of their response function around 1 THz[5],[6].

The introduction of electro-optic crystals for time-resolved detection of free-space propagating THz radiation has been an important means of overcoming the bandwidth limitation of antennas[7]. First results were reported almost simultaneously by three groups, Wu et al. [133], Jepsen et al. [134] and Nahata et al. [135].

In recent years, the electro-optic sampling technique, which was also employed in this work, became the technique of choice for several reasons. It can provide a large detection bandwidth. The recording of THz frequencies up to 70 THz [136] was reported. Additionally, in contrast to antennas (usually lab-built), electro-optic crystals are readily available on the market and their response function can be analytically modeled. Finally, the electro-optic sampling is easy to handle. The alignment of the experiment can be carried out with the help of the near-infrared beams which are visible. In the following, the physical background of electro-optic sampling will be discussed, leading the reader to the modeling of the detector response function.

4.3.2 Free-Space Electro-Optic Sampling

The technique is based on the linear electro-optic effect, known as the Pockels effect [137]. In the presence of an electric field, the optical properties of second-order nonlinear materials can be modified. This effect can be viewed as a three-wave mixing process, described by the second-order susceptibility tensor,

$$\chi^{(2)}_{ijk}(\omega, 0, -\omega)\,, \tag{4.8}$$

where one field is a DC or very low frequency field. The difference frequency mixing leads to a field dependent refractive index change which can be described by the electro-optic coefficient [138]

$$r = \frac{-2\pi}{n^4}\chi^{(2)}\,. \tag{4.9}$$

---

[5] Many report on the spectral response of their THz detection [127–129] peaking around 1 THz and having a strong roll-off at higher frequencies.

[6] Only very recently, Kono et al. [130] reported the detection of THz signals up to 40 THz by gating a low-temperature-grown GaAs antenna with ultrashort laser pulses, giving a bandwidth comparable to the electro-optic sampling technique.

[7] Broadband time-resolved detection of THz signals can also be realized with an interferometric technique [131, 132] which discards the phase information. Two laser pulses retrieved from a Michelson interferometer are sent onto the sample. The two subsequently emitted THz transients interfere on an incoherent broadband detector, a cooled bolometer. By scanning the time delay between the pulses an THz interferogram is recorded which contains information on the power spectrum only.

In a microscopic picture, an electric field acts as a perturbation of bound states of a crystal (the Stark effect) and in some cases leads to a slight deformation of the lattice. The fluctuations are usually anisotropic such that non-centrosymmetric crystals exhibit an electro-optic effect. The contribution linear in electric field, is known as the Pockels effect.

In the experiment, for an incident THz electric field, the Pockels effect leads to a birefringence of the sensor crystal which changes the polarization ellipticity of the gate beam passing through it. By monitoring this polarization change of the gate beam as function of the temporal delay between THz signal and gate pulse, the amplitude and the phase of the THz electric field can be mapped out.

For optimal performance, the phase matching condition has to be met, meaning that the THz phase velocity has to be equal to the group velocity of the optical pulse. If instead there is a velocity mismatch, the optical pulse would sweep temporally across the THz signal, smearing out the desired effect and reducing the detection bandwidth. Much work was done to find the best suited electro-optic crystal. It has to be transparent for the near-infrared gate beam, has to have a very small velocity mismatch and has to provide a large electro-optic coefficient. For first proof-of-principle measurements, $LiTaO_3$ crystals [133, 134] and a poled polymer [135] were used as electro-optic detectors, but with a poor signal to noise performance. An important step was the proposal by Wu et al. [139] who used ZnTe as the electro-optic material which combines all favorable properties. Fortunately, it was also possible to work in a phase matching regime where gate and THz beam propagate collinear through the crystal[8]. Besides ZnTe, GaP was proposed as an alternative electro-optic crystal, especially for measurements in the low frequency band up to 10 THz. GaP has the first TO phonon resonance at a higher frequency, near 11 THz [140], compared to ZnTe with its first TO phonon resonance at 5.3 THz [141]. A disadvantage of GaP, which exhibits a comparable phase-matching performance [142], is the smaller electro-optic coefficient, see Table 4.1.

THz detection by photo-conductive antennas has a signal to noise ratio similar to the electro-optic detection [143] but clearly out-performs antennas in terms of bandwidth, see [136, 144–146].

Spectral Response Function of Electro-Optic Detection

The spectral response of the electro-optic detection can be modeled analytically, following the approach reported in [136, 142]. Simulating the response is useful for choosing an adequate electro-optic crystal and its thickness according to its bandwidth and sensitivity. Once the response function is known, the measured THz signal can be corrected for the detector response.

---

[8] In contrast to the experiments using $LiTaO_3$ crystals [139], where the optical beam has to travel at an angle of 71° relative to the THz beam.

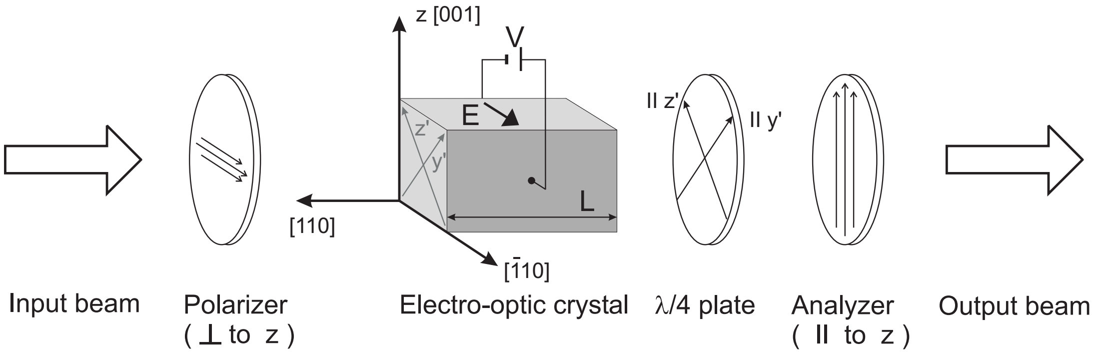

Figure 4.6: Electro-optic detection, schematically drawn as a Pockels cell. The electric field E_{THz} which is the experimentally measured quantity, is symbolized by a voltage V along the [$\bar{1}$10] direction. The optical beam is polarized parallel to the electric field and propagates along the [110] crystal direction. For zero field, the quarter-wave plate induces a circularly polarized beam. The main axes of the quarter-wave plate are parallel to the principle axes of the electric field induced refractive index ellipsoid (given as z' and y'). The change of the ellipticity, due to an applied field, is detected as intensity modulation behind the analyzing polarizer.

The Pockels effect induces a birefringence in the electro-optic material. Figure 4.6 is a schematic representation of a detection set-up in a Pockels cell configuration. As the detection crystal, $\{110\}$ cut zincblende materials, e.g., ZnTe and GaP, can be employed. Due to their symmetry, only one component of the electro-optic tensor, the coefficient r_{41}, is non-zero [137].
The optical beam is linearly polarized along the [$\bar{1}$10] direction. The high voltage is applied across the detection crystal parallel to the polarization of the optical beam to maximize the intensity modulation of the beam [147]. As shown in Figure 4.6, for crossed polarizers and a quarter-wave plate which induces a phase bias, the intensity modulation is given by

$$\frac{I}{I_0} = \frac{1}{2}\left[1 - sin\left(\frac{\pi E}{E_\pi}\right)\right], \tag{4.10}$$

where

$$E_\pi = \frac{\lambda}{2Ln^3 r_{41}},$$

is the electric field needed to induce a total phase retardation by π of the slow optical polarization component. Here, L is the length of the crystal and λ is the wavelength of the optical beam.

The quarter-wave plate is introduced because it linearizes the response (for $E \ll E_\pi$) of the detection[9]. In addition, to reach a useful signal-to-noise ratio, usually both polarization components of the optical beam are monitored and their difference is

---

[9] Without the quarter-wave plate, for the crossed-polarizer configuration, the intensity modulation would be $I/I_0 = \sin^2(\phi_E/2) = \sin^2(\pi E/2E_\pi)$, where ϕ_E is the induced phase retardation. With a quarter-wave plate, a circularly polarized beam is produced. Thus, the response is instead $I/I_0 = \sin^2(\pi/4 + \pi E/2E_\pi) = 1/2[1 - \sin(\pi E/E_\pi)] \approx 1/2[1 - \pi E/E_\pi]$.

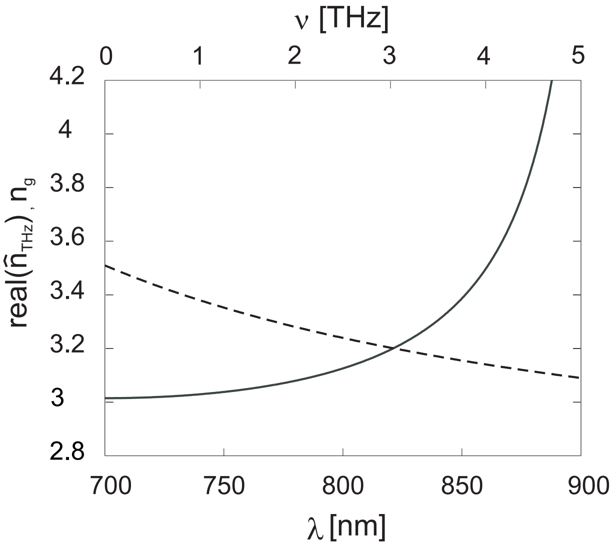

Figure 4.7: The graph compares the terahertz refractive index for ZnTe (*solid*), calculated from Equation 4.16, with the near-infrared group refractive index (*dashed*) which was calculated following Equation (3) in [144].

recorded. This doubles the signal and removes the large background. The intensity modulation then reads

$$\frac{\Delta I}{I_0} = (\frac{2\pi}{\lambda} n^3 r_{41} L) E \,, \tag{4.11}$$

which depends *linearly* on the electric field (the THz electric field amplitude).

Assuming an instantaneous response of the electro-optic material, in experiment, the THz pulse is measured time-resolved by sampling $\Delta I(\tau_\mathrm{d})/I_0$ a as function of the correlation time (the delay time τ_d) relative to the optical gate pulse.

Equation 4.11 is only valid if the phase-matching condition is met. This requires that the group velocity of the optical gate pulse and the phase velocity of the THz frequency components are equal. However, in particular the THz dielectric function of the electro-optic material shows significant dispersion (due to phonon resonances) which will always lead to some velocity mismatch. Figure 4.7 plots the refractive index of ZnTe in the THz region and the optical group refractive index for the near-infrared region. Both values show only small differences. This indicates a small velocity mismatch. Due to this advantage over other electro-optic materials [139], ZnTe became one of the more widely used material for this application.

In case of a certain velocity mismatch, the optical gate pulse will accumulate a temporal delay δ with respect to the THz frequency components when traveling through the crystal. It will be

$$\delta(\omega) = \frac{L}{c_0} \left(n_g(\lambda_c) - n_\mathrm{THz}(\omega) \right) \,, \tag{4.12}$$

where λ_c the central wavelength of the gate pulse. Consequently, the gate pulse averages over the THz electric field in the time interval δ and the intensity modulation for a specific correlation time τ_d of the experiment is given by

$$\frac{\Delta I(\tau_\mathrm{d})}{I_0} = (\frac{2\pi}{\lambda} n^3 r_{41} L) \frac{\mathsf{t}}{\delta} \int_{\tau_\mathrm{d}-\delta/2}^{\tau_\mathrm{d}+\delta/2} E(t^{'})dt^{'} \, , \tag{4.13}$$

where t is the Fresnel transmission coefficient of the THz field. It is written as $\mathsf{t} = 2/(1 + n_\mathrm{THz})$. The integral describes the convolution of the electric field with a rectangular time window. Taking the Fourier transformation of both sides of the equation leads to

$$\frac{\Delta \hat{I}(\omega)}{I_0} = (\frac{2\pi}{\lambda} n^3 r_{41} L) \, [\hat{E}(\omega) * \hat{\mathrm{G}}(\omega)] \, , \tag{4.14}$$

where $\Delta\hat{I}$ is the complex spectrum of the measured intensity modulation and $\hat{E}$ the complex spectrum of the THz field. Hence, $\hat{\mathrm{G}}(\omega)$ is the spectral response function of the detection,

$$\hat{\mathrm{G}}(\omega) = \hat{\mathsf{t}}(\omega) \left(\frac{\exp\left[i2\pi\omega\hat{\delta}(\omega)\right] - 1}{i2\pi\omega\hat{\delta}(\omega)} \right) . \tag{4.15}$$

Here, $\hat{\delta}(\omega)$ and $\hat{\mathsf{t}}(\omega)$ are complex because the refractive index of the polar lattice exhibits a strong dispersion due to phonon resonances in the THz frequency region. The refractive index can calculated parameterized in an oscillator model [136],

$$\hat{n}_\mathrm{THz}(\omega) = \sqrt{\left[1 + \left(\frac{(\hbar\omega_\mathrm{LO})^2 - (\hbar\omega_\mathrm{TO})^2}{(\hbar\omega_\mathrm{TO})^2 - (\hbar\omega)^2 - i\hbar\omega\gamma} \right)\right] \epsilon_\infty} \, , \tag{4.16}$$

where $\hbar\omega_\mathrm{LO}$, $\hbar\omega_\mathrm{TO}$ are the longitudinal, transverse phonon energies and γ the damping constant. The high-frequency dielectric constant is denoted as ϵ_∞. With $\hat{n} = \sqrt{\hat{\epsilon}} = n - i\kappa$ (where $\hat{\epsilon}$ is the complex dielectric function), the real part of $\hat{n}$ is the usual refractive index and the imaginary part describes the absorption of the THz radiation, see Figure 4.8.

Additionally, the electro-optic coefficient is in general dependent on the frequency since the response of the polar lattice also contributes to the effect. The ratio between electronic and lattice contribution to r_{41} is described by the Faust-Henry coefficient C. In the THz spectral range (away from electron resonances) the electron contribution is constant. An analytic expression for the dispersion of the electro-optic coefficient was given in the original paper by Faust and Henry [148]:

$$\hat{r}_{41}(\omega) = r_e \left[1 + C \left(1 - \frac{(\hbar\omega)^2 - i\hbar\omega\gamma}{(\hbar\omega_\mathrm{TO})^2} \right)^{-1} \right] , \tag{4.17}$$

where r_e is the electron contribution. The term led by C describes the lattice contribution. For ZnTe, C was found to be -0.07 [136], i.e., the lattice contribution in this material is small and only plays a role at the phonon resonance. However, at

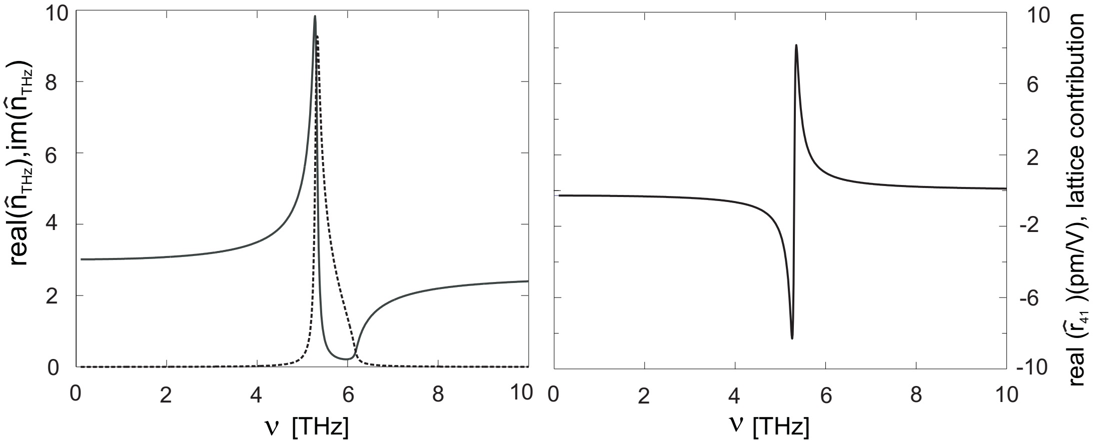

Figure 4.8: *Left*: The real (*solid*) and imaginary (*dashed*) part of the complex refractive index for ZnTe (after Equation 4.16) are plotted. *Right*: The lattice contribution to the electro-optic coefficient for ZnTe (second term of Equation 4.17) is shown.

the phonon resonance the THz radiation is strongly absorbed by the crystal. Hence, it will only be a minor effect.

Including the dispersion of $\hat{r}_{41}$, the total spectral response function of the detection can be defined as the complex product,

$$\hat{\mathrm{R}}(\omega) = \hat{r}_{41}(\omega) * \hat{\mathrm{G}}(\omega)\,, \tag{4.18}$$

where Equation 4.14 is modified to,

$$\frac{\Delta\hat{I}(\omega)}{I_0} = (\frac{2\pi}{\lambda} n^3 L)\,[\hat{E}(\omega) * \hat{\mathrm{R}}(\omega)]\,. \tag{4.19}$$

Using this expression, the measured THz electric field can be corrected for the detector response in the Fourier spectrum of the measured data, $\mathcal{FT}\{\Delta I(\tau_\mathrm{d})/I_0\}$.

The calculated spectral response function $\hat{\mathrm{R}}$ for $\{110\}$ cut ZnTe is shown in the left graph of Figure 4.9, where the response of crystals with increasing thickness, 200 μm, 300 μm and 1 mm are compared. It is seen that the phonon absorption at around 5 THz clearly defines the upper limit of a low frequency bandwidth window. Additionally, it becomes clear that for an increasing thickness, the velocity mismatch has a strong impact on the response. It leads to a narrowing of the bandwidth window

	ν_TO [THz]	ν_LO [THz]	γ [THz]	ϵ_∞	C	r_{41} [pm/V]
ZnTe	5.3 [141]	6.2 [141]	0.09 [141]	6.7 [141]	$-0.07^{+0.02}_{-0.05}$ [136]	4 [142]
GaP	11 [149]	12.1 [149]	0.13 [150]	9.11 [42]	-0.47 [151]	1 [142]

Table 4.1: Parameters used for the calculation of the response function.

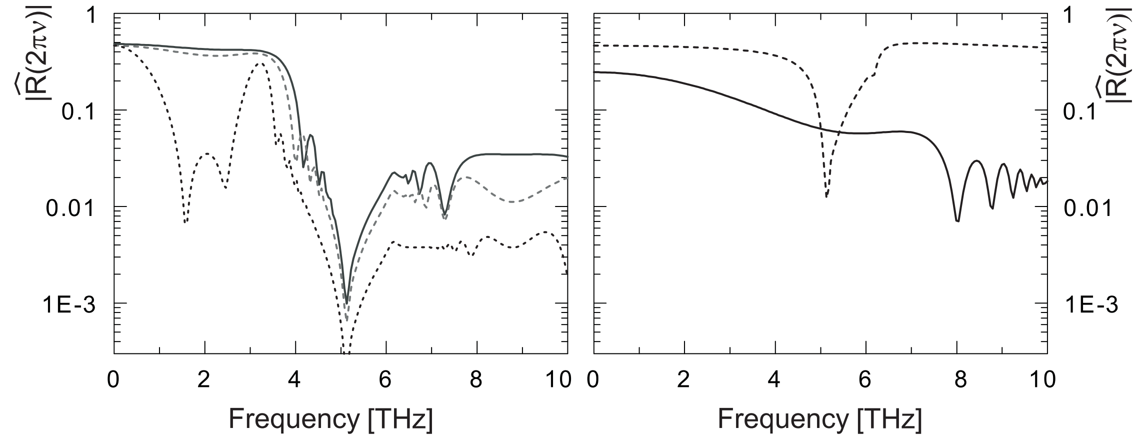

Figure 4.9: *Left*: Absolute value of the detector response function $\hat{\mathrm{R}}(\omega)$ of ZnTe crystals with thicknesses of 200 μm (*solid*), of 300 μm (*dashed*) and of 1 mm (*short dash*). *Right*: Absolute value of the detector response function $\hat{\mathrm{R}}(\omega)$ of a ZnTe crystal with a thickness of 15 μm (*dashed*) and of a GaP crystal, 200 μm (*solid*) thick. The central wavelength of the gate pulse is set to be 800 nm. For these calculations, the factor r_e in Equation 4.17 is set to unity. Consequently, the value R(0) describes the Fresnel loss at the surface of the crystal.

and spectral modulations. This is particular obvious for the response of the 1 mm thick ZnTe crystal which shows a significant minimum of sensitivity around 2 THz. Hence, thinner crystals are more favorable, since phase-matching is less restrictive. However, there exists a clear trade-off between bandwidth and signal amplitude, since the latter decreases linearly with thickness (Equation 4.11). In this work, ZnTe crystals with thicknesses of 200 μm and 300 μm are employed which provide an almost rectangular sensitivity window for low THz frequencies.

In the right graph of Figure 4.9, example calculations are shown to illustrate that for very thin ZnTe crystals, the detection bandwidth becomes very broad with a considerable sensitivity also for frequencies above the phonon resonance (demonstrated in References [136,152]). Additionally, the response function of a 200 μm thick {110} cut GaP crystal is plotted for comparison with the response of the 200 μm ZnTe crystal (see left graph). The phonon resonance at higher frequency opens up a broader low frequency bandwidth window. On the other hand, GaP exhibits a higher Fresnel loss, a stronger velocity mismatch and the electro-optic coefficient r_{41} is almost 4 times smaller than for ZnTe [142].
Since very small THz signals had to be detected in this work, ZnTe was employed, even though the bandwidth window up to only around 4 THz acted as limitation for some experiments.

4.4 Experimental Set-Up

In this Section, the practical realization of the time-domain THz experiment will be described. The set-up is depicted in Figure 4.10. The near-infrared laser pulses are generated by a standard Kerr-lens modelocked Ti:Sapphire laser system, the same as employed in the four-wave mixing experiments (Section 3.4).

A glass (BK7) beam-splitter first divides the beam into an intense pump and a weak gate beam which propagate along separate optical paths. After the excitation of the sample by the pump pulse, a THz transient is emitted. The THz signal which radiates in the direction of the transmitted pump beam (see Section 4.1) is collected and imaged by parabolic mirrors onto the electro-optic detector crystal. For the temporal overlap of THz pulse and optical gate pulse at the detector, the overall optical path lengths have to be equal starting from the initial beam-splitter. By varying the path length of the pump beam with the help of a computer controlled delay stage, the THz field is mapped out in time. The delay stage was installed in the pump beam rather than in the gate beam, because any potential sources of noise had to be excluded from the beginning: fluctuations of the gate beam intensity were the main noise source in the experiment.

An important part of this work were experiments which investigated the THz emission after *selective excitation* of optical transitions of the sample. This required a well controlled spectral shape for the pump beam and simultaneous monitoring of the energy spectrum of the sample.

The latter was performed by the installation of a weak monitor beam to measure the absorption spectrum of the sample. Before performing the experiment, the monitor beam was taken from the gate beam by a flipping mirror. It was weakened by a neutral density filter and focused on the sample with a lens (with a focal length of $f = 250\,\mathrm{mm}$). The spot size of the monitor beam was measured to be around $80\,\mu\mathrm{m}$ (FWHM) which is considerably smaller than the spot size of the pump beam. The pump beam was focused with a lens ($f = 1\,\mathrm{m}$) which was installed 700 mm from the sample, producing a large spot on the sample. The transmitted monitor beam was deflected out of the THz beam path by a pellicle beam-splitter, which was transparent to THz radiation, but had a 50% reflectivity for the near-infrared beam. To measure the spectrum of the monitor beam, it was coupled into the spectrometer system which was described above (see Section 3.4). Alternatively, the transmitted pump beam could also be coupled into the spectrometer.

To accomplish the spectrally selective excitation of the sample, the spectrum of the pump pulse was manipulated with the help of a pulse shaper apparatus which will be explained below.

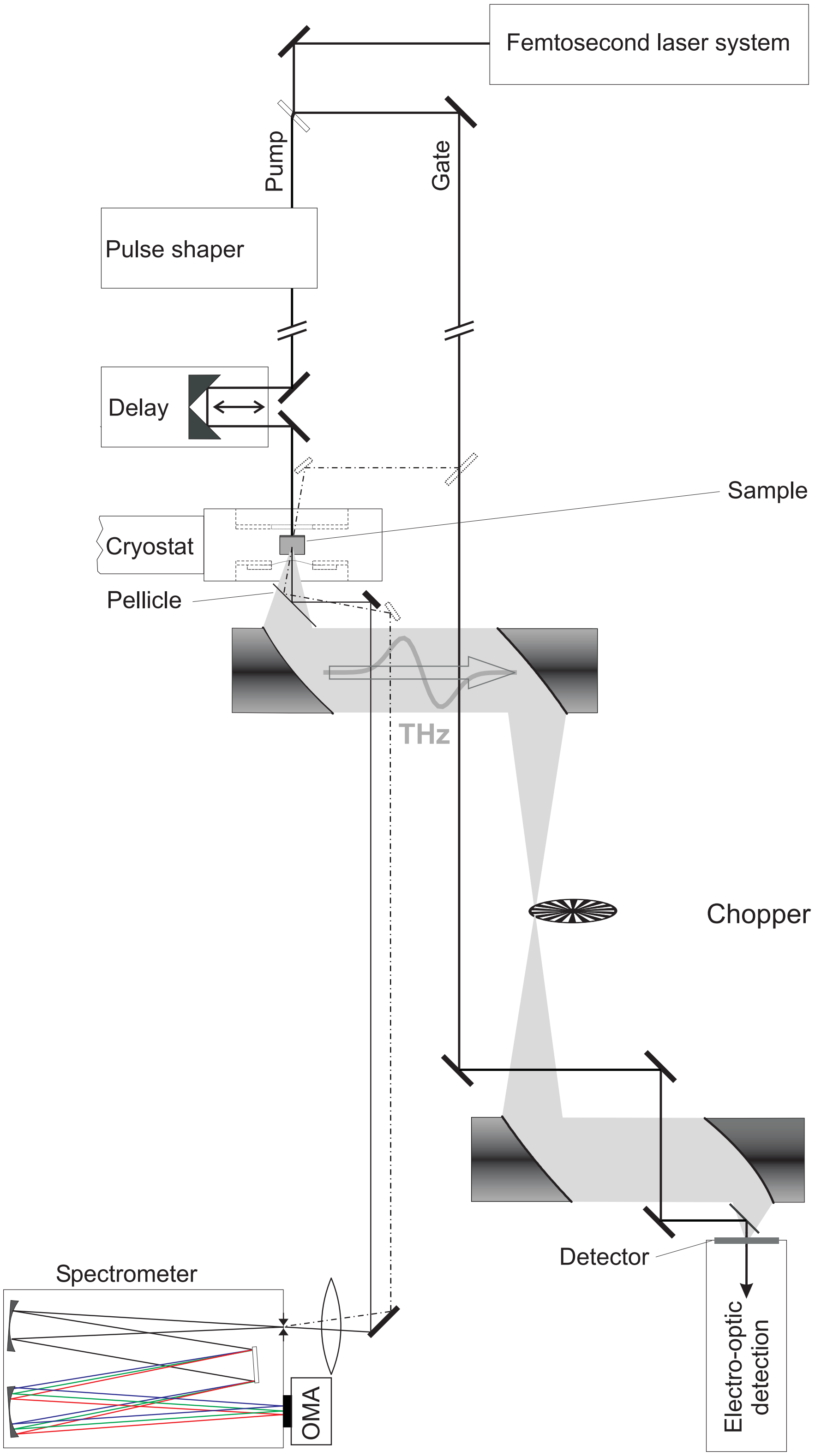

Figure 4.10: Schematic drawing of the experimental set-up which is described in the text. The monitor beam which is installed to measure the absorption spectrum of the sample is drawn as a *dash-dotted* line.

Terahertz Optical Components

The transient THz signal emitted by the sample was radiated into free space. The sample was mounted in a helium vapor driven cold-finger cryostat (Microstat manufactured by Oxford Instruments) tilted around its horizontal axis by an angle of 50°. The Microstat provided a large numerical aperture for the diverging THz radiation. In experiments, the sample was held at a temperature of 10 K. An ultrathin mylar polyester film with a thickness of 20 μm was installed as out-coupling window for the THz radiation, being also transparent in the visible spectral range.

The THz radiation was imaged by four 90°, off-axis parabolic, gold-coated, mirrors, with a diameter of 50.8 mm. The first mirror collected the radiation emitted by the sample and collimated it. The second one brought the beam to a focus, where a chopper was placed which modulated the THz signal. The chopper was installed for phase-sensitive detection using a lock-in amplifier for signal processing. The third mirror collimated the radiation again before it was brought to a tight focus onto the detector crystal by the last mirror. The alignment of the system had to be done with great care since misaligned parabolic mirrors can considerably distort the THz beam shape. The focal length of the first mirror was 76 mm, of the second and third 150.2 mm and of the fourth mirror 50.8 mm. The mirrors were mounted on 3D-micrometer stages to allow them to be manipulated with high precision and reliability. The use of reflecting optics has the great advantage that the THz radiation travels along the same optical path as the near-infrared pump beam. Consequently, the visible beams could be used for alignment. The whole THz beam path had to be enclosed to allow for purging with dry nitrogen. This prevented absorption by water vapor [124].

Working with long wavelength radiation introduces some experimental issues which can be neglected in optics with near-infrared beams. The size of the THz emission spot on the sample was comparable to the emitted wavelength and consequently the beam diverges from the sample at a wavelength-dependent divergence angle. Therefore, the first parabolic mirror was chosen to have a focal length as small as geometrically possible to ensure that the THz radiation was effectively collected. For the same reason, parabolic mirrors with a large diameter (50.8 mm) were employed and the spot size on the sample was maximized. To minimize the influence of possible lateral field fluctuations in the sample. The spot size was limited to the size of the sample area where the substrate layer could be homogeneously removed by wet-etching (see Section 3.3). In the experiment, the realized pump spot diameter was of about 600 μm (FWHM). Clearly, from these geometric limitations, a low frequency cut-off can be expected for the bandwidth of the experiment.

The same "diffraction" effect is present on the detection side where a wavelength dependent THz spot on the electro-optic crystal is expected. The gate beam integrates the electro-optic effect over its transverse intensity profile. There is a clear trade-off between the detection of low frequency radiation which requires a large gate spot, and the under-estimation of high frequency components which have a small spot size. Therefore, test measurements were carried out to search for the optimal geometry. As the THz source for these measurements, an $In_{0.56}Ga_{0.44}As$ surface emitter [153] was installed. The radiated broadband THz signal was recorded as function of the gate spot size. The latter was varied by shifting the focusing lens along the beam relative to the ZnTe crystal. Finally, the spot size was set in a way that further increase would not alter the detected THz spectrum.

Electro-Optic Detection Set-Up

In Figure 4.11, a more detailed drawing of the electro-optic detection set-up is shown. The gate beam is focused by a lens with a focal length of 250 mm and reflected into the THz beam path by a high resistivity silicon wafer. A 5 nm thin Au layer was evaporated onto the front side of the wafer to increase the reflectivity. This increased the optical power in the gate beam which is favorable for a low noise level[10]. The gate beam was aligned to propagate collinearly with the THz beam (spatially overlapping) through the detector crystal. For the pre-alignment of the overlap, the pump beam was used which was partially transmitted by the sample and thereby usefully imitated the THz beam. With the Si wafer removed, the expected position of the THz focus was determined by a pinhole installed instead of the ZnTe crystal. After installation of the Si wafer, the gate beam is aligned, taking into account the walk-off of the THz beam (by 300 μm) due to refraction in the wafer. For the final step of the alignment, in the experiment, the last parabolic mirror was translated parallel to the ZnTe surface on a micrometer range which shifted the THz spot across the gate spot. With this procedure, the set-up was aligned by searching for the maximum signal.

The polarization of the THz beam and the optical beam were adjusted in the same order as described in Section 4.3.2. The THz beam was linearly polarized perpendicular to the optical table, set by tilting the sample around a horizontal axis. The optical gate beam was emitted by the laser linearly polarized perpendicular to the optical table. A polarizer was installed to exclude possible polarization changes due to the optical components. Behind the ZnTe detector, an achromatic quarter-wave plate was employed to circularly polarize the gate beam. Finally, the polarization components of the beam were separated by projecting them onto the axis of a Wollaston prism. To analyze the THz field-induced polarization change of the gate beam, a balanced-detection scheme was used.

---

[10] The signal to noise ratio increases proportionally with $\sqrt{I}$.

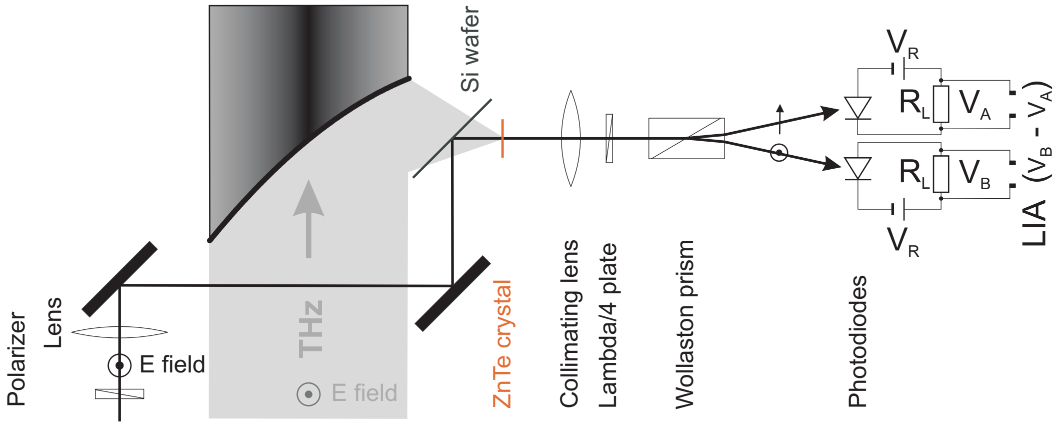

Figure 4.11: Schematic drawing of the experimental implementation of the electro-optic detection. The THz beam is linearly polarized perpendicular to the optical table. The optical beam is also linearly polarized, parallel the THz electric field and parallel to a ⟨110⟩ direction of the {110} cut ZnTe crystal.

Signal Processing

The balanced-detection scheme compares the intensities of the two polarization components by analyzing the differential signal. If instead only one polarization component were to be measured, the small signal would be on a large fluctuating background and it would be impossible to reach a sufficient signal-to-noise ratio.

The two beams after the Wollaston prisms were focused onto two large area Si photodiodes. The incident beams typically induced a photo current of around 2.5 mA which was converted to a voltage by a load resistor ($R_L = 2.7\,\mathrm{k}\Omega$). To ensure the linearity of the diodes, a reversed bias was applied ($V_R = 24\,\mathrm{V}$). The resulting signal voltages, V_A and V_B, were connected to the two input channels of a lock-in amplifier (Model SR830 from Stanford Research). The differential signal was produced by the built-in low noise differential amplifier and analyzed with the low-pass slope set to 24 dB/oct. For the dynamic reserve, the "Low Noise" setting was used. The time constant was typically chosen to be either 300 ms or 1 s. The lock-in amplifier was synchronized to the chopper which modulated the THz signal at a frequency around 3 kHz.

With the balanced-detection, the shot-noise limit could almost be reached. The shot-noise induced by the photo current, i_p, is given by

$$i_{\mathrm{s}}[\mathrm{rms}] = \sqrt{(2\,e\,i_{\mathrm{p}}\,B)}\,, \tag{4.20}$$

where e is the elementary charge and B the detection bandwidth. For the time constant of 300 ms, the bandwidth of the Lock-in amplifier (low pass filter slope = 24 dB/oct) is 0.3 Hz. A photo current of 2 mA would then result in a shot-noise voltage across the resistor of 40 nV. The (rms) noise amplitude of the detected signal was measured to be typically 100 nV which is close to the pure shot-noise amplitude.

The thermally activated Johnson noise over R_L was one order of magnitude smaller and can therefore be neglected.

In the experiment, the beams were accurately balanced by fine-tuning the quarter-wave plate to zero the difference of the diode's dc photo currents. A potential noise source was found to be the ZnTe detector crystal itself. It was important to find a "good" gate spot on the crystal, free from Te islands. Otherwise, the gate beam would have been depolarized by scattering off the islands and spatial fluctuations of the spot position during the experiment would have caused considerable noise.

In this experiment, it was ultimately possible to reach a signal-to-noise ratio sufficient to detect a relative signal, $\frac{\Delta I}{I_0}$, on the order of 10^{-6}.

4.4.1 Spectral Pulse Shaping

The pump pulse was spectrally shaped with the help of an optical set-up which is schematically shown in Figure 4.12. A review article on this kind of dispersion-free pulse shaper was published by Weiner et al. [154]. The laser beam is spatially dispersed by a gold coated diffraction grating, with 830 lines/mm which is placed at the focal plane of a lens ($f = 500\,\text{mm}$). Apart from collimating the diverging spectrum, the lens leads to a focus of the spectral components at the Fourier plane. The apparatus is built symmetric with respect to the Fourier plane, comprising a second lens and a second grating of the same kind. This second mirror-symmetric part combines the spectral components again to the output beam. For a precise alignment of the components and in the absence of a mask, the spectral, temporal and spatial profile of the pulse remains unaltered.

If a mask is introduced into the Fourier plane, the pulse spectrum can be shaped by influencing amplitude and phase of the spectral components [11]. In this work, spatially patterned intensity masks were used for pulse manipulation. For bandwidth-limited pulses, the spectral phase of the pulse is constant, and the Fourier transform of the intensity mask pattern directly gives the temporal pulse envelope.

The pulse shaper set-up (without mask) was aligned by iteratively approaching the transform-limit of the outcoming pulse, whereas an auto-correlation experiment[12] was employed to measure the duration of the laser pulse. Firstly, it was found that the temporal envelope of the un-shaped laser pulse can be described by a Gaussian function.

The bandwidth product of a Gaussian pulse which represents the interrelationship

---

[11] For an arbitrary shaping of ultrashort pulses, programmable liquid crystal arrays were reported to be a powerful tool which can be used for a simultaneous manipulation of spectral amplitude and phase [155].

[12] A standard second-order auto-correlation apparatus was installed employing a Barium Borate crystal for second harmonic generation and a photomultiplier tube for detection [156].

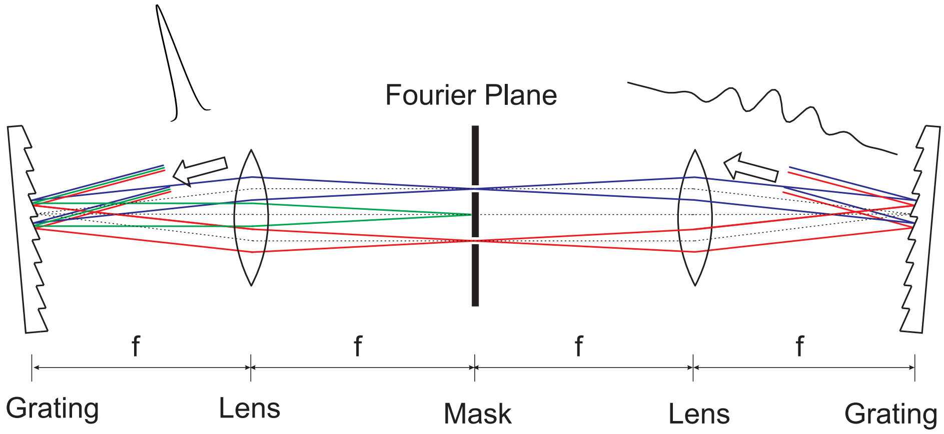

Figure 4.12: Schematic drawing of a pulse shaper apparatus with an installed intensity mask. Here, the intensity mask cuts all spectral components except two narrow spectral branches. The temporal form of the output pulse is given by the Fourier transform of the shaped spectrum. In the experiment, instead of the second lens and grating, a mirror was introduced at the Fourier plane reflecting the spectrum back onto the input optical axis. The mask was then installed very close to the mirror.

between spectral width, $\Delta\nu$ [Hz], and pulse duration, τ_p [s], (the numbers give the FWHM) is written as [157]

$$\tau_\mathrm{p}\,\Delta\nu \geq 0.441\,, \tag{4.21}$$

where the relation becomes an equality in case of a transform-limited pulse.

Secondly, the task was to prove that the pump pulse after the pulse shaper is transform limited. Therefore, the spectral width and the pulse duration were measured[13]. The spectral width (FWHM) of the pulse was found to be 27 meV which converts to $\Delta\nu = 6.5\,\mathrm{THz}$ (FWHM). The pulse duration was measured to be 65 fs (FWHM). Hence, the bandwidth product is 0.4 which is consistent with the transform-limit within an experimental error of ± 10%. Nevertheless, a transform-limited output pulse does not necessarily mean that the pulse which enters the pulse shaper is also transform-limited, because the apparatus can act as a grating compressor [154].

The latter question was answered by comparing the pulse duration before and after the apparatus, through an indirect measurement. For this, a cross-correlation experiment[14] was employed[15] and the gate pulse was assumed to be the same as the

---

[13] The pulse duration was determined by an auto-correlation experiment. For a Gaussian pulse, the relation between the temporal width of the auto-correlation scan τ_{ac} and the pulse duration τ_p is given by [157], $\tau_{ac}\,/\,\tau_p = 1.414$.

[14] The auto-correlation experiment could be easily converted into a cross-correlation apparatus [157], by reflecting the external reference pulse into one of the two beam paths of the set-up. For the cross-correlation experiment, the shaped pump pulse was "picked-up" just before the cryostat. The gate pulse was used as reference pulse.

[15] In general, the cross-correlation experiment was used to monitor the temporal form of the shaped pump pulse by measuring its convolution with an un-shaped, short reference pulse

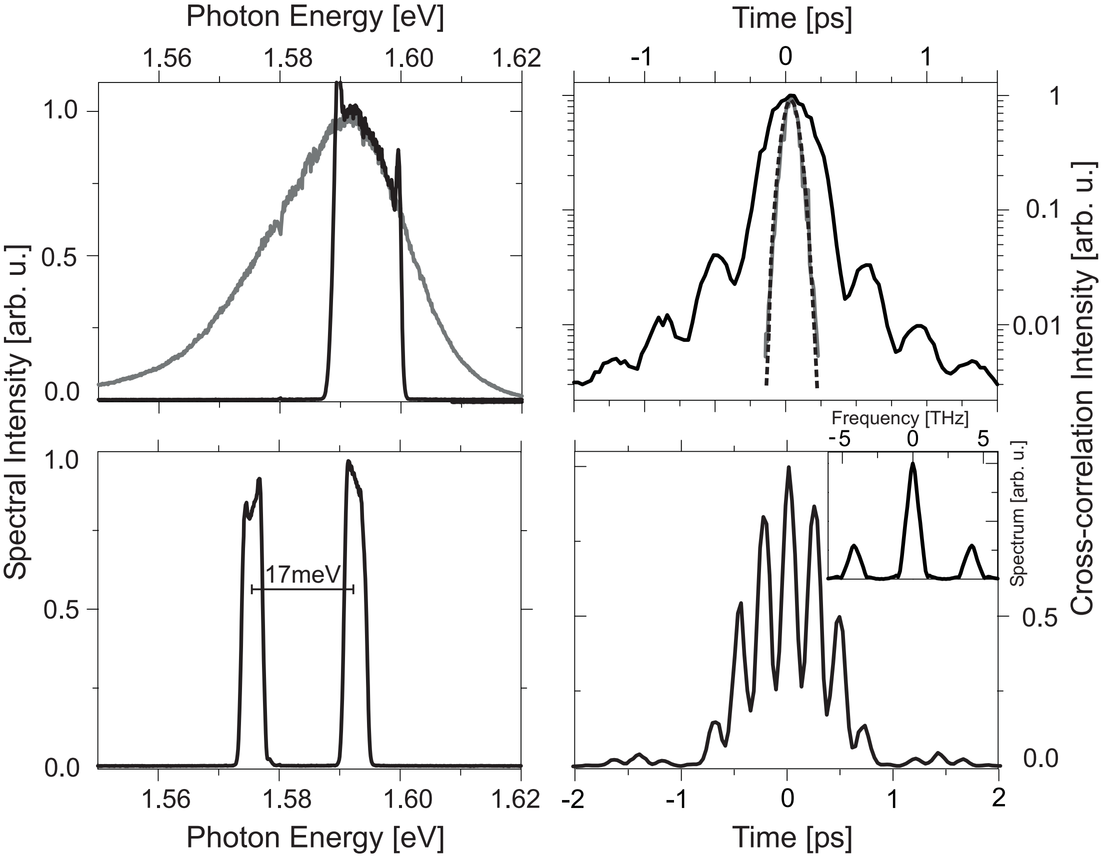

Figure 4.13: *Top, Left*: Un-shaped pulse spectrum and a rectangularly shaped pulse spectrum. *Top, Right*: Cross-correlation scans for the pulse spectra given in the left graph. The scan for the un-shaped, short pulse can be easily fitted by to a parabola, proving the Gaussian pulse form (*dashed line*). The rectangular shaped pulse gives a sinc^2 temporal pulse form. *Bottom*: The pulse spectrum consists of only two narrow spectral lines. The cross-correlation scan accordingly mirrors the resulting pulse train. The spectral width of the single line, rectangularly shaped, determines the duration of the pulse train envelope, also having a sinc^2 form. *Inset*: Fourier power spectrum of the scan.

pump pulse before the pulse shaper (both pass through the same dispersive optical components). The cross-correlation of the gate pulse with the transform-limited pump pulse after the pulse shaper was measured. The gate pulse duration was determined to be 90 fs (FWHM). This leads to the conclusion that the pulse before the pulse shaper was slightly chirped and was compressed to the bandwidth-limit by the apparatus.

For pulse shaping, apertures and slit masks mounted on micrometer translation stages were installed in the Fourier plane. The spatial dispersion of the grating, $dx/d\lambda = f[a\cos(\theta)]^{-1} = 0.42\,mm/nm$, with the grating constant $a = 1.2\,\mu m$ and the diffraction angle, $\theta = 5°$, allowed for a fine degree of control of the spectral shape of the pump pulse.

Figure 4.13 gives examples of shaped pulse spectra and the resulting temporal form of the pulses. The upper two graphs compare the un-shaped pump pulse with a rectangular shaped pulse spectrum. The results regarding the spectral width and the duration of the un-shaped pulse were discussed above. The shaped narrow rectangular pulse spectrum leads to a temporally long pulse with small oscillation at the pulse wings, clearly seen in the semi-logarithmic plot. This is well known, since the Fourier transform of a top hat spectrum is a $\mathrm{sinc}(x) = \sin(x)/x$ function. The graphs below present the results in the case where only two very narrow spectral branches, of equal width, can pass the mask. This bichromatic spectrum leads to interference beating seen as the fast oscillating feature in the cross-correlation scan. The Fourier spectrum of the cross-correlation scan shows two high-frequency peaks 4.1 THz apart. This corresponds to the energetic splitting of the lines by $\Delta = 17\,\mathrm{meV}$. The low frequency peak in the Fourier spectrum can be attributed to the envelope function which is defined by the rectangular shape of the branches, being a sinc function.

4.5 Experimental Results and Discussion

In this Section, the results of experiments are discussed investigating the THz emission of biased superlattices after ultrafast selective excitation of the carrier spectrum.

The Section begins with the introduction of the geometry of the employed superlattice. To characterize the field-dependent carrier spectrum of the superlattice structure, linear absorption spectra were measured. In a first set of THz experiments, the Wannier-Stark ladder spectrum was excited by a broadband laser pulse. The resulting oscillatory THz transient is verified to originate from Bloch oscillating wave packets. A detailed study of the field- and density-dependence of the THz emission follows. The transient creation of a depolarization field due to exciton formation is measured by means of pump-probe experiments. The main part of the Section is dedicated to the presentation of results of THz emission experiments which demonstrate the manipulation of the dynamics of Bloch oscillations after selective excitation. Next, experiments are reviewed in which the Wannier-Stark ladder was selectively excited by a narrow pump spectrum. In the final part, results on difference-frequency mixing under controlled optical excitation are discussed.

4.5.1 Superlattice Geometry and Characterization

For the investigation of the dynamics of Bloch oscillations, exclusively in the first miniband, a superlattice structure with high quantum barriers was used. From the chosen geometry, a large first minigap which effectively *inhibits intersubband Zener tunneling* follows.

The parameter of the GaAs/Al$_x$Ga$_{1-x}$As superlattice (which in the following will be termed SampleD) are summarized in Table 4.2. The miniband structure was calculated by Stephan Glutsch by numerically solving the Hamiltonian in the effective mass approximation [14]. The resulting electron dispersion relation is shown in Figure 4.14. The calculation yields a first miniband width of $\Delta_1 = 46\,\mathrm{meV}$ and a

Parameter	SampleD
a	6.7 nm
b	1.7 nm
d=a+b	8.4 nm
x_{Al}	0.3
ΔE_{cb}	220 meV
ΔE_{vb}	160 meV

Table 4.2: Parameter of the superlattice structure (SampleD) used for THz emission experiments: where a is the well width, b the barrier width and x_{Al} the Aluminum mole fraction. The conduction band barrier height is given by ΔE_{cb}. The valence band barrier height is represented by ΔE_{vb}.

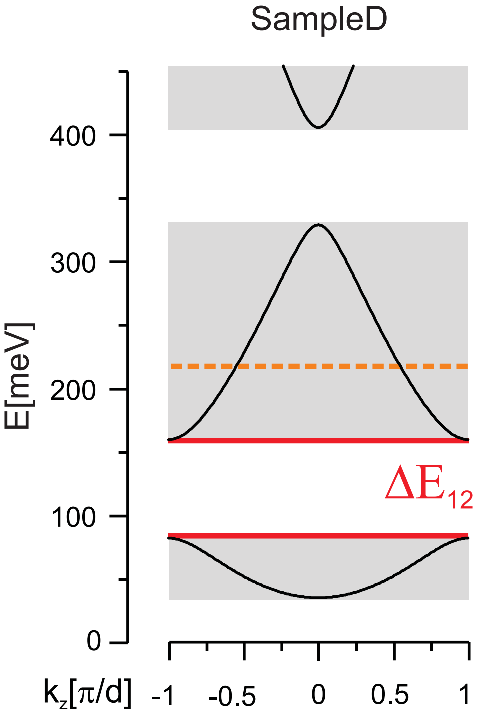

Figure 4.14: Electron miniband structure of the SampleD superlattice. The dashed line denotes the barrier height. The first minigap is denoted by ΔE_{12}.

first minigap of $\Delta E_{12} = 78\,\text{meV}$. The latter is substantially larger than the minigap sizes of the shallow superlattices (see Section 3.3).

The superlattice samples were grown by Klaus Köhler from the Fraunhofer-Institut für Angewandte Festkörperphysik in Freiburg with an analogous design of the superlattice (35 periods) and the buffer heterolayers as it was introduced in Section 3.3. The samples were prepared for transmission experiments in the same way as described in Section 3.3, whereas for the THz experiments, the sapphire substrate side was oriented towards the pump beam.

For characterization of SampleD, the low-density linear absorption spectra were measured as function of dc field. The experiment was carried out with the set-up described in Section 3.4. The results are plotted in Figure 4.15. In the measured energy interval, the transitions from the first heavy-hole to the first electron miniband as well as from the first light-hole to the first electron miniband are observed. The spectra were differentiated along the energy axis to enhance the visibility of weak transitions. In particular, this enhances the contrast of the exciton absorption resonances. The two emerging exciton Wannier-Stark ladder fans are indicated. The fan of the heavy-hole excitons is very prominent. The light-hole fan is weaker due to the smaller oscillator strength of light-hole transitions. The Wannier-Stark regime exists approximately in the internal field interval of $F = [5\dots35]\,\text{kV/cm}$. Features of the exciton Wannier-Stark ladder are noted which are introduced in Section 2.2.2[16]. The internal field was calibrated following the procedure described in Section 3.3. The

---

[16] The experimental plot can be directly compared to the theoretical 1s excitons fanchart of this superlattice structure shown in Figure 2.7.

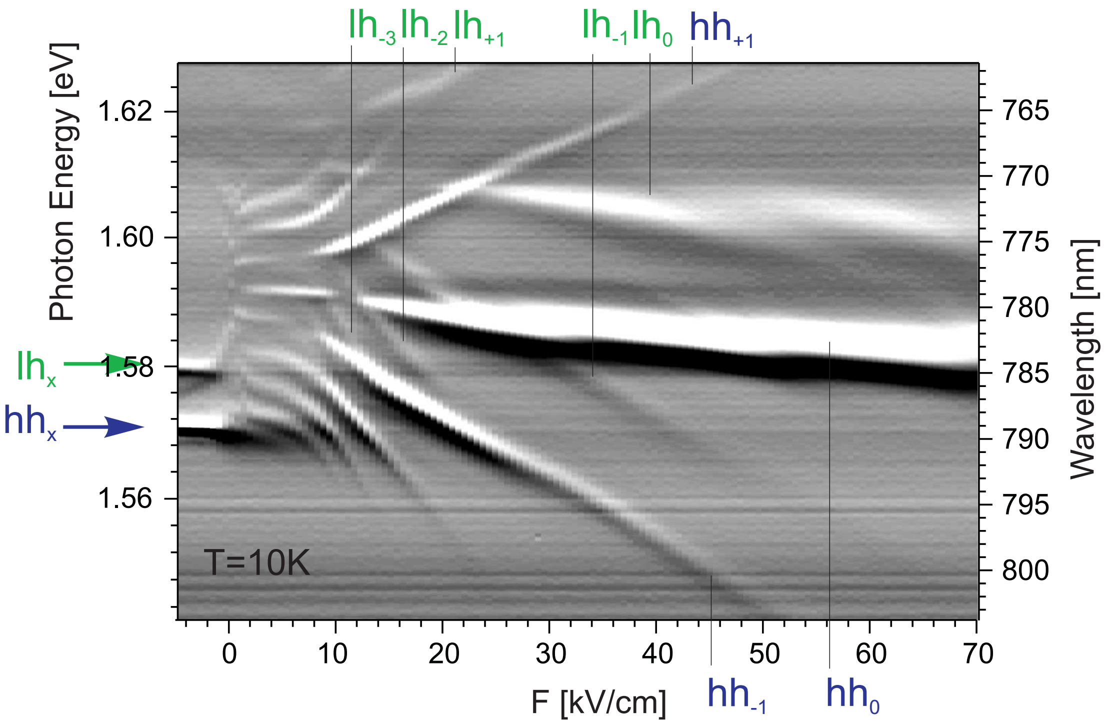

Figure 4.15: Gray scale map of linear absorption spectra of SampleD. Various exciton Wannier-Stark ladder states of both the heavy-hole (hh_η) and the light-hole (lh_η) ($\lambda = \lambda' = 1$) fans are marked. The flat-field exciton energies are marked by arrows. For very low field (around 4 kV/cm), the internal field does not change linearly with the applied voltage. This may be caused by the build-up of the screening field at the superlattice edge layers (discussed in Section 3.3).

resulting internal field axis was used as reference field axis for all experimental data presented in the Sections below.

4.5.2 Terahertz Emission of Bloch Oscillations: Investigation of Field- and Density-Dependence

Field Dependence

To proof that the THz emission observed in the experiment originates from Bloch oscillations, the THz emission of SampleD was measured as function of dc field. The experiment was carried out employing the set-up which was described in Section 4.4.

The following excitation parameters were kept constant for all measurements: The sample was excited by a spectrally broad laser pulse whose central energy was constant at $\varepsilon_\mathrm{L} = \hbar\omega_\mathrm{L} = 1.579\,\mathrm{eV}$. The spectral width of the pulse was $\hbar\Omega_\mathrm{L} = \Delta\varepsilon_\mathrm{L} = 24\,\mathrm{meV}$. For a pump spot diameter of $600\,\mu\mathrm{m}$, the carrier density was constant at $\mathrm{n_{cd}} = 6.5 * 10^9\mathrm{cm}^{-2}$ (Equation 3.27). For electro-optic detection, a $200\,\mu\mathrm{m}$ thick $\{110\}$ ZnTe crystal (from ISP Optics) was used, also in all experiments presented in

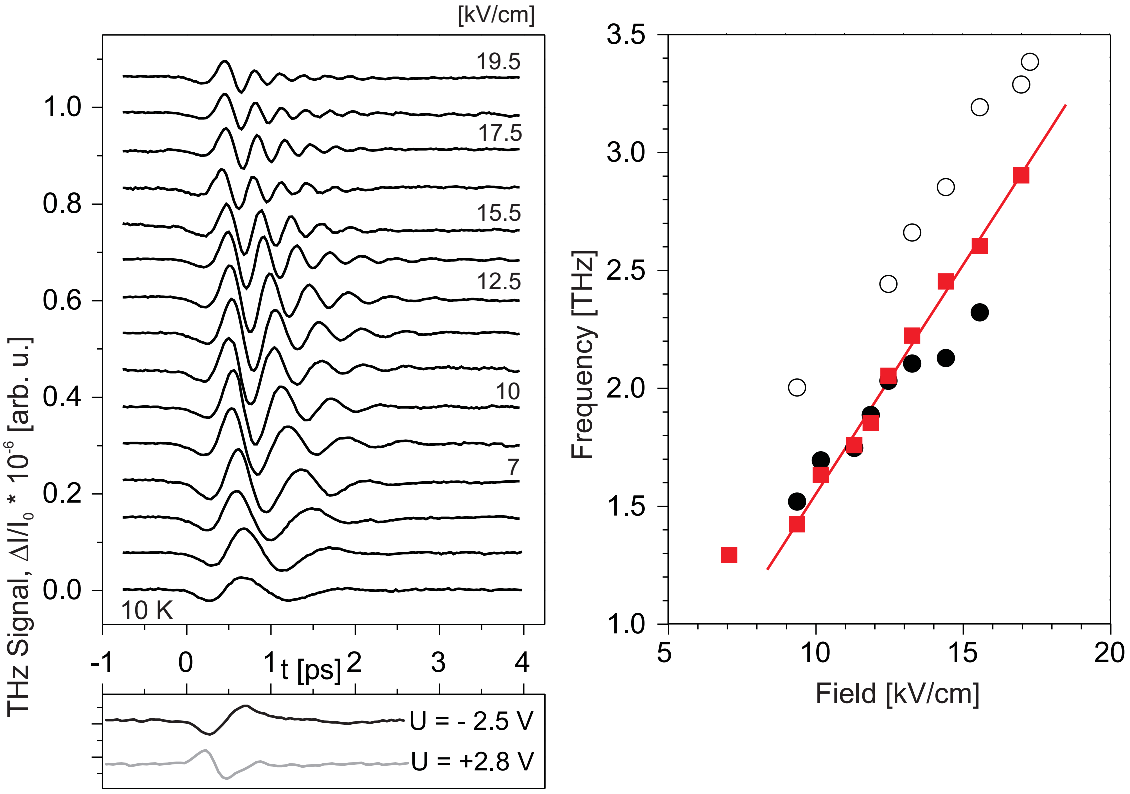

Figure 4.16: *Left*: Emitted THz transients due to Bloch oscillations in SampleD as function of dc field. Raw data are plotted as normalized balanced detection signal (Equation 4.11). The signal amplitude is on the order of 10^{-7}. For several transients, the internal field strength is given. *Left (Bottom)*: THz transients whilst biasing the superlattice with small reverse and forward bias. A phase change of the THz transient is observed. *Right*: (*squares*) Central frequency of the THz transients as function of the internal field. (*solid line*) The linear field-dependence is emphasized by a linear fit. Additionally, the energetic splitting between the $\mathrm{hh}_{-1} - \mathrm{hh}_0$ (*open circles*) and the $\mathrm{hh}_{-2} - \mathrm{hh}_{-1}$ (filled circles) excitons is plotted.

the Sections 4.5.4 and 4.5.5.

In a first step, to check for possible contributions caused by surface states of the semiconductor sample, the THz emission was measured for pulse energies well below the first miniband. No THz radiation was detected under this condition. Thus, the observed THz emission only originates from the superlattice states.

Figure 4.16 (left) shows the detected THz transients for increasing dc field. Oscillations are clearly observed which change in frequency with field. The central frequency of the traces was analyzed by fitting a Lorentzian to the emission peak in the THz power spectrum (calculated by Fourier transform). The results are plotted in the graph at the right hand side. A linear field-dependence with an emission frequency following the Wannier-Stark ladder splitting is evident in the graph. This proves that Bloch oscillations are the source of the THz radiation (Equation 2.26).

As a proof-of-principle measurement, the THz emission was tested for biasing the

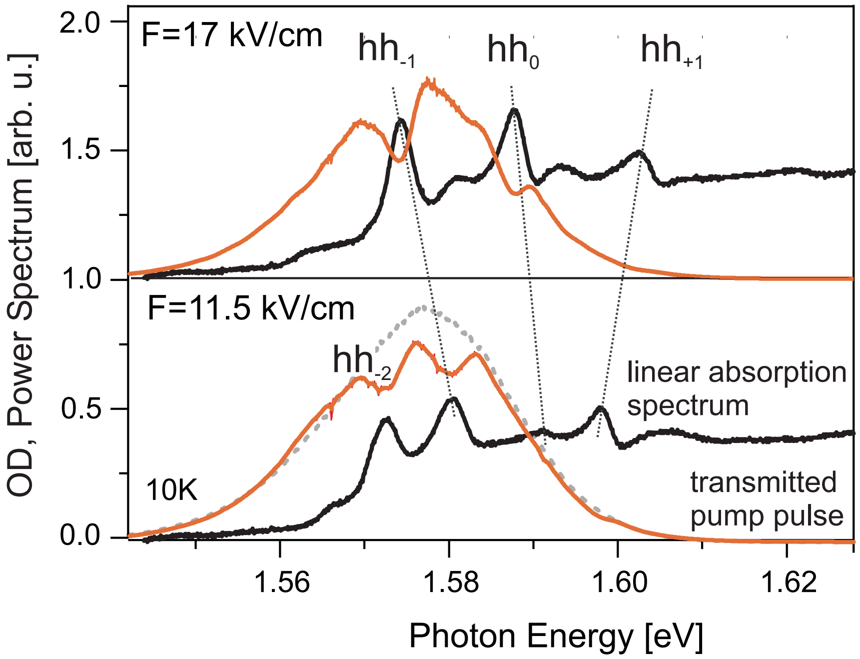

Figure 4.17: *Bottom*: (*solid line*) Spectrum of the transmitted pump pulse, for $F = 11.5\,\mathrm{kV/cm}$. It shows distinct absorption dips due to the excitation of the Wannier-Stark ladder excitons. For comparison, the corresponding low-density absorption spectrum is plotted. The pump pulse spectrum is given as *dashed line*. *Top*: The spectrum of the transmitted pump pulse and the corresponding absorption spectrum for $F = 17\,\mathrm{kV/cm}$. The *thin dashed lines* trace the transitions as they shift with field.

superlattice slightly in the forward direction. For comparison, the THz transients for small reverse and forward bias are shown in Figure 4.16 (Bottom). The phase of the signal changes in cases where the electrons are accelerated in the opposite direction. Thus, the experiment is demonstrated to be sensitive to the spatial phase of the intraband polarization.

For each experiment, the spectrum of the transmitted pump pulse was measured. Hence, the low-density absorption spectrum for the corresponding internal field strength could be determined, from which the nature of the excited optical transitions was identified. This is illustrated in Figure 4.17. Most importantly, it is shown that an "in-situ" monitoring of the superlattice spectrum and the excitation parameters was possible in the experiment.

The energetic difference between the Wannier-Stark ladder excitons was determined from the spectra and compared to the THz emission frequency. Figure 4.16 (right) presents the data. In the investigated field-regime, the hh_{-1} 1s exciton state is expected to have the largest exciton binding energy [50, 54] (also see discussion in Section 2.2.2). Consequently, a larger energetic splitting between the hh_{-1} exciton and the hh_0 exciton was observed than the splitting between the hh_{-2} and the hh_{-1} exciton. On the other hand, the free-particle Bloch frequency of the exciton

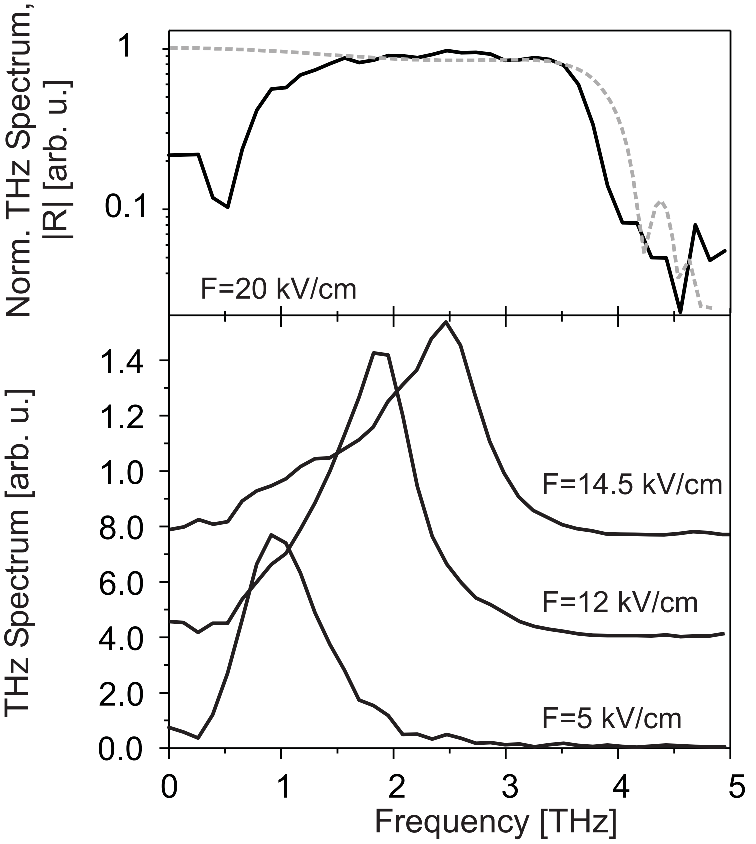

Figure 4.18: Terahertz power spectra for different dc fields. *Bottom*: With increasing field strength, the THz frequency due to Bloch oscillations is blue shifted. *Top*: The normalized broadband THz spectrum at high field strength marks the upper bandwidth limitation of the electro-optic detection. It is compared to the modeled and normalized detector response function (*dashed line*).

continuum is smaller than the $hh_{-1} - hh_0$ splitting. From the plot, it is noted that the THz emission frequency is smaller than the $hh_{-1} - hh_0$ exciton splitting at all dc fields. At low field, the THz frequency equals the $hh_{-2} - hh_{-1}$ exciton splitting, whereas in this field regime the hh_{-2} and the hh_{-1} excitons are the most prominent exciton resonances (see spectrum for $F = 11.5\,\mathrm{kV/cm}$ in Figure 4.17). For higher field strength, the hh_{-1} and the hh_0 1s exciton transitions are mainly excited, but the THz frequency is still systematically red-shifted. This indicates that for low field strength, the THz emission seems to be dominated by 1s excitons and at high field the admixture of continuum states (with a smaller Bloch oscillation frequency) plays a role. In the following Sections (4.5.4 and 4.5.5) we will focus on the investigation of the interplay of 1s excitons and continuum carriers in the intraband dynamics of the biased superlattice.

In conjunction with the results of the field-dependent measurements, the frequency response of the detection will be briefly discussed. From the fan chart graph (Figure 4.15) it is seen that the Wannier-Stark ladder regime extents up to a field of about 35 kV/cm, at which the Bloch frequency is about 7 THz. The observation of these high frequencies was not possible in the experiment, due to the bandwidth restrictions set by the electro-optic detection (discussed in Section 4.3.2). Thinner electro-optic crystals or, e.g., GaP as electro-optic detector could not be used because of the small signal amplitude.

In Figure 4.18, example THz power spectra are shown which shift to higher frequencies with increasing field. For $F = 12$ and $14.5\,\mathrm{kV/cm}$, the high-energy wing of the emission peak has a Lorentzian shape. This peak can be attributed to the emission of Bloch oscillations[17]. An underlying broadband signal is due to the excitation of a permanent intraband dipole. This initial dipole contribution dominates the first cycle of the THz transient. Its nature will be discussed in further detail below. For $F = 20\,\mathrm{kV/cm}$, the Bloch frequency ($\nu_\mathrm{B} = 4\,\mathrm{THz}$) already exceeds the detection bandwidth. Therefore, the broadband initial dipole signal dominates the spectrum. The modeled detector response function (Equation 4.18) well describes the observed frequency response.

For low field strength ($F = 5\,\mathrm{kV/cm}$), the THz emission is tested in the miniband regime, i.e., the transmission spectrum (not shown) does not show a Wannier-Stark ladder quantization. In this field-regime, the THz frequency is only weakly field-dependent. Different possible contributions to the signal were discussed in the literature (e.g., [25]) where the main emission mechanism was argued to be an overdamped Bloch oscillation. Additionally, it appears that the detection runs into its lower bandwidth limitation at these frequencies. This is caused by the wavelength-dependent diffraction of the THz radiation at the emission and the detection side of the experiment (see discussion in Section 4.4). This effect seems to cause the asymmetry of the peak for $F = 5\,\mathrm{kV/cm}$ with a steep low-energy wing.

Density Dependence

To characterize the dependence of the THz emission by Bloch oscillations on the density of photo-generated carriers, intensity-dependent measurements were carried out. In the experiments, the internal field was kept constant at $F = 13\,\mathrm{kV/cm}$. The latter was accomplished by monitoring the transmission spectrum of the pump beam. The external voltage was adjusted to compensate for the field screening due to the accumulation of photo-generated carriers at the edges of the superlattice (discussed in Section 3.3). Figure 4.19 gives the measured THz transients. The emitted THz field amplitude clearly increases with density. Additionally, the damping rate of the oscillation increases.

---

[17] Very recently, Shimada et al. [98] argued that the transient THz emission after ultrafast optical excitation measures the step-response of the electron system to a dc field. The authors fitted the THz emission spectrum of similar superlattice structures by the modeled high-frequency conductivity spectrum (following a semi-classical model by Ktitorov et al. [158] whose results were recently reproduced in a fully quantum-mechanical treatment [159]). In particular, the asymmetry of the emission peaks (a steep low-energy wing) was used to identified the model as correctly describing the system properties. The model predicts gain (absorption) for THz photons with energies smaller (larger) than the Bloch oscillation energy. Consequently, the authors claimed an indirect proof of THz gain from Bloch oscillating electrons in a biased superlattice. Our results do not support these findings. Here, an asymmetry in the THz emission spectrum is not observed in the Bloch oscillation regime. This may be due to the superimposed initial dipole spectrum.

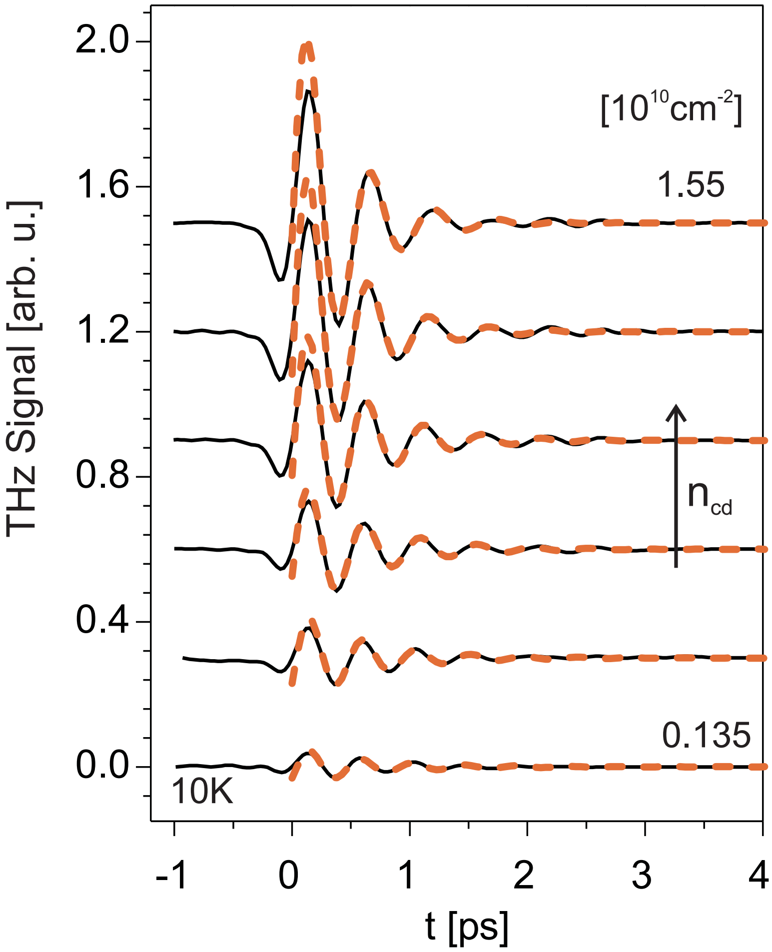

Figure 4.19: THz transients measured for increasing carrier density. The scans were shifted along the time axis to align all transients at an artificial $t = 0$. (*dotted lines*) The measured signals were fitted by a damped sinusoidal function.

The THz transients were fitted to exponentially damped sinusoidal functions (the oscillatory term in Equation 4.6). The fit function is given by

$$E_{\mathrm{THz}}(t) = E_{0\mathrm{THz}} \sin\left(\frac{2\pi(t-t_0)}{T_{\mathrm{B}}}\right) \exp\left(-\frac{(t-t_0)}{T_{12}}\right) , \tag{4.22}$$

where $E_{0\mathrm{THz}}$ is the THz signal amplitude, T_{B} is the Bloch frequency, and T_{12} the intraband dephasing time. The fits given in Figure 4.19 characterize the observed signals well. The fit does not account for the first cycle of the THz transient. It is dominated by the broadband initial dipole contribution which will be discussed in Section 4.5.5.

At first, the density-dependence of the THz amplitude will be discussed. This is plotted in Graph 4.20. A linear density-dependence is evident. Therefore, the time-averaged Poynting vector which gives the emitted power scales quadratically with the carrier density. This effect was discussed in the literature to be due to the superradiant emission of an ensemble of Bloch oscillating dipoles [94]. Superradiance is a collective emission of the non-inverted dipoles into the same electric field mode, in the case where the diameter of the emitting spot is comparable to the THz wavelength (see [119, 120] and references therein). Such a superradiant state of the system is

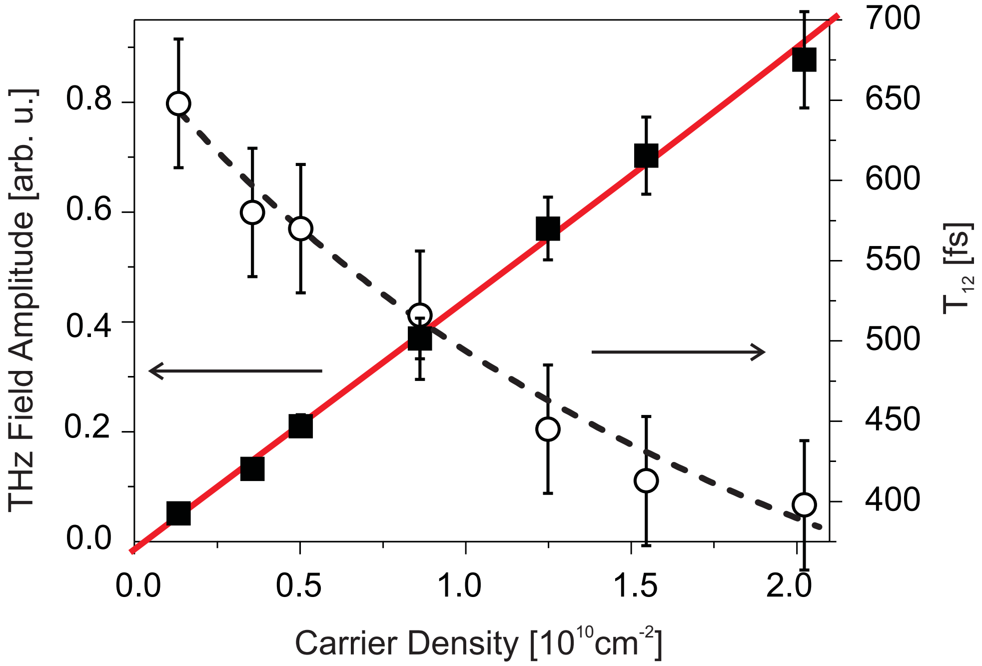

Figure 4.20: THz amplitude (*filled squares*) and the intraband dephasing time (*open circles*) plotted as function of the time-averaged carrier density per well. The THz emission amplitude grows linearly supported by the regression line. The intraband dephasing time is strongly density-dependent. The uncertainty interval of fitting T_{12} was estimated to be ±40fs.

equivalent to an optically excited macroscopic intraband polarization (represented by Equation 4.5).

From Figure 4.20, it is noted that the intraband dephasing time is strongly density-dependent. Thus, in this density regime, carrier-carrier scattering is evident as prominent dephasing channel. If the intraband dephasing rate is taken to be the sum of a density-dependent and a density-independent dephasing rate, the density-dependent contribution can be accounted for using a phenomenological constant B as in equation: $T_{12} = 1/(C + B\mathrm{n}_{\mathrm{cd}})$, where C sums over all density-independent scattering mechanisms. This corresponds to a linear increase of the line width of the THz emission as function of density (not shown). From the fitted hyperbola (given in Figure 4.20), the density-independent scattering constant C was extracted. The best fit value was 680 fs. It is interesting to compare this value to the C-value found for a very similar superlattice structure which was investigated by R. Martini [119]. For a superlattice with $a = 9.7\,\mathrm{nm}$, $b = 1.7\,\mathrm{nm}$, $x_{\mathrm{Al}} = 0.3$, Martini determined a value of C which was about 30% larger, approximately 1 ps. Let us briefly discuss the physical reason for the difference. Very recently, Sekine et al. [160] found that in the Wannier-Stark regime, alloy scattering in the barriers is the dominant intraband dephasing mechanism. Since SampleD and the sample investigated by Martini have the same barrier width and barrier height, this mechanism cannot account for the difference in C. However, the effect seems to arise from the difference in miniband

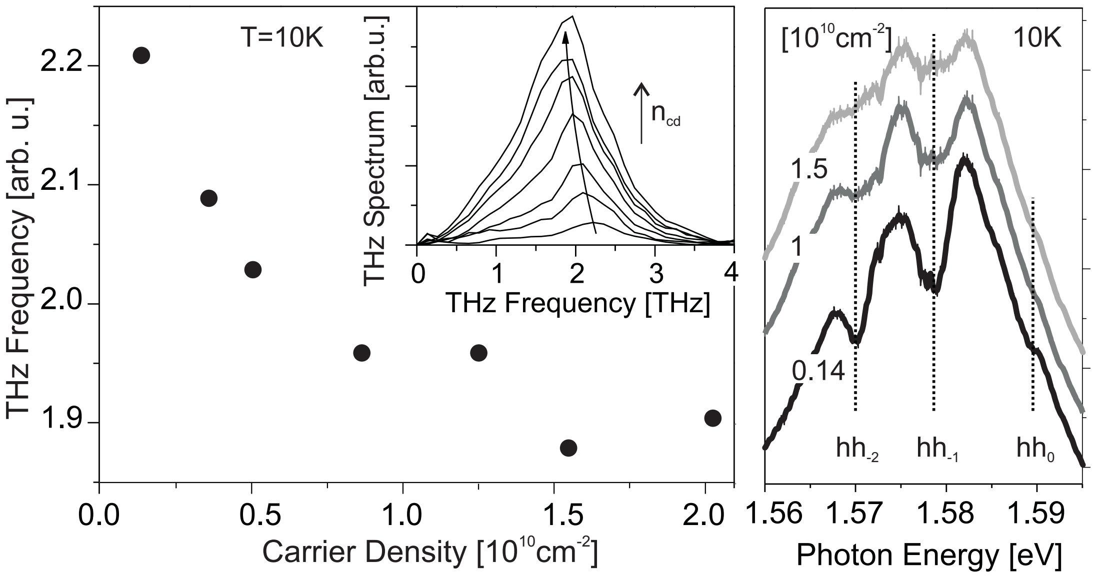

Figure 4.21: *Left*: Central frequency of the THz signal as function of carrier density for constant internal field. The emission frequency shifts to lower frequencies. *Inset*: THz spectra for increasing carrier density. *Right*: Spectra of the transmitted pump beam for three different carrier densities. The *dotted lines* mark the exciton absorption peaks.

width: SampleD (the sample investigated by Martini) had a miniband width larger (smaller) than the LO phonon energy of 36 meV. Therefore, inelastic phonon scattering can be identified to cause the faster intraband dephasing observed in SampleD[18].

Furthermore, the frequency of the emitted signal is discussed. The results are summarized in Figure 4.21. The graph on the right hand side plots the spectra of the transmitted pump pulse. The interband transitions show a considerable broadening for increasing density. It is well-known that carrier-carrier scattering leads to a density-dependent broadening of the interband transitions which dynamic analog is commonly termed as excitation-induced dephasing [162]. For high pump intensities, luminescence peaks of the Wannier-Stark ladder exciton transitions are superimposed on the transmitted spectra.

Despite the adjustment of the external voltage which maintained a constant internal field, a systematic *red shift* of the THz frequency is observed as function of carrier density (left hand side graph of Figure 4.21). In conjunction with the findings which are discussed in the following Section, it can be argued that the built-up of a transient depolarization field by the exciting pump pulse leads to a transient internal field change. This effect is density-dependent and would explain the increasing red-shift of the THz frequency with increasing density. Interestingly, a saturation of the red-shift is visible and seems to be followed by a slight blue-shift. For very high densities

---

[18] LO phonon scattering was shown to be an efficient scattering channel for Bloch oscillations in superlattices by Plessen et al. [161]

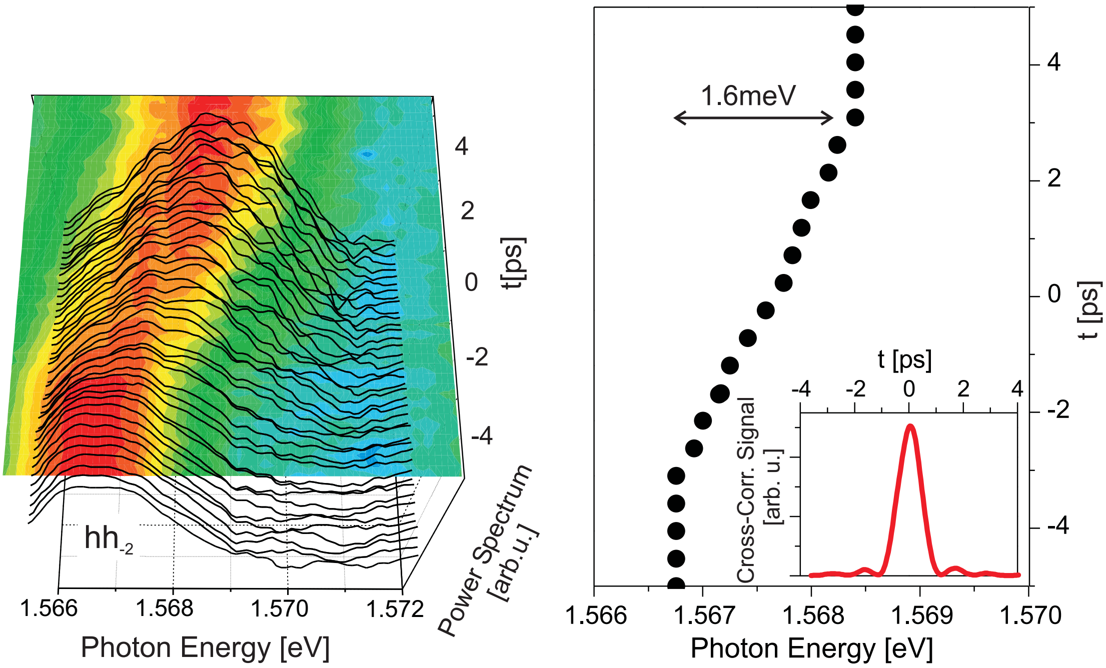

Figure 4.22: *Left*: Time-resolved, inverted spectrum of the transmitted monitor pulse. A small spectral interval around the hh$_{-2}$ exciton resonance is plotted. The pump-beam-induced blue-shift of the transition energy is clearly observed. *Right*: The transition energy of the hh$_{-2}$ exciton is plotted as function of delay relative to the intense pump pulse. The total blue-shift is measured to be about 1.6 meV. *Inset*: Cross-correlation of the pump pulse.

the intraband dipole of the excited excitons considerably changes the internal field. Loeser et al. [99] demonstrated the strong coupling of Bloch oscillations with coherent plasmons in this density regime which leads to anharmonic carrier motion and may account for the density-dependence of the THz frequency. The effect needs further investigation and will be subject of a subsequent publication.

4.5.3 Measurement of the Transient Depolarization Field

To identify the physical origin of the observed red shift, a spectrally-resolved pump-probe experiment was carried out which measured the transmission of a weak monitor pulse as function of time delay relative to an intense pump pulse. The pump pulse had a narrow rectangular spectral shape ($\Delta\varepsilon_L = 3.5\,\mathrm{meV}$) resonantly pumping the hh$_{-1}$ exciton transition for an internal field of $F = 14\,\mathrm{kV/cm}$. A carrier density of $n_{cd} = 9 * 10^9\mathrm{cm}^{-2}$ was excited.

The monitor beam was installed as described in Section 4.4 with an intensity one order of magnitude smaller than the pump beam. It overlapped spatially with the pump spot. The monitor beam was spectrally broad with a pulse duration of $\tau_p = 90\,\mathrm{fs}$. In the experiment, the exact time-overlap between monitor pulse and pump pulse could not be determined. By means of spectral interference fringes at the degenerate spectral interval of both pulses, the time-overlap could be roughly determined, using it as $t = 0$ of the delay axis.

The main result of the experiment is the observation of a considerable transient spectral shift of the Wannier-Stark ladder transition energies induced by the pump pulse[19]. The time-resolved spectral position of the hh_{-2} exciton resonance is plotted in Figure 4.22. The hh_{-2} exciton resonance shifts to higher frequencies which corresponds to a decrease of the internal field. Under these excitation conditions, the total internal field change is around $1\,\mathrm{kV/cm}$[20]. The effect can be attributed to the creation of a dc depolarization field, F^{depol}, by the excitation of polarized electron-hole pairs in the biased superlattice. The pump pulse mainly excites population in hh_{-1} exciton states. For Wannier-Stark ladder excitons with $\eta < 0$, the intraband dipole is oriented in such a way that it screens the externally applied field (see Figure 2.12). After the pump pulse, this rectification field acts as a static screening field of the applied field, $F' = F^{\mathrm{appl}} - F^{\mathrm{depol}}$. It should decay with the carrier recombination time T_1 and can therefore be seen as quasi-constant during the much shorter intraband coherence time. Explaining the dynamics of the peak shift is more complicated and beyond the scope of this work. Clearly, the effect can only be described by higher-order nonlinear interactions (beyond the second-order) of the optical fields. By a theory including higher-order effects to an (in principle) infinite-order, the experimental findings, in particular the red-shift of the Bloch oscillation frequency could be nicely reproduced. The mechanism is further discussed in Section 4.5.5 and will be subject of a subsequent publication [163]. A closely related phenomenon was reported by Turchinovich et al. [164]. The authors observed in THz emission experiments the complete screening of the internal bias field of quantum wells for the excitation at very high carrier densities. It should be pointed out that the build-up of the observed transient depolarization field is the spectral analog of the initial dipole THz emission predicted by Equation 4.6.

In summary, the above findings underline that the THz experiments are performed in a highly nonlinear regime due to strong exciton-exciton interactions. In general, it was intended to keep the carrier density in the experiments as small as possible. However, to obtain a reasonable signal-to-noise-ratio a carrier density on the order of $10^9\mathrm{cm}^{-2}$ was usually excited.

---

[19] The peak-shift observed in this spectrally resolved pump-probe experiment is of the same nature as predicted in theory [33] and observed in experiment for time-overlap of pump and probe pulse in spectrally resolved Four-Wave-Mixing (e.g., in Ref. [32]).

[20] The transient field screening effect partially explains the results presented in Section 4.5.2 (see Figure 4.16), where a THz emission frequency smaller than the energetic splitting between the hh_{-1} and the hh_0 exciton was reported. The depolarization field present in the field-dependent measurement will here be estimated in a simplified picture. Assuming a linear density-dependence of the depolarization field with carrier density, the total field change is roughly estimated as $0.7\,\mathrm{kV/cm}$ which corresponds to a change in Bloch oscillation frequency of $0.15\,\mathrm{THz}$. However, the observed difference between the THz emission frequency and exciton splitting was larger. Therefore, the conclusions drawn in Section 4.5.2 are still valid.

Additionally, let us briefly discuss that the effect of the transient depolarization field has nothing to do with the internal field screening due to the accumulation of photo-generated carriers at the superlattice edge barriers (as discussed in Section 3.3). The latter effect was found to happen at a much longer time-scale. The superlattice device reacts to photocurrent changes on a millisecond time-scale. This was explored by placing a chopper in the pump beam (modulating the pump beam at around 3 kHz) which induced a carrier density comparable to what was used in the THz experiments. In the spectrum of the transmitted pump pulse, the Wannier-Stark transitions were observed to show a considerable broadening compared to the situation of an unchopped pump beam inducing the same carrier density. The effect can be attributed to internal field fluctuations on the time-scale of the chopper period. Thus, to ensure a static internal field in the sample, the pump beam was not modulated. Instead, the chopper was placed in the THz beam path (see Section 4.4).

4.5.4 Manipulation of the Intraband Dynamics of Exciton Bloch Oscillations

In the following, let us discuss the results of experiments on the manipulation of the Bloch oscillation dynamics by selective optical excitation. It was argued in Section 2.3.1 that in a one-dimensional free-particle picture[21], the phase of the Bloch oscillation is expected to change sign when the exciting laser spectrum is energetically tuned through the Wannier-Stark ladder center (the transition energy of the hh_0 exciton). The Bloch oscillation amplitude is expected to be maximal for a wave packet which is excited spectrally far away from the Wannier-Stark ladder center and decreases for pump pulse energies close to the center. For an excitation symmetric about the Wannier-Stark ladder center, a breathing motion with zero amplitude is predicted.

To address a comparative measurement of the Bloch oscillation amplitude as function of the pump pulse energy, the THz emission was detected under well-defined excitation conditions: The internal field was kept constant ($F = 14\,\mathrm{kV/cm}$), while the energy spectrum of the superlattice was monitored by measuring the spectrum of the transmitted pump pulse. Great care was also taken to keep the carrier density constant at $\mathrm{n}_{\mathrm{cd}} = 7 * 10^9\,\mathrm{cm}^2$. The laser pulse energy was tuned by the wavelength selection of the Ti:Sapphire laser, but the output power of the laser varied with the central wavelength. Consequentially, the power in the gate beam varied. A correction for this was made by normalizing the measured difference signal to the gate beam power. The spectral width of the Gaussian laser pulse was kept constant at $\Delta\varepsilon_{\mathrm{L}} = 25\,\mathrm{meV}$ which corresponds to a duration of $\tau_{\mathrm{p}} = 75\,\mathrm{fs}$. Altering the gate pulse wavelength, also changes the response function of the electro-optic detection. Therefore, the THz transients were corrected for the calculated detector response function (Equation 4.18) at the particular gate pulse wavelengths.

In the analysis below, the pump pulse energy is given relative to the hh_0 exciton energy by the detuning parameter ϱ_{L}, where $\varrho_{\mathrm{L}} = (\varepsilon_{\mathrm{L}} - \varepsilon_{\eta=0})/\hbar\omega_{\mathrm{B}}$, with $\hbar\omega_{\mathrm{B}}$ being the Bloch oscillation energy.

Figure 4.23 shows four examples of measured THz transients. For $\varrho_{\mathrm{L}} = -2.7$, the Wannier-Stark ladder spectrum was pumped at low energy, i.e., the Bloch oscillating wave packet was composed mainly of Wannier-Stark ladder excitons with negative index η. The excitation around the Wannier-Stark ladder center is represented by the transients yielded at $\varrho_{\mathrm{L}} = -1.1$ and $\varrho_{\mathrm{L}} = 1.4$. The result for the excitation by a high-energy pump pulse is given for $\varrho_{\mathrm{L}} = +2.3$. For all excitation parameters, a damped oscillation was observed whose amplitude decreases with increasing ϱ_{L}. However, contrary to expectation, the Bloch oscillating wave packet *does not show a zero amplitude, breathing mode motion,* for the excitation at the Wannier-Stark

---

[21] In a one-dimensional exciton picture, one expects mainly the same results (as discussed in Section 2.3.1).

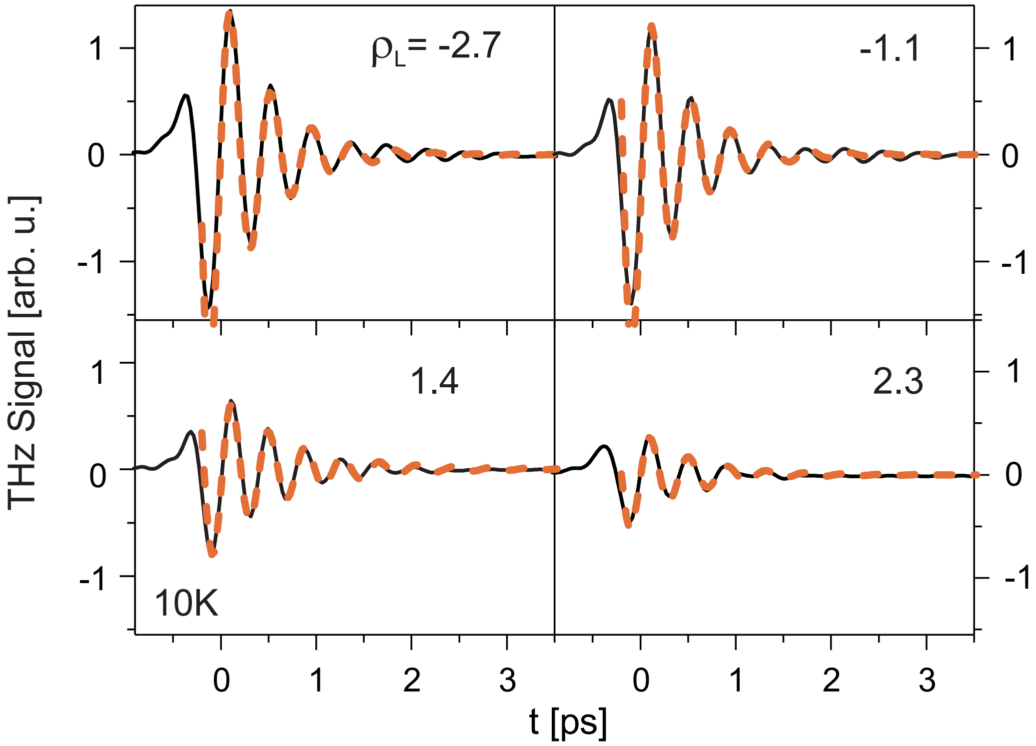

Figure 4.23: Measured THz signals of Bloch oscillating wave packets under excitation with different pump pulse energies. From experiment, the exact zero time delay can not be determined. Therefore, the traces were shifted manually to an artificial $t = 0$. The fitting curves by Equation 4.22 are shown as *dashed lines*.

ladder center. It also *does not change sign* when comparing the excitation of the Wannier-Stark ladder at low and at high energy.

In Figure 4.24, the results are summarized. In the top panel, the excitation conditions are illustrated, depicting the total detuning interval of the pump pulse energy. In the respective low-density absorption spectrum for $F = 14\,\mathrm{kV/cm}$, the exciton resonances are marked. From Equation 4.6, it follows that the amplitude of the damped oscillatory THz signal is a measure of the Bloch oscillation amplitude. Consequently, a damped sinusoidal function was fitted to the transients (Equation 4.22). The lower graph of Figure 4.24 plots the amplitude as function of pulse energy. A distinct decrease in Bloch oscillation amplitude is evident for increasing ϱ_L. However, the amplitude does not show the sign change even for far positive detuning, but saturates at a positive value.

It becomes clear that the experimental findings cannot be explained by the arguments derived from an one-dimensional picture. In the following, it will be shown that the results can only be understood in a *full exciton picture* which includes higher excited exciton states, in addition to the (one-dimensional) 1s exciton states. This is explained by means of Figure 4.25. For a low-energy pump pulse, mainly 1s exciton states (with $\eta < 0$) are excited. Thus, for $\varrho_\mathrm{L} < 0$, the 1s model should be appro-

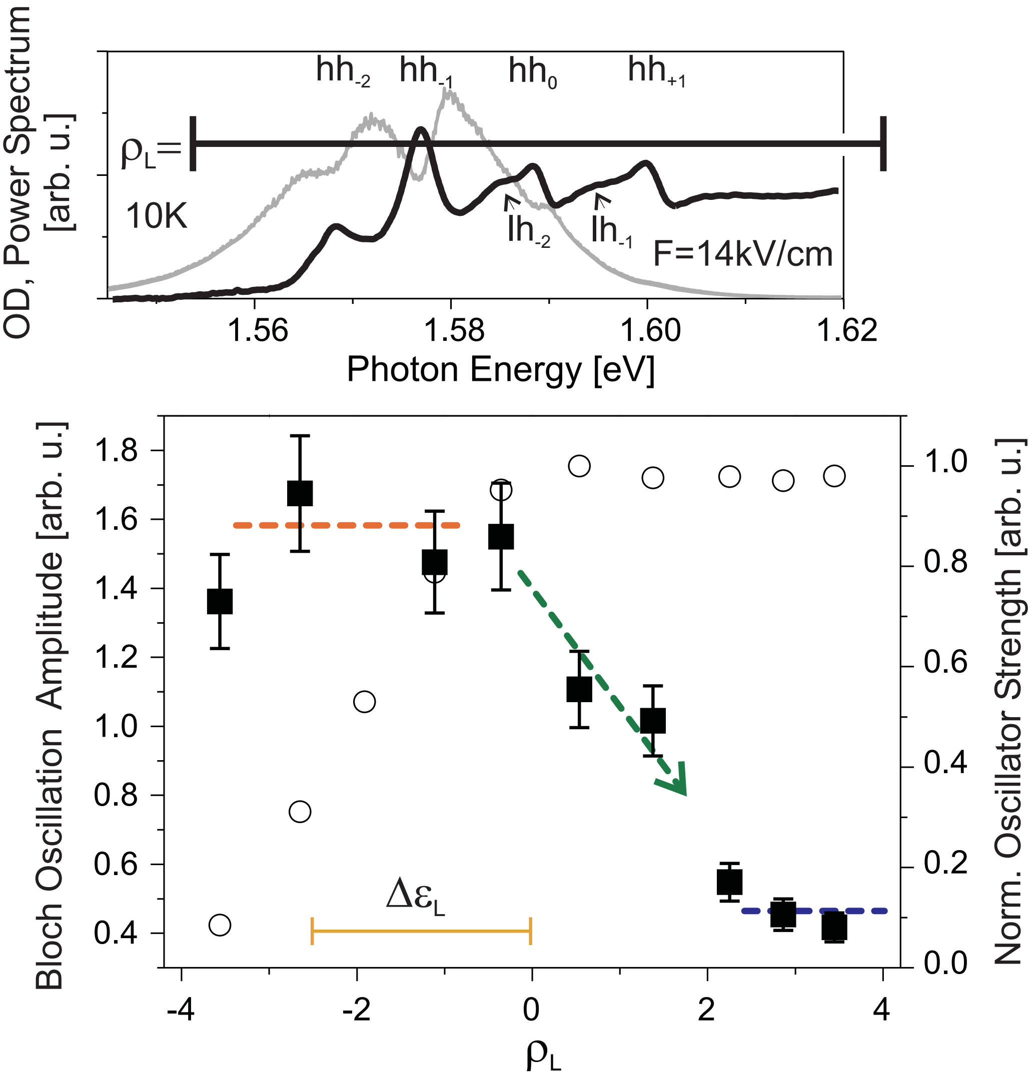

Figure 4.24: *Top*: Excitation conditions: the plot shows an example spectrum of the transmitted pump pulse (for $\varrho_{\mathrm{L}} = -1.1$) (*gray solid line*) together with the respective low-density absorption spectrum for $F = 14\,\mathrm{kV/cm}$. The heavy-hole exciton resonances (and also the weak lh exciton resonances) are labeled. The bar gives the total detuning interval. *Bottom*: (*filled squares*) The Bloch oscillation amplitude is plotted as function of the pump pulse energy (for the calculation of ϱ_{L}, a $\hbar\omega_{\mathrm{B}}$ of 10.1 meV (2.44 THz) was used). The Bloch oscillation amplitude clearly decreases when the pulse energy is tuned through the Wannier-Stark ladder center, $\varrho_{\mathrm{L}} \approx 0$. (*open circles*) The integrated oscillator strength as function of ϱ_{L}. In the experiment, the incident pump power had to be adjusted over one order of magnitude to keep the carrier density constant. The bar indicates the spectral width (FWHM) of the pump pulse.

priate. However, for the excitation at high energy, the pulse spectrum encompasses apart from the 1s states with $\eta > 0$ also states of the degenerate exciton continuum with $\eta < 0$. The latter carry opposing intraband dipoles (see Figure 2.12). Since the experiment does not show a sign change of the intraband dipole, it seems that for $\varrho_{\mathrm{L}} > 0$, the intraband dipole of the continuum states with $\eta < 0$ over-compensates

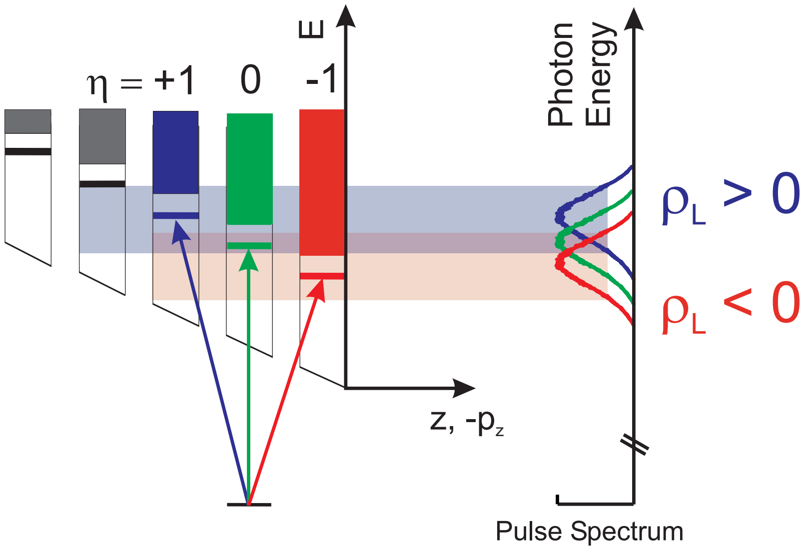

Figure 4.25: Excitation scheme including the discrete 1s exciton states as well as the exciton continuum. For $\varrho_{\mathrm{L}} < 0$, mainly 1s exciton states (*bars*) with $\eta < 0$ are excited. For the excitation at high energy, the wave packet also comprises the states of the exciton continuum (*shaded*) (states of unbound in-plane motion) with $\eta < 0$ (compare to Figure 2.9). Thus, for $\varrho_{\mathrm{L}} > 0$, the wave packet comprises states with opposing intraband dipoles (see Figure 2.12). The the intraband dipole of the continuum with $\eta < 0$ seems to dominate.

the intraband dipole of the 1s excitons with $\eta > 0$.

This picture is supported by a theory of the intraband dynamics in a full exciton picture. The model was developed by Yang et al. [53] and its results were directly compared to the experimental findings presented in this work [53]. As introduced in Section 2.2.2, higher excited exciton states are included by expanding the exciton basis into states with growing in-plane Bohr radius. In a first step, the exciton absorption spectrum was calculated and compared with experiment [53]. This gives a lower limit of the number of in-plane states which have to be included in the numerical calculations. It was found that states up to $60a_0$ (with a_0 being the Bohr radius) have to be considered to reproduce the experimental spectrum. The theoretical absorption spectrum for $F_{theo} = 12.5\,\mathrm{kV/cm}$ was found to match the experimental exciton Wannier-Stark ladder splittings for $F_{exp} = 14\,\mathrm{kV/cm}$ best. In a second step, the dynamic equations were solved up to second-order in the optical field to give the intraband polarization. Finally, the THz signal was calculated by taking the second derivative with respect to time.

Figure 4.26 plots the theoretical results for the same parameter ϱ_{L} as given in the experimental plot above (Figure 4.23). The results of the one-dimensional model, considering only 1s states, are directly compared to the simulations including the full exciton spectrum. The upper graphs give the intraband polarization. It is seen that the intraband polarization first grows almost step-like during excitation by the pump pulse and then oscillates around a constant intraband dipole. During the

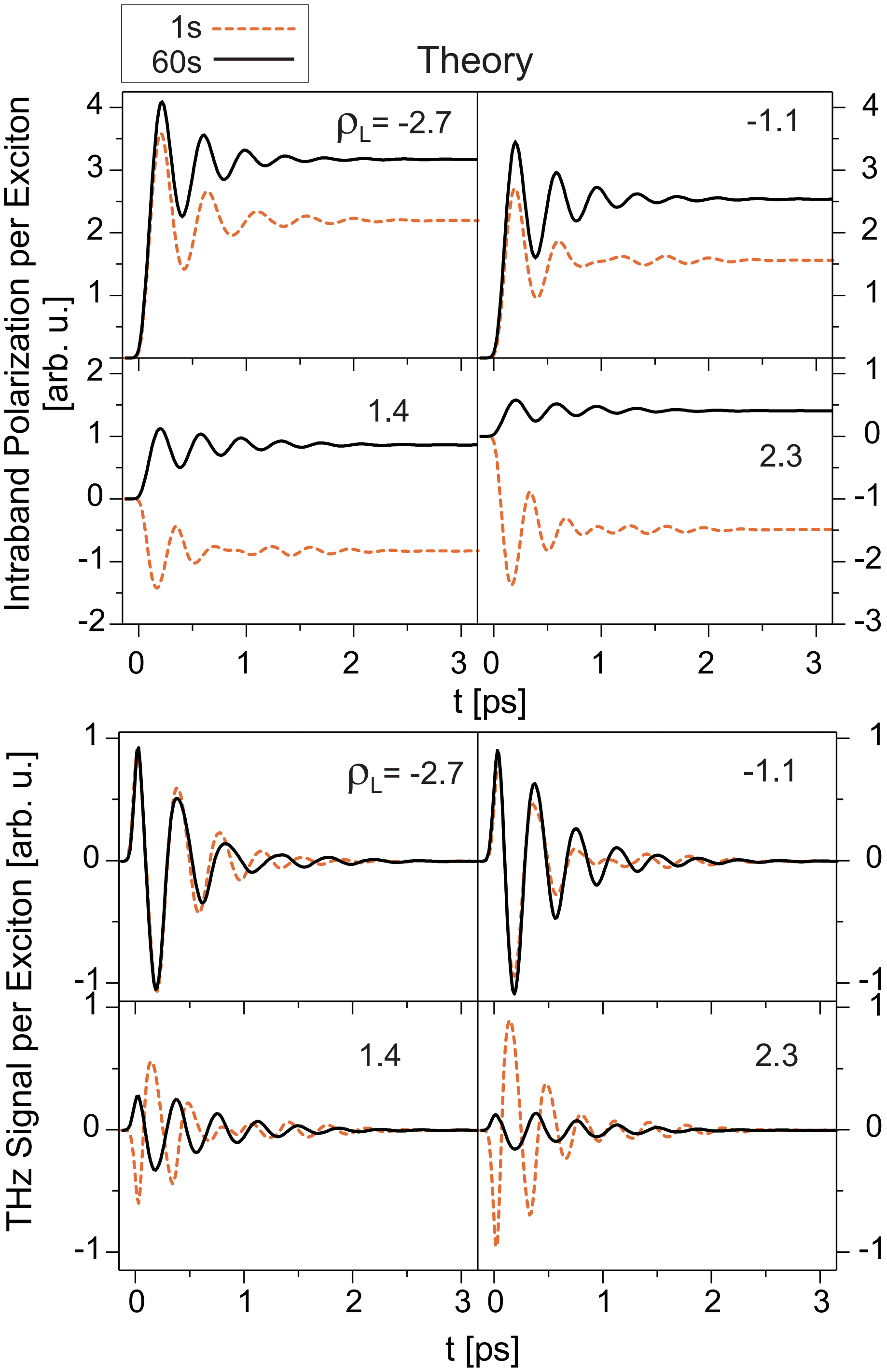

Figure 4.26: *Top*: Calculated intraband polarization as function of ρ_L. The results of the 1s exciton model (*dashed lines*) are compared to the calculation including higher excited exciton states up to 60s (*solid lines*). *Bottom*: Calculated THz signals corresponding to the polarizations given in the top graphs. The results are discussed in the text. Both, the intraband polarization and the THz field were normalized by the carrier density. The data are taken from [53].

pump pulse, population is built-up in Wannier-Stark states which have a permanent intraband dipole. This effect was referred to above as the *transient depolarization field*. After the excitation, this dipole of polarized electron-hole pairs decays with $T_1 \gg T_{12}$. The oscillating signal around the quasi-constant dipole is due to the evolving *Bloch oscillating wave packet*. The theory clearly shows that in the 1s model, the polarity of the permanent dipole as well as the phase of the wave packet is inverted when ϱ_{L} changes sign. Additionally, the size of the permanent dipole and the Bloch oscillation amplitude follows $\mid \varrho_{\mathrm{L}} \mid$ (the trace for minimum amplitudes is not shown). Interestingly, in the 1s model, beating effects of the wave packet oscillations are noted which are caused by the non-equidistant energy splitting of the exciton Wannier-Stark ladder. If higher excited exciton states are included[22], the intraband polarization is shown to decrease in amplitude with increasing ϱ_{L}. However, its polarity is not inverted for $\varrho_{\mathrm{L}} > 0$. Thus, theory also describes that the intraband dipole of the continuum states with $\eta < 0$ dominantes for the excitation of the wave packet at high energy. For high-energy pump pulses, beating effects are not observed due to the equidistant Wannier-Stark ladder splitting of the continuum.

In the lower graph of Figure 4.26, the calculated THz traces are presented. For $\varrho_{\mathrm{L}} < 0$, the intraband dynamics are dominated by the 1s exciton states since the 1s model and the 60s model give almost the same THz transient. However, for $\varrho_{\mathrm{L}} > 0$, the results of both models are distinctively different, with the 60s model describing the behavior found in experiment. This underlines the fact that *the exciton continuum plays a decisive role in the intraband dynamics* for the excitation of the Wannier-Stark ladder at high energies [53].

As a supplementary result, the damping time of the wave packet oscillation can be analyzed by fitting the experimental THz transients. In Figure 4.27, the intraband polarization decay time is plotted as function of ϱ_{L}. The damping time shows a slight increase when the laser spectrum is tuned through $\varrho_{\mathrm{L}} = 0$. Under this condition, the laser pulse mainly excites exciton continuum states. Thus, the graph shows an exceptionally long intraband coherence of the exciton continuum states which supports earlier experimental findings [165, 166]. The smaller T_{12} for $\varrho_{\mathrm{L}} < 0$ may be due to quantum beating of mainly 1s exciton states which was discussed above. This induces a faster polarization decay.

The experiment was repeated for smaller dc field strengths at which the overall contribution of the 1s exciton states with large $|\eta|$ is stronger. However, under all investigated conditions, continuum states dominated the intraband dynamics for the high-energy excitation covering the sign change of the 1s exciton dipole. Additionally, theory calculated the intraband polarization for different spectral widths of the pump pulse. Also for the excitation of a Bloch oscillating wave packet by a spectrally narrow laser pulse, no parameter set was found for which a sign change of the intraband dipole could be predicted.

---

[22] Theory assumes equal $T_{12} = 500 fs$ for 1s exciton states and the continuum.

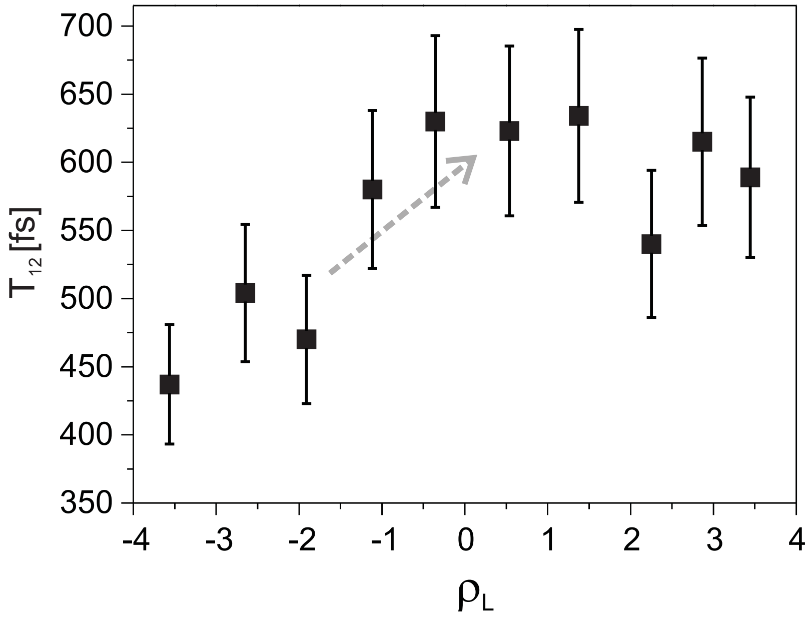

Figure 4.27: Intraband dephasing time as function of ϱ_{L}, was extracted from fitting Equation 4.22 to the THz traces. T_{12} is found to increase around $\varrho_{\mathrm{L}} = 0$.

4.5.5 Intraband Dipole of Wannier-Stark Ladder Excitons

This Section covers experiments which address the intraband dipole of single Wannier-Stark ladder excitons. Furthermore, effects of the highly nonlinear intraband response of the biased superlattice are investigated. The results are compared with a theory which adequately treats the nonlinearity and reproduces the experiment well.

As discussed above, the ultrafast excitation of Wannier-Stark ladder excitons carrying a permanent intraband dipole leads to THz radiation. The amplitude of the signal is a direct measure of the size of the dipole. Terahertz radiation due to the creation of polarized electron-hole pairs was first demonstrated by Planken et al. [122] in a double quantum well sample. As an interesting example, the technique was later applied to measure the charge transfer in organic crystals [167].

A THz signal is only emitted during the excitation process, when the population is time-dependent, i.e., the depolarization field is built-up. This initial dipole response leads roughly to a single-cycle oscillation. According to Equation 4.6, it follows that the amplitude of the THz initial dipole signal is proportional to the intraband dipole amplitude of the states and their population.

Clearly, ultrashort pulses result in a broadband THz signal, whereas the limited bandwidth of the electro-optic detection inhibits the undistorted detection. In this work, a spectrally narrow pump pulse was employed which induced THz frequencies within the detection bandwidth. Thus, the dynamics of the initial dipole THz transient was monitored without bandwidth limitation artefacts.

A pulse-shaped, narrow pump spectrum was used to selectively excite the exciton Wannier-Stark ladder. The intraband dipole of the excited states was then measured as function of the pump pulse energy. Again, a detuning parameter is defined by $\varrho_{\mathrm{L}} = (\varepsilon_{\mathrm{L}} - \varepsilon_{\eta=0})/\Delta\varepsilon_{\mathrm{hh_0,hh_{-1}}}$, with $\Delta\varepsilon_{\mathrm{hh_0,hh_{-1}}}$ being the energy splitting between the $\mathrm{hh_0}$ and the $\mathrm{hh_{-1}}$ exciton states. For a direct comparison of the emitted signals, a constant pulse duration and carrier density ($\mathrm{n_{cd}} = 4.5 * 10^9 \mathrm{cm}^{-2}$) had to be ensured. The internal field was kept constant at $F = 16\,\mathrm{kV/cm}$.

In Table 4.3, the energetic splittings between the exciton resonances for $F = 16\,\mathrm{kV/cm}$ are given. An almost rectangular pulse spectrum was produced with a spectral width of $\Delta\varepsilon_{\mathrm{L}} = 10.5\mathrm{meV}$ which was smaller than the energetic splitting between the most pronounced exciton resonances, $\Delta\varepsilon_{\mathrm{hh_0,hh_{-1}}} = 13\,\mathrm{meV}$. Therefore, the pump pulse mainly excited single Wannier-Stark ladder transitions.

In the left column of Figure 4.28, the excitation conditions for example ϱ_{L} are shown. A weak broadband monitor pulse (which impinged the sample temporally before the pump pulse) was used to detect the Wannier-Stark ladder spectrum with incident pump beam. In this way, a constant dc field was ensured by adjusting the external voltage for the particular excitation conditions. In comparison with the corresponding low-density absorption spectrum, the Wannier-Stark ladder transitions were clearly identified which were excited for different pump pulse energies.

In the right column of Figure 4.28, the measured THz transients are plotted for the corresponding ϱ_{L}. The THz signals were corrected to account for the detector response function (Equation 4.18) because the gate pulse wavelength changed: To cover the whole detuning interval, the central wavelength of the laser had to be spectrally shifted. The transients are dominated by the single-cycle initial dipole signal.

Firstly, the amplitude of the single-cycle oscillation was analyzed. As discussed above, it is a measure of the excited states intraband dipole strength. Consequently, in Figure 4.29, the intraband dipole is plotted as function of ϱ_{L}. A step-like dependence is visible which nicely proves the *discrete intraband dipole of Wannier-Stark ladder excitons* which in the one-dimensional picture is expected to scale with ηd. The intraband dipole decreases when shifting the pump pulse to higher energies and saturates for $\varrho_{\mathrm{L}} > 0$. As argued above, a 1s exciton model predicts an inversion

	$\mathrm{hh_{-2}}$	$\mathrm{hh_{-1}}$	$\mathrm{hh_0}$	$\mathrm{hh_{+1}}$
ε [eV]	1.5655	1.5754	1.5882	1.6015
$\Delta\varepsilon_{\mathrm{hh_\eta,hh_{\eta-1}}}$ [meV]		10	13	13

Table 4.3: Transition energies of heavy-hole Wannier-Stark ladder excitons and the corresponding energetic splittings (for $F = 16\,\mathrm{kV/cm}$) taken from the absorption spectrum (plotted in Figure 4.28). The data illustrate the non-equidistant level splitting of the exciton Wannier-Stark ladder.

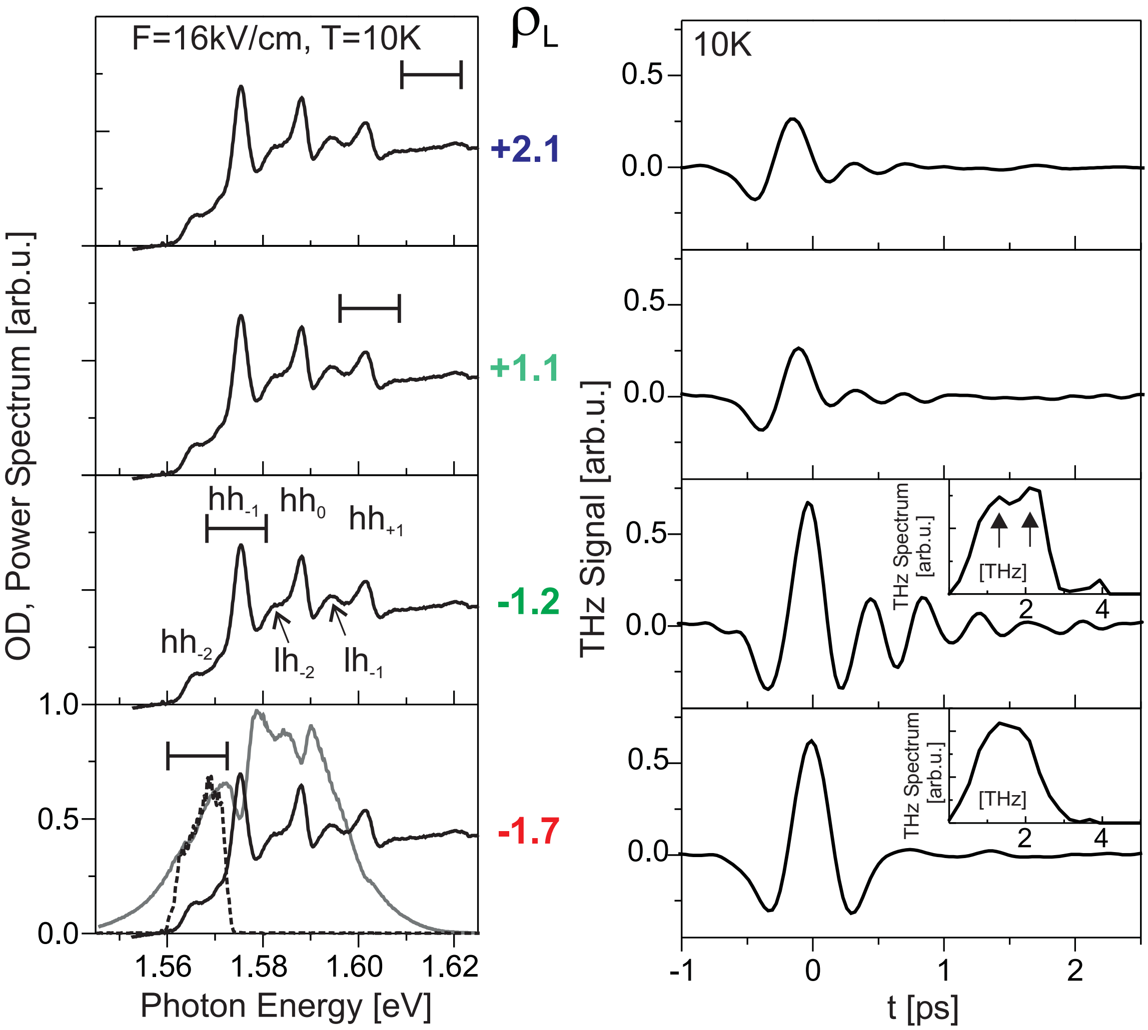

Figure 4.28: *Left*: Selective optical excitation of the Wannier-Stark ladder spectrum by a narrow pump spectrum (for $F = 16\,\mathrm{kV/cm}$). For $\varrho_\mathrm{L} = -1.7$, the spectrum of the monitor beam and the respective low-density absorption spectrum are given. Additionally, the spectrum of the transmitted pump pulse is shown (*dashed line*). In the graphs for larger ϱ_L, bars mark the pump pulse spectrum at various central energies. *Right*: Corresponding THz transients. For comparison, the axes are equally scaled. *Insets*: Power spectra of the THz signals. For $\varrho_\mathrm{L} = -1.7$, the THz spectrum is dominated by the initial dipole signal. It is seen to be within the detection bandwidth window (see upper graph in Figure 4.18) of the experiment. Thus, the initial dipole signal is measured without distortion.

of the initial dipole signal when the pump energy passes $\varrho_\mathrm{L} = 0$. The associated depolarization field would consequently change sign. However, this sign change is not observed. In the same way as in the previous Section 4.5.4, the findings can be understood in an exciton picture which includes higher excited exciton states. Thus, it can be concluded that the intraband dipole of the continuum states with $\eta < 0$ over-compensates the dipole of the 1s excitons with $\eta > 0$ for $\varrho_\mathrm{L} > 0$. Clearly, the change of the intraband dipole (the "step-height" in Figure 4.29) depends on the

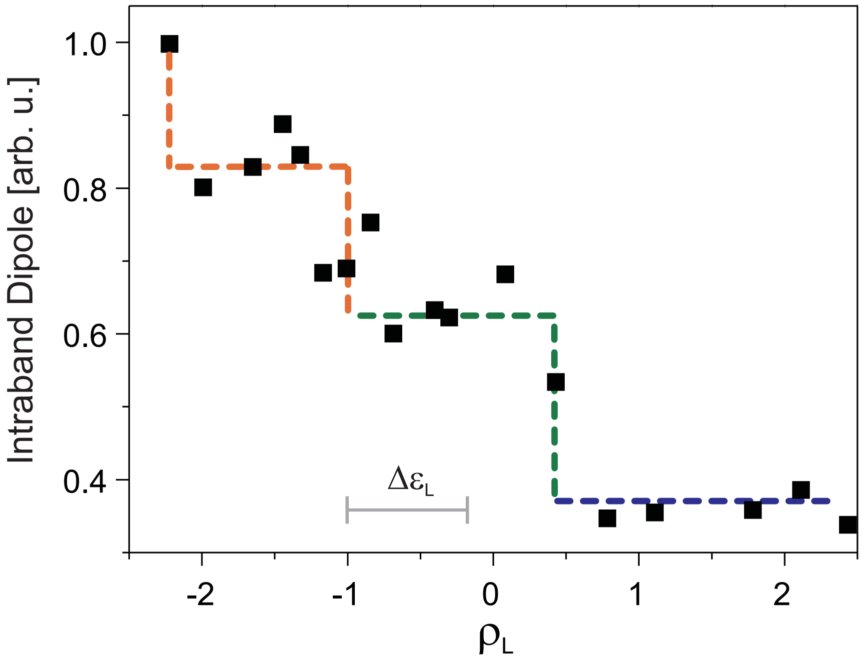

Figure 4.29: Intraband dipole of selectively excited exciton Wannier-Stark ladder states as function of pump pulse energy. The dashed line guides the eye along the step-like dependence which can be attributed to the discrete intraband dipoles of single Wannier-Stark excitons. The data are obtained by analyzing the amplitude of the first cycle THz signal. The bar denotes the spectral width of the rectangular pump pulse spectrum.

oscillator strength of the contributing exciton and continuum states. It seems that the step between hh_0 and hh_{+1} is smeared out, merged to one larger step, by the onset of the hh_0 exciton continuum (and possibly also due to the contribution of lh states).

Secondly, let us discuss the characteristics of the particular THz transients (Figure 4.28). After the initial dipole signal, all transients show further oscillations[23]. This is surprising since the spectral width is smaller than the main exciton splittings which should inhibit the excitation of wave packets. For $\varrho_\mathrm{L} = -1.7$, a second minimum is observed. For $\varrho_\mathrm{L} = -1.2$, a strong oscillation is visible. Only for $\varrho_\mathrm{L} > 0$, an almost pure single-cycle signal with only marginal oscillations is seen.

Let us discuss the situation for $\varrho_\mathrm{L} = -1.2$, where the pump pulse is almost centered at the hh_{-1} exciton state exciting only a single transition. However, a pronounced oscillation is visible. The corresponding peak in the THz spectrum is well separated from the spectrum of the initial dipole signal. As discussed above, the pump-pulse builds-up a considerable depolarization field (Section 4.5.3).This mechanism could explain the creation of an oscillating wave packet. It will be further discussed below. To describe this nonlinear response, one would certainly have to go beyond the

---

[23] The oscillations cannot be explained by the small satellite pulses of the pump pulse due to the sharp rectangular spectral shape (see Figure 4.13). The effect would be symmetric around the initial dipole cycle.

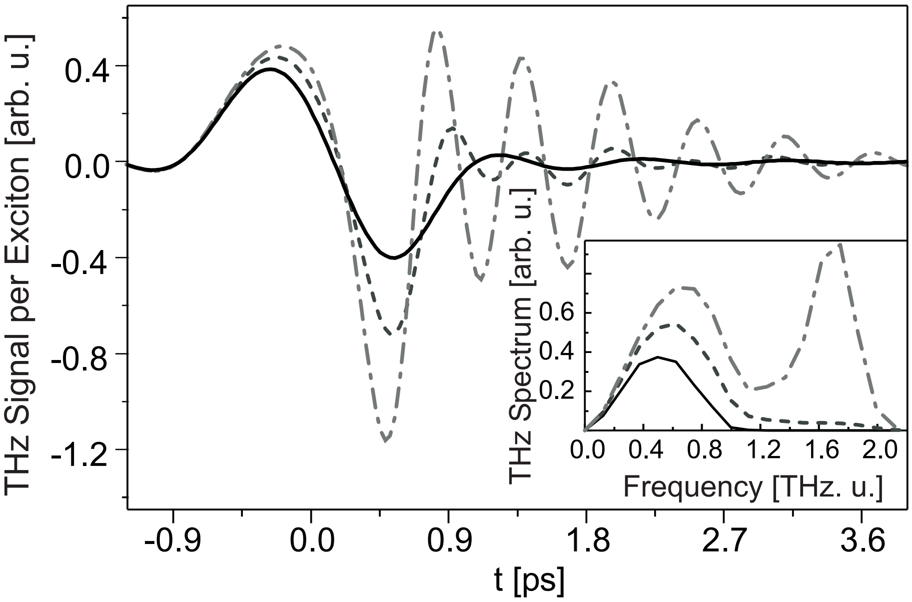

Figure 4.30: Calculated infinite-order THz response for the excitation by a narrow laser spectrum ($\Delta\varepsilon_\mathrm{L} = 4.6\,\mathrm{meV}$) resonantly pumping the hh_{-1} exciton transition for $F_\mathrm{theo} = 12.5\mathrm{kV/cm}$ as function of carrier density: (*solid line*) $\mathrm{n_{cd}} = 0.46 * 10^{10}\mathrm{cm}^{-2}$, (*dashed line*) $1.23 * 10^{10}\mathrm{cm}^{-2}$, (*dash dotted line*) $1.63 * 10^{10}\mathrm{cm}^{-2}$. For higher densities strong Bloch oscillations arise. *Inset*: THz power spectra. Taken from [163].

second-order of interaction with the optical field.

The experimental findings triggered the modeling of the situation by theory which treats the optical response of the biased superlattice to an (in principle) infinite-order in field while retaining the exciton correlations (based on the theory by Hawton et al. [101]). In the calculation, prominent oscillations became evident, too. The highly nonlinear character of the effect becomes very clear in the density-dependent calculation of the emitted THz signal. In Figure 4.30, the results are given, where the theory treats the illustrative situation of the excitation of SampleD by a very narrow rectangular spectrum ($\Delta\varepsilon_\mathrm{L} = 4.6\,\mathrm{meV}$) resonantly pumping the hh_{-1} 1s exciton transition. In this situation, the spectral width of the pump pulse is much narrower than the energetic spacing of the exciton states of approximately 2.6 THz. The infinite-order calculation models the intraband dynamics including, apart from the 1s exciton states, the states of the exciton continuum [53, 163]. For the lowest density, there are almost no oscillations visible. The THz signal is dominated by the initial dipole signal. However, for higher densities, appreciable oscillations begin to appear and the amplitude of the THz signal increases strongly. The corresponding power spectra are plotted in the inset. For all densities, there is a low-frequency peak arising from the initial dipole response. However, for the higher densities, the frequency of the initial dipole peak is blue-shifted and a strong high-frequency peak of the oscillation appears which is higher in frequency than the spectral width of the pump pulse. This is a clear indication of the highly-nonlinear response of the system.

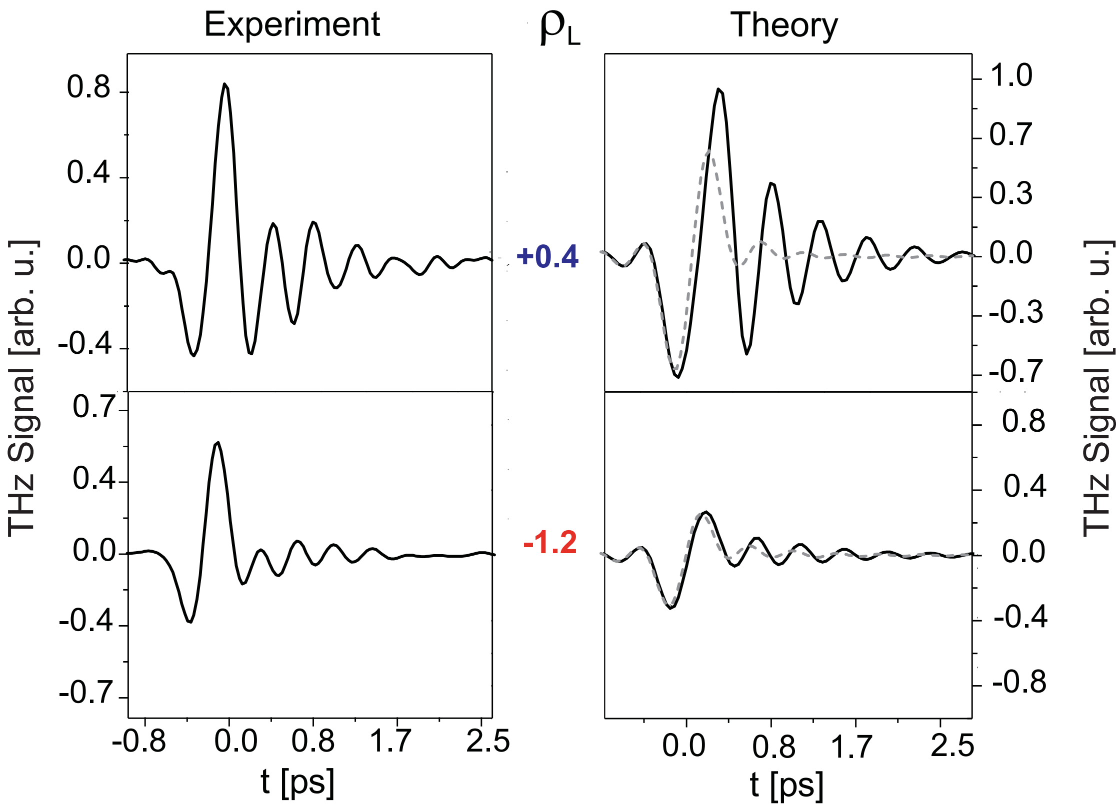

Figure 4.31: Calculated THz signals corresponding to the experimental results presented in Figure 4.28 for two different central pump pulse energies. *Left*: Experiment. *Right*: Theory. (*dashed line*) Results of the second-order calculation. (*solid line*) Results of the infinite-order calculation. The experiment can only be reproduced in the higher-order calculation. Theory had to use carrier densities of $n_{cd} = 1.67 * 10^{10}\mathrm{cm}^{-2}$, to match the Bloch oscillation amplitudes. Taken from [163].

For the physical explanation of the mechanism, one has to consider that with the excitation of more excitons, the amplitude of the depolarization field increases. The field change is non-adiabatic because it happens on the order of the Bloch oscillation period. The excitons initially created are no longer eigenstates of the system of the screened internal field. Instead, a wave packet is created which performs Bloch oscillations [163][24]. In other words, the strong ultrafast perturbation of the system leads to the coherent superposition of quantum-mechanical states.

Apart from the non-adiabatic effect, a superposition of states also arises due to the shifting of the Wannier-Stark ladder energies with time. However, detailed calculations show that this is a secondary effect for the conditions examined here and strong Bloch oscillations arise, even in the absence of this effect [163].

In a second step, the experimental situation was modeled, where the results of

---

[24] The mechanism can also be understood by higher-order frequency mixing of the optical and THz fields which becomes visible in this system due to strong exciton-exciton interaction.

the calculation to the second-order and the infinite-order in field are compared. In Figure 4.31, the findings for different $\varrho_{\mathrm{L}} = -1.2, +0.4$ are presented. Since the intraband dipole and consequently the depolarization field strongly depends on ϱ_{L}, such a dependence is analogous to a density-dependence. Indeed, it is found that for $\varrho_{\mathrm{L}} = -1.2$, the Bloch oscillation amplitude is much larger than for $\varrho_{\mathrm{L}} = +0.4$. Furthermore, it is visible that only the infinite-order calculation can reproduce the pronounced oscillations whereas the carrier density in the theory had to be slightly adjusted to match the oscillation amplitudes[25].

4.5.6 Difference-Frequency Mixing of Exciton Wannier-Stark Ladder Transitions

Let us discuss in the following Section results on the difference-frequency response of a SampleD superlattice (see, Table 4.2, for parameter). The sample was held at 10 K. The set of measurements was carried out in transmission geometry by employing the THz detection set-up as it is specified in Section 4.4. For electro-optic detection, a $300\,\mu$m thick $\{110\}$ ZnTe crystal (from CrysTec) was used.

In the experiments, the strength of the second-order susceptibility of the sample under selective excitation by a bichromatic laser spectrum was addressed and compared for different excitation conditions. For constant intensity of the pump beam, the amplitude of the emitted THz radiation is a measure of the difference-frequency susceptibility, following the relation, $\chi^{(2)}(\omega_{\mathrm{THz}}) = P^{(2)}(\omega_{\mathrm{THz}})/E(\omega_1)E(\omega_2)$.

For the intense pulse-shaped pump beam incident on the sample, a weak, spectrally broad monitor beam was coupled in. By measuring the transmission spectrum of the monitor beam, the spectrum of the superlattice was monitored to have precise control over the selective excitation of the Wannier-Stark ladder spectrum.

To generate a bichromatic interband pump beam, a double-slit mask was introduced in the pulse shaper (described in Section 4.4.1). Thus, two narrow spectral lines were cut out of the broadband laser spectrum. The average energy of the two lines, $\varepsilon_{\mathrm{bi}} = (\hbar\omega_1 + \hbar\omega_2)/2$, and the energetic splitting of the two spectral components, $\Delta\varepsilon_{\mathrm{bi}} = (\hbar\omega_1 - \hbar\omega_2)$ were freely adjustable[26]. As introduced in Section 4.4.1, the beating of the electric fields of the two laser lines leads to a pulse train which periodically drives the sample.

---

[25] Within the same formalism, the density-dependent red-shift of the Bloch oscillation frequency which was reported above (see Figure 4.21) could be nicely reproduced [163].

[26] Sohn et al. [168] proved this technique to be a powerful tool to generate tunable THz radiation, by photomixing interband transitions of a laterally biased bulk GaAs sample.

Experiments with Constant Bichromatic Splitting

The THz emission of the superlattice was measured as function of the spectral position of the bichromatic excitation ($\varepsilon_{\mathrm{bi}}$) for a constant field of $F = 12\,\mathrm{kV/cm}$. The energetic splitting of the lines was kept constant at $\Delta\varepsilon_{\mathrm{bi}} = 7\,\mathrm{meV}$ (which corresponds to 1.7 THz). Both laser lines had a width of 2.8 meV.

In Figure 4.32 (*a*), the excitation conditions are shown. The absorption spectrum of the first miniband is plotted. Features of the exciton Wannier-Stark ladder are visible which were discussed above, e.g., in Section 2.2.2. At this field strength, the vertical Wannier-Stark ladder transition (hh_0) has almost no oscillator strength. This is due to the characteristic wave function minimum in the central well for low fields, close to the Franz-Keldysh regime [169]. Furthermore, the underlying absorption of the exciton continuum is observed. In the spectrum, *different exciton Bloch oscillation frequencies* can be identified, because the Wannier-Stark ladder splitting of neighboring 1s exciton states is different (see Table 4.4). Another Bloch oscillation frequency is defined by the Wannier-Stark ladder splitting of the exciton continuum which is essentially independent of the Wannier-Stark ladder index.

Firstly, the exciton enhancement of the THz emission is examined. Figure 4.32 (*b*) plots the integrated power of the THz signal (the peak integral of the THz power spectrum) as function of ρ_{bi} which is the detuning of $\varepsilon_{\mathrm{bi}}$ relative to the vertical hh_0 1s state ($\rho_{\mathrm{bi}} = (\varepsilon_{\mathrm{bi}} - \varepsilon_{\mathrm{hh}_0})/(\varepsilon_{\mathrm{hh}_0} - \varepsilon_{\mathrm{hh}_{-1}})$). The power in the pump beam was kept constant. Hence, the plot compares the efficiency of difference-frequency mixing as function of $\varepsilon_{\mathrm{bi}}$. The bichromatic splitting, $\Delta\varepsilon_{\mathrm{bi}}$, was chosen such that $\Delta\varepsilon_{\mathrm{bi}} \approx \varepsilon_{\mathrm{hh}_{-1}} - \varepsilon_{\mathrm{hh}_{-2}}$. A clear maximum is observed when the two 1s exciton transitions (hh_{-2} and hh_{-1}) are resonantly excited. In this case, the repetitive excitation synchronously drives sustained Bloch oscillations [116, 170]. The inset shows the corresponding THz transient. Long-lasting oscillations are observed that can be attributed to the coherent wave packet dynamics after the driving pulse train has passed. Two other resonant peaks are also evident (4th and 6th points in Figure 4.32 (*b*)). These are due to doubly-resonant excitation of the hh_{-1} and hh_0 1s states and the hh_0 and hh_{+1} 1s states respectively. For other energetic positions, the pump spectrum mainly excites continuum states. Although Bloch oscillations may occur for doubly-resonant excitation of continuum states (as it will be demonstrated below), the

	hh_{-2}	hh_{-1}	hh_0	hh_{+1}
ε [eV]	1.5713	1.5797	1.5895	1.5983
$\Delta\varepsilon_{\mathrm{hh}_\eta,\mathrm{hh}_{\eta-1}}$ [meV]		8.4	9.8	8.8

Table 4.4: Transition energies of heavy-hole excitons and energy differences between the exciton Wannier-Stark resonances (for $F = 12\,\mathrm{kV/cm}$) taken from the absorption spectrum (Figure 4.32 (*a*)). The data illustrate the non-equidistant level splitting of the exciton Wannier-Stark ladder.

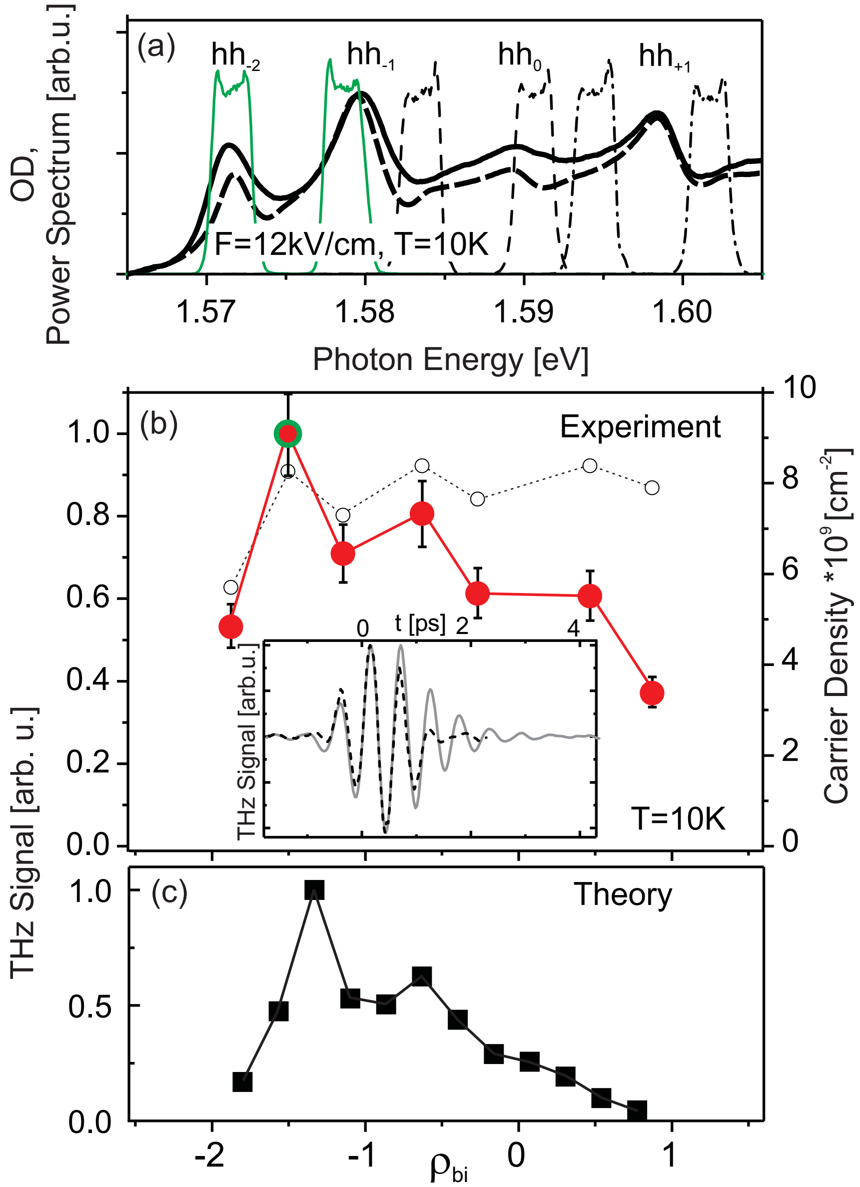

Figure 4.32: (a) : (*solid line*) Experimental interband absorption spectrum for $F = 12$ kV/cm. The heavy-hole exciton Wannier-Stark ladder transitions are labeled. (*long dash line*) The theoretical absorption spectrum. Three example bichromatic pump spectra are shown, including the pump spectrum for which the maximal THz signal was observed (*solid line*). (b) : (*filled circles*) Integrated THz power for difference-frequency mixing as function of ϱ_{bi}. The ϱ_{bi} axis is scaled to match the energy axis of (a). (*open circles*) The carrier density for constant pump power. *Inset* : (*solid line*) The THz transient for maximum amplitude. (*dashed line*) Derivative of cross-correlation signal of the pump pulse. Long-lasting coherent THz emission due to Bloch oscillations is visible. (c) : Theoretical results corresponding to (b).

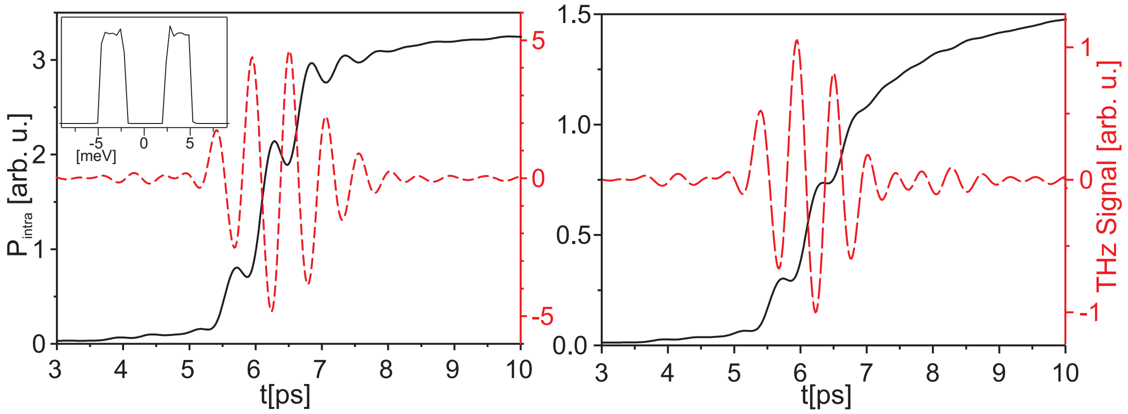

Figure 4.33: Calculated THz transients corresponding to Figure 4.32(c). *Left*: *(solid line)* Intraband polarization for maximal THz amplitude at $\varrho_{\mathrm{bi}} = -1.35$. (*dashed line*) The resulting THz signal. *Inset*: Theory uses the same pulse spectrum as employed in the experiment. *Right*: Results for $\varrho_{\mathrm{bi}} = +0.4$.

optical pulse is not quite in resonance with dipole-coupled continuum states due to the larger energetic spacing of continuum Wannier-Stark ladder states. In this case, the population-driven effect contributes relatively more to the THz emission than Bloch oscillations. For $\rho_{\mathrm{bi}} < -1.5$ (first point) the THz signal decreases due to a smaller interband oscillator strength. For $\rho_{bi} > 0$, the carrier density is constant to within ±7% around $\mathrm{n_{cd}} = 8 * 10^9\ \mathrm{cm}^{-2}$ (Figure 4.32 (b)). Here, the decrease of the THz signal is due an admixtures of states (1s excitons and continuum states) that have opposing dipole moments (for $\eta > 0$). This results in a decrease of the total intraband polarization (see Section 4.5).

Figure 4.32 (c) gives the theoretical results. The simulations were carried out by Lijun Yang applying a fully exciton model (including 1s excitons and continuum states) [53, 171] (as it was also used in Section 4.5.4). In a first step, the absorption spectrum was compared with experiment (shown in Figure 4.32 (a)). It was found that for $F_{\mathrm{theo}} = 11.25\,\mathrm{kV/cm}$, theory reproduces the experimental Wannier-Stark ladder splittings at best. The theory spectrum was shifted by about 5 meV along the energy axis to "align" both spectra. Figure 4.32 (c) plots the integrated THz power as function ρ_{bi}. The overall behavior corresponds nicely to the experimental findings reproducing the resonances at the same spectral position. It is found that the exciton enhancement is largely due to the larger intraband dipole matrix elements of the 1s excitons, relative to continuum states for the range of excitation frequencies considered here. The slight detuning of the bichromatic splitting from the continuum Wannier-Stark ladder splitting also plays some role. The change in carrier density with ρ_{bi} is a comparatively less important factor for $\rho_{\mathrm{bi}} > -1.5$. The falloff in signal at large ρ_{bi} is more rapid in the theoretical results. This may be due to the fact that the intraband dephasing constant assumed in the simulations was too large. In the calculation T_{12} was set to 0.52 ps. This is in the order of what was found in the density-dependent measurement (see results in Figure 4.27). However, the

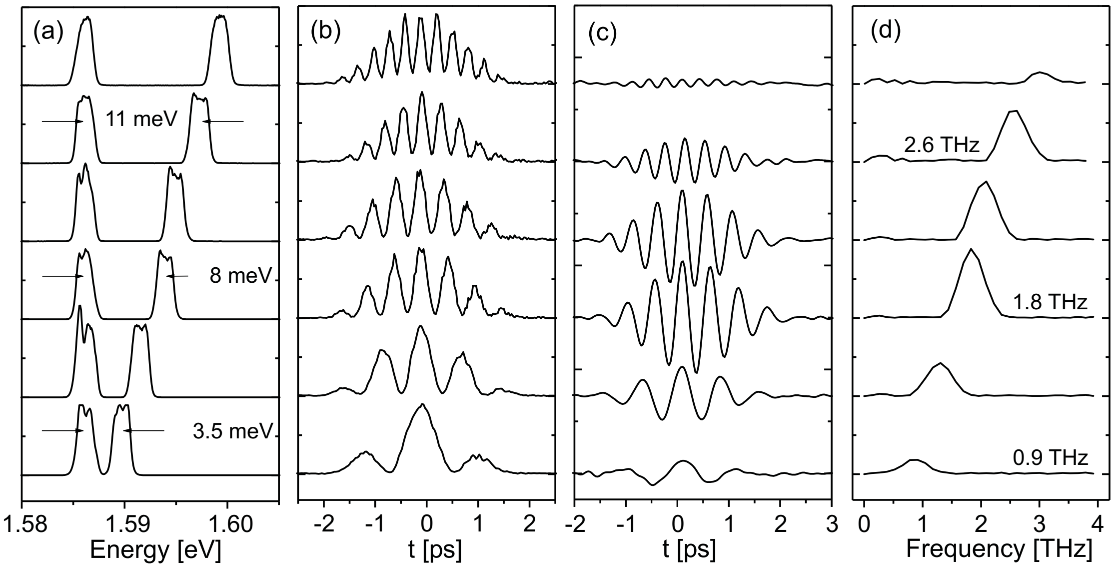

Figure 4.34: $(a):$ Spectra of bichromatic pump pulses with different energetic splitting. $(b):$ Corresponding cross-correlation signals. $(c):$ Corresponding terahertz signals for $F = 11.5\,\mathrm{kV/cm}$. The frequency of the THz signal follows the bichromatic splitting of the pump pulse. The amplitude of the signal shows a maximum for the excitation with $\Delta\varepsilon_{\mathrm{bi}} = 8\,\mathrm{meV}$. $(d):$ Power spectra of THz transients.

results are very sensitive to this parameter. A small intraband dephasing constant translates to sharper intraband resonances.

Two sets of illustrative theoretical data are shown in Figure 4.33. Theory also gives long-lasting oscillations for the THz signal with maximal amplitude (shown in the left graph). The driving of the 1s exciton wave packet leads to oscillations of the intraband polarization superimposed onto the "steps" of the population-built-up. The THz signal follows from the second derivative. For a spectral position of $\varrho_{\mathrm{bi}} = +0.4$, mainly population-driven THz emission is observed. The intraband polarization increases in "steps". The THz signal for $\varrho_{\mathrm{bi}} = +0.4$ decreases in amplitude by a factor of about 5 compared to $\varrho_{\mathrm{bi}} = -1.35$.

Experiments with Variable Bichromatic Splitting

Difference-frequency mixing (in principle) provides the possibility to extract from the system a wide range of THz frequencies. To show tunability and to examine the second-order response arising from Bloch oscillations of continuum states, measurements were conducted as function of the bichromatic splitting.

Figure 4.34 illustrates the potential of the method, plotting pump pulses with different bichromatic splitting and the corresponding THz emission. Figure 4.34 (a) shows the spectra of the pump pulses. The temporal form of the pump pulses was monitored by cross-correlation measurements (see Figure 4.34 (b)). The THz signal

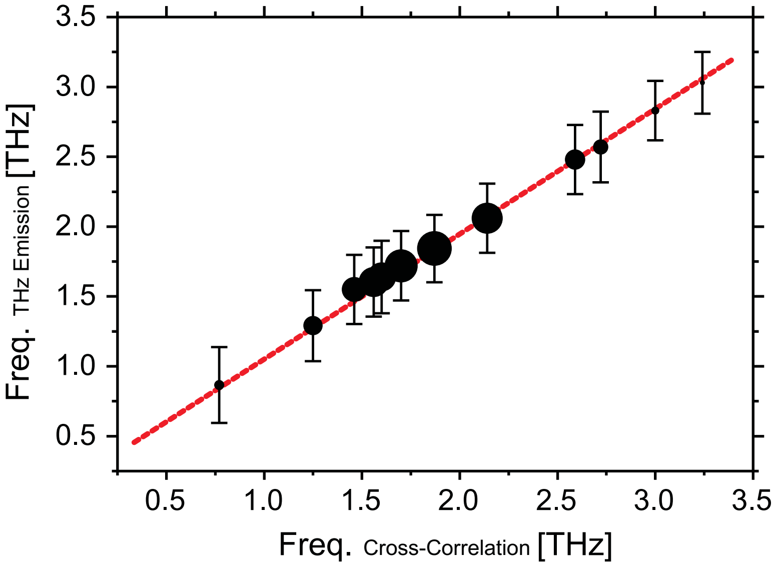

Figure 4.35: Frequency of the generated THz radiation as function of $\Delta\varepsilon_{\mathrm{bi}}$ for a constant field, $F = 11.5\,\mathrm{kV/cm}$. The bars plot (± HWHM) the spectral width of the THz emission peak.

of the superlattice sample after excitation by the bichromatic pump pulses with different $\Delta\varepsilon_{\mathrm{bi}}$ was measured for a constant field strength ($F = 11.5\,\mathrm{kV/cm}$). In Figure 4.34 (c), the results are plotted. It is observed that the frequency of the emitted THz signal increases with the increasing energetic splitting of the exciting laser lines. Additionally, the amplitude of the THz radiation changes. The power spectra of the THz scans are shown in Figure 4.34 (d).

The results prove that biased superlattices can be used as nonlinear medium to generate *tunable THz radiation* by difference-frequency mixing. This is underlined in Figure 4.35. The central frequency of the THz radiation is plotted as function of $\Delta\varepsilon_{\mathrm{bi}}$.

In the following, results are presented on the investigation of the second-order susceptibility spectrum of continuum states, whereas the THz emission was measured for two fields, $F = 9.5\ kV/cm$ and $F = 11.5\ kV/cm$, as function of the bichromatic splitting. The low-energy laser line was fixed at one spectral position lying midway between the hh_{-1} and the hh_0 1s states. In Figure 4.36 (a) the excitation conditions are shown. Since the low-energy line excites only continuum carriers, the THz signal amplitude is a measure of the intraband dipole matrix element between in-plane states with different Wannier-Stark ladder indices. In Figure 4.36 (b), the THz emission strength is plotted as function of $\Delta\varepsilon_{\mathrm{bi}}$. For comparison, the data were normalized to the pump power which was different for the two sets of experiments[27]. For both fields, the plot shows a strong resonance. The maximum

---

[27] In first order, the signal is linear dependent on density (pure $\chi^{(2)}$ process). Thus, the difference-frequency susceptibility can be directly compared after normalization to the pump power. The average carrier density was for $F = 9.5\,\mathrm{kV/cm}$: $\mathrm{n}_{\mathrm{cd}} = 6 * 10^9\mathrm{cm}^{-2}$ and for $F = 11.5\,\mathrm{kV/cm}$:

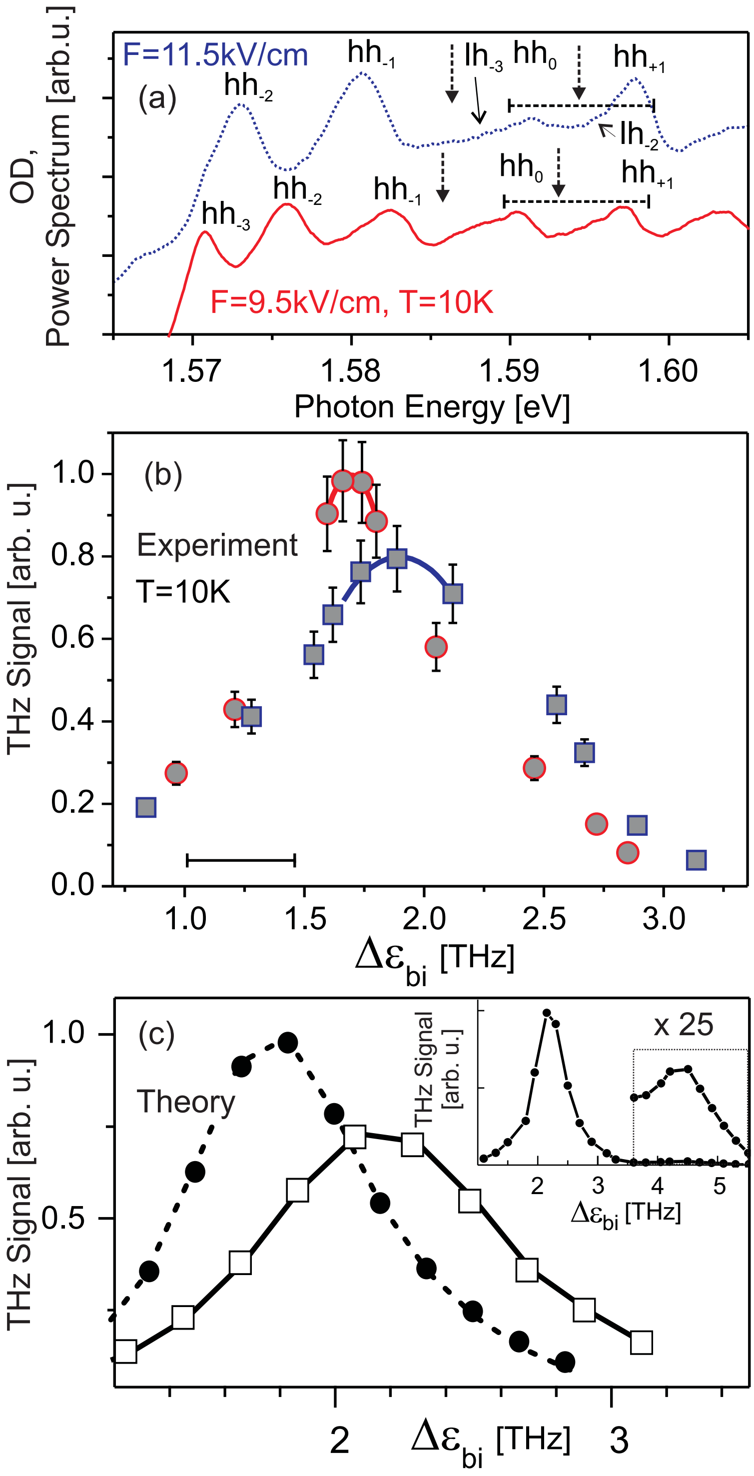

Figure 4.36: (a): Experimental interband absorption spectra. The spectrum for $F = 11.5$ kV/cm (*dashed line*) is shifted relative to the $F = 9.5$ kV/cm spectrum (*solid line*) by adding a constant factor. The dashed arrows mark the bichromatic spectrum for which the maximal THz signal was measured. The horizontal dashed bars give the tuning interval of the high-energy laser line. (b): Amplitude of the generated THz emission as function of $\Delta\varepsilon_{\mathrm{bi}}$ (for $F = 9.5$ kV/cm (*circles*) and $F = 11.5$ kV/cm (*squares*). The bar gives the spectral width (FWHM) of the bichromatic excitation. (c): Theoretical results corresponding to (b). (*Inset*) Theoretical result showing the second resonance for driving the system at the double Bloch oscillation frequency, i.e., $\Delta\varepsilon_{\mathrm{bi}} = 2\hbar\omega_{\mathrm{B}}$.

is expected for the excitation of in-plane states which undergo intraband transitions with $\Delta \mathrm{k}_\mathrm{x} \approx \Delta \mathrm{k}_\mathrm{y} \approx 0$. In this case, $\Delta\varepsilon_{\mathrm{bi}}$ equals the Wannier-Stark ladder splitting of the continuum states and the double-resonance condition is satisfied[28]. For the lower field strength ($F = 9.5\,\mathrm{kV/cm}$), the maximum is at a lower bichromatic splitting (at $\Delta\varepsilon_{\mathrm{bi}} = 1.7\,\mathrm{THz}$) due to a smaller Wannier-Stark ladder splitting.
For $F = 11.5\,\mathrm{kV/cm}$, the resonance is observed at 1.9 THz. The difference of the spectral position of the resonances for the two field strengths is smaller than the theoretical value of 0.4 THz (for $\Delta F = 2\,\mathrm{kV/cm}$). This discrepancy may be due to an experimental error in the internal field by ±0.5 kV/cm. Additionally, the THz emission of quantum beats of excited light-hole (lh) transitions (marked in Figure 4.36 (*a*)) may be affecting the result.

For $F = 9.5\,\mathrm{kV/cm}$, a larger resonance amplitude is observed. One potential reason could be that in-plane states with larger intraband dipole (smaller Wannier-Stark ladder index) contribute for the lower field strength. In addition, a larger overall oscillator strength (more excited carriers per pump power) for the lower field was noted in the experiment. However, it was found in the simulations that the intraband dephasing time plays a decisive role. The theoretical results are shown in Figure 4.36 (*c*)). The model reproduced the two distinct resonances. As expected, the peak positions are apart by 0.4 THz. To reproduce the same peak widths and especially the same relative peak heights, the intraband dephasing constant was adjusted. For $F = 9.5\,\mathrm{kV/cm}$, an intraband dephasing T_{12} of 0.5 ps was found which results in a peak width of = 0.7 THz (FWHM), for $F = 11.5\,\mathrm{kV/cm}$, $T_{12} = 0.3\,\mathrm{ps}$ (peak width = 1.1 THz (FWHM)) was determined, respectively.

The inset of Figure 4.36 (*c*) shows a supplementary result of the modeling. If the simulation considers next-nearest-neighbor coupling, a second maximum is observed for the coupling of Wannier-Stark ladder states with $|\Delta\eta| = 2$ driving the system at the double Bloch oscillation frequency. This is not evident in the experimental results due to the bandwidth limitations of the THz detection.

$\mathrm{n}_{\mathrm{cd}} = 9 * 10^9\mathrm{cm}^{-2}$. As function of $\Delta\varepsilon_{\mathrm{bi}}$, the carrier density was almost constant for both sets of measurement. Only a slight increase was observed (in maximum by ≈ 10% for large $\Delta\varepsilon_{\mathrm{bi}}$).

[28] At the resonance, coherent oscillations after the driving pulse were observed in the THz experiments (not shown) which can be attributed to Bloch oscillations of continuum carriers.

Conclusions

Zener Tunneling in Semiconductor Superlattices

Zener tunneling was studied in the electron miniband structure of biased semiconductor superlattices. The signature of the electrical breakdown was traced in the optical spectrum of the samples. In superlattice structures with shallow barriers, Zener tunneling was observed to occur in a very pronounced manner. In these structures the complex interplay of non-resonant and resonant tunneling was investigated in dependence of the particular electron dispersion relation.

Three different field-regimes could be clearly identified. For low fields, the formation of Wannier-Stark ladders was visible. In the medium field regime, the states localized due to the well-known Wannier-Stark ladder localization. However, for high fields, the picture of Wannier-Stark ladders was observed to become invalid. The optical spectrum deviates strongly from the Wannier-Stark ladder high-field limit, i.e. a field-independent absorption peak of the vertical Wannier-Stark ladder transition. Instead, the absorption lines strongly broaden, shift to lower energies, and at high, but attainable fields, the transitions ultimately vanish. To model the carrier spectrum over the whole field range, one-band approximations are no longer tenable. The field-regime of Zener tunneling can only be correctly described in a framework which includes an (in principle) infinite number of bands. These observations are supported by the results of full numerical calculations [22] which well model the experimental findings.

In the employed shallow superlattice samples, tunneling in the electron Wannier-Stark ladder spectrum is addressed as coupling of the electron states of a single bound below-barrier band to the states of the above-barrier spectrum. It is shown that with the help of the original Zener equation the overall continuous increase of the tunneling probability can be well described. The latter fact is due to the coupling to the quasi-continuum of above-barrier states. Superimposed on this behavior, oscillations are visible which are caused by the resonant crossing of above-barrier Wannier-Stark ladder states. The particular interplay between resonant and non-resonant tunneling was derived from the miniband structure of the samples, when two specifically designed superlattice geometries were compared. It was demonstrated that depending on the size of the second band gap, the formation of a Wannier-Stark ladder originating from the second miniband, which is energetically above the barrier, can be observed. This effect is especially prominent for SampleA which has a large second band gap. On the other hand, in SampleB distinctively different tunneling characteristics were observed. The small second band gap of SampleB leads to the strong mixing of the above-barrier bands. In this case, almost pure non-resonant Zener tunneling occurs. Additionally, a different overall increase of the tunneling probability as function of field was observed which is defined by the size of the first band gap. A larger increase was found for SampleA than for SampleB because of the smaller first band gap of SampleA.

Zener tunneling to higher bands was proven to lead a field-induced delocalization of the Wannier-Stark ladder states. This was shown by the analysis of the oscillator strength of the (1,1) hh_0 transition in the optical absorption spectrum as function of field which significantly decreases when Zener tunneling comes into play.

The Zener tunneling probability was determined by the analysis of the linewidth of the (1,1) hh_0 transition as function of field. For high fields a strong continuous increase was observed. This non-resonant Zener tunneling behavior was well approximated by the original Zener theory, whereas the fitting parameters nicely corresponded to the band gap sizes which followed from the calculation of the flat-field dispersion relation. Additionally, superimposed oscillations were visible which were attributed to resonant crossings with Wannier-Stark ladder states of higher minibands. The results were compared to the findings of a complex-energy theory by Glück et al. [71] which directly calculated the tunneling lifetime of Wannier-Stark ladder states. In the Zener regime, the interplay of non-resonant and resonant tunneling is well described. It nicely underlines that Zener tunneling becomes the dominant dephasing channel for high fields.

The dynamics of Zener tunneling was investigated by four-wave mixing experiments. Employing this time-resolved technique, Zener tunneling was demonstrated to lead to a dominant homogeneous line broadening. Furthermore, an effective electron tunneling time into above-barrier states was evaluated.

Terahertz Emission of Exciton Wave Packets in Semiconductor Superlattices

By means of THz experiments, the coherent intraband dynamics of exciton wave packets in biased superlattices after the selective ultrafast excitation of the Wannier-Stark ladder spectrum was addressed. For the investigations, a strongly-coupled superlattice geometry with high barriers was employed, where the minibands were separated by large band gaps inhibiting Zener tunneling.

In general, two basic mechanisms are responsible for coherent THz emission: (i) the time-varying macroscopic intraband polarization of Bloch oscillations of dipole-coupled states and (ii) the population-driven emission due to the ultrafast creation of polarized electron-hole pairs. Based on these two effects the measurement of the dynamics of the intraband dipole of wave packets as well as the dipole strength of single Wannier-Stark ladder excitons was performed.

Bloch oscillations were investigated under broadband excitation. A damped oscillatory THz signal was observed whose frequency was shown to be linearly dependent on the applied field. With the help of an "in-situ" monitoring of the carrier spectrum, the excitation conditions could be accurately controlled. In the field-dependent measurements, the Bloch oscillation frequency was found to show a systematic red-shift relative to the energetic splitting of the excited bound Wannier-Stark ladder excitons. These findings indicated that apart from 1s excitons, higher in-plane exciton states contribute to the emitted THz signal. In density-dependent measurements, the superradiant THz emission of Bloch oscillations was proved.

The manipulation of the Bloch oscillation dynamics was demonstrated by measuring the THz emission as function of pump pulse energy. A strong influence on the Bloch oscillation amplitude was found. For tuning the energy of the exciting pulse through the Wannier-Stark ladder spectrum, starting at low energy, the amplitude was observed to decrease when passing the energetic Wannier-Stark ladder center and to saturate for high energies. However, a phase change of the wave packet oscillation was not observed. Furthermore, the breathing mode motion of the Bloch oscillation was not found. Thus, the findings did not reproduce the predictions of the one-dimensional model. On the contrary, the intraband dynamics can only be understood in a *full exciton picture* which includes 1s excitons as well as the in-plane exciton continuum. It was demonstrated that the states of the exciton continuum dominate the intraband dynamics of the wave packet for the excitation of the Wannier-Stark ladder at high energies. Furthermore, the experiments prove an exceptionally long intraband dephasing time of the continuum states.

The decisive role that play higher in-plane states in the intraband dynamics of superlattices was also found in other works: in THz experiments [93, 94, 96] and by interband experiments which time-resolved the electro-optically induced birefringence of the superlattice sample [165, 166]. In 1997, Bolivar et al. [35] were first to demonstrate exciton effects in the THz emission of a superlattice. Nevertheless,

in subsequent works, the findings of THz experiments are discussed in the single-particle picture.
In this work, in the experiments using selective optical excitation, exciton effects became clearly evident in the intraband dynamics of superlattices. Therefore, a conclusive exciton picture was formulated which explains the experimental findings well by considering the full exciton spectrum, bound 1s exciton states and the associated exciton in-plane continuum. This is supported by theoretical results which were gained by Yang et al. [53]. The model incorporates exciton-exciton interactions on a very basic level, where the exciton basis comprises bound and higher excited exciton states.

The prominent influence of the exciton continuum states on the intraband dynamics stands in clear contrast to what was found in interband experiments. Interband nonlinear experiments such as four-wave-mixing are observed to be selectively sensitive to exciton resonances: Firstly, the four-wave-mixing signal is proportional to the eighth order of the interband transition matrix element [91]. Therefore, only 1s exciton resonances are usually visible in four-wave-mixing spectra[29]. The dynamics of the interband polarization is also dominated by bound exciton states due to their long-living interband coherence. The broad k-space distribution of the continuum states leads to an almost immediate interference decay of their interband polarization [61].

Furthermore, this work presented results on THz emission after narrowband excitation. The intraband dipole of single Wannier-Stark ladder excitons was measured by exciting the Wannier-Stark ladder with a spectrally narrow rectangular pump pulse. An initial dipole, single-cycle, oscillation resulted due to the sudden creation of the polarized electron-hole pairs. The intraband dipole of the excitons was evaluated by analyzing the amplitude of the THz signal. It was found to scale in discrete steps with the Wannier-Stark ladder index. Furthermore, it was demonstrated that the net dipole decreases and finally saturates when the pump spectrum is energetically shifted to higher energies. Again, the phase change of the intraband dipole of the excited excitons, which would be expected in a purely 1s exciton model, was not visible. Therefore, the findings have to be explained in a full exciton picture. For the excitation of the Wannier-Stark ladder at high energies, the intraband polarization was observed to be dominated by exciton continuum states.

In addition, experiments employing narrowband excitation revealed a previously unknown mechanism for the generation of Bloch oscillating exciton wave packets. This was demonstrated for an incident pump spectrum which was too narrow to excite a superposition of Wannier-Stark ladder states. The effect is based on the sudden, non-adiabatic, change in the net dc internal field due to creation of electron-hole pairs with permanent dipole moments. Due to the rapid increase in this depolarization field as the exciton population is built-up by the exciting laser pulse,

---

[29] For example, see Figure 1 in Reference [32]. It gives a four-wave-mixing spectrum for a superlattice sample with the same geometry as it was used in this work.

excitons that are initially created in a single state of the Wannier-Stark ladder in the initial dc field transform into a superposition state formed from the Wannier-Stark ladder states of the final internal field. Because this effect requires the generation of a relatively large internal field, it is strongly density-dependent. Thus, Bloch oscillations are only observed when the exciton density is high, or the internal dipole moments are large. The non-adiabatic generation of Bloch oscillations is a highly nonlinear effect mediated by strong exciton-exciton interactions.
In experiment, pronounced oscillations were observed when pumping the Wannier-Stark ladder spectrum at low energy, i.e. exciting excitons with large intraband dipole. The oscillations were not visible for high energy excitation, where the net intraband dipole of the exciton states is small.
A related higher-order nonlinear effect was found for the excitation of the Wannier-Stark ladder with a broadband pump spectrum as function of exciton density. For constant internal field, a red-shift of the Bloch oscillation frequency was observed. The effect was attributed to the creation of a depolarization field when building up the exciton population. The rapid internal field change was additionally detected in spectrally-resolved pump-probe experiments as transient spectral shifts of the Wannier-Stark ladder transition energies.

The experimental findings were well reproduced by a theory recently developed by Yang et al. [163]. It models the intraband response of the system to an (in principle) infinite-order in optical field while retaining the exciton correlations. It was illustratively demonstrated that the observed effects are higher order in the optical field.

The central role that play exciton-exciton interactions in the intraband dynamics became especially evident when the Wannier-Stark ladder was selectively excited by two spectrally narrow laser lines. In this way, the intraband transition probability between selectively addressed exciton states was measured. The resonant enhancement of the intraband transition matrix element due to Coulomb interaction could be experimentally demonstrated. The experiments revealed that enhanced THz emission arises when either continuum or 1s exciton wavepackets are excited, and that maximum emission appears from excitation of the 1s exciton wave packets [171]. The latter proves the exciton enhancement of the intraband dipole matrix elements. By tuning the applied dc field and tuning the bichromatic excitation, the system can be easily adjusted to meet the double-resonance condition for maximum output. By variation of the bichromatic splitting, tunable THz radiation was extracted from the system. The experimental results were convincingly modeled in a full exciton theory calculating the coherent exciton dynamics [53].

Outlook

Zener Tunneling in Semiconductor Superlattices

Semiconductor superlattices are shown to be a powerful tool for the investigation of fundamental high-field transport phenomena. For the investigation of Zener tunneling, superlattices with shallow barriers were demonstrated to be very suitable.

Future experiments should further investigate the influence of the interplay of non-resonant and resonant tunneling on the carrier dynamics. Its correct description is still a topic of theoretical debate [172]. A particular fundamental question is the influence of tunneling on the dephasing of Bloch oscillations. This topic can be nicely studied in the shallow superlattices, such as investigated in this work, because the Wannier-Stark ladder field-regime and the Zener tunneling regime partly overlap. In different works [80, 173], the results of pump-probe experiments were presented, in which the fast interference decay of Bloch oscillations due to resonant Zener tunneling was demonstrated in a superlattice of SampleB geometry. In a subsequent work, Meinhold et al. [85] observed a wave packet revival in such a superlattice sample in conjunction with resonant tunneling. However, in the SampleB structure the effect could only be investigated for a small field interval, because the Zener effect only starts to influence the Bloch oscillation dynamics at rather high fields. Based on the findings of this work, the interplay of resonant and non-resonant tunneling, affecting the intraband dephasing, should be more pronounced in a SampleA superlattice structure. For SampleA strong tunneling resonances were observed, which are expected to lead to pronounced multiple Bloch wave packet revivals. Furthermore, the interplay of resonant and non-resonant tunneling is expected to lead to oscillations in the intraband dephasing rate as function of field. As demonstrated in this work, THz emission spectroscopy is a suitable tool to directly probe the intraband dynamics of the carriers in the Zener regime [30].

Moreover, future experiments should address the demonstration of the interpolating resonant and non-resonant Zener tunneling in transport experiments. The undoped samples which were used in this work were not suitable for such experiments. Their current-voltage curve was dominated by the electrical properties of the contacts. Furthermore, one has no control into which states the carriers are injected.

---

[30] Recently, with THz experiments, Shimada et al. [174] gave experimental evidence of resonant tunneling between different Wannier-Stark ladders.

This may be overcome by selective photo-injection or by embedding the sample into a three-terminal hot-electron transistor as demonstrated by Ranch et al. [175].

Intraband Dynamics of Exciton Wannier-Stark Ladder Wave Packets

In this work, THz emission experiments were performed to demonstrate the manipulation of the Bloch oscillation dynamics. This powerful experimental technique can be employed to further investigate the control of the coherent dynamics of Bloch oscillations. It would give direct access to measure intraband interference phenomena of Bloch oscillations after the excitation of wave packets with definite phase relation. As an example, by the variation of the phase between the exciting pulses it should be possible to tune between co-propagating and counter-propagating wave packets. Recently, four-wave mixing experiments were performed employing coherently controlled optical pulses. The findings gave evidence of the manipulation of the Bloch oscillation dynamics by tuning the optical phase of different spectral components of the exciting pulse [176]. It is desirable to experimentally proof this kind of manipulation by THz spectroscopy because it directly monitors the intraband dynamics of the whole excited carrier ensemble, bound and continuum exciton states.

In this work, experimental finding were presented which demonstrated a highly nonlinear THz response of the biased superlattice induced by Coulomb interaction. In particular, the mechanism of a non-adiabatic excitation of Bloch oscillations was revealed [163]. The phenomenon demands further investigation to map out the density dependence of the effect. In a first step, the THz response should be investigated after narrowband excitation as function of carrier density. The findings can then be compared to theory which predicts (see Figure 4.19) distinctively different density regimes.

At this point, let us briefly discuss the longstanding question whether biased superlattices exhibit THz gain tunable in frequency by the external electric field. So far, a direct experimental proof of existence and strength of the gain predicted by semiclassical [177] and quantum-mechanical models [159] has not been given. In addition, very recently, Lachaine et al. [37] predicted a gain mechanism based on the exciton non-equidistant of the Wannier-Stark ladder. The latter mechanism was addressed by experiments which were performed during this work (results are not shown). The superlattice itself was used as THz source. By pumping high energy continuum states with a bichromatic laser spectrum, a spectrally narrow THz field was induced which frequency was resonant with the $hh_{-1} - hh_{-2}$ 1s exciton intraband transition. The THz emission was then probed for pre-pumping the sample with a spectrally narrow pulse to produced an incoherent population of the hh_{-1} 1s exciton state. Gain would be expected for a particular internal field range at which the intraband transition probability down the exciton Wannier-Stark ladder is predicted to be larger than up the Wannier-Stark ladder [37]. In the experiments, increased THz emission due to gain could not be observed. The hypotheses to explain this finding are: (i) The nonlinear THz response of the sample on the intense pre-pump beam, in particular the built-up of a large depolarization field drives the system out of the gain condition. (ii) The superimposed intraband dynamics of the exciton continuum states which Wannier-Stark ladder spectrum is equidistant, i.e. no gain effect is expected for the continuum. Therefore, it would be a fascinating task to repeat the experiment employing an external THz source, where the THz transmission through the biased superlattice is detected under selective optical excitation.

List of Symbols

This list comprises selected symbols:

Symbol	**Meaning**
$\mathrm{A_z}$	effective spatial displacement of the Bloch oscillating wave packet
c_0	speed of light in vacuum
C_η	amplitude of Wannier-Stark ladder state in the Bloch oscillation wave packet
d	superlattice period
$D(\omega)$	optical density of states
e	elementary charge
E	electro-magnetic field amplitude
E	energy
$\Delta\mathrm{E}$	band gap
$f(z)$	carrier single-well eigenfunction, basis of tight-binding expansion
F	electric dc field
I	optical intensity
J_n	Bessel function of the first kind of order n
$\boldsymbol{k}$	reciprocal space vector, wave vector
$\mathcal{L}$	localization length of the Wannier-Stark ladder state
L	length of the electro-optical detector crystal
L_B	semiclassical Bloch oscillation amplitude
m^*	effective carrier mass
n	refractive index, population of a carrier eigenstate
$\mathrm{n_{cd}}$	carrier sheet density per well
P^n	macroscopic polarization to the n(th) order
$\hat{\mathrm{R}}(\omega)$	complex response function of the electro-optic detection
r_{41}	electro-optic coefficient
T_1	interband population relaxation time (longitudinal relaxation time)
T_2	interband polarization relaxation time (transverse relaxation time)
T_{12}	intraband polarization relaxation time
T_B	Bloch oscillation period
$\mathcal{U}(z)$	superlattice potential
$u_{\lambda,\boldsymbol{k}}(\boldsymbol{r})$	lattice periodic Bloch function of wave vector $\boldsymbol{k}$ and miniband index λ

α	absorption coefficient
Δ	miniband width
ε	optical transition energy
ε_{L}	central energy of laser pulse
$\Delta\varepsilon_{\mathrm{L}}$	spectral width of laser pulse (FWHM)
$\varepsilon_{\mathrm{bi}}$	central energy of bichromatic laser spectrum
$\Delta\varepsilon_{\mathrm{bi}}$	energetic splitting of bichromatric laser lines
η	Wannier-Stark ladder index
γ	damping constant in dielectric function, Zener tunneling rate
Γ	linewidth
λ	miniband index, wavelength
μ	dipole operator
ν	frequency
ρ	density matrix operator
ρ_{L}	energetic detuning of the pump spectrum relative to the vertical Wannier-Stark ladder transition
Φ	Bloch oscillation wave packet
τ_{p}	pulse duration (FWHM)
τ_{d}	delay time of the correlation experiment
τ_{fwm}	decay constant of the time-integrated four-wave mixing intensity
χ	carrier envelope function
$\chi^{(2)}$	second-order optical susceptibility
ψ	carrier eigenfunction
Ψ	general quantum-mechanical state
Ω_{L}	$1/e^2$ spectral width of the laser pulse

Bibliography

[1] F. Bloch, Z. Phys. **52**, 555 (1928).

[2] C. Zener, Proc. Roy. Soc. London, Ser. A **145**, 523 (1934).

[3] L. Esaki and R. Tsu, IBM J. Res. Dev. **4**, 61 (1970).

[4] K. Leo, *High-Field Transport in Semiconductor Superlattices* (Springer Tracts in Modern Physics, Vol. 187, Springer-Verlag, Berlin, 2004).

[5] H. T. Grahn, ed., *Semiconductor Superlattices - Growth and Electronic Properties* (World Scientific, Singapore, 1995).

[6] A. Wacker, Phys. Rep. **357**, 1 (2002).

[7] L. Esaki and L. L. Chang, Phys. Rev. Lett. **33**, 495 (1974).

[8] E. E. Mendez, F. Agulló-Rueda, and J. M. Hong, Phys. Rev. Lett. **60**, 2426 (1988).

[9] P. Voisin, J. Bleuse, C. Bouche, S. Gaillard, C. Alibert, and A. Regrency, Phys. Rev. Lett. **61**, 1639 (1988).

[10] J. Feldmann, K. Leo, J. Shah, D. A. B. Miller, J. E. Cunningham, T. Meier, G. von Plessen, A. Schulze, P. Thomas, and S. Schmitt-Rink, Phys. Rev. B **46**, 7252 (1992).

[11] K. Leo, P. H. Bolivar, F. Brüggemann, R. Schwedler, and K. Köhler, Solid State Commun. **84**, 943 (1992).

[12] G. H. Wannier, Phys. Rev. **117**, 432 (1960).

[13] J. E. Avron, J. Zak, A. Grossmann, and L. Gunther, J. Math. Phys. **18**, 918 (1977).

[14] S. Glutsch, *Excitons in Low-Dimensional Semiconductors* (Springer Series in Solid State Science, Vol. 141, Springer-Verlag, Berlin, 2004).

[15] M. Glück, A. R. Kolovsky, H. J. Korsch, and F. Zimmer, Phys. Rev. B **65**, 115302 (2002).

[16] J. Leo and A. MacKinnon, J. Phys.: Condensed Matter **1**, 1449 (1989).

[17] H. Schneider, H. T. Grahn, K. v. Klitzing, and K. Ploog, Phys. Rev. Lett. **65**, 2720 (1990).

[18] M. Nakayama, I. Tanaka, H. Nishimura, K. Kawashima, and F. Fujiwara, Phys. Rev. B **44**, 5935 (1991).

[19] K. Fujiwara, K. Kawashima, and T. Imanishi, Phys. Rev. B **54**, 17724 (1996).

[20] A. Sibille, J. F. Palmier, and F. Laruelle, Phys. Rev. Lett. **80**, 4506 (1998).

[21] M. Helm, W. Hilber, G. Strasser, R. D. Meester, F. M. Peeters, and A. Wacker, Phys. Rev. Lett. **82**, 3120 (1999).

[22] S. Glutsch and F. Bechstedt, Phys. Rev. B **60**, 16584 (1999).

[23] B. Rosam, *Diplomarbeit* (Technische Universität Dresden, 1999).

[24] I. Brener, P. C. M. Planken, M. C. Nuss, M. S. C. Luo, S. L. Chuang, L. Pfeiffer, D. E. Leaird, and A. M. Weiner, J. Opt. Soc. Am. B **11**, 2457 (1994).

[25] H. G. Roskos, Festkörperprobleme / Advances in Solid State Physics, Vol. 34, Vieweg & Sohn Verlagsgesellschaft, Wiesbaden, pp. 297–315 (1995).

[26] K. Leo, J. Shah, E. O. Göbel, T. C. Damen, W. S. S. Schmitt-Rink, and K. Köhler, Phys. Rev. Lett. **66**, 201 (1991).

[27] H. G. Roskos, M. C. Nuss, J. Shah, K. Leo, and D. A. B. Miller, Phys. Rev. Lett. **68**, 2216 (1992).

[28] C. Waschke, P. Leisching, P. H. Bolivar, R. Schwedler, F. Brüggemann, H. G. Roskos, K. Leo, H. Kurz, and K. Köhler, Solid-State Electron. **37**, 1321 (1994).

[29] G. Bastard, J. Bleuse, R. Ferreira, and P. Voisin, Superlatt. Microstruct. **6**, 77 (1989).

[30] M. Dignam, J. E. Sipe, and J. Shah, Phys. Rev. B **49**, 10502 (1994).

[31] A. M. Bouchard and M. Luban, Phys. Rev. B **52**, 5105 (1995).

[32] M. Sudzius, V. G. Lyssenko, F. Löser, K. Leo, M. M. Dignam, and K. Köhler, Phys. Rev. B **57**, 12693 (1998).

[33] M. M. Dignam, Phys. Rev. B **59**, 5770 (1999).

[34] R.-B. Liu and B.-F. Zhu, Phys. Rev. B **59**, 5759 (1999).

[35] P. H. Bolivar, F. Wolter, A. Müller, H. G. Roskos, H. Kurz, and K. Köhler, Phys. Rev. Lett. **78**, 2232 (1997).

[36] V. M. Axt, G. Bartels, and A. Stahl, Phys. Rev. Lett. **76**, 2543 (1996).

[37] J. M. Lachaine, M. Hawton, J. E. Sipe, and M. M. Dignam, Phys. Rev. B **62**, R4829 (2000).

[38] R.-B. Liu and B.-F. Zhu, Appl. Phys. Lett. **84**, 2730 (2004).

[39] K. Fujiwara, *Semiconductor Superlattices - Growth and Electronic Properties* (World Scientific, Singapore, 1995).

[40] O. Madelung, *Landoldt-Börnstein, New Series, Group III*, vol. 22 (a) (Springer-Verlag, Berlin, 1987).

[41] S. Adachi, *GaAs and Related Materials* (World Scientific, Singapore, 1994).

[42] O. Madelung, *Semiconductors–Basic Data* (Springer-Verlag, Berlin, Heidelberg, New York, 1996).

[43] P. Y. Yu and M. Cardona, *Fundamentals of Semiconductors* (Springer-Verlag, Berlin, 1996).

[44] C. Weisbuch and B. Vinter, *Quantum Semiconductor Structures* (Academic Press, Boston, 1991).

[45] J. Bleuse, G. Bastard, and P. Voisin, Phys. Rev. Lett. **60**, 220 (1988).

[46] D. M. Whittaker, Phys. Rev. B **41**, 3238 (1990).

[47] M. M. Dignam and J. E. Sipe, Phys. Rev. B **41**, 2865 (1990).

[48] M. M. Dignam and J. E. Sipe, Phys. Rev. Lett. **64**, 1797 (1990).

[49] D. M. Whittaker, M. S. Skolnick, G. W. Smith, and C. R. Whitehouse, Phys. Rev. B **42**, 3591 (1990).

[50] M. M. Dignam and J. E. Sipe, Phys. Rev. B **43**, 4097 (1991).

[51] D. M. Whittaker, Europhys. Lett. **31**, 55 (1995).

[52] G. Bastard, E. E. Mendez, L. L. Chang, and L. Esaki, Phys. Rev. B **26**, 1974 (1982).

[53] L. Yang, B. Rosam, J.-M. Lachaine, K. Leo, and M. M. Dignam, Phys. Rev. B **69**, 165310 (2004).

[54] N. Linder, Phys. Rev. B **55**(20), 13664 (1997).

[55] U. Fano, Phys. Rev. **124**, 1866 (1961).

[56] S. Glutsch and D. S. Chemla, Phys. Rev. B **51**, 16885 (1995).

[57] C. P. Holfeld, F. Löser, M. Sudzius, K. Leo, D. M. Whittaker, and K. Köhler, Phys. Rev. Lett. **81**, 874 (1998).

[58] F. Rossi, Semicond. Sci. Technol. **13**, 147 (1998).

[59] V. W. Houston, Phys. Rev. **57**, 184 (1940).

[60] N. W. Ashcroft and N. D. Mermin, *Solid State Physics* (Harcourt Brace College Publishers, Fort Worth, 1976).

[61] A. Lohner, K. Rick, P. Leisching, A. Leitenstorfer, T. Elsaesser, T. Kuhn, F. Rossi, and W. Stolz, Phys. Rev. Lett. **71**, 77 (1993).

[62] J. Shah, *Ultafast Spectroscopy of Semiconductors and Semiconductor Nanostructures* (Springer Series in Solid-State Science, Vol. 115, Springer-Verlag, Berlin, 1999).

[63] A. Leitenstorfer, S. Hunsche, J. Shah, M. C. Nuss, and W. H. Knox, Phys. Rev. Lett. **82**, 5140 (1999).

[64] M. B. Dahan, E. Peik, J. Reichel, Y. Castin, and C. Salomon, Phys. Rev. Lett. **76**, 4508 (1996).

[65] T. Pertsch, P. Dannberg, W. Elflein, and A. Bräuer, Phys. Rev. Lett. **83**, 4752 (1999).

[66] R. Sapienza, P. Costantino, D. Wiersma, M. G. C. J. Oton, and L. Pavesi, Phys. Rev. Lett. **91**, 263902 (2003).

[67] A. M. Bouchard and M. Luban, Phys. Rev. B **47**, 6815 (1993).

[68] E. O. Kane, J. Phys. Chem. Solids **12**, 181 (1959).

[69] M. Holthaus, Journal of Optics B: Quantum Semiclass. Opt. **2**, 589 (2000).

[70] C. F. Bharucha, K. W. Madison, P. R. Morrow, S. R. Wilkinson, B. Sundaram, and M. G. Raizen, Phys. Rev. A **55**, R857 (1997).

[71] M. Glück, A. R. Kolovsky, and H. J. Korsch, Phys. Rev. Lett. **83**, 891 (1999).

[72] M. Glück, A. R. Kolovsky, and H. J. Korsch, Phys. Rep. **366**, 103 (2002).

[73] B. Rosam, K. Leo, M. Glück, F. Keck, H. J. Korsch, F. Zimmer, and K. Köhler, Phys. Rev. B **68**, 125301 (2003).

[74] M. Wagner and H. Mizuta, Phys. Rev. B **48**, 14393 (1993).

[75] D. S. Chemla and J. Shah, Nature **411**, 549 (2001).

[76] Y. R. Shen, *The Principles of Nonlinear Optics* (John Wiley & Sons, New York, 1984).

[77] J. Wang, J. P. Leburton, C. M. Herzinger, T. A. de Temple, and J. J. Coleman, PRB **47**, 4783 (1993).

[78] C. F. Klingshirn, *Semiconductor Optics* (Springer-Verlag, 1997).

[79] T. Yajima and Y. Taira, J. Phys. Soc. Jp. **47**, 1620 (1979).

[80] B. Rosam, D. Meinhold, F. Löser, V. G. Lyssenko, S. Glutsch, F. Bechstedt, F. Rossi, K. Köhler, and K. Leo, Phys. Rev. Lett. **86**, 1307 (2001).

[81] D. A. B. Miller and A. M. Fox, *Tunneling Resonance - TRMF software* (1989).

[82] J. J. LePore, J. Appl. Phys. **51**, 6441 (1980).

[83] B. Rosam, D. Meinhold, F. Löser, V. G. Lyssenko, K. Leo, S. Glutsch, F. Bechstedt, and K. Köhler, phys. stat. sol. (b) **221**, 463 (2000).

[84] S. Glutsch, F. Bechstedt, B. Rosam, and K. Leo, Phys. Rev. B **63**, 085307 (2001).

[85] D. Meinhold, B. Rosam, F. Löser, V. G. Lyssenko, F. Rossi, J.-Z. Zhang, K. Köhler, and K. Leo, Phys. Rev. B **65**, 1133027 (2002).

[86] A. B. Hummel, T. Bauer, H. G. Roskos, S. Glutsch, and K. Köhler, Phys. Rev. B **67**, 0453191 (2003).

[87] E. F. Schubert, E. O. Göbel, Y. Horikoshi, K. Ploog, and H. J. Queisser, Phys. Rev. B **30**, 813 (1984).

[88] R. Klann, H. T. Grahn, and K. Fujiwara, Phys. Rev. B **51**(15), 10232 (1995).

[89] A. Ourmazd, W. Tsang, J. Rentschler, and D. Taylor, Appl. Phys. Lett. **50**(20), 1417 (1987).

[90] J. M. Ziman, *Principles of the Theory of Solids* (Cambridge University Press, Cambridge, Second Edition, 1972).

[91] K. Leo, J. Shah, T. C. Damen, A. Schulze, T. Meier, S. Schmitt-Rink, P. Thomas, E. O. Göbel, S. L. Chuang, M. C. Luo, W. Schäfer, K. Köhler, *et al.*, IEEE J. Quantum Electron. **28**, 2498 (1992).

[92] B. Ferguson and X.-C. Zhang, Nature Materials **1**, 26 (2002).

[93] H. G. Roskos, C. Waschke, R. Schwedler, P. Leisching, Y. Dhaibi, H. Kurz, and K. Köhler, Superlatt. Microstruct. **15**, 281 (1994).

[94] R. Martini, G. Klose, H. G. Roskos, H. Kurz, H. T. Grahn, and R. Hey, Phys. Rev. B **54**, R14325 (1996).

[95] S. Madhavi, M. Abe, Y. Shimada, and K. Hirakawa, Phys. Rev. B **65**, 193308 (2002).

[96] Y. Shimada, K. Hirakawa, and S.-W. Lee, Appl. Phys. Lett. **81**, 1642 (2002).

[97] K. Jin, M. Odnoblyudov, Y. Shimada, K. Hirakawa, and K. A. Chao, Phys. Rev. B **68**, 153315 (2003).

[98] Y. Shimada, K. Hirakawa, M. Odnoblioudov, and K. A. Chao, Phys. Rev. Lett. **90**, 046806 (2003).

[99] F. Löser, Y. A. Kosevich, K. Köhler, and K. Leo, Phys. Rev. B **61**, R13373 (2000).

[100] V. G. Lyssenko, G. Valušis, F. Löser, T. Hasche, K. Leo, M. M. Dignam, and K. Köhler, Phys. Rev. Lett. **79**, 301 (1997).

[101] M. Hawton and M. M. Dignam, Phys. Rev. Lett. **91**, 267402 (2003).

[102] T. Dekorsy, P. Leisching, K. Köhler, and H. Kurz, Phys. Rev. B **50**, 8106 (1994).

[103] M. Först, G. Segschneider, T. Dekorsy, H. Kurz, and K. Köhler, Phys. Rev. B **61**, R10563 (2000).

[104] R. Huber, A. Brodschelm, F. Tauser, and A. Leitenstorfer, Appl. Phys. Lett. **76**, 3191 (2000).

[105] M. M. Fejer, S. J. B. Yoo, R. L. Byer, A. Harwit, and J. S. Harris, Phys. Rev. Lett. **62**, 1041 (1989).

[106] P. Boucaud, F. H. Julien, D. D. Yang, J.-M. Lourtioz, E. Rosencher, P. Bois, and J. Nagle, Appl. Phys. Lett. **57**, 215 (1990).

[107] C. Sirtori, F. Capasso, D. L. Sivco, A. L. Hutchinson, and A. Y. Cho, Appl. Phys. Lett. **60**, 151 (1991).

[108] C. Sirtori, F. Capasso, D. L. Sivco, and A. Y. Cho, Phys. Rev. Lett. **68**, 1010 (1992).

[109] C. Sirtori, F. Capasso, J. Faist, L. N. Pfeiffer, and K. W. West, Appl. Phys. Lett. **65**, 445 (1994).

[110] A. A. Belyanin, F. Capasso, V. V. Kocharovsky, Vl. V. Kocharovsky, and M. O. Scully, Phys. Rev. A **63**, 053803 (053803).

[111] A. Belyanin, V. Kocharovsky, Vl. Kocharovsky, and M. Scully, Phys. Rev. A **65**, 053824 (2002).

[112] R. Köhler, A. Tredicucci, F. Beltram, H. E. Beere, E. H. Linfield, A. G. Davies, D. A. Ritchie, R. C. Iotti, and F. Rossi, Nature **417**, 156 (2002).

[113] B. S. Williams, S. Kumar, H. Callebaut, Q. Hu, and J. L. Reno, Appl. Phys. Lett. **83**, 5142 (2003).

[114] R. Köhler, A. Tredicucci, F. Beltram, H. E. Beere, E. H. Linfield, A. G. Davies, D. A. Ritchie, S. S. Dhillon, and C. Sirtori, Appl. Phys. Lett. **82**, 1518 (2003).

[115] A. V. Korovin, F. T. Vasko, and V. V. Mitin, Phys. Rev. B **62**, 8192 (2000).

[116] R.-B. Liu and B.-F. Zhu, Europhys. Lett. **50**, 526 (2000).

[117] A. V. Korovin, F. T. Vasko, and V. V. Mitin, Phys. Rev. B **66**, 085302 (2002).

[118] B. B. Hu, J. T. Darrow, X.-C. Zhang, D. H. Auston, and P. R. Smith, Appl. Phys. Lett. **56**, 886 (1990).

[119] R. Martini, *PhD-Thesis: Verstärkung kohärenter THz-Emission aus impulsiv angeregten Halbleitern und Halbleiterheterostrukturen* (Shaker Verlag, Aachen, 1999).

[120] K. Victor, H. G. Roskos, and C. Waschke, J. Opt. Soc. Am. B **11**, 2470 (1994).

[121] M. S. C. Luo, S. L. Chuang, P. C. M. Planken, I. Brener, and M. C. Nuss, Phys. Rev. B **48**, 11043 (1993).

[122] P. C. M. Planken, M. C. Nuss, W. H. Knox, D. A. B. Miller, and K. W. Goosen, Appl. Phys. Lett. **61**, 2009 (1992).

[123] M. C. Nuss and J. Orenstein, *Terahertz Time-Domain Spectroscopy* (Topics in Applied Physics, Vol. 47, Springer-Verlag, Berlin, 1998).

[124] M. van Exter, C. Fattinger, and D. Grischkowsky, Appl. Phys. Lett. **55**, 337 (1989).

[125] D. H. Auston, K. P. Cheung, and P. R. Smith, Appl. Phys. Lett. **45**, 284 (1984).

[126] K. A. McIntosh, K. B. Nichols, S. Verghese, and E. R. Brown, Appl. Phys. Lett. **70**, 354 (1997).

[127] M. van Exter and D. R. Grischkowsky, IEEE Trans. Microwave Theory Tech. **38**, 1684 (1990).

[128] M. Tani, R. Fukasawa, H. Abe, S. Matsurura, and K. Sakai, Appl. Phys. Lett. **83**, 2473 (1990).

[129] C. Waschke, H. G. Roskos, R. Schwedler, K. Leo, H. Kurz, and K. Köhler, Phys. Rev. Lett. **70**, 3319 (1993).

[130] S. Kono, M. Tani, and K. Sakai, Appl. Phys. Lett. **79**, 898 (2001).

[131] M. Joffre, A. Bonvalet, A. Migus, and J.-L. Martin, Opt. Lett. **21**, 964 (1996).

[132] R. Kersting, K. Unterrainer, G. Strasser, H. F. Kauffmann, and E. Gornik, Phys. Rev. Lett. **79**, 3038 (1997).

[133] Q. Wu and X.-C. Zhang, Appl. Phys. Lett. **67**, 3523 (1995).

[134] P. U. Jepsen, C. Winnewisser, M. Schall, V. Schyja, S. R. Keiding, and H. Helm, Phys. Rev. E **53**, R3052 (1996).

[135] A. Nahata, D. H. Auston, and T. F. Heinz, Appl. Phys. Lett. **68**, 150 (1996).

[136] A. Leitenstorfer, S. Hunsche, J. Shah, M. C. Nuss, and W. H. Knox, Appl. Phys. Lett. **74**, 1516 (1999).

[137] A. Yariv, *Quantum Electronics* (John Wiley & Sons, New York, 1989).

[138] P. N. Prasad and D. J. Williams, *Introduction to Nonlinear Optical Effects in Molecules and Polymers* (John Wiley & Sons, New York, Chichester, Brisbane, 1991).

[139] Q. Wu and X.-C. Zhang, Appl. Phys. Lett. **68**, 1604 (1996).

[140] D. T. F. Marple, J. Appl. Phys. **35**, 539 (1964).

[141] E. D. Palik, *Handbook of Optical Constants of Solids II* (Academic Press, Boston, 1991).

[142] Q. Wu and X.-C. Zhang, Appl. Phys. Lett. **70**, 1784 (1997).

[143] Y. Cai, I. Brener, J. Lopata, J. Wynn, L. Pfeiffer, J. B. Stark, Q. Wu, X. C. Zhang, and J. F. Federici, Appl. Phys. Lett. **73**, 444 (1998).

[144] A. Nahata, A. S. Weling, and T. F. Heinz, Appl. Phys. Lett. **69**, 2321 (1996).

[145] Q. Wu, M. Litz, and X.-C. Zhang, Appl. Phys. Lett. **68**, 2924 (1996).

[146] Q. Wu and X.-C. Zhang, Appl. Phys. Lett. **71**, 1285 (1997).

[147] P. C. M. Planken, H.-K. Nienhuys, H. J. Bakker, and T. Wenckenbach, J. Opt. Soc. Am. B **18**, 313 (2001).

[148] W. L. Faust and C. H. Henry, Phys. Rev. Lett. **17**, 1265 (1966).

[149] A. Mooradian and G. B. Wright, Solid State Commun. **4**, 431 (1966).

[150] B. A. Weinstein and G. S. Piermarini, Phys. Rev. B **12**, 1172 (1975).

[151] W. L. Faust, C. H. Henry, and R. H. Eick, Phys. Rev. **173**, 781 (1968).

[152] P. Y. Han and X.-C. Zhang, Appl. Phys. Lett. **73**, 3049 (1998).

[153] X.-C. Zhang, J. T. Darrow, B. B. Hu, C. H. Auston, M. T. Schmidt, P. Tham, and E. S. Yang, Appl. Phys. Lett. **56**, 2228 (1990).

[154] A. M. Weiner, J. P. Heritage, and E. M. Kirschner, J. Opt. Soc. Am. B **5**, 1563 (1988).

[155] A. M. Weiner, Rev. Sci. Instrum. **71**, 1929 (2000).

[156] C. Ruilliere, *Femtosecond Laser Pulses* (Springer-Verlag, Berlin, 1998).

[157] J.-C. Diels and W. Rudolph, *Ultrashort Laser Pulse Phenomena* (Academic Press, San Diego, 1996).

[158] S. A. Ktitorov, G. S. Simin, and V. Y. Sindalovskii, Sov. Phys. Solid State **13**, 1872 (1972).

[159] H. Willenberg, G. H. Döhler, and J. Faist, Phys. Rev. B **67**, 085315 (2003).

[160] N. Sekine, Y. Shimada, and K. Hirakawa, Appl. Phys. Lett. **83**, 4794 (2003).

[161] G. von Plessen, T. Meier, J. Feldmann, E. O. Göbel, and P. Thomas, Phys. Rev. B **49**, 14058 (1994).

[162] H. Wang, K. B. Ferrio, D. G. Steel, P. R. Berman, Y. Z. Hu, R. Binder, and S. W. Koch, Phys. Rev. A **49**, R1551 (1994).

[163] L. Yang, B. Rosam, and M. M. Dignam, Phys. Rev. B, submitted .

[164] D. Turchinovich, P. Uhd Jepsen, B. S. Monozon, and M. Koch, Phys. Rev. B **68**, 241307 (2003).

[165] P. Leisching, T. Dekorsy, H. J. Bakker, H. Kurz, and K. Köhler, Phys. Rev. B **51**, 18015 (1995).

[166] T. Dekorsy, A. M. T. Kim, G. C. Cho, S. Hunsche, H. J. Bakker, H. Kurz, S. L. Chuang, and K.Köhler, Phys. Rev. Lett. **77**, 3045 (196).

[167] J. J. Carey, K. Wynne, R. T. Bailey, D. Pugh, J. N. Sherwood, and F. R. Cruickshank, Appl. Phys. Lett. **81**, 4335 (2002).

[168] J. Y. Sohn, Y. H. Ahn, D. J. Park, E. Oh, and D. S. Kim, Appl. Phys. Lett. **81**, 13 (2002).

[169] N. Linder, K. H. Schmidt, W. Geisselbrecht, G. H. Döhler, H. T. Grahn, K. Ploog, and H. Schneider, Phys. Rev. B **52**, 17352 (1995).

[170] I. Brener, P. C. M. Planken, M. C. Nuss, L. Pfeiffer, D. E. Leaird, and A. M. Weiner, Appl. Phys. Lett. **63**, 2213 (1993).

[171] B. Rosam, L. Yang, K. Leo, and M. M. Dignam, Appl. Phys. Lett. **85**, 4612 (2004).

[172] S. Glutsch, Phys. Rev. B **69**, 2353171 (2004).

[173] D. Meinhold, *Diplomarbeit* (Technische Universität Dresden, 2000).

[174] Y. Shimada, N. Sekine, and K. Hirakawa, Appl. Phys. Lett. **84**, 4926 (2004).

[175] C. Rauch, G. Strasser, K. U. W. Boxleitner, E. Gornik, and A. Wacker, Phys. Rev. Lett. **81**, 3495 (1998).

[176] R. Franculli, A. M. Weiner, M. M. Dignam, D. Meinhold, and K. Leo, Phys. Rev. B, submitted .

[177] S. Ktitorov, G. Simin, and V. Sindalovskii, Fiz. Tverd. Tela (Leningrad) **13**, 2230 (1971).

Danksagung

An dieser Stelle möchte ich all denen danken, die zum Erfolg dieser Arbeit beigetragen haben:

Mein Dank gilt zuvorderst meinem Betreuer Prof. Dr. Karl Leo für seine Unterstützung und Förderung, zahlreiche Hinweise und Anregungen sowie für das stets angenehm offene Arbeitsklima. Sein Engagement bei der Beschaffung von Projektgeldern hat die Durchführung der Experimente in einem bestens ausgestatteten Labor ermöglicht.

Ich danke Prof. Dr. Vadim Lyssenko für die stimulierenden Diskussionen, in denen manche experimentelle Idee geboren wurde. Ich konnte mir von ihm einige wichtige Kniffe des erfahrenen Experimentators abschauen.

Meinen Kollegen der Kurzzeit-Spektroskopie: Dr. Tobias Canzler, Egbert Engel, André Holzhey, Christian Holfeld, Marco Koschorrek, Falk Löser, Dirk Meinhold und Dr. Markas Sudzius danke ich für ihre konstruktive Mitwirkung in einer freundschaftlichen Arbeitsatmosphäre.

PD Dr. Stephan Glutsch danke ich für die fruchtbare Zusammenarbeit. Er hat mit seinen Ergebnissen das Thema Zener-Tunneln von Seiten der Theorie entscheidend vorangetrieben.

Der Arbeitsgruppe um Prof. Dr. Hans Jürgen Korsch, im speziellen Dr. Frank Keck und Dr. Andrey Kolovsky, danke ich für ihr Engagement bei der Modellierung der Zener-Tunnel-Rate von Wannier-Stark-Leiter-Zuständen.

Eine sehr wichtige und konstruktive Kooperation fand statt mit Dr. Marc Dignam und Dr. Lijun Yang, deren Modellrechnungen die Ergebnisse der THz-Experimente hervorragend erklären konnten. Die Arbeit an gemeinsamen Veröffentlichungen haben das Thema entscheidend vorangebracht.

Prof. X.-C. Zhang danke ich für einen lehrreichen Forschungsaufenthalt in seiner Arbeitsgruppe am Rensselaer Polytechnic Institute in Troy.

Dr. Klaus Köhler danke ich für die Herstellung der hervorragenden Proben.

Ich danke meinem Freund Dr. Paul Coe für seine Mühe bei der Korrektur meiner

Dissertation.

Für ihre Hilfe und Unterstützung danke ich den wichtigen Fachkräften unseres Institutes: Herrn Volker Trepte in der mechanischen Werkstatt, Herrn Kai Schmidt bei IT-Problemen und Frau Eva Schmidt in der Verwaltung.

Meiner Familie und meinen Freunden danke ich für Ihre große Unterstützung.

Dem ganzen Team des Instituts für Angewandte Photophysik danke ich für ein wunderbares Arbeitsklima und eine schöne Zeit.

Versicherung

Hiermit versichere ich, dass ich die vorliegende Arbeit ohne unzulässige Hilfe Dritter und ohne Benutzung anderer als der angegebenen Hilfsmittel angefertigt habe. Gedanken, die aus fremden Quellen direkt oder indirekt übernommen wurden, sind als solche kenntlich gemacht. Die Arbeit wurde bisher weder im Inland noch im Ausland in gleicher oder ähnlicher Form einer anderen Prüfungsbehörde vorgelegt. Ich erkenne die Promotionsordnung der Technischen Universität Dresden an.

Diese Arbeit wurde am Institut für Angewandte Photophysik der Technischen Universität Dresden unter der wissenschaftlichen Betreuung von Prof. Dr. Karl Leo angefertigt.

Dresden, den 15.12.2004

Ben Rosam